

BULGARIAN CHEMICAL COMMUNICATIONS

2020 Volume 52 / Number 1

*Journal of the Chemical Institutes
of the Bulgarian Academy of Sciences
and of the Union of Chemists in Bulgaria*

Optimization technology of large-size Si(Li) p-i-n structures for X-ray detectors

R. A. Muminov¹, S. A. Radzhapov¹, A. K. Saymbetov^{2*}, R. K. Manatbayev²,
Yo. K. Toshmurodov¹, N. M. Japashov², N. B. Kuttybay², A. G. Georgiev³

¹Physico-Technical Institute of the Academy of Sciences of Uzbekistan, Uzbekistan

²Al-Farabi Kazakh National University, Faculty of Physics and Technology, Kazakhstan

³Technical University - Sofia, Plovdiv Branch, Faculty of Mechanical Engineering, Department of Mechanics, Bulgaria

Received January 8, 2018; Revised December 13, 2019

In this work, the features of manufacturing and investigating the electrophysical characteristics of Si(Li) p-i-n structures for detectors with a big volume of working area were considered. The technology of manufacturing of big-area (up to 110 mm) semiconductor detector structures with thickness of sensitive area up to 10 mm, from low-resistance silicon grown by the Czochralski process and with high-resistance silicon obtained by the floating zone melting method was developed. The I-V, C-V and noise vs voltage dependences of detectors produced from these crystals were compared. Moreover, the methods of double-sided diffusion and drift of lithium ions were applied to these crystals. Also, the methods of providing highly uniform compensated regions of detectors were considered and methods for laying uniform effective ohmic contacts on a big area of the structure were developed.

Keywords: Diffusion of lithium, Drift of lithium ions, p-i-n structure, Si(Li) detectors.

INTRODUCTION

It is well known that silicon detectors are widely used in the detection of various particles and radiations. One of the main advantages of such detectors is low energy, high braking power, highly efficient statistics set, good radiation resistance, etc. [1-2]. Due to these characteristics, silicon detectors are the object of research and production of various laboratories around the world. The literature data analysis [3-5] shows that every presented semiconductor detector material (Si, Ge, GaAs), and detectors from this material, have significant disadvantages. Therefore, the important problem of semiconductor detector structures is to apply nontraditional, radiation-resistant and heat-stable materials in manufacturing semiconductor detectors that have similar characteristics with silicon, as silicon is the most useable material not only for detector manufacturing, but also for all semiconductor electronics. It is necessary to provide small reverse currents without using cooling, noises and to create extended sensitive area of a large volume. Moreover, the material should have high lifetime and mobility of charge carriers, small concentration of capture centers of recombination and should withstand a high electric field for obtaining good energy resolution.

Nowadays, in the world practice, detectors of relatively small size are sufficiently developed [6,7]. Simultaneously, there is an urgent need for development of semiconductor detectors of large sizes [8-10]. However, their development has their own physical, technical and technological

peculiarities and difficulties. They are associated with the manifestation of the effects caused by parameters of initial crystals of big diameter and by manufacturing on their basis effective detectors of nuclear radiation. The technology of manufacturing semiconductor detectors of nuclear radiation is sufficiently complicated, and consists of mechanical, chemical and thermal operations, also it needs structural decorations. Every operation has its own purpose and needs certain control. Necessity of manufacturing of detectors of nuclear radiation with reproducible parameters and preserving the characteristics for a sufficiently long time determined the technology of manufacturing semiconductor detectors for detection of nuclear radiation. The most tested industrial detector materials of big-diameter silicon have significant heterogeneity of distribution of the electrical parameters in the crystal volume. Local and impurity strips existing in the sensitive volume of semiconductor detectors significantly impair their radiometric characteristics.

MATERIALS, TECHNOLOGY AND METHODS

Accuracy of compensation of initial semiconductor material is the most important characteristic of quality of Si(Li) p-i-n structures. However, despite the anomalously high mobility of lithium ions in silicon, they need long time for diffusion – drift compensation in big volumes (thickness ~ 10 mm, surface ≈ 110 mm). In order to significantly reduce the compensation process time of silicon in big volumes and to eliminate the

* To whom all correspondence should be sent:

E-mail: asaymbetov@gmail.com

negative effects of prolonged withstanding of crystal under high temperature and voltage, we developed the methods of creating Si(Li) p-i-n+ structures [11]. Reducing compensation time helps to minimize inhomogeneities in the detector crystal and improves the energy resolution of the detector.

For detector fabrication two types of silicon crystals were used. The first one was the dislocation-free monocrystalline silicon of p-type grown in an argon atmosphere by the Czochralski process, with diameter of 110 mm, high resistivity $\rho = 10 \div 12 \text{ Ohm.cm}$ and a lifetime $\tau \geq 50 \mu\text{s}$, chosen as an initial material. The concentration of oxygen was $N_o = 2 \cdot 10^{17} \text{ cm}^{-3}$. Second was the high-resistance silicon crystal obtained by the float-zone method, with a high resistivity $\rho = 1000 \div 5000 \text{ Ohm.cm}$ and a lifetime $\tau \geq 500 \mu\text{s}$.

Furthermore, by using these crystals, a p-i-n structure was created. The process of manufacturing p-i-n structures consists of the following stages:

- To remove damaged layer during the cutting, double sided grinding on a grinding machine with micropowders M-14, M-5 was used with a consequent reduction in the abrasive diameter. Wherein, at least $50 \mu\text{m}$ thick layer was removed from each side. After grinding, the plates were flushed with de-ionized water containing alkaline-free soap.

- The initial structure was obtained by diffusion of lithium. Lithium diffusion was carried out from two sides in a vacuum $p \sim 10^{-5} \text{ mm Hg}$ at a depth of $300 \mu\text{m}$ on the entire surface of the plate for $t = 3 \text{ min}$ at a temperature of 450°C . Detailed description of physical procedure of double sided diffusions of lithium atoms into silicon was shown in a work [12].

- Etching in a polishing etchant (1:3:1 mixture of $\text{HF}:\text{HNO}_3:\text{CH}_2\text{COOH}_2$) and in an aniline etchant.

- Drift of lithium ions in the electric field of the p-n junction should be carried out at a temperature of $(70-80)^\circ\text{C}$ and a reverse bias voltage of $100 \div 400 \text{ V}$ during 10-20 days, depending on the thickness of the sensitive region.

- After finishing drift process, to detect the i-region, one of the sides of the crystal of the n + - region of n + -i-p structures was grinded on a glass disk with silicon carbide micropowder. The thickness of the layer to be removed was assessed taking into account the diffusion profile blurring. The thickness of the grinded layer was usually $50 \div 400 \mu\text{m}$. Reduction of the i-region was performed using a decorating etchant $\text{HNO}_3:\text{HF}=1:1000$. The i-region was considered completely obtained when its contours were close to a circle with a diameter

equal to the diameter of the diffusion region. To obtain ohmic metal contacts, gold and aluminum coatings were used (Fig. 1).

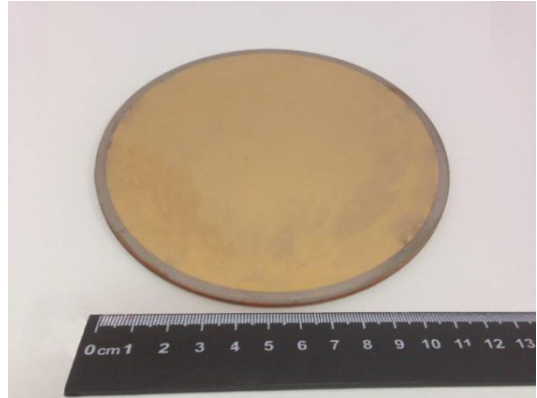


Fig. 1. General view of Si(Li) p-i-n detector structure

For the method of double-sided diffusion and drift of lithium ions it is possible to estimate the compensated area depth by using the well known equation proposed by Pell (1960)[13]:

$$W = 0.5 (\rho U)^{1/2} \quad (1)$$

where ρ is resistivity in Ohm.cm and U – drift voltage.

The rate of growth of the compensated area depth is defined as:

$$R = \frac{dW}{dt} = \mu E = \mu U / W \quad (2)$$

$$\text{or} \quad W = \sqrt{2\mu U t}, \quad (3)$$

where: μ - mobility of lithium ions, t – drift time.

In the case of bilateral drift the path traveled by the lithium ions is reduced by half.

$$\frac{W}{2} = \sqrt{2\mu U t} \quad (4)$$

Consequently, the expression for the time of compensation in the case of double sided drift is:

$$\sqrt{\frac{t_1}{t_2}} = 2 \quad t_2 = \frac{1}{4} t_1 \quad (5)$$

The result shows, that in the proposed method the compensation time of specified volume of p-Si crystal is reduced 4 times. This is obvious from this empirical expression for the time dependence of compensated area depth in case of unilateral drift.

RESULTS AND DISCUSSION

The variation of characteristics of lithium distribution depending on the initial material parameters and basically on dislocation density and specific resistance in the Si(Li) p-i-n area has drawn particular interest. It is widely believed that first, at the process of drift all inhomogeneities of

the initial material are corrected and the specific resistance of the compensated area is equal to the specific resistance of the initial material. Second, electric field distribution in the compensated area is almost uniform.

Consequently, during the drift process, the intrinsic conduction corresponding to the drift temperature is almost achieved. The difference between resistance of compensated area and initial material resistance is the result of influence of drift process of mobile thermal generated carriers. The temperature, necessary to exploit semiconductor detectors, is usually much lower than the drift temperature, consequently, under working conditions the quantity of thermally generated vapor is reduced because the equilibrium of mobile carriers, donor and acceptor impurities is violated. As a result, the basic area of Si(Li) p-i-n structure can be highly overcompensated with a notable excessive impurity gradient. Obviously, this influence will appear intensively on low-resistance materials. The effect can be reduced by using additional drift process under lower temperature, wherein a weakening of fixed spatial charge occurs that allows the lithium ions to be redistributed. Under uniform compensation conditions, the applied voltage of reversed bias leads to a static electric field at every point of the compensated region – it is the ideal state in terms of carrier formation. With the increase in specific resistivity of initial silicon the ratio of thermally generated carriers and donor and acceptor impurities varies, also the specific resistivity of compensated region increases.

During the work of semiconductor detectors, the values of current and capacitance play an important role when reverse bias voltage is applied. For the big-size semiconductor detectors the flatness of p-n junctions of the entire area of its sensitive surface is of great importance. The direct determination of the current-voltage characteristics (CVC) gives useful information. The CVC during application of reverse bias voltage to Si(Li) p-i-n structure were investigated. On Fig. 2 the typical CVC of Si (Li) p-i-n structures are shown, made with low-resistance silicon, grown by the Czochralski process (1) and with high-resistance silicon obtained by the float-zone method (2). It is obvious from the figure that the low-resistance silicon grown by the Czochralski process (1) has the advantages of manufacturing lithium drift detectors with a big volume, small reversed current and high exploitation characteristics. On a par with values of reversed current, the good characteristic of the structure is high breakdown voltage, indicating that the surface of the structure is sufficiently clean.

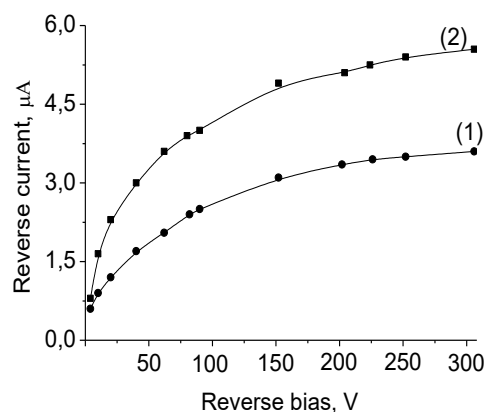


Fig. 2. The reverse branch of CVC of Si(Li) p-i-n structure grown by the Czochralski process (1) and by the float-zone method (2).

The capacitance of Si(Li) p-i-n structure is directly connected with thickness of the depletion layer and with a specific resistance of initial material. Therefore, by measuring this, it is possible to identify the specific resistance of compensated area of silicon in the prepared structure and predict the values of maximum energy of charged particle, under the conditions of its totally absorption in the depletion layer. The same samples, which were taken to investigate the CVC, were taken to study farad – voltage characteristics (FVC). On Fig. 3, the FVC of Si(Li) p-i-n structure are shown, made with low-resistance silicon, grown by the Czochralski process (1) and with high-resistance silicon obtained by float-zone method (2).

One of the main exploitation characteristics of semiconductor detectors of nuclear radiation is the energetic equivalent of noise value. This parameter determines the radiometric abilities and efficiency of detection.

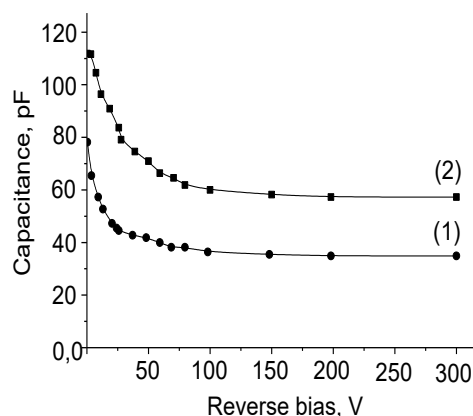


Fig. 3. FVC of Si(Li) p-i-n structure grown by the Czochralski process (1) and by the float-zone method (2).

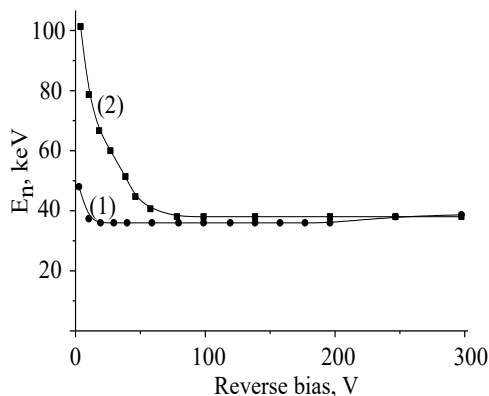


Fig. 4. Volt-noise characteristics of Si(Li) p-i-n detectors made of silicon, grown by the Czochralski process (1) and by the float-zone method (2).

On Fig. 4, curve (1) corresponds to the initial crystal with high resistivity - $\rho = 10\div 12 \text{ Ohm}\cdot\text{cm}$ grown by the Czochralski process, and curve (2) corresponds to the crystal with high resistivity $\rho = 5000 \text{ Ohm}\cdot\text{cm}$ grown by the float-zone method.

On Fig. 5, the investigation of amplitude spectra of β -particles from the ^{207}Bi source is illustrated. The energy resolution of detectors for β -particles from the ^{207}Bi source is 1 MeV, $R_{\beta} = 38 \text{ keV}$ taken at $T = 300 \text{ }^{\circ}\text{C}$.

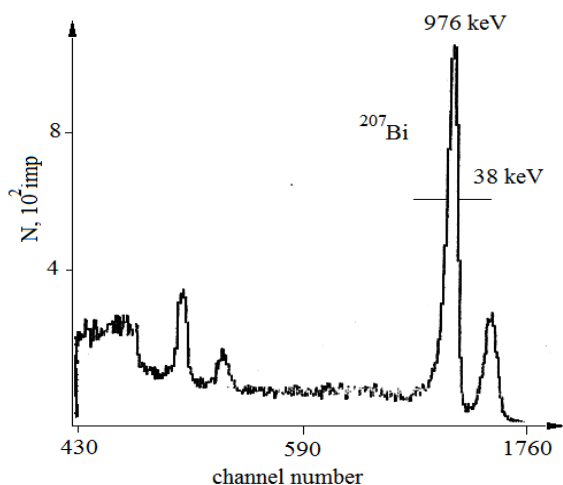


Fig. 5. The energy resolution of the detector for β -particles from ^{207}Bi .

CONCLUSIONS

In conclusion, it should be noted that all results of this work have scientific and practical value and can be used in broad areas of science and technology. In particular, the technology of manufacturing big-area (up to 110 mm) semiconductor detector structures with thickness of sensitive area up to 10 mm from low-resistance silicon grown by the Czochralski process and with

high-resistance silicon obtained by the floating zone melting method was developed. From the CVC it is obvious that the reverse current in the crystals grown by the Czochralski process is lower than in the crystals grown by the float-zone method.

The method of double-sided diffusion and drift of lithium ions was proposed. It was shown that the proposed method of compensation of predetermined crystal volume reduces the time of drift 4 times and notably improves compensation quality. This is due to the suppression of the influence of free carriers generated at the drift temperature. The method of double-sided diffusion and drift of lithium ions can optimize the manufacturing process and improve electro-physical and radiometrical characteristics of Si(Li) p-i-n detectors.

REFERENCES

1. Yu. K. Akimov, *Instruments and Experimental Techniques*, **50**, 1 (2007).
2. S. A. Azimov, *Silicon-Lithium Nuclear Radiation Detectors*, FAN, Tashkent, 1981.
3. Kanno, Ikuo, *J. of Nuclear Science and Technology*, **28**, 87 (1991).
4. R. Durak, S. Erzenoglu, Y. Kurucu, Y. Sahin, *Instrumentation Science & Technology*, **25**, 335, (1997).
5. A. Šagátová, *Radiation Effects and Defects in Solids*, **170**, 192 (2015).
6. P. Lechner, C. Fiorini, R. Hartmann, J. Kemmer, N. Krause, P. Leutenegger, L. Strüder, *Nuclear Instruments and Methods in Physics Research Section A: Accelerators, Spectrometers, Detectors and Associated Equipment*, **458**, 281 (2001).
7. G. F. Knoll, *Radiation Detection and Measurement*, John Wiley & Sons, 2010.
8. R. A. Muminov, A. K. Saymbetov, Yo. K. Toshmurodov, *Instruments and Experimental Techniques*, **56**, 32 (2013).
9. R. A. Muminov, S. A. Radzhapov, A. K. Saimbetov, *Technical Physics Letters*, **35**, 768 (2009).
10. R. A. Muminov, S. A. Radzhapov, A. K. Saimbetov, *Atomic Energy*, **106**, 141 (2009).
11. R. A. Muminov, A. K. Saymbetov, A. A. Mansurova, S. A. Radzhapov, B. K. Mukhametkali, N. K. Sissenov, N. B. Kuttybay, *J. of Semiconductor Technology and Science*, **17**, 591 (2017).
12. R. A. Muminov, A. K. Saymbetov, N. M. Japashov, Y. K. Toshmurodov, S. A. Radzhapov, N. B. Kuttybay, M. K. Nurgaliyev, *Journal of Nano- and Electronic Physics*, **11**, 02031 (2019).
13. E. M. Pell, *Journal of Applied Physics*, **31**, 291 (1960).

Synthesis, X-ray crystal structure and spectroscopic studies of benzothiazole Schiff base

Y. S. Demircioğlu¹, H. C. Sakarya^{2*}, Y. Süzen³

¹ Eskisehir Technical University, Faculty of Science, Department of Chemistry, Yunusemre campus P.R. 26470, Eskisehir, Turkey

² Eskişehir Osmangazi University, Department of Chemistry, Faculty of Arts and Science, 26480, Eskişehir, Turkey

³ Anadolu University, Faculty of Science, Department of Chemistry, P.O. Box: 26470 Eskisehir Turkey

Received March 16, 2028; Accepted September 25, 2019

The new Schiff base **3** was synthesized by reacting 6-methyl-2-aminobenzothiazole and 2-methoxy-1-naphthaldehyde in ethyl L- lactate as a green solvent. Compound **3** was characterized by FT-IR, ¹H NMR, ¹³C NMR, single crystal X-ray diffraction study and elemental analysis. The compound crystallizes in the monoclinic space group P21/n, with a= 8.1077(15), b=17.302(3), c=22.790(4) Å, β= 95.799(7), V= 3180.7(1) Å³, absorption coefficient= 0.212 mm⁻¹. The asymmetric unit contains two crystallographically independent molecules with intramolecular C-H···N and intermolecular C-H···Cg interactions.

Keywords: Benzothiazole, Schiff base, Ethyl L-lactate, X-ray structure

INTRODUCTION

The reaction of primary amines with aldehydes or ketones leads to Schiff bases containing the imine C=N double bond. The Schiff base formation reaction was carried out by Hugo Schiff in 1864 and the compounds obtained from this reaction were named Schiff bases [1]. If the aryl group is not bound to the carbon or nitrogen atom of the imine group, the Schiff base immediately polymerises or decomposes [2]. Schiff bases have an important role in the development of coordination chemistry, since the transition metals easily form stable complexes with many species [3-5].

Schiff bases are the most widely used organic compounds both as synthetic intermediates and in coordination chemistry [6]. Schiff bases are an important ligand that coordinates to metal ions *via* azomethine nitrogen. Some Schiff bases have been reported to have antibacterial, antifungal, anticancer and diuretic activities. It is also known that Schiff bases are widely used in food industry, paint industry, analytical chemistry, catalysis, fungicide, agricultural chemical and biological activities [7-9]. Imines are also intermediates in many enzymatic and pharmaceutical reactions. Conventional syntheses often require the use of toxic solvents such as methylene chloride [10] or refluxing in petroleum-based solvents such as toluene as azeotropic agents [11]. More recently, green chemistry solvents are used in imine synthesis [12-17]. Here, new naphthaldehyde-derivatized Schiff bases were synthesized using ethyl lactate as a solvent and the process was identified as green

synthesis. Water was used as a cosolvent. By optimizing the solvent polarity, the formation of the product is accelerated.

EXPERIMENTAL

Materials and Methods

6-Methyl-2-amino benzothiazole and 2-methoxy-1-naphthaldehyde were of commercial quality or purified before use. Organic solvents used were of HPLC grade. The melting point was determined using a Gallenkamp apparatus. The ¹H NMR and ¹³C NMR spectra were recorded on a Bruker DPX FT NMR spectrometer (at 500 MHz and 125 MHz, respectively) at 298 K. Chemical shifts are given in δ (ppm) relative to TMS (DMSO-*d*₆) as the internal standard. The infrared spectrum was recorded on a Perkin Elmer Precisely Spectrum 100 FT-IR spectrophotometer as pressed KBr disc. Elemental analysis was performed on Elementar Analysensysteme GmbH vario MICRO CHNS (Turkish Technical and Scientific Research Council Laboratories, Ankara, Turkey). TLC was performed on pre-coated silica gel plates (Merck 60, F254, 0.25 mm).

Synthesis of (2-methoxy-1-naphthyl methylene)-6-methyl-benzothiazole-2-yl-amine (3)

General procedure A for preparation of (2-methoxy-1-naphthyl methylene)-6-methyl-benzothiazole-2-yl-amine (3): the Schiff base was synthesized by the method given in [18]. A mixture of 6-methyl-2-amino benzothiazole (**1**, 0.082115 g, 0.5 mmol) and methoxy-1-naphthalene (**2**, 0.093105 g, 0.5 mmol) in ethyl lactate - water

* To whom all correspondence should be sent:
E-mail: hsakarya@ogu.edu.tr

H. Demircioğlu et al.: Synthesis, X-ray crystal structure and spectroscopic studies of benzothiazole Schiff base system (3 mL, 80%) was stirred at room temperature for a period of time (Table 1).

Table 1. Effect of solvent polarity and catalyst on the yield for the synthesis of (2-methoxy-1-naphthyl methylene)-6-methyl-benzothiazole-2-yl-amine^d (3)

Procedure	Time (min)	Solvent (%EL)	% Yield ^c
A	60	80	77
B	120	70	72
C	30	100 ^a	80
D	10	100 ^b	90

^a Sc(OTf)₃

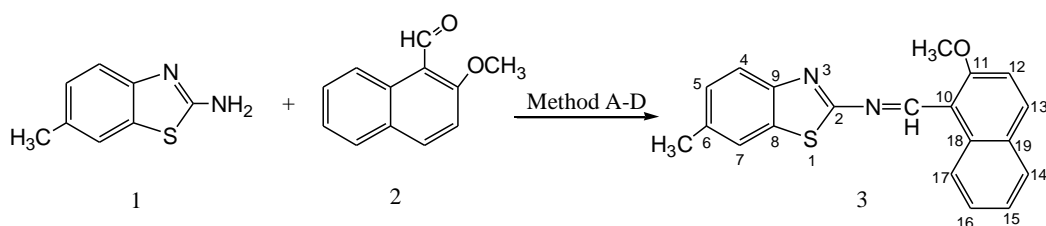
^b Yb(OTf)₃

^c isolated yield

^d reactions were carried out at room temperature

The reaction was terminated by TLC checking and left at room temperature overnight. The resulting precipitate was filtered off and washed with petroleum ether. The resulting crude product (3) was recrystallized from a mixture of ethyl acetate: n-hexane and ethanol solvent (1:6:0.008). Yield 77%.

General procedure B for preparation of (2-methoxy-1-naphthyl methylene)-6-methyl-benzothiazole-2-yl-amine (3): A mixture of 6-methyl-2-amino benzothiazole (1, 0.082115 g, 0.5 mmol) and 2-methoxy-1-naphthaldehyde (2, 0.093105 g, 0.5 mmol) in ethyl lactate - water system (3 mL, 70%) was stirred at room temperature for a period of time (Table 1).



A: 80% Ethyl L-lactate, room temperature, 60 min, yield 77%

B: 70% Ethyl L-lactate, room temperature, 120 min, yield 72%

C: Ethyl L-lactate, room temperature, 30 min, yield 80%

D: Ethyl L-lactate, room temperature, 10 min, yield 90%

Scheme 1. Schematic representation of the formation of (2-methoxy-1-naphthyl methylene)-6-methyl-benzothiazole-2-yl-amine (3)

The reaction was terminated by TLC checking and left at room temperature overnight. The resulting crude product (3) was recrystallized from a mixture of ethyl acetate: n-hexane and ethanol solvent (1:6:0.008). Yield 72%.

General procedure C for preparation of (2-methoxy-1-naphthyl methylene)-6-methyl-benzothiazole-2-yl-amine (3): A mixture of 6-methyl-2-amino benzothiazole (1, 0.082115 g, 0.5 mmol) and 2-methoxy-1-naphthaldehyde (2, 0.093105 g, 0.5 mmol) in ethyl L-lactate - water (3 mL, 99%) and Sc(OTf)₃ (0.0098432 g, 0.02 mmol) was stirred at room temperature for period of time (Table 1). The reaction was terminated by TLC checking and left at room temperature overnight. The resulting crude product (3) was recrystallized from a mixture of ethyl acetate: n-hexane and ethanol solvent (1:6:0.008). Yield 80%

General procedure D for preparation of (2-methoxy-1-naphthyl methylene)-6-methyl-benzothiazole-2-yl-amine (3): A mixture of 6-methyl-2-amino benzothiazole (1, 0.082115 g, 0.5 mmol) and 2-methoxy-1-naphthaldehyde (2, 0.093105 g, 0.5 mmol) in ethyl L-lactate - water (3 mL, 99%) and Yb(OTf)₃ (0.012405 g, 0.02 mmol) was stirred at room temperature for period of time

(Table 1). The reaction was terminated by TLC checking and left at room temperature overnight. The resulting crude product (3) was recrystallized from a mixture of ethyl acetate: n-hexane and ethanol solvent (1:6:0.008). Yield 90%.

Elemental analysis (%): Formula C₂₀H₁₆N₂SO: Found: C- 72.19; H- 4.79; N- 8.40; O- 4.78; S- 9.61%; Calculated: C- 72.26; H- 4.85; N- 8.43; O- 4.81; S- 9.65%; IR (KBr): 3012.72 cm⁻¹ (m, Ar-H), 2974.14 cm⁻¹ (m, CH₃), 2939.43 cm⁻¹ (m, CH₃), 1622.08 cm⁻¹ (m, CH=N), 1585.44 cm⁻¹ (s, Ar-H), 1512.15 cm⁻¹ (s, Ar-H), 1458.14 cm⁻¹ (s, Ar-H); ¹H-NMR (DMSO-*d*₆, 500 MHz, δ ppm): 1.6 (s, 3H, CH₃-benzothiazole); 4.1 (s, 3H, OCH₃ - naphthaldehyde); 7.29 (d, J=6.26 Hz, 1H, H4); 7.33 (d, J=9.10 Hz, 1H, H12); 7.48 (t, J=7.47 Hz, 1H, H15); 7.66 (s, 1H, H7); 7.7 (t, J=7.79 Hz, 1H, H16); 7.83 (d, J=8.03 Hz, 1H, H-17); 7.92 (d, J=8.25 Hz, 1H, H5); 8.07 (d, J=9.11 Hz, 1H, H-13); 9.8 (d, J= 8.68 Hz, 1H, H14); 9.9 (s, 1H, -CH=N-); ¹³C-NMR (CDCl₃, 125 MHz, δ ppm): 21.63; 56.67; 112.14; 115.29; 121.46; 122.55; 124.77; 126.56; 127.80; 128.49; 128.97; 129.59; 132.11; 134.38; 135.00; 136.72; 150.07; 162.01; 164.06; 172.49.

The suitable crystals of the title compound were crystallized from ethyl acetate : *n*-hexane : ethanol (1:6:0.008) at room temperature. Crystallographic data were recorded on a Bruker Kappa APEXII CCD area-detector diffractometer using Mo K α radiation ($\lambda=0.71073$ Å) at T=150(2) K. Multi-scan absorption correction was applied [19]. The structure was elucidated by direct methods and clarified by full-matrix least squares against F² using all data [20]. All of the H atoms were anisotropically refined. Methine H atoms, aromatic H atoms and methylene H atoms were geometrically located at 0.95 (CH), 0.95 (aromatic) and 0.98 (CH₃) distances from the parent O and C atoms; the U_{iso} (H) values during refinement process were limited to 1.2 U_{eq} (for aromatic carrier atoms) and 1.5 U_{eq} (for methyl carrier atoms) using a sliding model.

RESULTS AND DISCUSSION

The novel Schiff base (3) was synthesized according to the route shown in Scheme 1. We performed an effective synthesis using ethyl lactate, a green solvent. The reaction was carried out using the ethyl lactate-water system and then the polarity of the reaction medium was adjusted with water. In the medium where 100% ethyl lactate and Yb (OTf)₃ were used, it was observed that the reaction was very rapid and yielded a product with maximum efficiency (Table 1). The structure of Schiff base 3 was determined through spectroscopic and elemental analysis. When the IR spectrum of compound 3 was examined, it was observed that the peak observed at 1622 cm⁻¹ belonged to the azomethine group. ¹HNMR spectrum of compound 3 showed a characteristic singlet signal at 9.9 ppm, which might be attributed to the CH=N group. Two sharp singlets were also observed at δ 4.1 and 1.6 ppm for methoxy (OCH₃-naphth) and methyl protons (CH₃-benzth), respectively. For the aromatic ring protons, two triplets, six doublets and one singlet signal were assigned at δ 7.7, 7.48, 9.8, 8.07, 7.33, 7.83 and 7.66 ppm, corresponding to H16, H15, H14, H13, H12, H17 and H7 protons, respectively (Scheme 1). In the ¹³C NMR spectrum of the compound 3, the signals observed at 56.67 and 21.63 ppm were assigned to methoxy and methyl carbons, respectively. Furthermore, one downfield signal observed at 172.49 ppm was assigned to azomethine carbon (C=N). Finally, by single crystal X-ray analysis of compound 3, the relative stereochemical outcome was determined.

The crystal structure of the compound and the atomic numbering scheme of the compound are shown in Fig. 1.

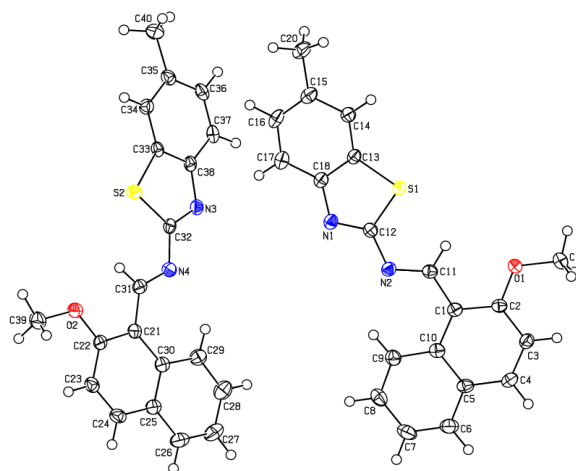


Fig. 1. ORTEP-3 [21] the atom numbering drawing scheme of compound 3. Displacement ellipsoids are drawn at the 50% probability level.

Table 2. Crystal data and structure refinement for compound 3

Empirical formula	C ₄₀ H ₃₂ N ₄ O ₂ S ₂
Colour/shape	yellow/block
Formula weight	664.82
T (K)	99(2)
Radiation used, graphite monochr.	Mo K α ($\lambda = 0.71073$ Å)
Crystal system	Monoclinic
Space group	P 2 ₁ /n
a (Å)	8.1077 (15)
b (Å)	17.302 (3)
c (Å)	22.790 (4)
α (°)	90
β (°)	95.799 (7)
γ (°)	90
V (Å ³)	3180.7 (1)
Z	4
Absorption coefficient (mm ⁻¹)	0.212
ρ_{calc} (mg mm ⁻³)	1.388
Crystal dimensions (mm)	0.31 × 0.24 × 0.21
θ (Max.) (°)	23.25
θ (Min.) (°)	2.76
Reflections measured	4535
Range of h, k, l	-8 < h < 8 -19 < k < 19 -25 < l < 25
No of reflections with I > 2 σ (I)	4222
Corrections applied	Lorentz-polarization
Structure solution	Direct methods
Treatment of H atoms	Geometric calculations
No. of parameters var	437
Goodness-of-fit S	1.079
R = $\ F_o\ - F_c / F_o $	0.0296
R _w	0.0867
R _{int}	0.0279
(Δ/ρ) _{max} (e Å ⁻³)	0.165
(Δ/ρ) _{min} (e Å ⁻³)	-0.257

Table 3. Bond lengths (Å), bond angles (°) and torsion angles (°) for compound **3**

S1-C13	1.7340(17)	O1-C19	1.427(2)	N3-C32	1.301(2)	C11-C1	1.447(2)
S1-C12	1.7875(18)	O2-C22	1.360(2)	N3-C38	1.389(2)	C21-C31	1.449(2)
S2-C33	1.7325(17)	O2-C39	1.432(2)	C20-C15	1.510(3)	C31-N4	1.290(2)
S2-C32	1.7840(18)	N1-C12	1.295(2)	C12-N2	1.381(2)	N4-C32	1.384(2)
O1-C2	1.362(2)	N1-C18	1.390(2)	N2-C11	1.289(2)	C35-C40	1.507(3)
C13-S1-C12	88.46(8)	N1-C12-N2	122.35(16)	N1-C18-C13	115.90(15)	C38-C33-S2	109.59(13)
C33-S2-C32	88.71(8)	N1-C12-S1	115.44(13)	O1-C2-C1	116.58(15)	N3-C38-C37	125.61(16)
C2-O1-C19	118.04(14)	N2-C12-S1	122.19(13)	O1-C2-C3	121.51(16)	N3-C38-C33	115.82(15)
C22-O2-C39	118.69(14)	C11-N2-C12	117.94(15)	C22-C21-C31	116.59(16)	O2-C22-C21	116.66(15)
C12-N1-C18	110.48(15)	N2-C11-C1	125.88(16)	N3-C32-N4	121.81(16)	O2-C22-C23	121.44(16)
C32-N3-C38	110.60(15)	N3-C32-S2	115.25(13)	N3-C32-S2	115.25(13)	N1-C18-C13	115.90(15)
C14-C13-S1	128.55(14)	C2-C1-C11	116.62(15)	N4-C32-S2	122.94(13)	N1-C18-C17	125.12(17)
C18-C13-S1	109.64(13)	C10-C1-C11	124.87(16)	C34-C33-S2	128.60(14)	C33-S2-C32-N4	-178.76(15)
C20-C15-C14-C13	179.57(16)	N2-C11-C1-C2	-174.43(17)	C10-C1-C2-O1	174.96(15)	C33-C34-C35-C40	175.32(17)
C15-C14-C13-C18	-1.8(3)	N2-C11-C1-C10	6.3(3)	C11-C1-C2-O1	-4.3(2)	C32-N3-C38-C37	-178.28(17)
C15-C14-C13-S1	179.85(14)	C20-C15-C16-C17	-178.04(17)	O1-C2-C3-C4	-178.30(17)	C32-N3-C38-C33	0.7(2)
C18-N1-C12-N2	-178.23(15)	C33-S2-C32-N3	1.91(14)	C22-C21-C31-N4	-179.85(16)	S2-C33-C38-C37	179.78(13)
C18-N1-C12-S1	3.21(19)	C12-N1-C18-C13	-2.4(2)	C30-C21-C31-N4	0.5(3)	C39-O2-C22-C21	175.46(16)
C13-S1-C12-N1	-2.53(14)	S1-C13-C18-C17	2.3(3)	C31-N4-C32-N3	-175.67(16)	C39-O2-C22-C23	-4.7(2)
N1-C12-N2-C11	161.10(16)	C19-O1-C2-C1	-178.71(17)	C12-N1-C18-C17	177.10(17)	C12-N2-C11-C1	177.72(16)
S1-C12-N2-C11	-20.4(2)	C19-O1-C2-C3	1.5(3)	C31-N4-C32-S2	5.0(2)	C21-C31-N4-C32	-178.69(16)

Table 4. Hydrogen-bond geometry (Å, °)

D-H...A	D-H	H...A	D...A	D-H...A
C9-H9...N2	0.95	2.28	2.929(2)	125
C29-H29...N4	0.95	2.26	2.927(2)	126
C36-H36...Cg3 ⁱ	0.95	2.90	3.590(2)	130
C36-H36...Cg4 ⁱ	0.95	2.98	3.777(2)	142

Symmetry code: (i) -1+x, y, z. Cg3 and Cg4 are the centroids of the rings C(N1/S1/C12/C13/C18) and D(C13-C18), respectively.

The asymmetric unit contains two crystallographically independent molecules, while the bond lengths and angles are in the normal range. The crystallographic data, and the selected bond lengths, bond angles and torsion angles are given in Tables 2 and 3, respectively.

The C1-C11=N2-C12 [177.72(16)°] and C21-C31=N4-C32 [-178.69(16)°] torsion angles show that the configurations about the C=N bonds are *anti* (1*E*). The planar rings A(C1-C5/C10), B(C5-C10),

C(N1/S1/C12/C13/C18) D(C13-C18) and E(C21-C25/C30), F(C25-C30), G(N3/S2/C32/C33/C38), H(C33-C38) are oriented at dihedral angles of A/B=4.65(5)°, C/D=0.95(5)° and E/F=0.35(6)°, G/H=2.45(6)°. So, rings C, D and E, F are coplanar. The coplanar rings I(N1/S1/C12-C18) and J(C21-C30) are oriented with respect to rings A, B and G, H at dihedral angles of A/I=15.12(4)°, B/I=2.24(5)° and G/J=5.84(4)°, H/J=5.58(4)°. The compound **3** has intramolecular C-H...N hydrogen bonds (Table 4).

Molecules are stacked along the a-axis in the crystal structure, extending along the c-axis (Fig. 2). The $\pi \cdots \pi$ contacts between the rings, Cg3---Cg1ⁱ, Cg3---Cg2ⁱ, Cg7---Cg5, Cg1---Cg1ⁱⁱ and Cg5---Cg8 where Cg1, Cg2, Cg3, Cg5, Cg7 and Cg8 are the centroids of the rings A, B, C, E, G and H with centroid-centroid distances of 3.595(1) Å, 3.784(1) Å, 3.600(1) Å, 3.900(1) Å and 3.554(1) Å, respectively, and the C-H \cdots π interactions may be effective in the stabilization of the crystal packing (Table 4).

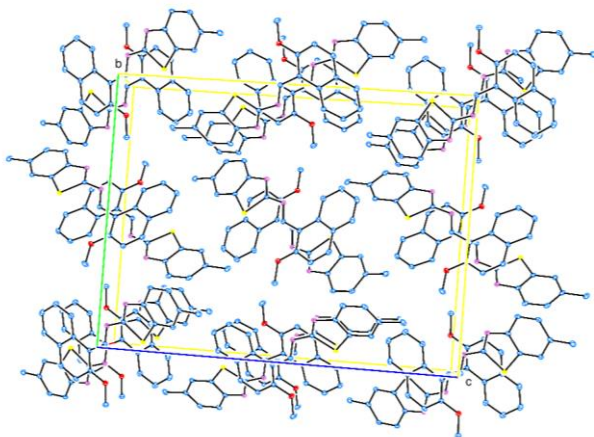


Fig. 2. A partial packing scheme that looks down on an axis. Hydrogen atoms are omitted for clarity.

Acknowledgements: This work has been supported by Eskişehir Osmangazi University Scientific Research Foundation. Project number: 2012/19D10.

REFERENCES

1. H. Schiff, *Ann. Chem. Pharm. Suppl.* **3**, 343 (1864).
2. G. Wilkinson, R. Gillard, J. A. McCleverty, *Comprehensive Coordination Chemistry. The Synthesis, Reactions, Properties and Applications of Coordination Compounds*, in: Coordination

- Compounds en gros and en détail, **28**, 786, Pergamon Press, Oxford, 1987
3. H. Demirelli, M. Tümer, A. Gölcü, *Bull. Chem. Soc. Jpn.*, **79** (6), 867 (2006).
4. A. Gölcü, M. Tümer, H. Demirelli., R. A. Wheatley, *Inorg. Chim. Acta*, **358** (6), 1785 (2005).
5. Dolaz M., Tümer M. *Transition Met. Chem.*, **29** (5), 516 (2004).
6. T. T. Tidwell, *Angew. Chem., Int. Ed.* **47** (6), 1016, (2008).
7. S. Gaur, *Asian J. Chem.*, **15** (1), 250 (2003).
8. A. Prakash, D. Adhikari, *Int. J. ChemTech Res.*, **3** (4), 1891 (2011)
9. V. Mirkhani, R. Kia, A. R. Vartooni, H.-K. Fun, *Polyhedron*, **29** (6), 1600 (2010).
10. M. S. Manhas, M. Ghosh, A.K. Bose, *J. Org. Chem.*, **55** (2), 575 (1990).
11. J. H. Billman, K. M. Tai, *J. Org. Chem.*, **23** (4), 535 (1958).
12. J. Schmeyers, F. Toda, J. Boyb, G. Kaupp, *J. Chem. Soc., Perkin Trans.*, **2**, 4, 989 (1998).
13. R. S. Varma, R. Dahiya, S. Kumar, *Tetrahedron Lett.*, **38** (12), 2039 (1997).
14. P. C. Andrews, A. C. Peatt, C. L. Raston, *Tetrahedron Lett.*, **45** (2), 243 (2004).
15. K. Tanaka, R. Shiraishi, *Green Chem.*, **2** (6), 272 (2000).
16. A. Simion, C. Simion, T. Kanda, S. Nagashima, Y. Mitoma, T. Yamada, K. Mimura, M. Tashiro, *J. Chem. Soc., Perkin Trans.* **1** (17), 2071 (2001).
17. K. P. Guzen, A. S. Guarezemini, A. T. G. Órfão, R. Cella, C. M. P. Pereira, H. A. Stefani, *Tetrahedron Lett.*, **48** (10), 1845 (2007).
18. A. Dandia, A. K. Jain, A. K. Laxkar, *Tetrahedron Lett.*, **54** (30), 3929 (2013).
19. Bruker SADABS. Bruker AXS Inc. Madison, Wisconsin, USA, 2005.
20. G. M. Sheldrick, *Acta Cryst. Sect. A, Found. Cryst.*, **64**, 112 (2008).
21. L. J. Farrugia, *J. Appl. Cryst.*, **30** (5), 565 (1997).

The antioxidant and antimutagenic properties of different extracts of *Crataegus monogyna subsp. monogyna* collected from the Eastern Anatolia region of Turkey

S. Ceker^{1*}, O. Capik², M. Sengül², R. Jaber³, G. Agar²

¹Agri Ibrahim Cecen University, Department of Basic Pharmaceutical Sciences, Faculty of Pharmacy, Agri, TR-04140, Turkey

²Ataturk University, Faculty of Science, Department of Biology, Erzurum, TR-25240 Turkey

³Ataturk University, Faculty of Agriculture, Department of Food Engineering, Erzurum, TR-25240, Turkey

Received March 13, 2018, Accepted December 12, 2019

In the present study, we aimed to investigate the genotoxic and anti-genotoxic potencies of fruits of *Crataegus monogyna subsp. monogyna* (C.M.) by using the micronucleus (MN) and sister chromatid change (SCE) tests in human blood cells. According to the results obtained from the MN and SCE tests, all extracts of C.M. have antimutagenic effect. The most effective extracts were in methanol and acetone. The 40-80 µg/mL doses of C.M. were more effective than other doses. In addition, we evaluated the antioxidant activity in order to clarify the possible mechanisms that may contribute to the anti-genotoxic activity of C.M. Similarly, all extracts displayed antioxidant activity; the most effective extracts were in methanol and acetone. The order of the antigenotoxic and antioxidant effect of the most effective extracts was as follows: CMA (*Crataegus monogyna* acetone) > CMM (*Crataegus monogyna* methanol) > CME (*Crataegus monogyna* ethanol) > CMW (*Crataegus monogyna* water).

Key words: *Crataegus monogyna subsp. monogyna*, antimutagenic, antioxidant, MN, SCE

INTRODUCTION

Crataegus monogyna is one of the most common species called “hawthorn” in traditional herbalism. The plant is native to Europe, northwest Africa and western Asia. It has been introduced in many other parts of the world. The hawthorn is a shrub or small tree of 5-14 m height, with a dense crown. The leaves are 20 to 40 mm long, obovate and deeply lobed, sometimes almost to the midrib, with the lobes spreading at a wide angle. The hermaphrodite flowers are produced in carymbose of 5–25 together with five white petals, numerous red stamens and a single stem. Flowers are pollinated by midges, bees and insects and bear numerous haws. The haw is a small, oval, dark-red fruit about 10 mm long berry. Haws are important for wildlife in winter [1-3].

The plant parts used are usually both leaves and flowers or alternatively the fruit. Hawthorn has been investigated in medicine for treating cardiac insufficiency. On the other hand, *Crataegus monogyna* is a source of antioxidant phytochemicals, especially the extracts of hawthorn leaves with flowers. The *Crataegus* species is well distributed in Turkey as a wild plant and is used as herbal medicine [4].

Earlier findings of *Crataegus monogyna* have shown its pharmacological properties such as antimicrobial, antioxidant, antitumor, antiviral, cardioprotective, neuroprotective, nephroprotective hepatoprotective and anti-inflammatory [3, 5]. On

the other hand, although *Crataegus monogyna* species have been studied for its biological properties, its anti-mutagenic properties have not been reported up to the present.

Bernatoniene *et al.* [6] reported that extracts of hawthorn berries have antioxidant capacity and its ethanolic extracts have higher antioxidant activity than aqueous extracts. Mot *et al.* [7] suggested that *Crataegus monogyna* have pharmacological properties due to monoterpenes, sesquiterpenes, aliphatic and aromatic aldehydes (benzaldehyde, 3-pyridine carboxaldehyde), ketones, alcohols and esters (4-methoxybenzoic acid methyl ester). Leskovac *et al.* [8] showed that *in vitro* treatment of human peripheral blood lymphocytes with *Crataegus monogyna* fruit extract reduced micronuclei induced by gamma irradiation.

There are several reports on the antioxidant capacity of hawthorn species, due to the presence of different bioactive compounds, such as epicatechin, hyperoside and chlorogenic acid, epigallocatechin gallate, gallic acid, quercetin 7,4-dimethyl ether-3-O-rutinoside, methyl (4-caffeoyl)-quinic acid, quinic acid, malvidin-3-O-(4''coumaroyl)-rutinoside-5-O-glucose, peonidin-3-O-(4''coumaroyl)-rutinoside-5-O-glucose, petunidin-3-O-(4''coumaroyl)-rutinoside-5-O-glucose, 8-Methoxy-Kaempferol-3-O-glucose.

These compounds are reported to have many pharmacological effects [1, 9].

However, to the best of our knowledge, there has not been any attempt to evaluate the anti-

* To whom all correspondence should be sent:

E-mail: selcukceker06@gmail.com

mutagenic activities of different extracts of *Crataegus monogyna subsp. monogyna* species until now. Therefore, the aim of this study was to investigate the antioxidant capacity of the antimutagenic activity different extracts of *C. monogyna subsp. monogyna*.

MATERIALS AND METHODS

Fruit samples of *C. monogyna species* were collected from different locations in the vicinity of Erzurum, located in eastern Anatolia, Turkey (the taxonomic identification of the plant materials was confirmed by a senior plant taxonomist, Dr. Meryem Sengul, Department of Biology, Atatürk University, Erzurum, Turkey). The collected fruit materials - the fruits - were ground in a grinder with 2 mm mesh size.

Preparation of the extract

The fresh fruits (100 g) were extracted with 1 L of methanol, ethanol, acetone or pure water using a Soxhlet extractor (ISOPAD, Heidelberg, Germany) for 72 h at a temperature not exceeding the boiling point of the solvent. The extract was filtered using Whatman filter paper (no. 1), and then concentrated *in vacuo* at 60°C using a rotary evaporator (Buchi Labortechnik AG, Flawil, Switzerland). Plant extracts were then lyophilized and kept in the dark at + 4°C until being tested.

Antimutagenicity assay

Peripheral blood lymphocytes were taken from four nonsmoking healthy donors between the ages of 22 and 25. Lymphocyte cultures were set up by adding 0.5 mL of heparinized whole blood to RPMI-1640 chromosome medium supplemented with 15% heat-inactivated fetal calf serum, 100 IU/mL streptomycin, 100 IU/mL penicillin and 1% L-glutamine. Lymphocytes were stimulated to divide by 1% phytohemagglutinin. Aflatoxin B₁ (AFB₁; 5 µM), *Crataegus monogyna* acetone (CMA), *Crataegus monogyna* ethanol (CME), *Crataegus monogyna* methanol (CMM) and *Crataegus monogyna* water (CMW) (in concentrations of 5; 10; 20; 40 and 80 µg/mL) were added to the cultures just before incubation.

For sister chromatid exchange (SCE) demonstration, the cultures were incubated at 37 °C for 72 h, and 5-bromo 2-deoxyuridine (BrdU) at 8 mg/mL was added at the initiation of cultures. All cultures were kept in darkness. Next, 0.1 mg/mL of colcemide was added 3 h before harvesting to arrest the cells at metaphase. The cultures were centrifuged at 1200 rpm for 10 min. The supernatants were used for enzyme analysis. Cells were harvested and treated for 28 min with

hypotonic solution (0.075 M KCl) and fixed in a 1:3 mixture of acetic acid/methanol (v/v). BrdU incorporated metaphase chromosomes were stained by fluorescent plus Giemsa technique as described by Perry and Evans [10]. In SCE study, by selecting 60 satisfactory metaphases, the results of SCE are shown in Table 2. For each treatment condition, well-spread second division metaphases containing 42–46 chromosomes in each cell were scored, and the values obtained were calculated as SCEs per cell [11].

In the MN test system, cytochalasin B (3 µg/mL) was added to the whole blood samples at 44 h incubation. After 72 h incubation, the cells were harvested by centrifugation (1000 rpm, 10 min), and the supernatant was removed. 6 mL of 0.05 M KCl was added to the pellet containing lymphocyte cells, vortexed and incubated at 37 °C for 7 min. After the incubation period, the lymphocyte cells were harvested by centrifugation (1000 rpm, 10 min) and the supernatant was removed. 6 mL of fresh fixative solution (acetic acid and methanol (1:3)) was added dropwise to the pellet. The fixation procedure was repeated three times and the tube was centrifuged (1000 rpm, 10 min). The cell pellet was re-suspended in 1 mL of fresh fixative solution, and then the suspension was dropped on to clean labeled microscope slides and incubated at room temperature for 72 h. After the incubation period, the slides were stained with 5% giemsa dye solution for 10 min and excess giemsa dye was removed with distilled water. The slides were air-dried and only bi-nucleated cells were scored for MN analysis. For each experimental group, approximately 1000 bi-nucleated cells were analyzed for the presence of MN [12].

Antioxidant status assays

DPPH scavenging activity. The scavenging activity of the samples was measured according to the method described by Barku *et al.* [13] with some modification. Extracts of different concentrations were added to 0.5 mL of a methanolic DPPH solution (0.1 mmol). The estimated time of reaction (30 min) was determined by considering the reduction of the absorbance at 517 nm. The absorbance was measured at room temperature, in darkness, against a blank. The absorbance of the control (3 ml of methanol in 0.5 mL of DPPH solution) was measured. All assays were conducted in triplicate. The percentage activity for the DPPH technique was calculated as follows:

$$\% \text{ inhibition activity} = 100 \times ((A_0 - A_1) / A_0)$$

where A₀ is the absorbance of the control samples

S. Ceker et al.: Antioxidant and antimutagenic properties of extracts of *Crataegus monogyna* subsp. *monogyna* ... and A₁ is the absorbance of the test compound. The results are expressed as sample concentration in the extract causing a decrease in DPPH radical solution. Concentrations are expressed in µg/mL.

RESULTS

The extracts of the fruits of *C. monogyna* subsp. *monogyna* showed significant anti-mutagenic activity in the study groups (Tables 2 and 3).

The most effective extracts of CM were CMA and CMM. The effects of the extracts of CM on the frequencies of SCE and MN were related to their concentrations. The 40-80 µg/mL doses of CM were more effective than other doses. The various extracts of *C. monogyna* have different antioxidant activity as shown in Table 1. The acetone and methanol extracts of CM displayed higher antioxidant activity than other extracts. These findings show that MN and SCE are parallel.

DISCUSSION

The antigenotoxic activities of CM were

assessed by evaluating MN and SCE frequencies as shown in Tables 2 and 3. All extracts of CM were found to have antigenotoxic and antioxidant activities. Although the biological activities of *C. monogyna* such as antimicrobial, antioxidant, antitumor, antiviral, cardioprotective, neuroprotective, nephroprotective, hepatoprotective and anti-inflammatory are thoroughly studied, up to present there are limited investigations about their antimutagenic effects [3, 5, 14].

The present study focused on assessing the mutagenic effects of different extracts of *C. monogyna* and the antigenotoxicity mechanisms of CM are associated with its antioxidant nature. The results obtained from the mutagenicity assays showed that the four *C. monogyna* extracts have no mutagenic activity in any concentration. In the antimutagenicity assays, it was shown that all extracts of *C. monogyna* species have antimutagenic activity on human lymphocytes *in vitro* at all concentrations.

Table 1. DPPH free radical-scavenging activity of the different extracts

Plant species	Used solvent	Abbreviation	Mean % inhibition
<i>Crataegus monogyna</i> subsp. <i>monogyna</i>	Acetone	CMA	91.252
<i>Crataegus monogyna</i> subsp. <i>monogyna</i>	Ethanol	CME	88.109
<i>Crataegus monogyna</i> subsp. <i>monogyna</i>	Methanol	CMM	90.034
<i>Crataegus monogyna</i> subsp. <i>monogyna</i>	Pure water	CMW	52.144

Table 2. The effects of AFB₁ and extracts of *Crataegus monogyna* subsp. *monogyna* (CM) on SCE

Test Items	Concentrations	SCE Frequency ± S. E (CMA)	SCE Frequency ± S. E (CME)	SCE Frequency ± S. E (CMM)	SCE Frequency ± S. E (CMW)
Control		6.27 ± 0.7 ^a			
AFB ₁	5 µM	14.00 ± 0.60 ^e			
CM	20 µg/mL	6.29 ± 0.53 ^a	6.31 ± 0.30 ^a	6.30 ± 0.77 ^a	6.33 ± 0.49 ^a
AFB ₁ + CM	5 µM + 5 µg/mL	11.51 ± 0.78 ^d	12.98 ± 0.40 ^e	11.97 ± 0.81 ^d	13.30 ± 0.66 ^e
AFB ₁ + CM	5 µM + 10 µg/mL	10.18 ± 0.38 ^c	10.90 ± 0.21 ^{cd}	10.20 ± 0.93 ^c	12.43 ± 0.76 ^{de}
AFB ₁ + CM	5 µM + 20 µg/mL	8.34 ± 0.33 ^b	8.93 ± 0.33 ^b	8.61 ± 0.47 ^b	10.73 ± 0.41 ^c
AFB ₁ + CM	5 µM + 40 µg/mL	7.01 ± 0.25 ^a	7.74 ± 0.18 ^{ab}	7.18 ± 0.57 ^a	8.99 ± 0.51 ^b
AFB ₁ + CM	5 µM + 80 µg/mL	6.35 ± 0.88 ^a	6.81 ± 0.65 ^a	6.51 ± 0.29 ^a	6.97 ± 0.63 ^a

Aflatoxin B₁ (AFB₁) was used as a positive control for human blood cells. Values of SCE (^{a, b, c, d, e}) are significantly different compared to negative control (P < 0.05).

Table 3. The effects of AFB₁ and extracts of *Crataegus monogyna subsp. monogyna* (C.M.) on MN

Test Items	Concentrations	MN Frequency ± S. E (CMA)	MN Frequency ± S. E (CME)	MN Frequency ± S. E (CMM)	MN Frequency ± S. E (CMW)
Control		4.44 ± 0.84 ^a			
AFB ₁	5 µM	9.50 ± 0.90 ^e			
CM	20 µg/mL	4.51 ± 0.44 ^a	4.37 ± 0.99 ^a	4.47 ± 0.72 ^a	4.46 ± 0.55 ^a
AFB ₁ + CM	5 µM + 5 µg/mL	8.17 ± 0.79 ^{de}	8.71 ± 0.77 ^e	8.42 ± 0.45 ^e	8.91 ± 0.69 ^e
AFB ₁ + CM	5 µM + 10 µg/mL	7.13 ± 0.36 ^c	7.78 ± 0.60 ^d	7.44 ± 0.39 ^{cd}	7.85 ± 0.76 ^d
AFB ₁ + CM	5 µM + 20 µg/mL	6.08 ± 0.47 ^b	6.46 ± 0.41 ^c	6.12 ± 0.42 ^{bc}	6.59 ± 0.38 ^c
AFB ₁ + CM	5 µM + 40 µg/mL	5.04 ± 0.66 ^a	5.54 ± 0.53 ^b	5.06 ± 0.95 ^a	5.86 ± 0.44 ^b
AFB ₁ + CM	5 µM + 80 µg/mL	4.13 ± 0.61 ^a	4.89 ± 0.56 ^a	4.18 ± 0.70 ^a	4.97 ± 0.83 ^{ab}

Aflatoxin B₁ (AFB₁) was used as a positive control for human blood cells. Values of MN (^{a, b, c, d, e}) are significantly different compared to negative control (P < 0.05).

In the present study the antioxidant capacity of C.M. was determined. Our results showed that all C.M. extracts have antioxidant capacity, as well as antimutagenic activities. Previous studies reported that hawthorn fruit possesses potent antioxidant and free radical scavenging activities and these studies suggested that the antioxidant capacity is due to the presence of different bioactive compounds such as epicatechin, hyperoside, and chlorogenic acid [1, 15]. The results of our study indicate that the antigenotoxic effects of C.M. could be related to its antioxidant potential. However, the bioactive compounds in C.M. needed isolation and identification in order to understand the mechanism underlying its chemoprotective and antigenotoxic effects. Our future studies will be focused on the fractionation and isolation of the crude extract of *C. monogyna*. Nonetheless, we can suggest C.M. fruits as medicines with antioxidant and antimutagenic effect.

REFERENCES

1. S. F. Nabavi, S. Habtemariam, T. Ahmed, A. Sureda, M. Daglia, E. Sobarzo-Sánchez, S. M. Nabavi, *Nutrients.*, **7**(9), 7708 (2015).
2. R. Philips, *Trees of North America and Europe*, Random House, INC. New York, 1979.
3. T. Bahorun, E. Aumjaud, H. Ramphul, M. Rycha, A. Luximon-Ramma, F. Trotin, O. I. Aruoma, *Molecular Nutrition & Food Research*, **47**(3), 191 (2003).
4. A. Sahin Yaghlouglu, F. Eser, S. Tekin, A. Onal, *Frontiers in Life Science*, **9**(1), 69 (2016).
5. A. Kirakosyan, E. Seymour, P. B. Kaufman, S. Warber, S. Bolling, S. C. Chang, *Journal of Agricultural and Food Chemistry*, **51**(14), 3973 (2003).
6. J. Bernatoniene, R. Masteikova, D. Majiene, A. Savickas, E. Kovelaitis, R. Bernatoniene, R. Pečiūra, *Medicina*, **44**(9), 706 (2008).
7. C. A. Mot, D. Copolovici, E. Madosa, G. Mot, L. Copolovici, *Journal of Biotechnology*, **231**, S59 (2016).
8. A. Leskovic, G. Joksic, T. Jankovic, K. Savikin, N. Menkovic, *Planta Medica*, **73**(11), 1169 (2007).
9. L. Barros, A. M. Carvalho, J. S. Morais, I. C. Ferreira, *Food Chemistry*, **120**(1), 247 (2010).
10. P. Perry, H. J. Evans, *Nature*, **258**(5531), 121 (1975).
11. S. Ceker, F. Orhan, H. E. Kizil, L. Alpsoy, M. Gulluce, A. Aslan, G. Agar, *Toxicology and Industrial Health*, **31**(11), 990 (2015).
12. F. Orhan, S. Ceker, M. Anar, G. Agar, T. Arasoglu, M. Gulluce, *Medicinal Chemistry Research*, **25**(11), 2567 (2016).
13. V. Y. A. Barku, Y. Opoku-Boahen, E. Owusu-Ansah, E. F. Mensah, *Asian Journal of Plant Science and Research*, **3**(1), 69 (2013).
14. I. Orhan, B. Özçelik, M. Kartal, B. Özdeveci, H. Duman, *Chromatographia*, **66**(1), 153 (2007).
15. M. J. Simirgiotis, *Molecules*, **18**(2), 2061 (2013).

Synthesis, characterization and biological evaluation of some new pyrazolyl bipyridyl substituted dicoumarins

N. N. Gohil*, D. I. Brahmhatt*

Department of Chemistry, Sardar Patel University, Vallabh Vidyanagar-388120, Gujarat, India

Received July 31, 2018; Revised June 29, 2019

The present study describes the synthesis of pyrazolyl bipyridyl substituted dicoumarin derivatives carried out by the reaction of various 3-[3-{3-(coumarin-3-yl)-1-phenyl-1H-pyrazol-4-yl}acryloyl]coumarins (coumarin chalcones) (**4a-f**) with appropriate pyridoyl methyl pyridinium iodide salts (**5-7**) in the presence of ammonium acetate in refluxing acetic acid. All synthesized target compounds (**8a-f**), (**9a-f**) and (**10a-f**) were characterized by IR, ¹H-NMR, ¹³C-APT and representative mass spectral data. The compounds were subjected to *in vitro* antimicrobial screening against a representative panel of bacteria (*Bacillus subtilis*, *Staphylococcus aureus*, *Escherichia coli*, *Salmonella typhi*) and fungi (*Aspergillus niger*, *Candida albicans*).

Keywords: coumarins, coumarin chalcones, Krohnke reaction, antimicrobial screening.

INTRODUCTION

Coumarins are the best known aromatic lactones isolated from various natural sources. Over the past decades coumarins have attracted strong scientific interest stemming from their broad spectrum of pharmacological properties such as antimicrobial [1], anti-inflammatory [2], CNS depressant [3], antioxidant [4], antitumor [5], antiviral [6], antiasthmatic [7], antiulcer [8], cytotoxic properties [9], etc. The actual trend in the field of synthetic chemistry of coumarins is the introduction of a heterocyclic moiety as a substituent either in the lactone or benzene ring in a coumarin core structure possessing various biological activities [10-14] in which pyrazolyl-substituted coumarins are well documented in the literature and known for their various biological properties like antimicrobial [15], anticonvulsant [16], antioxidant, antihyperglycemic [17], etc. They also show fluorescent and absorption emission characteristics [18].

Bipyridines are compounds formed by coupling of two pyridine rings. Bipyridines are widely used in coordination and supramolecular chemistry [19]. They also possess effective biological properties like antibacterial [20], antifungal [21], antimycoplasmal [22], antimalarial [23], antitumor activity [24], etc. Moreover, a large number of bipyridines are used in photocatalysis [25], as chemosensors [26] and luminescent probes for biomolecular systems [27].

Thus, considering the importance of pyrazolyl-substituted coumarins and bipyridines, it was thought worthwhile to synthesize some new coumarin derivatives having both of these structural

features in a single molecule. Therefore, in the present work, synthesis of various pyrazolyl-bipyridyl-substituted dicoumarins was carried out and all synthesized compounds were screened for their antimicrobial activity.

EXPERIMENTAL

All melting points are uncorrected. All reactions were performed with commercially available reagents used without further purification. Organic solvents were purified by standard methods and stored over molecular sieves. All IR spectra (KBr disc) were recorded on a Shimadzu FTIR 8400-S spectrometer. ¹H-NMR and ¹³C-APT spectra were recorded on a Bruker Advance 400 spectrometer operating at 400 MHz for ¹H-NMR and 100 MHz for ¹³C-APT. The chemical shift (δ) is reported in ppm using chloroform-d as a solvent and calibrated standard solvent signal. Mass spectra were recorded on a Shimadzu QP 2010 spectrometer. All compounds were routinely checked for completion of the reaction on silica gel 60 F254 TLC plates and their spots were visualized by exposure to a UV lamp, iodine vapour or KMnO₄ reagents. In the present work, various 3-{4'-[3'''-(coumarin-3'''-yl)-1'''-phenyl-1H-pyrazol-4'''-yl]-2',2''-bipyridin-6'-yl}coumarins (**8a-f**), 3-{4'-[3'''-(coumarin-3'''-yl)-1'''-phenyl-1H-pyrazol-4'''-yl]-2',3''-bipyridin-6'-yl}coumarins (**9a-f**) and 3-{4'-[3'''-(coumarin-3'''-yl)-1'''-phenyl-1H-pyrazol-4'''-yl]-2',4''-bipyridin-6'-yl}coumarins (**10a-f**) were synthesized by the reaction of various 3-[3-{3-(coumarin-3-yl)-1-phenyl-1H-pyrazol-4-yl} acryloyl]coumarins (coumarin chalcones) (**4a-f**) with appropriate pyridoyl methyl pyridinium iodide salts (**5-7**) under Krohnke's reaction conditions.

* To whom all correspondence should be sent:

E-mail: drdib317@gmail.com, nehru.gohil@gmail.com

© 2020 Bulgarian Academy of Sciences, Union of Chemists in Bulgaria

Compounds (**5-7**) were prepared according to the procedure given in [28].

General procedure for the preparation of 3-[3-{3-(coumarin-3-yl)-1-phenyl-1H-pyrazol-4-yl}acryloyl]coumarins (4a-f) (coumarin chalcones).

In a 100-mL round bottom flask, an appropriate 3-[(1-phenyl-4-formyl)pyrazol-3-yl]coumarin (0.01 mole) and an appropriate 3-acetyl coumarin (0.01 mole) were taken in 50 mL of ethanol. Catalytic amount of piperidine was added and the reaction mixture was stirred for 10 min at room temperature. The mixture was then refluxed on a water bath for 4 h. It was allowed to cool to room temperature. The solid product separated out was filtered off, washed with cold ethanol and dried. It was recrystallized from ethanol. Coumarin chalcones **4a**, **4b**, **4d** and **4e** were prepared according to procedure [29].

5,6-Benzo-3-[3-{3-(coumarin-3-yl)-1-phenyl-1H-pyrazol-4-yl}acryloyl]coumarin (4c): IR(KBr, ν_{\max} , cm^{-1}): 1736(C=O stretching of δ -lactone of coumarin), 1697(α,β unsaturated carbonyl group), 1651 and 1543(aromatic C=C and C=N stretchings), 748 and 687(C-H bending vibrations of mono substituted benzene ring), 3063(aromatic C-H stretching). ^1H NMR(400MHz, CDCl_3 , δ): 7.36-8.49 (18H, multiplet, fifteen aromatic protons + two olefinic proton + C_5' proton of pyrazole ring), 9.36 and 9.41(2H, two singlets, C_4 and C_4'' protons of coumarin).

5,6-Benzo-8''-methoxy-3-[3-{3-(coumarin-3-yl)-1-phenyl-1H-pyrazol-4-yl}acryloyl] coumarin (4f): IR(KBr, ν_{\max} , cm^{-1}): 1705(C=O stretching of δ -lactone of coumarin), 1682(α,β unsaturated carbonyl group), 1605 and 1535(aromatic C=C and C=N stretchings), 748(C-H bending vibrations of mono substituted benzene ring), 3055(aromatic C-H stretching). ^1H NMR(400MHz, CDCl_3 , δ): 4.03(3H, singlet, OCH_3), 7.18-8.48(17H, multiplet, fourteen aromatic protons + two olefinic proton + C_5' proton of pyrazole ring), 9.35 and 9.38(2H, two singlets, C_4 and C_4'' protons of coumarin).

General procedure for the synthesis of 3-{4'-[3'''-(coumarin-3'''-yl)-1'''-phenyl-1H-pyrazol-4'''-yl]-2',2''-bipyridin-6'-yl}coumarins (8a-f), 3-{4'-[3'''-(coumarin-3'''-yl)-1'''-phenyl-1H-pyrazol-4'''-yl]-2',3''-bipyridin-6'-yl}coumarins (9a-f) and 3-{4'-[3'''-(coumarin-3'''-yl)-1'''-phenyl-1H-pyrazol-4'''-yl]-2',4''-bipyridin-6'-yl} coumarins (10a-f).

In a 100-mL round bottom flask equipped with a condenser, guard tube and magnetic needle, an appropriate pyridoyl methyl pyridinium iodide salt (**5**) or (**6**) or (**7**) (0.003 mole) in glacial acetic acid

(15mL) was taken. To this ammonium acetate (0.03 mole) was added under stirring at room temperature. Then a solution of an appropriate 3-[3-{3-(coumarin-3-yl)-1-phenyl-1H-pyrazol-4-yl}acryloyl]coumarin (coumarin chalcone) (**4a-f**) (0.003 mole) in glacial acetic acid (15 mL) was added under stirring at room temperature and the reaction mixture was further stirred for 1 h at room temperature and then refluxed for 8 h at 140°C . It was then allowed to cool to room temperature and was poured into ice-cold water (75 mL). The crude solid obtained was extracted with chloroform (3×30 mL). The organic layer was washed with 5% sodium bicarbonate solution (3×20 mL), water (2×20 mL) and dried over anhydrous sodium sulphate. The removal of chloroform under reduced pressure gave a crude material which was subjected to column chromatography using silica gel and chloroform-ethylacetate (9:1) as an eluent to give compounds (**8a-f**), (**9a-f**) and (**10a-f**). The compounds were recrystallized from chloroform-hexane.

3-{4'-[3'''-(coumarin-3'''-yl)-1'''-phenyl-1H-pyrazol-4'''-yl]-2',2''-bipyridin-6'-yl} coumarin (8a): Yield: 65%, m.p. $184-185^\circ\text{C}$, IR(KBr, ν_{\max} , cm^{-1}): 1729(C=O stretching of δ -lactone of coumarin), 1605 and 1478(aromatic C=C and C=N stretchings), 758 and 691(C-H bending vibrations of mono substituted benzene ring), 3062(aromatic C-H stretching). ^1H -NMR(400 MHz, CDCl_3 , δ): 7.32-7.91 (15H, multiplet, aromatic protons except C_5''' -H, C_4''' -H, C_3' -H, C_5' -H, C_3'' -H, C_6'' -H, C_4 -H), 8.27(1H, singlet, C_5''' -H), 8.52-8.58(4H, multiplet, protons at C_4''' , C_3' , C_5' and C_3''), 8.66(1H, poorly resolved doublet of doublet, C_6'' -H), 9.00(1H, singlet, C_4 -H). ^{13}C -APT(100 MHz, CDCl_3 , δ): 116.28(CH), 116.68(CH), 118.52(CH), 119.29(CH), 119.49(C), 119.57(C), 121.34(CH), 121.67(C), 121.98(CH), 122.38(C), 123.83(CH), 124.47(CH), 124.49(CH), 125.16(C), 127.27(CH), 127.35(CH), 128.47(CH), 128.92(CH), 129.62(CH), 131.96(CH), 132.01(CH), 136.89(CH), 139.54(C), 142.04(C), 142.46(CH), 143.50(CH), 145.81(C), 149.02(CH), 150.64(C), 153.90(C), 154.35(C), 155.73(C), 155.93(C), 159.66(CO of coumarin), 160.09(CO of coumarin). Mass (m/z): M^+ 586(24%), 562(18%), 456(26%), 328(12%), 91(17%), 77(100%), 56(28%). Anal. Calcd. for $\text{C}_{37}\text{H}_{22}\text{N}_4\text{O}_4$: C, 75.76; H, 3.78; N, 9.55 %. Found: C, 75.88; H, 3.87; N, 9.59 %.

8-Methoxy-3-{4'-[3'''-(coumarin-3'''-yl)-1'''-phenyl-1H-pyrazol-4'''-yl]-2',2''-bipyridin-6'-yl} coumarin (8b): Yield: 60%, m.p. $170-172^\circ\text{C}$, IR(KBr, ν_{\max} , cm^{-1}): 1720(C=O stretching of δ -

lactone of coumarin), 1612 and 1497(aromatic C=C and C=N stretchings), 756 and 694(C-H bending vibrations of mono substituted benzene ring), 2839(aliphatic C-H stretching), 3063(aromatic C-H stretching). ¹H-NMR(400MHz, CDCl₃, δ): 4.01(3H, singlet, OCH₃), 7.09-7.89(14H, multiplet, aromatic protons except C₅^{'''}-H, C₄^{'''}-H, C₃[']-H, C₅[']-H, C₃^{''}-H, C₆^{''}-H, C₄-H), 8.27(1H, singlet, C₅^{'''}-H), 8.49-8.56(4H, multiplet, protons at C₄^{'''}, C₃['], C₅['] and C₃^{''}), 8.63(1H, poorly resolved doublet of doublet, C₆^{''}-H), 8.94(1H, singlet, C₄-H). ¹³C-APT(100MHz, CDCl₃, δ): 56.25(OCH₃), 113.80(CH), 116.05(CH), 116.78(CH), 118.60(CH), 119.25(C), 119.60(CH), 120.16(C), 120.33(CH), 121.33(CH), 121.55(C), 122.07(CH), 122.41(C), 123.88(CH), 124.32(CH), 124.58(CH), 125.27(C), 127.42(CH), 128.68(CH), 129.67(CH), 131.93(CH), 133.83(C), 136.99(CH), 139.61(C), 140.15(C), 142.32(C), 142.95(CH), 143.85(CH), 146.02(C), 146.92(C), 150.80(C), 154.33(C), 155.86(C), 158.57(CO of coumarin), 159.56(CO of coumarin). Anal.Calcd. for C₃₈H₂₄N₄O₅: C, 74.02; H, 3.92; N, 9.09 %. Found: C, 74.10; H, 4.00; N, 9.13 %.

5,6-Benzo3-{4'-[3'''-(coumarin-3''''-yl)-1'''-phenyl-1H-pyrazol-4''''-yl]-2',2''-bipyridin-6'-yl}coumarin (8c): Yield: 72%, m.p.207-209°C, IR(KBr, ν_{max}, cm⁻¹): 1712(C=O stretching of δ-lactone of coumarin), 1604 and 1474(aromatic C=C and C=N stretchings), 763 and 686(C-H bending vibrations of mono substituted benzene ring), 3055(aromatic C-H stretching). ¹H-NMR(400MHz, CDCl₃, δ): 7.33-8.01(17H, multiplet, aromatic protons except C₅^{'''}-H, C₄^{'''}-H, C₃[']-H, C₅[']-H, C₃^{''}-H, C₆^{''}-H, C₄-H), 8.26(1H, singlet, C₅^{'''}-H), 8.47-8.63(5H, multiplet, protons at C₄^{'''}, C₃['], C₅['], C₃^{''} and C₆^{''}), 9.75(1H, singlet, C₄-H). ¹³C-APT (100MHz, CDCl₃, δ): 113.82(C), 116.27(CH), 116.59(CH), 116.70(C), 117.15(C), 117.77(CH), 118.45(C), 119.31(CH), 119.51(CH), 120.78(CH), 121.24(CH), 121.73(C), 121.89(CH), 121.99(C), 122.48(C), 123.82(CH), 123.97(C), 124.47(CH), 126.11(CH), 127.25(CH), 127.34(C), 128.37(CH), 128.48(CH), 129.11(CH), 129.71(CH), 130.40(C), 131.96(CH), 133.48(CH), 136.93(CH), 138.13(CH), 139.60(C), 142.09(C), 143.56(CH), 149.13(CH), 151.01(C), 155.89(C), 156.10(C), 159.69(CO of coumarin), 160.16 (CO of coumarin). Anal.Calcd. for C₄₁H₂₄N₄O₄: C, 77.08; H, 3.80; N, 8.80 %. Found: C, 77.13; H, 3.89; N, 8.96 %.

8''''-Methoxy-3-{4'-[3'''-(coumarin-3''''-yl)-1'''-phenyl-1H-pyrazol-4''''-yl]-2',2''-bipyridin-6'-yl}coumarin (8d): Yield: 67%, m.p.230-231°C, IR(KBr, ν_{max}, cm⁻¹): 1728(C=O stretching of δ-lactone of coumarin) 1620 and 1481(aromatic

C=C and C=N stretchings), 748 and 678(C-H bending vibrations of mono substituted benzene ring), 2847(aliphatic C-H stretching), 3070(aromatic C-H stretching). ¹H-NMR(400MHz, CDCl₃, δ): 3.96(3H, singlet, OCH₃), 7.12-7.89(14H, multiplet, aromatic protons except C₅^{'''}-H, C₄^{'''}-H, C₃[']-H, C₅[']-H, C₃^{''}-H, C₆^{''}-H, C₄-H), 8.26(1H, singlet, C₅^{'''}-H), 8.47-8.56(4H, multiplet, protons at C₄^{'''}, C₃['], C₅['] and C₃^{''}), 8.63(1H, poorly resolved doublet of doublet, C₆^{''}-H), 8.94(1H, singlet, C₄-H). ¹³C-APT(100MHz, CDCl₃, δ): 56.34(OCH₃), 114.22(CH), 114.82(C), 116.23(CH), 118.70(CH), 119.52(CH), 120.09(CH), 121.50(CH), 122.09(CH), 123.88(CH), 124.32(CH), 124.54(CH), 126.99(C), 127.24(CH), 127.46(CH), 129.09(CH), 129.72(CH), 130.31(C), 132.01(CH), 135.77(C), 137.12(C), 138.25(C), 139.50(C), 141.07(CH), 142.30(CH), 142.70(C), 143.71(C), 145.75(CH), 146.03(C), 148.98(CH), 150.67(C), 151.86(C), 153.87(C), 154.53(C), 159.11(CO of coumarin), 160.11(CO of coumarin). Anal.Calcd. for C₃₈H₂₄N₄O₅: C, 74.02; H, 3.92; N, 9.09 %. Found: C, 74.16; H, 4.02; N, 9.19 %.

8,8''''-Dimethoxy-3-{4'-[3'''-(coumarin-3''''-yl)-1'''-phenyl-1H-pyrazol-4''''-yl]-2',2''-bipyridin-6'-yl}coumarin (8e): Yield: 64%, m.p.200-202°C, IR(KBr, ν_{max}, cm⁻¹): 1713(C=O stretching of δ-lactone of coumarin), 1605 and 1474(aromatic C=C and C=N stretchings), 756 and 694(C-H bending vibrations of mono substituted benzene ring), 2908(aliphatic C-H stretching), 3063(aromatic C-H stretching). ¹H-NMR(400MHz, CDCl₃, δ): 3.96(3H, singlet, OCH₃), 3.98(3H, singlet, OCH₃), 7.10-7.88(13H, multiplet, aromatic protons except C₅^{'''}-H, C₄^{'''}-H, C₃[']-H, C₅[']-H, C₃^{''}-H, C₆^{''}-H, C₄-H), 8.25(1H, singlet, C₅^{'''}-H), 8.47-8.57(4H, multiplet, protons at C₄^{'''}, C₃['], C₅['] and C₃^{''}), 8.65(1H, poorly resolved doublet of doublet, C₆^{''}-H), 8.95(1H, singlet, C₄-H). ¹³C-APT(100MHz, CDCl₃, δ): 56.23(OCH₃), 56.32(OCH₃), 113.75(CH), 114.14(CH), 118.65(CH), 119.19(CH), 119.44(CH), 119.92(CH), 120.01(C), 120.22(C), 120.40(CH), 121.35(CH), 121.78(C), 122.13(CH), 122.44(C), 122.53(C), 123.79(CH), 124.28(CH), 124.34(CH), 125.40(C), 127.23(CH), 127.41(CH), 136.87(CH), 139.56(C), 142.21(C), 142.64(CH), 143.60(CH), 144.10(C), 145.79(C), 146.80(C), 147.07(C), 149.02(CH), 150.60(C), 155.70(C), 155.97(C), 158.99(CO of coumarin), 159.52(CO of coumarin). Anal.Calcd. for C₃₉H₂₆N₄O₆: C, 72.44; H, 4.05; N, 8.66 %. Found: C, 72.63; H, 4.19; N, 8.73 %.

5,6-Benzo-8''''-methoxy-3-{4'-[3'''-(coumarin-3''''-yl)-1'''-phenyl-1H-pyrazol-4''''-yl]-2',2''-

bipyridin-6'-yl}coumarin (8f): Yield: 70%, m.p.255-256°C, IR(KBr, ν_{\max} , cm^{-1}): 1720(C=O stretching of δ -lactone of coumarin), 1604 and 1504(aromatic C=C and C=N stretchings), 771 and 671(C-H bending vibrations of mono substituted benzene ring), 2893(aliphatic C-H stretching), 3078 (aromatic C-H stretching). $^1\text{H-NMR}$ (400MHz, CDCl_3 , δ): 3.94(3H, singlet, OCH_3), 7.37-8.36(18H, multiplet, aromatic protons except $\text{C}_4''''\text{-H}$, $\text{C}_3'\text{-H}$, $\text{C}_5'\text{-H}$, $\text{C}_6''\text{-H}$, $\text{C}_4\text{-H}$), 8.46(1H, poorly resolved doublet of doublet, $\text{C}_6''\text{-H}$), 8.65(1H, singlet, $\text{C}_4''''\text{-H}$), 8.80(2H, poorly resolved doublet, $\text{C}_3'\text{-H}$ and $\text{C}_5'\text{-H}$), 9.65(1H, singlet, $\text{C}_4\text{-H}$). $^{13}\text{C-APT}$ (100MHz, CDCl_3 , δ): 56.35(OCH_3), 110.07(C), 112.91(C), 113.29(C), 113.76(C), 114.37(CH), 115.72(C), 116.05(CH), 116.83(CH), 116.98(CH), 118.56(C), 119.14(C), 119.54(C), 120.65(CH), 120.80(CH), 121.43(CH), 122.56(CH), 122.75(CH), 123.03(CH), 126.35(CH), 126.48(CH), 128.44(CH), 129.06(C), 129.39(CH), 129.69(CH), 130.04(CH), 130.37(CH), 130.80(C), 131.78(C), 132.30(CH), 138.21(C), 139.46(CH), 145.32(C), 146.55(CH), 147.73(CH), 149.74(C), 154.99(C), 156.78(C), 160.02(CO of coumarin), 161.25(CO of coumarin). Anal.Calc'd. for $\text{C}_{42}\text{H}_{26}\text{N}_4\text{O}_5$: C, 75.67; H, 3.93; N, 8.40 %. Found: C, 75.82; H, 4.03; N, 8.52 %.

3-{4'-[3'''-(coumarin-3''''-yl)-1'''-phenyl-1H-pyrazol-4''''-yl]-2',3''-bipyridin-6'-yl}coumarin (9a): Yield: 69%, m.p.184-185°C, IR(KBr, ν_{\max} , cm^{-1}): 1735(C=O stretching of δ -lactone of coumarin), 1605 and 1466(aromatic C=C and C=N stretchings), 756 and 625(C-H bending vibrations of mono substituted benzene ring), 3062(aromatic C-H stretching). $^1\text{H-NMR}$ (400 MHz, CDCl_3 , δ): 7.25-8.31(18H, multiplet, aromatic protons + $\text{C}_4''''\text{-H}$ except $\text{C}_3'\text{-H}$, $\text{C}_6''\text{-H}$, $\text{C}_4\text{-H}$ and $\text{C}_2''\text{-H}$), 8.46(1H, doublet, $J=1.2$ Hz, $\text{C}_3'\text{-H}$), 8.58(1H, poorly resolved doublet of doublet, $\text{C}_6''\text{-H}$), 8.90(1H, singlet, $\text{C}_4\text{-H}$), 9.20(1H, poorly resolved doublet, $\text{C}_2''\text{-H}$). $^{13}\text{C-APT}$ (100MHz, CDCl_3 , δ): 114.48(CH), 114.97(C), 116.26(CH), 116.75(CH), 117.92(CH), 119.16(C), 119.45(CH), 119.49(C), 121.16(CH), 121.40(C), 122.06(C), 123.55(CH), 124.58(CH), 124.69(CH), 127.35(CH), 128.49(CH), 129.06(CH), 129.62(CH), 132.21(CH), 134.50(CH), 134.73(C), 139.38(C), 142.29(C), 142.79(CH), 143.66(CH), 145.59(C), 148.25(CH), 149.70(CH), 151.29(C), 153.90(C), 154.28(C), 159.73(CO of coumarin), 160.11(CO of coumarin). Anal.Calc'd. for $\text{C}_{37}\text{H}_{22}\text{N}_4\text{O}_4$: C, 75.76; H, 3.78; N, 9.55 %. Found: C, 75.88; H, 3.87; N, 9.59 %.

8-Methoxy-3-{4'-[3'''-(coumarin-3''''-yl)-1'''-phenyl-1H-pyrazol-4''''-yl]-2',3''-bipyridin-6'-yl}coumarin (9b): Yield: 68%, m.p.168-170°C, IR(KBr, ν_{\max} , cm^{-1}): 1718(C=O stretching of δ -lactone of coumarin), 1597 and 1474(aromatic C=C and C=N stretchings), 763 and 694(C-H bending vibrations of mono substituted benzene ring), 2962(aliphatic C-H stretching), 3055(aromatic C-H stretching). $^1\text{H-NMR}$ (400MHz, CDCl_3 , δ): 3.97(3H, singlet, OCH_3), 7.09-8.37(17H, multiplet, aromatic protons + $\text{C}_4''''\text{-H}$ except $\text{C}_3'\text{-H}$, $\text{C}_6''\text{-H}$, $\text{C}_4\text{-H}$ and $\text{C}_2''\text{-H}$), 8.54(1H, doublet, $J=1.2$ Hz, $\text{C}_3'\text{-H}$), 8.64(1H, poorly resolved doublet of doublet, $\text{C}_6''\text{-H}$), 8.94(1H, singlet, $\text{C}_4\text{-H}$), 9.26(1H, doublet, $J=1.6$ Hz, $\text{C}_2''\text{-H}$). $^{13}\text{C-APT}$ (100MHz, CDCl_3 , δ): 56.41(OCH_3), 114.23(CH), 116.31(CH), 118.55(CH), 119.51(C), 119.57(C), 119.80(CH), 119.96(CH), 121.27(CH), 121.61(C), 122.08(C), 122.24(CH), 124.56(CH), 124.64(CH), 124.92(C), 127.33(CH), 127.41(CH), 129.07(CH), 129.64(CH), 131.03(C), 132.27(CH), 139.42(C), 139.63(CH), 142.50(C), 142.94(CH), 143.84(CH), 144.02(CH), 145.65(C), 146.42(C), 147.18(C), 150.34(CH), 151.53(C), 153.98(C), 154.34(C), 160.19(CO of coumarin), 160.64(CO of coumarin). Anal.Calc'd. for $\text{C}_{38}\text{H}_{24}\text{N}_4\text{O}_5$: C, 74.02; H, 3.92; N, 9.09 %. Found: C, 74.13; H, 4.01; N, 9.17 %.

5,6-Benzo3-{4'-[3'''-(coumarin-3''''-yl)-1'''-phenyl-1H-pyrazol-4''''-yl]-2',3''-bipyridin-6'-yl}coumarin (9c): Yield: 70%, m.p.207-209°C, IR(KBr, ν_{\max} , cm^{-1}): 1720(C=O stretching of δ -lactone of coumarin), 1603 and 1497(aromatic C=C and C=N stretchings), 748 and 687(C-H bending vibrations of mono substituted benzene ring), 3070(aromatic C-H stretching). $^1\text{H-NMR}$ (400MHz, CDCl_3 , δ): 7.35- 8.46(20H, multiplet, aromatic protons + $\text{C}_4''''\text{-H}$ except $\text{C}_3'\text{-H}$, $\text{C}_6''\text{-H}$, $\text{C}_4\text{-H}$ and $\text{C}_2''\text{-H}$), 8.63(1H, doublet, $J=0.8$ Hz, $\text{C}_3'\text{-H}$), 8.68(1H, poorly resolved doublet of doublet, $\text{C}_6''\text{-H}$), 9.37(1H, poorly resolved doublet, $\text{C}_2''\text{-H}$), 9.77(1H, singlet, $\text{C}_4\text{-H}$). $^{13}\text{C-APT}$ (100MHz, CDCl_3 , δ): 113.23(C), 113.78(C), 114.45(C), 114.88(CH), 115.73(C), 116.48(CH), 116.78(CH), 117.98(CH), 119.17(C), 119.56(CH), 121.27(CH), 121.42(C), 121.96(CH), 123.37(C), 123.70(C), 124.71(CH), 126.22(CH), 127.33(CH), 127.43(CH), 128.50(CH), 128.60(CH), 129.00(CH), 129.66(C), 130.32(C), 132.23(CH), 133.76(CH), 134.63(CH), 138.49(CH), 139.45(C), 142.44(C), 143.68(CH), 148.27(CH), 149.62(CH), 151.66(C), 154.30(C), 159.73(CO of coumarin), 160.01(CO of coumarin). Anal.Calc'd. for $\text{C}_{41}\text{H}_{24}\text{N}_4\text{O}_4$: C, 77.08; H, 3.80; N, 8.80 %. Found: C, 77.13; H, 3.89; N, 8.96 %.

8'''-Methoxy-3-{4'-[3'''-(coumarin-3'''-yl)-1'''-phenyl-1H-pyrazol-4'''-yl]-2',3''-bipyridin-6'-yl} coumarin (9d): Yield: 72%, m.p.230-231°C, IR(KBr, ν_{\max} , cm^{-1}): 1713(C=O stretching of δ -lactone of coumarin), 1605 and 1458(aromatic C=C and C=N stretchings), 756 and 694(C-H bending vibrations of mono substituted benzene ring), 2977(aliphatic C-H stretching), 3055(aromatic C-H stretching). $^1\text{H-NMR}$ (400MHz, CDCl_3 , δ): 3.97(3H, singlet, OCH_3), 7.13-8.39(17H, multiplet, aromatic protons + $\text{C}_4'''\text{-H}$ except $\text{C}_3'\text{-H}$, $\text{C}_6''\text{-H}$, $\text{C}_4\text{-H}$ and $\text{C}_2''\text{-H}$), 8.52(1H, doublet, $J=1.2$ Hz, $\text{C}_3'\text{-H}$), 8.65(1H, doublet of doublet, $J=4.8$ and 1.2 Hz, $\text{C}_6''\text{-H}$), 8.96(1H, singlet, $\text{C}_4\text{-H}$), 9.29(1H, doublet, $J=1.6$ Hz, $\text{C}_2''\text{-H}$). $^{13}\text{C-APT}$ (100 MHz, CDCl_3 , δ): 56.32(OCH_3), 114.23(CH), 116.27(CH), 118.21(CH), 119.54(C), 119.56(CH), 119.80(C), 119.95(CH), 121.43(CH), 121.58(C), 122.23(C), 123.68(CH), 124.55(CH), 124.61(CH), 127.42(CH), 128.48(CH), 129.06(CH), 129.71(CH), 132.26(CH), 134.86(CH), 135.03(C), 139.43(C), 141.07(C), 142.49(C), 142.92(CH), 143.81(CH), 146.10(C), 147.11(C), 148.07(CH), 149.45(CH), 151.44(C), 153.99(C), 159.12(CO of coumarin), 161.00(CO of coumarin). Anal.Calcd. for $\text{C}_{38}\text{H}_{24}\text{N}_4\text{O}_5$: C, 74.02; H, 3.92; N, 9.09 %. Found: C, 74.16; H, 4.02; N, 9.19 %.

8,8'''-Dimethoxy-3-{4'-[3'''-(coumarin-3'''-yl)-1'''-phenyl-1H-pyrazol-4'''-yl]-2',3''-bipyridin-6'-yl} coumarin (9e): Yield: 64%, m.p.198-200°C, IR(KBr, ν_{\max} , cm^{-1}): 1720(C=O stretching of δ -lactone of coumarin), 1504 and 1478(aromatic C=C and C=N stretchings), 771 and 694(C-H bending vibrations of mono substituted benzene ring), 2962(aliphatic C-H stretching), 3063(aromatic C-H stretching). $^1\text{H-NMR}$ (400MHz, CDCl_3 , δ): 3.95 and 3.97(6H, two singlets, $2 \times \text{OCH}_3$), 7.09-8.57(18H, multiplet, aromatic protons + $\text{C}_4'''\text{-H}$ except $\text{C}_4\text{-H}$ and $\text{C}_2''\text{-H}$), 8.65(1H, singlet, $\text{C}_4\text{-H}$), 8.93(1H, poorly resolved doublet, $\text{C}_2''\text{-H}$). $^{13}\text{C-APT}$ (100MHz, CDCl_3 , δ): 56.25(OCH_3), 56.34(OCH_3), 114.17(CH), 114.88(C), 118.71(CH), 119.21(C), 119.54(CH), 119.92(C), 120.05(CH), 120.27(C), 120.42(CH), 121.41(CH), 121.79(C), 122.21(CH), 122.51(C), 122.60(CH), 123.06(C), 123.81(CH), 123.94(C), 124.23(CH), 124.34(C), 127.26(CH), 127.44(CH), 129.74(CH), 137.02(CH), 139.08(CH), 139.66(C), 142.64(C), 143.47(CH), 144.13(CH), 144.96(C), 147.02(C), 149.17(CH), 150.74(C), 159.01(C), 161.82(CO of coumarin), 163.97(CO of coumarin). Anal.Calcd. for $\text{C}_{39}\text{H}_{26}\text{N}_4\text{O}_6$: C, 72.44; H, 4.05; N, 8.66 %. Found: C, 72.63; H, 4.19; N, 8.73 %.

5,6-Benzo-8'''-methoxy-3-{4'-[3'''-(coumarin-3'''-yl)-1'''-phenyl-1H-pyrazol-4'''-yl]-2',3''-bipyridin-6'-yl} coumarin (9f): Yield: 68%, m.p.255-256°C, IR(KBr, ν_{\max} , cm^{-1}): 1728(C=O stretching of δ -lactone of coumarin), 1605 and 1474(aromatic C=C and C=N stretchings), 779 and 686(C-H bending vibrations of mono substituted benzene ring), 2932(aliphatic C-H stretching), 3062(aromatic C-H stretching). $^1\text{H-NMR}$ (400MHz, CDCl_3 , δ): 3.97(3H, singlet, OCH_3), 7.13-8.52 (19H, multiplet, aromatic protons + $\text{C}_4'''\text{-H}$ except $\text{C}_3'\text{-H}$, $\text{C}_6''\text{-H}$, $\text{C}_4\text{-H}$ and $\text{C}_2''\text{-H}$), 8.65(1H, poorly resolved doublet, $\text{C}_3'\text{-H}$), 8.71(1H, doublet, poorly resolved doublet of doublet, $\text{C}_6''\text{-H}$), 9.41(1H, poorly resolved doublet, $\text{C}_2''\text{-H}$), 9.83(1H, singlet, $\text{C}_4\text{-H}$). $^{13}\text{C-APT}$ (100MHz, CDCl_3 , δ): 56.32(OCH_3), 115.61(C), 115.98(CH), 116.04(CH), 117.59(C), 118.44(C), 119.06(C), 119.48(C), 120.76(CH), 121.01(CH), 121.31(CH), 122.34(CH), 123.22(CH), 126.51(CH), 128.09(CH), 128.57(CH), 128.94(C), 129.70(CH), 129.80(CH), 130.09(CH), 130.51(CH), 130.87(C), 131.69(CH), 131.74(C), 137.87(C), 140.04(CH), 141.77(CH), 143.13(C), 143.90(CH), 144.22(C), 144.53(CH), 145.24(C), 145.88(CH), 146.70(C), 148.13(CH), 148.59(C), 152.39(C), 155.63(C), 161.09(CO of coumarin), 161.52(CO of coumarin). Anal.Calcd. for $\text{C}_{42}\text{H}_{26}\text{N}_4\text{O}_5$: C, 75.67; H, 3.93; N, 8.40 %. Found: C, 75.82; H, 4.03; N, 8.52 %.

3-{4'-[3'''-(coumarin-3'''-yl)-1'''-phenyl-1H-pyrazol-4'''-yl]-2',4''-bipyridin-6'-yl} coumarin (10a): Yield: 63%, m.p.184-185°C, IR(KBr, ν_{\max} , cm^{-1}): 1713(C=O stretching of δ -lactone of coumarin), 1604 and 1466(aromatic C=C and C=N stretchings), 748 and 686(C-H bending vibrations of mono substituted benzene ring), 3063(aromatic C-H stretching). $^1\text{H-NMR}$ (400MHz, CDCl_3 , δ): 7.34-7.96 (16H, multiplet, aromatic protons except $\text{C}_5'''\text{-H}$, $\text{C}_4'''\text{-H}$, $\text{C}_3'\text{-H}$, $\text{C}_2''\text{-H}$, $\text{C}_6''\text{-H}$, $\text{C}_4\text{-H}$), 8.27(1H, singlet, $\text{C}_5'''\text{-H}$), 8.40(1H, singlet, $\text{C}_4'''\text{-H}$), 8.59(1H, poorly resolved doublet, $\text{C}_3'\text{-H}$), 8.74(2H, doublet, $J=6.0\text{Hz}$, $\text{C}_2''\text{-H}$ and $\text{C}_6''\text{-H}$), 8.98 (1H, singlet, $\text{C}_4\text{-H}$). $^{13}\text{C-APT}$ (100MHz, CDCl_3 , δ): 107.79(C), 110.30(C), 113.13(C), 115.97(CH), 116.89(CH), 117.11(CH), 118.08(CH), 118.40(C), 118.80(C), 119.53(CH), 120.70(CH), 126.07(CH), 126.30(CH), 126.77(CH), 129.18(CH), 129.42(CH), 130.13(CH), 134.15(CH), 136.45(CH), 138.18(C), 143.14(CH), 145.28(C), 147.62(CH), 149.45(CH), 149.94(C), 150.41(C), 153.71(C), 154.08(C), 154.39(C), 159.80(CO of coumarin), 160.03(CO of coumarin). Anal.Calcd. for $\text{C}_{37}\text{H}_{22}\text{N}_4\text{O}_4$: C,

N. N. Gohil, D. I. Brahmhatt: *Synthesis, characterization and biological evaluation of some new pyrazolyl bipyridyl...*
75.76; H, 3.78; N, 9.55 %. Found: C, 75.88; H, 3.87; N, 9.59 %.

8-Methoxy-3-{4'-[3'''-(coumarin-3''''-yl)-1'''-phenyl-1H-pyrazol-4''''-yl]-2',4''-bipyridin-6'-yl} coumarin (10b): Yield: 66%, m.p.170-172°C, IR(KBr, ν_{\max} , cm^{-1}): 1728(C=O stretching of δ -lactone of coumarin), 1605 and 1504(aromatic C=C and C=N stretchings), 756 and 694(C-H bending vibrations of mono substituted benzene ring), 2970(aliphatic C-H stretching), 3055(aromatic C-H stretching). $^1\text{H-NMR}$ (400MHz, CDCl_3 , δ): 4.00(3H, singlet, OCH_3), 7.13-7.96(15H, multiplet, aromatic protons except C_5''' -H, C_4''' -H, C_3' -H, C_2'' -H, C_6'' -H, C_4 -H), 8.27(1H, singlet, C_5''' -H), 8.40(1H, singlet, C_4''' -H), 8.59(1H, poorly resolved doublet, C_3' -H), 8.74(2H, poorly resolved doublet, C_2'' -H and C_6'' -H), 8.96(1H, singlet, C_4 -H). $^{13}\text{C-APT}$ (100MHz, CDCl_3 , δ): 56.51(OCH_3), 110.13(C), 112.96(C), 115.79(C), 116.93(CH), 117.54(C), 118.19(C), 118.62(C), 118.78(C), 119.04(C), 120.66(CH), 121.16(CH), 122.11(CH), 122.35(C), 123.43(C), 123.98(CH), 124.13(CH), 124.88(CH), 124.99(CH), 125.36(CH), 125.85(CH), 126.00(CH), 126.19(CH), 126.48(C), 129.20(CH), 129.94(CH), 130.39(CH), 134.04(CH), 136.07(C), 138.24(C), 142.64(CH), 153.71(C), 159.83(CO of coumarin), 160.28(CO of coumarin). Anal.Calcd. for $\text{C}_{38}\text{H}_{24}\text{N}_4\text{O}_5$: C, 74.02; H, 3.92; N, 9.09 %. Found: C, 74.14; H, 4.02; N, 9.18 %.

5,6-Benzo3-{4'-[3'''-(coumarin-3''''-yl)-1'''-phenyl-1H-pyrazol-4''''-yl]-2',4''-bipyridin-6'-yl} coumarin (10c): Yield: 70%, m.p.205-207°C, IR(KBr, ν_{\max} , cm^{-1}): 1735(C=O stretching of δ -lactone of coumarin), 1612 and 1496(aromatic C=C and C=N stretchings), 779 and 678(C-H bending vibrations of mono substituted benzene ring), 3047(aromatic C-H stretching). $^1\text{H-NMR}$ (400MHz, CDCl_3 , δ): 7.12-7.96(18H, multiplet, aromatic protons except C_5''' -H, C_4''' -H, C_3' -H, C_2'' -H, C_6'' -H, C_4 -H), 8.26(1H, singlet, C_5''' -H), 8.40(1H, singlet, C_4''' -H), 8.58(1H, poorly resolved doublet, C_3' -H), 8.73(2H, poorly resolved doublet, C_2'' -H and C_6'' -H), 9.28(1H, singlet, C_4 -H). $^{13}\text{C-APT}$ (100MHz, CDCl_3 , δ): 109.93(C), 112.75(C), 113.87(C), 115.58(C), 116.83(CH), 117.08(C), 118.41(CH), 118.57(C), 118.67(C), 118.73(C), 118.95(CH), 120.98(CH), 121.52(CH), 122.93(CH), 123.63(CH), 126.55(CH), 127.18(CH), 128.53(CH), 129.34(CH), 129.76(CH), 130.09(CH), 131.65(CH), 131.72(C), 134.51(CH), 137.81(C), 143.51(C), 144.60(C), 146.19(CH), 147.07(CH), 147.76(CH), 147.98(C), 149.69(CH), 152.78(C), 153.54(C), 160.98(CO of coumarin), 162.27(CO of coumarin). Anal.Calcd.

for $\text{C}_{41}\text{H}_{24}\text{N}_4\text{O}_4$: C, 77.08; H, 3.80; N, 8.80 %. Found: C, 77.13; H, 3.89; N, 8.96 %.

8''''-Methoxy-3-{4'-[3'''-(coumarin-3''''-yl)-1'''-phenyl-1H-pyrazol-4''''-yl]-2',4''-bipyridin-6'-yl} coumarin (10d): Yield: 67%, m.p.230-231°C, IR(KBr, ν_{\max} , cm^{-1}): 1720(C=O stretching of δ -lactone of coumarin), 1597 and 1458(aromatic C=C and C=N stretchings), 748 and 694(C-H bending vibrations of mono substituted benzene ring), 2970(aliphatic C-H stretching), 3063(aromatic C-H stretching). $^1\text{H-NMR}$ (400MHz, CDCl_3 , δ): 3.97(3H, singlet, OCH_3), 7.16-7.94(15H, multiplet, aromatic protons except C_5''' -H, C_4''' -H, C_3' -H, C_2'' -H, C_6'' -H, C_4 -H), 8.23(1H, singlet, C_5''' -H), 8.38(1H, singlet, C_4''' -H), 8.54(1H, poorly resolved doublet, C_3' -H), 8.72(2H, doublet, $J=4.4$ Hz, C_2'' -H and C_6'' -H), 8.94(1H, singlet, C_4 -H). $^{13}\text{C-APT}$ (100MHz, CDCl_3 , δ): 56.24(OCH_3), 116.71(C), 118.57(CH), 119.28(C), 119.51(CH), 120.22(CH), 120.36(C), 121.29(CH), 121.62(CH), 122.05(C), 122.43(C), 123.80(CH), 124.28(CH), 124.47(CH), 125.33(C), 127.24(CH), 128.45(CH), 129.60(CH), 131.92(CH), 136.84(CH), 139.56(C), 140.09(C), 142.14(C), 142.60(CH), 143.46(CH), 145.82(CH), 146.85(C), 149.03(CH), 150.59(C), 154.34(C), 155.70(C), 155.92(C), 159.48(CO of coumarin), 159.60(CO of coumarin). Anal.Calcd. for $\text{C}_{38}\text{H}_{24}\text{N}_4\text{O}_5$: C, 74.02; H, 3.92; N, 9.09 %. Found: C, 74.16; H, 4.02; N, 9.19 %.

8,8''''-Dimethoxy-3-{4'-[3'''-(coumarin-3''''-yl)-1'''-phenyl-1H-pyrazol-4''''-yl]-2',4''-bipyridin-6'-yl} coumarin (10e): Yield: 69%, m.p.200-202°C, IR(KBr, ν_{\max} , cm^{-1}): 1713(C=O stretching of δ -lactone of coumarin), 1612 and 1497(aromatic C=C and C=N stretchings), 771 and 686(C-H bending vibrations of mono substituted benzene ring), 2962(aliphatic C-H stretching), 3070(aromatic C-H stretching). $^1\text{H-NMR}$ (400MHz, CDCl_3 , δ): 3.97(3H, singlet, OCH_3), 4.00(3H, singlet, OCH_3), 7.13-7.96(14H, multiplet, aromatic protons except C_5''' -H, C_4''' -H, C_3' -H, C_2'' -H, C_6'' -H, C_4 -H), 8.24(1H, singlet, C_5''' -H), 8.38(1H, singlet, C_4''' -H), 8.57(1H, poorly resolved doublet, C_3' -H), 8.73(2H, doublet, $J=5.2$ Hz, C_2'' -H and C_6'' -H), 8.95(1H, singlet, C_4 -H). $^{13}\text{C-APT}$ (100MHz, CDCl_3 , δ): 56.32(OCH_3), 56.41(OCH_3), 113.78(C), 116.07(C), 116.80(C), 118.62(CH), 119.25(C), 119.60(CH), 120.15(C), 120.35(CH), 121.33(CH), 121.55(C), 122.03(CH), 122.41(C), 123.88(CH), 124.32(CH), 124.57(CH), 125.28(CH), 127.43(CH), 128.69(CH), 129.67(CH), 131.92(CH), 133.83(C), 136.96(CH), 139.60(C), 140.18(C), 142.35(C), 142.93(CH), 143.85(CH), 146.04(C), 146.92(C), 150.81(C), 154.35(C), 160.06(CO of coumarin), 161.17(CO

N. N. Gohil, D. I. Brahmhatt: Synthesis, characterization and biological evaluation of some new pyrazolyl bipyridyl... of coumarin). Anal. Calcd. for C₃₉H₂₆N₄O₆: C, 72.44; H, 4.05; N, 8.66 %. Found: C, 72.63; H, 4.19; N, 8.73 %.

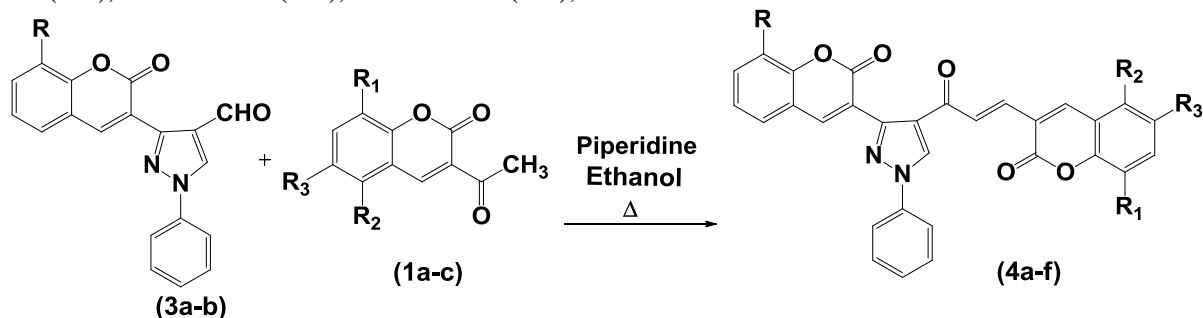
5,6-Benzo-8'''-methoxy-3-{4'-[3'''-(coumarin-3'''-yl)-1'''-phenyl-1H-pyrazol-4'''-yl]-2',4''-bipyridin-6'-yl}coumarin (10f): Yield: 70%, m.p. 255-256°C, IR (KBr, ν_{\max} , cm⁻¹): 1728 (C=O stretching of δ -lactone of coumarin), 1604 and 1488 (aromatic C=C and C=N stretchings), 779 and 663 (C-H bending vibrations of mono substituted benzene ring), 2977 (aliphatic C-H stretching), 3062 (aromatic C-H stretching). ¹H-NMR (400 MHz, CDCl₃, δ): 3.98 (3H, singlet, OCH₃), 7.14-7.96 (17H, multiplet, aromatic protons except C_{5'''}-H, C_{4'''}-H, C_{3'''}-H, C_{2'''}-H, C_{6'''}-H, C₄-H), 8.24 (1H, singlet, C_{5'''}-H), 8.39 (1H, singlet, C_{4'''}-H), 8.55 (1H, doublet, J=1.2 Hz C_{3'''}-H), 8.72 (2H, doublet, J=5.2 Hz, C_{2'''}-H and C_{6'''}-H), 9.60 (1H, singlet, C₄-H). ¹³C-APT (100 MHz, CDCl₃, δ): 56.38 (OCH₃), 111.93 (C), 116.12 (C), 117.58 (CH), 117.73 (C), 119.85 (C), 121.09 (CH), 121.19 (CH), 122.21 (C), 122.31 (C), 123.06 (CH), 123.16 (CH), 123.21 (CH), 123.26 (C), 123.42 (CH), 124.00 (CH), 124.09 (CH), 125.11 (CH),

126.25 (CH), 126.37 (CH), 127.38 (CH), 127.44 (CH), 129.11 (CH), 129.31 (C), 130.40 (C), 131.98 (CH), 133.96 (CH), 137.03 (C), 138.13 (C), 139.63 (CH), 142.09 (C), 143.56 (CH), 147.11 (C), 149.00 (C), 152.89 (C), 153.10 (C), 159.71 (CO of coumarin), 160.19 (CO of coumarin). Anal. Calcd. for C₄₂H₂₆N₄O₅: C, 75.67; H, 3.93; N, 8.40 %. Found: C, 75.82; H, 4.03; N, 8.52 %.

RESULTS AND DISCUSSION

CHEMISTRY

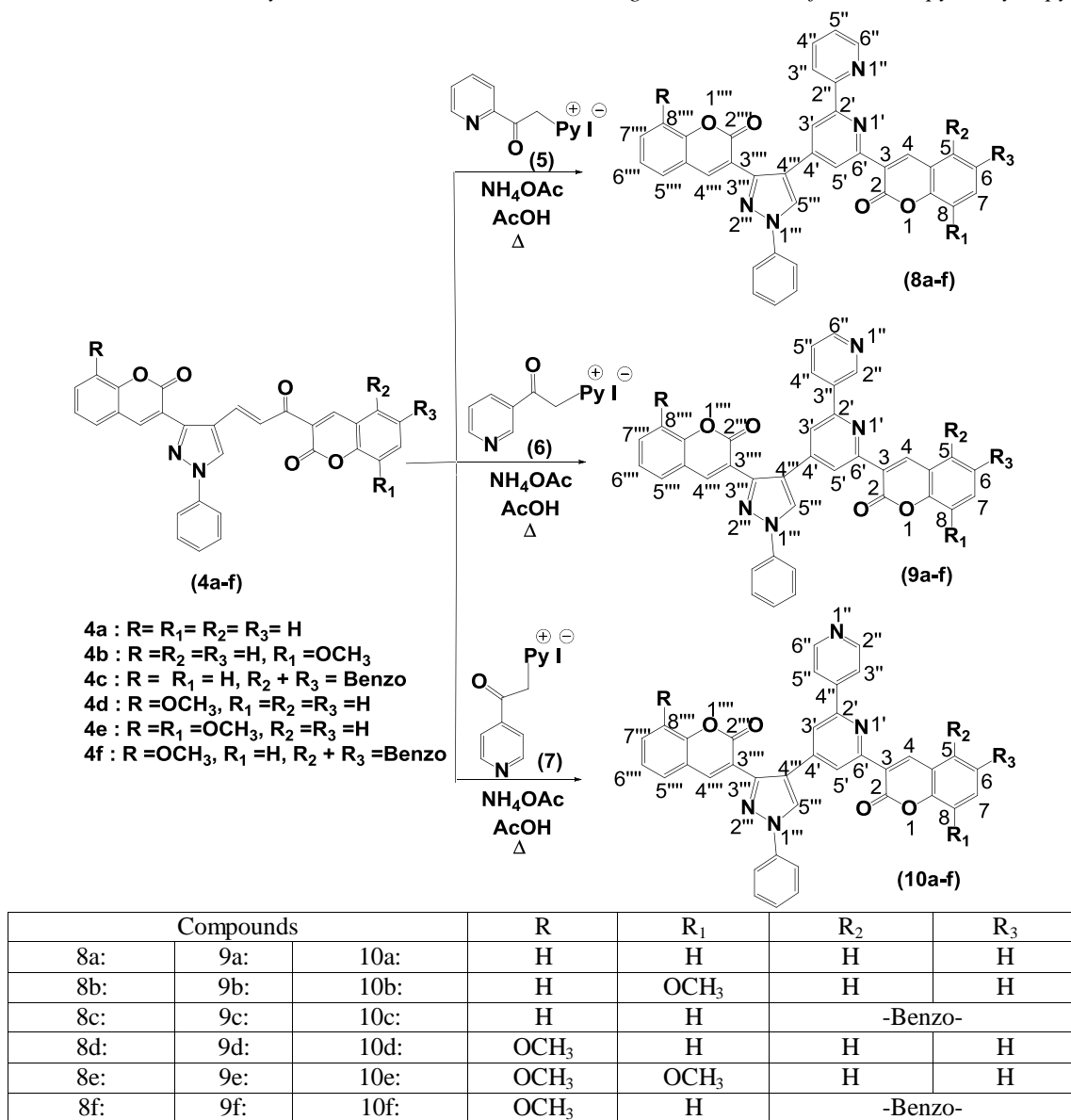
The synthetic pathway adopted to obtain target compounds (**8a-f**), (**9a-f**) and (**10a-f**) which were synthesized by reacting various 3-[3-{3-(coumarin-3-yl)-1-phenyl-1H-pyrazol-4-yl}acryloyl]coumarins (coumarin chalcones) (**4a-f**) with appropriate pyridoyl methyl pyridinium iodide salt (**5-7**) in the presence of ammonium acetate in refluxing acetic acid, is shown in Scheme 1. The structures of all synthesized compounds, supported by IR, ¹H-NMR, ¹³C-APT and representative mass spectral data are shown in the experimental section.



3a : R= H
3b : R= OCH₃

1a : R₁= R₂= R₃= H
1b : R₁= OCH₃, R₂= R₃= H
1c : R₁= H, R₂+ R₃= benzo

4a : R= R₁= R₂= R₃= H
4b : R= R₂= R₃= H, R₁= OCH₃
4c : R= R₁= H, R₂+ R₃= Benzo
4d : R= OCH₃, R₁= R₂= R₃= H
4e : R= R₁= OCH₃, R₂= R₃= H
4f : R= OCH₃, R₁= H, R₂+ R₃= Benzo



Scheme 1. Synthetic pathway for the synthesis of the target compounds (**8a-f**), (**9a-f**) and (**10a-f**)

BIOLOGICAL RESULTS

Antimicrobial Activity

The synthesized target compounds (**8a-f**), (**9a-f**) and (**10a-f**) were evaluated for their *in vitro* antibacterial activity against two Gram positive bacteria *Staphylococcus aureus* (MTCC 96) and *Bacillus subtilis* (MTCC 441) and two Gram negative bacteria *Escherichia coli* (MTCC 443) and *Salmonella typhi* (MTCC 98). They were also evaluated for their *in vitro* antifungal activity against *Candida albicans* (MTCC 227) and *Aspergillus niger* (MTCC 282) as fungal strains. Broth dilution method was used for the determination of the antibacterial and antifungal activity as recommended by NCCLS [30]. Ampicillin, chloramphenicol, ciprofloxacin, norfloxacin and gentamycin were used as standard

antibacterial drugs whereas griseofulvin and nystatin were used as standard antifungal drugs. All MTCC cultures were collected from the Institute of Microbial Technology, Chandigarh and tested against the above mentioned drugs. Mueller-Hinton broth was used as the nutrient medium for the test bacteria and Sabouraud dextrose broth was used for the test fungi. Inoculum size for the test strains was adjusted to 10⁸ CFU (Colony Forming Units) per millilitre by comparing the turbidity. Each synthesized compound was diluted with DMSO so as to have a stock solution of 2000 µg/mL concentration. The results were recorded in the form of primary and secondary screening. The synthesized compounds (**8a-f**), (**9a-f**) and (**10a-f**) were screened for their antibacterial and antifungal activity at the concentration of 1000, 500 and 250 µg/mL for the primary screening. The synthesized compound showing activity against microbes in the

N. N. Gohil, D. I. Brahmhatt: Synthesis, characterization and biological evaluation of some new pyrazolyl bipyridyl...

primary screening were further screened in a second set of dilutions at concentrations of 200, 100, 62.5, 50 and 25 µg/mL. The suspension of 10 µL from each well was further incubated and growth was noted at 37°C after 24 h for bacteria and 48 h for fungi. The lowest concentration which showed no visible growth (turbidity) after spot subculture was considered as the minimum inhibitory concentration (MIC) for each compound.

The investigation of the data summarized in Table 1 reveals that many compounds were found to be active against Gram positive bacteria while some of the compounds were found to be active against Gram-negative bacterial and fungal species

as compared to that of the standard antimicrobial drugs.

Antimicrobial Results

The final compounds (**8a-f**), (**9a-f**) and (**10a-f**) were screened for their *in vitro* antibacterial and antifungal evaluation against various bacterial and fungal pathogens by the broth dilution method. Ampicillin, chloramphenicol, norfloxacin, ciprofloxacin, gentamycin, griseofulvin and nystatin were used as standard drugs. The values of MIC are summarized in Table 1.

Table-1 Antimicrobial activity of compounds (8a-f), (9a-f) and (10a-f)

Compound	Minimum Inhibitory Concentration (MIC, µgmL ⁻¹)						
	Gram positive bacteria		Gram negative bacteria		Fungi		
	<i>B.s.</i>	<i>S.a.</i>	<i>E.c.</i>	<i>S.t.</i>	<i>A.n.</i>	<i>C.a.</i>	
8a	500	500	100	100	500	>1000	
8b	500	500	125	100	500	>1000	
8c	250	250	200	250	>1000	1000	
8d	250	200	200	250	500	1000	
8e	500	500	250	500	500	250	
8f	100	200	62.5	200	>1000	250	
9a	200	200	120	100	1000	250	
9b	500	500	200	250	1000	500	
9c	100	250	250	200	>1000	1000	
9d	500	500	500	100	1000	250	
9e	125	125	250	100	500	1000	
9f	100	250	125	100	500	250	
10a	500	250	500	500	>1000	500	
10b	100	250	200	100	1000	500	
10c	250	125	250	100	>1000	500	
10d	200	100	200	250	500	1000	
10e	100	100	250	125	1000	250	
10f	250	250	100	200	500	1000	
Ampicillin	250	250	100	100	-	-	
Chloramphenicol	50	50	50	50	-	-	
Ciprofloxacin	50	50	25	25	-	-	
Norfloxacin	100	10	10	10	-	-	
Gentamycin	1	0.25	0.05	5	-	-	
Griseofulvin	-	-	-	-	100	500	
Nystatin	-	-	-	-	100	100	

B.s.: Bacillus subtilis, S.a.: Staphylococcus aureus, E.c.: Escherichia coli, S.t.: Salmonella typhi, A.n.: Aspergillus niger, C.a.: Candida albicans

The assessment of antimicrobial screening data reveals that compounds **8f**, **9c**, **9f**, **10b** and **10e** (MIC=100 µg/mL) exerted excellent inhibitory

activity against Gram positive bacteria *Bacillus subtilis* as compared to standard drug ampicillin (MIC=250 µg/mL) and equal activity to norfloxacin (MIC=100 µg/mL). Compound **9e** (MIC=125

$\mu\text{g/mL}$) and compounds **9a** and **10d** ($\text{MIC}=200 \mu\text{g/mL}$) showed good activity compared to ampicillin ($\text{MIC}=250 \mu\text{g/mL}$) against *Bacillus subtilis*. Compounds **8c**, **8d**, **10c** and **10f** ($\text{MIC}=250 \mu\text{g/mL}$) were found to be equipotent to ampicillin ($\text{MIC}=250 \mu\text{g/mL}$) against *Bacillus subtilis*. Compounds **10d** and **10e** ($\text{MIC}=100 \mu\text{g/mL}$) exhibited excellent activity compared to ampicillin ($\text{MIC}=250 \mu\text{g/mL}$) against *Staphylococcus aureus*. Compounds **9e**, **10c** ($\text{MIC}=125 \mu\text{g/mL}$) and compounds **8d**, **8f** and **9a** ($\text{MIC}=200 \mu\text{g/mL}$) showed good activity compared to ampicillin ($\text{MIC}=250 \mu\text{g/mL}$) against *Staphylococcus aureus*. Compounds **8c**, **9c**, **9f**, **10a**, **10b** and **10f** ($\text{MIC}=250 \mu\text{g/mL}$) were found comparable to ampicillin ($\text{MIC}=250 \mu\text{g/mL}$) against *Staphylococcus aureus*. Compound **8f** ($\text{MIC}=62.5 \mu\text{g/mL}$) showed excellent activity and compounds **8a** and **10f** ($\text{MIC}=100 \mu\text{g/mL}$) showed equipotent activity against Gram negative bacteria *Escherichia coli* compared to ampicillin ($\text{MIC}=100 \mu\text{g/mL}$). The compounds **8a**, **8b**, **9a**, **9d**, **9e**, **9f**, **10b** and **10c** ($\text{MIC}=100 \mu\text{g/mL}$) were found to be equipotent to ampicillin ($\text{MIC}=100 \mu\text{g/mL}$) against Gram negative bacteria *Salmonella typhi*. Compounds **8e**, **8f**, **9a**, **9d**, **9f** and **10e** ($\text{MIC}=250 \mu\text{g/mL}$) were found to be more active than griseofulvin ($\text{MIC}=500 \mu\text{g/mL}$) whereas, compounds **9b**, **10a**, **10b** and **10c** were found to be equipotent to griseofulvin ($\text{MIC}=500 \mu\text{g/mL}$) against *Candida albicans*. None of the tested compounds showed better activity against *Aspergillus Niger* than standard drugs. Upon examining the antimicrobial data it is apparent that some of the compounds exhibit good or equal potency to standard drugs against Gram positive bacterial strains.

CONCLUSION

In summary, we have synthesized pyrazolyl-bipyridyl- substituted dicoumarin derivatives and screened for their *in vitro* antimicrobial evaluation. The present synthetic compounds have the potential to exhibit antimicrobial activity. In particular, they have shown promising antibacterial and antifungal activity against several bacterial and fungal pathogens as compared to standard drugs. These compounds can be considered as lead molecules for future investigations.

Acknowledgement: We are grateful to the Head, Department of Chemistry, Sardar Patel University for providing research facilities. This research financially supported by UGC, New Delhi, India, to Neha N. Gohil in the form of UGC BSR Research Fellowship.

REFERENCES

1. M. C. Bahubali, L. S. Samundeeswari, H. Megharaja, A. S. Lokesh, S. M. Sunil K. V. Ramesh, *Medicinal Chemistry Research*, **24**, 4128 (2015).
2. J. M. Timonen, R. M. Nieminen, O. Sareila, *Eur. J. Med. Chem.*, **46**, 3845 (2011).
3. R. B. Moffett, *J. Med. Chem.*, **7**, 446 (1964).
4. C. Xiao, X. L. Yang, D. J. Li, H. Lu, Z. Q. Liu, Z. G. Song, Y. H. Jin, *Eur. J. Med. Chem.*, **53**, 159 (2012).
5. C. Taechowisan, C. H. Lu, Y. M. Shen, *J. Cancer Res. Ther.*, **3**, 86 (2007).
6. Y. Donglei, M. Suzuki, X. Lan, S. Morris-Natschke, K. Lee, *Med. Res. Rev.*, **23**, 322 (2003).
7. A. S. Recillas, G. N. Vazquez, S. H. Figueroa, M. Y. Rios, M. I. Barajas, S. E. Soto, *Eur. J. Med. Chem.*, **77**, 400 (2014).
8. A. R. K. Arora, N. Kaur, Y. Bansal, G. Bansal, *Acta Pharmaceutica Sinica B*, **4**, 368 (2014).
9. A. I. Kostova, *Curr. Med. Chem. Anticancer Agents*, **5**, 29 (2005).
10. I. Sahoo, K. Suman, Mekap, K. PaidisettySudhir, *Journal of Taibah University of Science*, **9**, 187 (2015).
11. A. I. S. Mounir, I. M. Magda, M. E. K. Azza, *Molecules*, **21**, 249 (2016).
12. H. M. Dharmesh, P. Christophe, D. C. Erik, H. C. Kishor, *Arch. Pharm. Chem. Life Sci.*, **342**, 281 (2009).
13. A. M. Shaimaa, A. F. Abdelbasset, N. A. N. Magda, S. T. Atif, *Saudi Pharmaceutical Journal*, **25**, 873 (2017).
14. A. Z. Kurt, I. Gazioglu, F. Sonmez, M. Kucukislamoglu, *Bioorg. Chem.*, **59**, 80 (2015).
15. N. R. Thakare, V. S. Jamode, *Asian J. Chem.*, **19**, 3633 (2007).
16. P. Aragade, S. Kolhe, H. Kamble, D. Baheti, V. Maddi, *Int. J. of Drug Design and Discovery*, **3**, 688 (2012).
17. R. Kenchappa, Y. D. Bodke, A. Chandrashekar, M. Sindhe, S. K. Peethambar, *Arabian Journal of Chemistry*, **10**, 3895 (2017).
18. V. S. Moskvina, V. P. Khilya, A. A. Ishchenko, K. Vys, *Energ.*, **46**, 177 (2012).
19. V. N. Kozhevnikov, D. N. Kozhevnikov, O. V. Shabunina, V. L. Rusinov, O. N. Chupakhin, *Tetrahedron Lett.*, **46**, 1791 (2005).
20. I. Denny, L. Novotny, P. W. J. West, M. Blesova, J. Zamocka, *Med. Princ. Pract.*, **14**, 377 (2005).
21. B. M. Kelly-Basetti, D. J. Cundy, S. M. Pereira, W. H. F. Sasse, G. P. Savage, W. Simpson, *Bioorg. Med. Chem. Lett.*, **5**, 2989 (1995).
22. De. Zwart, H. M. M. Bastiaans, H. Goot, H. Timmerman, *J. Med. Chem.*, **34**, 1193 (1991).
23. J. Egan, K. R. Koch, P. L. Swan, C. Clarkson, D. A. Schalkwyk, P. J. Smith, *J. Med. Chem.*, **47**, 2926 (2004).
24. J. Yoo, Y. S. Sohn, Y. Do, *Journal of Inorganic Biochemistry*, **73**, 187 (1999).

- N. N. Gohil, D. I. Brahmhatt: Synthesis, characterization and biological evaluation of some new pyrazolyl bipyridyl...*
25. R. Ziessel, in: *Photosensitization and Photocatalysis Using Inorganic and Organic Compounds*, K. Kalyanasundaram, M. Gratzel, (eds.), Kluwer Academic, Dordrecht, 1993, p. 217.
 26. H. Keefe, K. D. Benkstein, J. T. Hupp, *Coord. Chem. Rev.*, **205**, 201 (2000).
 27. A. K. Saha, K. Kross, E. D. Kloszewski, D. A. Upson, J. L. Toner, R. A. Snow, C. D. Black, V. C. Desai, *J. Am. Chem. Soc.*, **115**, 11032 (1993).
 28. A. Basnet, P. Thapa, R. Karki, Y. Na, Y. Jahng, B.-S. Jeong, T. C. Jeong, C.-S. Lee, E.-S. Lee, *Bioorg. & Med. Chem.*, **15**, 4351 (2007).
 29. V.G. Bhila, Ph. D. Thesis, "Studies on Synthesis and Antimicrobial efficiency of Pyridine and Pyrazole substituted/fused Coumarin derivatives", Sardar Patel University, Vallabh Vidyanagar, 2012.
 30. National Committee for Clinical Laboratory Standards (NCCLS), 940, West Valley Road, Suite 1400, Wayne, Pennsylvania 19087-1898, USA. Performance Standards for Antimicrobial Susceptibility Testing; Twelfth Informational Supplement (ISBN 1-56238-454-6), M100-S12 (M7), 2002.

Mechanical analysis of additively manufactured polylactic acid in fused deposition modelling

A. Mushtaq^{1*}, A. Israr¹, M. Fahad², J. Ahmed¹

¹Polymer and Petrochemical Engineering Department,

²Industrial Manufacturing Department, NED University of Engineering & Technology, Karachi, Sindh, Pakistan

Received September 8, 2018, Revised August 19, 2019

Additive manufacturing technology is a most widely used technique to manufacture 3D printed objects by adding layer over layer of specific material. Additive manufacturing referred physical fabrication of 3D model by accumulating many layers of different materials, providing vast flexibility in physical structure and geometry. This study focused on Fused Deposition Model (FDM) that will help to analyze two basic parameters (raster angle and number of contours) of 3D model objects to determine the tensile strength of different specimen made from polylactic acid (PLA) having a constant infill density of 25%. The part build with concentric pattern shows the highest tensile strength with number of contours 2, 3 and 4. With the mathematical models for four different raster angles there is a better understanding of how the FDM manufactured objects of PLA material would behave under loading.

Keywords: 3D printing; Additive manufacturing; Fused Deposition Modelling; Polylactic acid.

INTRODUCTION

According to ASTM international committee (F 42), additive manufacturing technology is defined as “the process of joining material to make an object from three-dimensional (3D) model data usually layer by layer as opposed to substrate manufacturing methodology” [1]. Additive manufacturing (AM) is a computer-assisted process that helps in the physical fabrication of 3D objects using metals, plastics, ceramics, compost and biological material, deposited layer over layer and forming a 3D structure. Additive manufacturing is an effective reverse engineering technique that

helps in redesigning and manipulating a product that already exists [2]. The concept of additive manufacturing, also known as 3D printing, rapid prototyping and solid free form was developed in the early 1980s by Charles Hull. In 1986 Hull developed a 3D system under the name of stereolithography (STL), in which he established a format of STL file with the help of computer-aided design (CAD) software to get a 3D object printed [3]. After the inception of assistive manufacturing in the mid-1980s, the technology has evolved, so much that a number of different methodologies have been discovered.

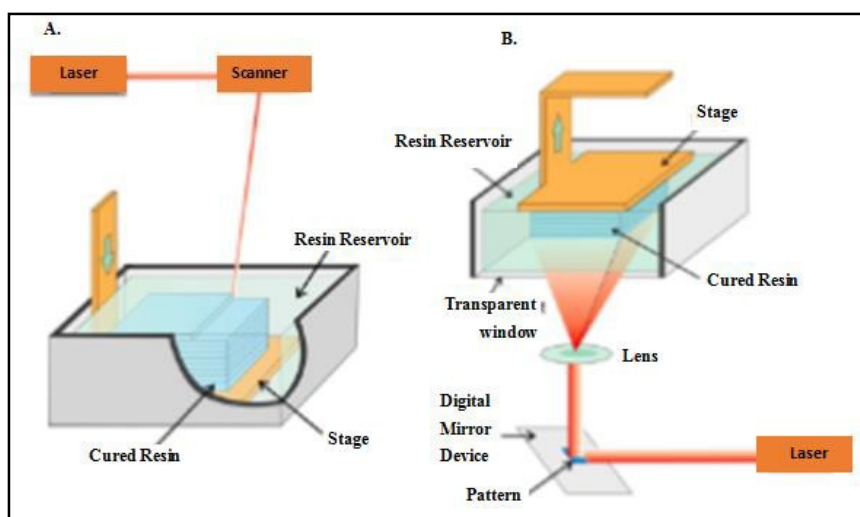


Fig. 1. Schematic of stereolithography

* To whom all correspondence should be sent:
E-mail: engrasimmushtaq@yahoo.com

The major additive manufacturing processes are stereolithography, fused deposition modelling (FDM), inkjet printing, selective laser sintering, 3D printing, laminated object manufacturing and laser metal deposition [1].

Hull invented in 1986 the first additive manufacturing process named stereolithography. It was the first AM technique used commercially by 3D System Inc. [3]. Stereolithography is an additive manufacturing (AM) technique which is used to fabricate a complete 3D structure of a plastic monomer using computer-aided design (CAD) data by different binding layers of photopolymers under the process of photo polymerization [4].

In Figure 1 the process of stereolithography initiates when a spot beam of ultra violet (UV) light moves across the surface of curable plastic monomer. The incident UV light initiates the polymerization reaction across the surface of the liquid monomer and start solidifying. Once a layer of solidified material with a required thickness is formed the solid material is taken below the liquid surface and new liquid monomer, in turn, starts to solidify under programmed manner. The newly formed layer then immediately adheres to the preceding layer. The process continues until the 3D object is completely formed [4].

UV curable resins, waxes and ceramics are extensively used in stereolithography [3]. Fused Deposition Model is the most widely additive manufacturing technique. It was developed by Scott Crump in 1989. The technique was patented by Stratasys [3]. The most common additive manufacturing technique is fused deposition modelling (FDM). In FDM process the first step is to generate the 3D model of the part using computer aid design (CAD).

The model is then exported to FDM machine software where it converts the design into basic components of a 2D small triangular structure. This information is further used in the physical generation of the model [3, 5]. Once a 3d model is formed in CAD software, a molten state thermoplastic is extruded form the machine and deposits layer over layer forming a 3 D structure [3].

Thermoplastics and waxes can be used in FDM machines as shown in Figure 2. Selective laser sintering (SLS) techniques were invented by Deckard and Beaman in 1980 [3]. Selective laser sintering (SLS) is a technique used in additive manufacturing. The process involves manufacturing of 3D object by using powder material that selectively fuses by laser radiation and deposits layer over layer to form a three-dimensional product. The laser radiation helps to initiate the

process by partially melting the product; the liquid form by molten material binds the surrounding powder, solidifies and consolidates once the temperature decreases [6-8].

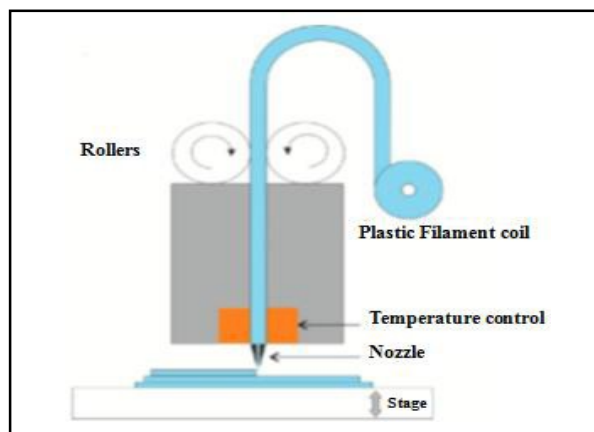


Fig. 2. Schematic of fused deposition model [3].

In a laser sintering process the powder material is sintered selectively by a laser beam to produce an initial sintered layer of specific dimensions as shown in Figure 3. The first formed sintered layer corresponds to the initial structure of the desired product. The sintering process continues until a three-dimensional structure with a specific design is formed. The laser beam in the sintering process helps to selectively sinter the powder material with specific boundaries and desired structure [6]. Thermoplastics and metals can be used in SLS.

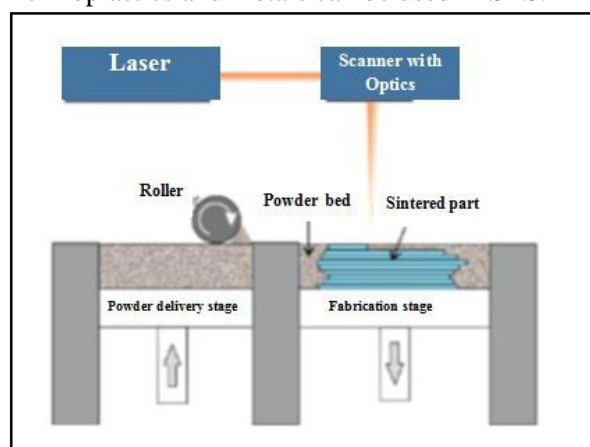


Fig. 3. Schematic of selective laser sintering [3].

The initial concept of the inkjet printer was developed in 1878 by Lord Rayleigh. In 1951, Siemens patented the 2D inkjet type printer called "Rayleigh breakup inkjet device" as shown in Figure 4. Inkjet printing is a powder-based 3D manufacturing process. In inkjet printing, the powder material is bound together by printing liquid that helps in binding the powder and results in the formation of a 3D structure [3].

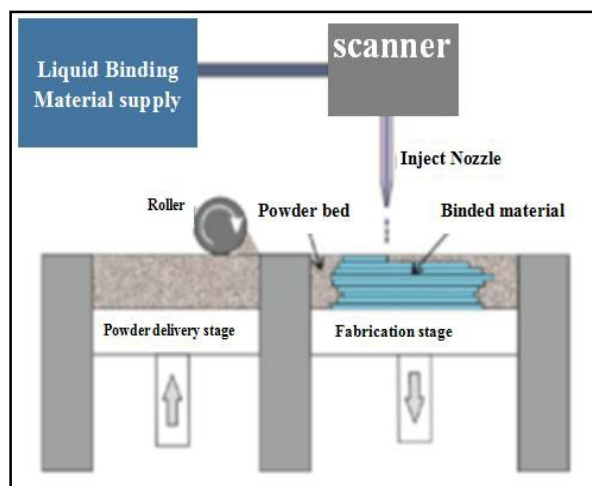


Fig. 4. Schematic of inkjet printing.

A layer of evenly distributed powder material was formed with the help of rollers which form the initial stage of the inkjet process. Once a layer is formed, the printer drops binding liquid material onto the powder making a specific shape. After the completion of the first stage, the second layer of powder is distributed and selectively binds with the initial layer of material. The process is repeatedly performed until a 3D structure is formed. Once the desired product is formed the model is heated to enhance the binding strength between the layers. Unlike other 3D processes, inkjet printing has an edge of providing support material in terms of unbound powder material which can be reused after the material is printed [3, 9]. Composites, polymer-ceramics and metals are used for inkjet printers.

All discussed techniques are being used in the rapid prototyping for the production of consumer end product. 3D Systems Inc. and Stratasys Inc. have acquired the largest market share in 3D prototyping due to their modern technique.

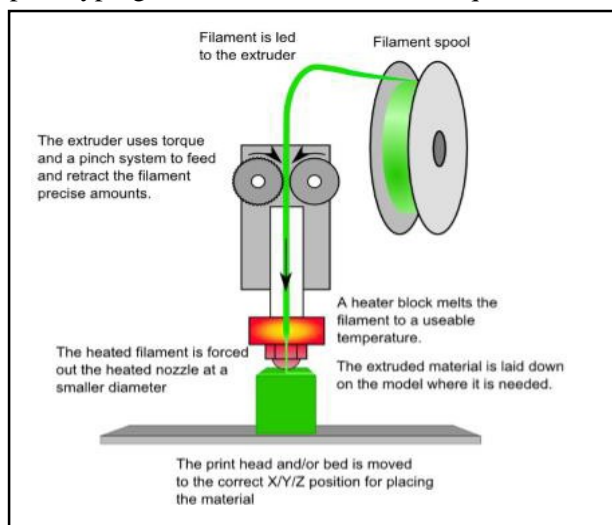


Fig. 5. Schematic of Fused Deposition Modelling [11].

Fused deposition modelling (FDM) is the most popular additive manufacturing technique that produces a physically fabricated model using computer-aided design. The FDM technology is patented by Stratasys Inc. This technology basically relies on the robotic arm with a head which extrudes the melted thermoplastic filament. Stratasys first sold their machine in 1992 by the name of 3D modeller. The early product of the company could replicate different 3D models. However, the machine was not able to take big markets to share due to its low volume productivity so in 1993 Stratasys introduced its second product by the name of "The Benchtop", which was roughly the size of a refrigerator. The machine not only has the ability to deal with high volume but is also suitable to manufacture industrial-scale prototype [10].

In the mid 1980's IBM developed a small 3D printer that works on an extrusion system similar to that of Stratasys. The major difference between the two products was the feeding system. In 1995 Stratasys offered IBM to co-develop a 3D printer which resulted in the introduction of "the Genisys" 3D printer. The product found an overwhelming response of market in its first year. However, it faced a number of major problems including the contaminant wafer that could not melt properly at the operating temperature, leaving small particles that jammed the nozzles. It also has a drawback that once the model gets cooled it has the tendency to curl along the edges. In 1998 after selling 130 units, Stratasys stopped the production of Genisys, and returned the product with the name of "Genisys Xs" [10].

In 1997 Stratasys got the clearance from the department of food and drug administration and started working in the field of medicine. They introduced their "Med Modeler" system which was specifically designed to serve in the field of medicine by producing anatomical parts for MRI and CT scan [10]. Stratasys further introduced its product named "FDM Quantum" that offers a large envelope for an additive manufacturing system. The product offers a proper networking system which enables a number of uses to work together [10]. In 2000, Stratasys introduced "prodigy" which was capable of making sample typed 8×8×12 inches with three different layer thicknesses. In late 2000, Stratasys released "FDM Maxum" with a big envelope modeller and water work support which reduces the processing time by reducing the post-processing work by clean prototype [10]. The product replaced the IBM wafer system by a plastic filament that was fed in the nozzle by heating the

A. Mushtaq et al.: Mechanical analysis of additively manufactured polylactic acid in fused deposition modelling material to its melting temperature, as shown in Figure 5.

This not only simplified the process but also reduced the manufacturing time by adopting a simple mechanism. With the introduction of “dimension”. Stratasys regained his market share, a month further after the introduction of “dimension”, Stratasys presented his new products named “Prodigy Pus” and “FDM Vintage” [10]. In 2004 Stratasys introduced “Dimension SST”, which was capable of producing complex models and prototypes [10]. The main components of the FDM machine are the nozzle or the liquid head, the axes, the building envelope and the controller. There is a number of thermoplastic materials which can be used in the FDM machine. Acrylonitrile butadiene-styrene (ABS) is the most commonly used material in FDM [5]. However, in recent advancement in the field of 3D printing, high advanced material such as ULTEM™ 9085 resin can also be incorporated in FDM machines [12, 13]. With the emergence of Open source 3D printer polylactic acid is the most widely used material in printers due to its vast durability and low processing temperature [5].

Recent advancement in the field of the polymer has paid much attention to a biodegradable polymer. Polylactic acid is the most widely used material in 3D printing that is a linear aliphatic thermoplastic degrading biologically. The thermal stability of polylactic acid was studied by F. Carrasco who explained that using TGA data at low processing temperature the amount of fumes released from the sample is of very less amount which makes it environmentally friendly [14]. The mesostructure of polylactic acid explains that due to the small methyl group linked with the main C-C chain, the chain can easily slide making it easy to extrude the material; hence it is easy to process. The melt flow index (MFI) lies in the range of 7g/10 min to 10.7g/10 min depending upon the crystallinity of PLA .which shows that there is a linear relation between the chain alignment and MFI.

Similarly, if we compare polylactic acid with acrylonitrile butadiene (ABS) it is witnessed that due to the high melting point the deposited layer deforms due to high- temperature gradient which makes it difficult to process. It is also shown that the temperature distribution in the fiber is highly non-uniform due to which the building structure deforms [15]. The melting point of acrylonitrile butadiene nitrile (ABS) is around 230 °C at which the fumes released consist of phenols, styrene and butadiene, which make the environment unsafe when printing [16].

FDM process deals with a number of parameters that need control for optimizing the process. The

selection of parameters solely depends on the application of a product which is being manufactured. The control parameters likely affect the mechanical properties, final finish and processing temperature of the part. The final parameters that could affect the final product processing by FDM technology are build orientation, nozzle and bed temperature, layer thickness, contour (vertical shells), infill density, raster angle and horizontal shell [17]. The build orientation of FDM manufactured part refers to the direction of beads of material concerning the loading of the part. At first, the specimen is configured to which axis it is geometrically built [18].

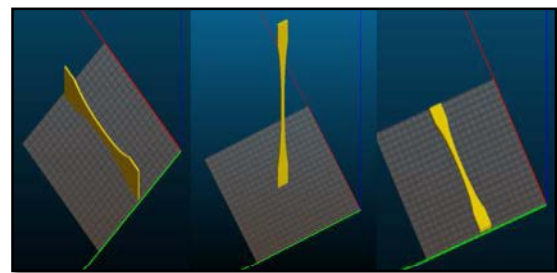


Fig. 6. Build orientation at x, y and z-direction

The built specimen can be in the direction of x, y and z-axis, as shown in Fig. 6. However, all three build directions have a different effect on the mechanical properties of the sample. Figure 6 shows the build orientation of different samples; the first picture shows the building of sample at x direction, similarly the other two pictures show the build orientation at y and z-direction, respectively. A further illustration of different orientations concerning different build angle is shown in Figure 7. With every different orientation, the tensile strength varies depending upon the filaments alignment, applied force and build pattern.

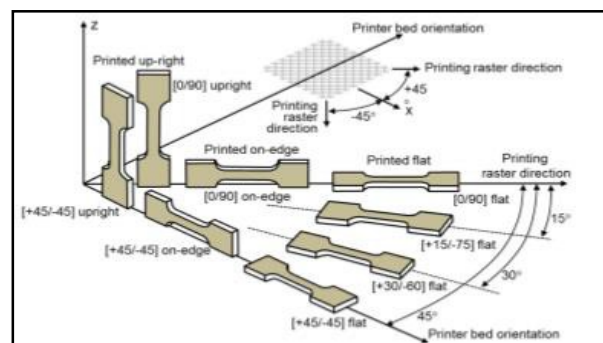


Fig. 7. Sample built with different raster angles and build orientation [19].

Nozzle and bed temperature

The selection of nozzle and bed temperature is a function of the material used. Typically for PLA the

A. Mushtaq et al.: Mechanical analysis of additively manufactured polylactic acid in fused deposition modelling nozzle temperature ranges from 200 to 210 °C and bed temperature could be in the range of 0-60 °C.

Layer thickness

The layer thickness is the amount of material that could be deposited from the nozzle. The amount of material is determined by the nozzle diameter. The layer thickness also depends upon the feed rate of the machine. At maximum feed rate, the deposited layer shows consistency in diameter, hence shows constant layer thickness.

Contour (number of shells)

After build orientation, the number of contouring is the major factor that determines the properties of the sample. A number of contours determine the outer layer thickness of the sample. The higher the number of the layers the more finished manufactured model will be. In Figure 8 the samples are built with a number of outer perimeters 4 and 1, respectively. The number of the contours can vary depending upon the layer thickness and build pattern.

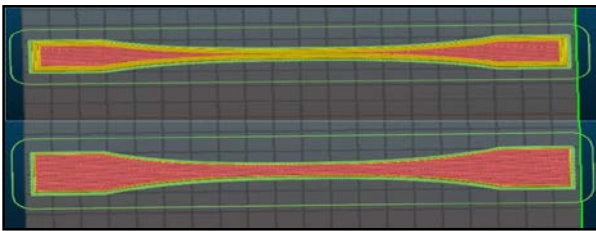


Fig. 8. Samples with number of contours 4 (top) and 1 (bottom).

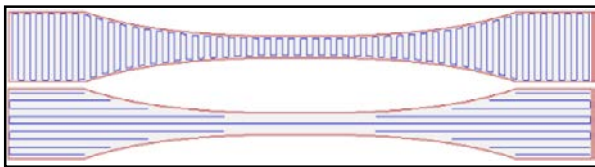


Fig. 9. Samples with infill density of 100% and raster orientation 0°.

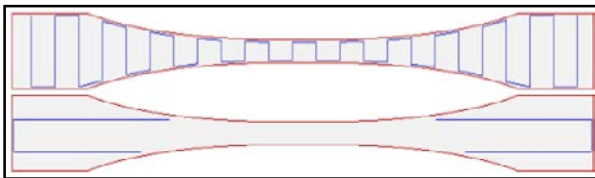


Fig. 10. Samples with infill density of 25% and raster orientation 0°.

Infill density

Infill density refers to the distance between two layers. The larger the gap between the layers, less dense is the sample at short processing time. Although a sample with no gap between the layers is denser at a longer processing time. The infill

density ranges from 0 to 100 % as shown in Figure 9.

The above figure illustrates that the higher the infill density, the denser the sample would be, but the effect of infill density on tensile strength decreases after reaching the point where tensile strength is maximum as shown in Figure 10.

Raster angle

Raster angle is the direction at which the bead of material moves relative to the direction at which part is loaded. The value of raster angle ranges from 0° to 45°.

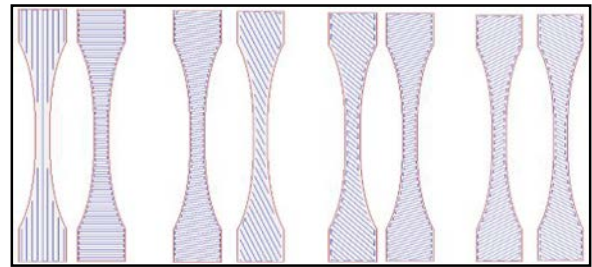
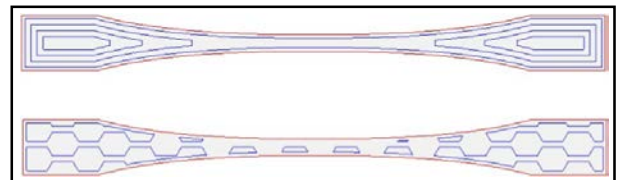


Fig. 11. Raster angle: (i) 0°, (ii) 15°, (iii) 30° and (iv) 45°.

Figure 11 shows the build pattern of different samples made with the raster angle 0°, 15°, 30° and 45°, respectively. Similarly, figure 12 shows that besides build pattern with a certain angle the sample can be made using build pattern of



concentric and honey comb structure.

Fig. 12. Fill pattern: concentric (top) and honey comb (bottom)

Horizontal shells

Horizontal layers refer to the extreme top and bottom layers having the infill density of 100%. The solid top and bottom layers of the fabricated part help enhancing the finish and tensile strength of the final product.

Speed

The speed of the deposited material is determined by the OEM. However, with maximum build speed the time to fabricate a material decreases. Process parameters are some of the key factors that determine the quality and the strength of the finished good. A number of process parameters can be varied so that their influence can be studied on the final manufactured good. Various

A. Mushtaq *et al.*: Mechanical analysis of additively manufactured polylactic acid in fused deposition modelling design, methods and strategies have been studied to assist the manufacturing process of prototyping.

Es-Said *et al.* examined the tensile strength of an ABS sample with different layer orientations indicating the relation of yield and ultimate strength with orientation [20]. Experimental data collected were analyzed by a three-point methodology which illustrated that modulus of rupture is greater when the sample layers are oriented at 0° . However, the value decreases when the layer orientation is 90° , this is because the FDM sample has weak interlayer bonding or porosity. He also concluded that due to different layer deposition the overall sample exhibits an anisotropic characteristic. Since the sample shows an anisotropic property, the layer orientation with a different angle (e.g. 45° / -45° , 0° / 45° , 90°) has a significant effect on the tensile strength. Therefore it can be concluded that anisotropy is affected by the angle at which the sample is produced depending upon the porosity and layer orientation.

Montero *et al.* have found that the physical parameters of FDM sample (i.e. air gap and raster orientation) had great effect on the tensile strength of parts, however, temperature has little effect [21]. The investigation showed that tensile strength of the part produced by crisscross orientation (45° / -45°) shows isotropic characteristics. It was noticed that axial orientation is higher as compared to transverse orientation. The crisscross orientation with zero elastic module is higher as compared to the negative air gap. The stress-strain curve of the sample produced when layers are axially oriented revealed that with an increase in the percentage of strain the stress increases reaching to a point after which the percentage change in strain has little effect on stress, however the stress-strain curve in transverse raster orientation exhibits brittle behavior.

Ahn *et al.* have comparatively analyzed the tensile strength of an ABS sample produced by FDM and an ABS sample produced by injection moulding process [18]. The FDM sample was fabricated with 12 layers with different raster angles and having a certain air gap. The investigation of the results showed that the sample produced with raster angle $0^\circ/0^\circ$ and $0^\circ/90^\circ$ had higher tensile strength as compared to a sample produced with the crisscross orientation of raster angle 45° / -45° . However, the sample oriented at the angle of 90° showed the least value of tensile strength as compared to the sample produced by injection molding. This magnifies the results that in the axial direction 0° the gap in-between the fibres decreases the effective cross-sectional area whereas in a transverse direction 90° the tensile load is

distributed only on the bond, not on the fibres, hence showing a lower tensile strength. The crisscross specimen shows a shear failure at the angle of 45° which is because of the repetitive application of tension and shear force.

Sun *et al.* conducted experiments in which the relation between process conditions and quantity of layer formed in FDM processed parts was studied [22, 23]. The findings were based on the neck formation between the two deposited layers and the failure under the application of flexural load. The result concluded that as regards the flexural strength, the temperature has great influence on FDM parts. The further results showed that the temperature of the bottom layer of the FDM parts remains higher than the glass transition temperature over a longer period of time. As the number of the deposited layer increases, the phenomenon of stress generation due to greater temperature gradient is more prominent. A study conducted by Sood *et al.* showed the relation between tensile strength and layer thickness, part build orientation, raster angle, raster to raster gap and raster width [17]. The parts were fabricated using FDM, and experimental data were collected by forced centered central design (FCCD) run where the contour width was kept constant at the value of 0.4064 mm. The results showed that tensile strength and flexural strength of a sample fabricated using ISO R527:1966 can be significantly affected by the physical processing properties.

In a three-point analysis process where the range of layer thickness was from 0.1270 mm to 0.2540 mm, raster angle from 0° to 60° , raster width from 0.04064 mm to 0.5064 mm and air gap from 0.00 mm to 0.0080 mm, the investigation results showed that the tensile strength of the sample first decreased and then increased due to the increase in layer thickness. The main reason for the decrease in the strength is the interlayer bonding which deteriorates on the application of higher temperature. Once the layer thickness increases to a certain level the effect of temperature minimizes and the tensile strength starts increasing. Similarly, the tensile strength increases with the higher raster angle, because the higher angle produces a small raster, hence causing less deterioration. It is also observed that the decrease in space between the layers due to larger air gap also improves the tensile strength of the sample because the positive air gap provides a high amount of heat dissipation thus improving the strength.

Bagsik *et al.* conducted a tensile test at a specific temperature of 230° C to investigate the strength of specimen with different orientations [12]. The result showed that the specimen built in

A. Mushtaq *et al.*: Mechanical analysis of additively manufactured polylactic acid in fused deposition modelling the direction of X-axis showed maximum strength whereas the sample built in Z-axis showed the least value of tensile strength. The microscopic analysis showed that the bonding between the layers in a specimen built in the Z-direction is not strong enough to resist the loading, hence showing a lower value of tensile strength. He also concluded that the effective cross-sectional area of the sample built in the Z-direction is smaller, due to which the tensile strength decreased.

Sood *et al.* analyzed the change in specimen dimensions over the application of temperature [24]. It was noticed that with the application of temperature the process of shrinkage was predominant in the width and length direction and the dimensions increased over the thickness. The shrinkage process is due to the stress generated due to the application of temperature, resulting in contraction of fibres. However, it was also observed that once the temperature passes to the glass transition temperature and cooling of the fibres, the uneven temperature gradient results in accumulation of heat stress which decreases the range of tensile load.

Giordano *et al.* analyzed the infill pattern with the layer thickness and print performance [25]. The study explains that a filament with a thicker diameter provides better mechanical properties with the build orientation in X and Y plane. However, a thin filament shows higher tensile strength at building in the Z-direction. This also explains that with higher infill density a higher value of strength is endured until it reaches a point where infill density does not have a significant effect on tensile strength of the sample.

Luzanin *et al.* examined the influence of layer thickness, deposition angle and infill density on the flexural strength of the specimen produced by polylactic acid (PLA) [26]. The range of infill density used was from 10 % to 30 %. The experimental results showed that the layer thickness has a dominant and significant effect on the flexural strength of the PLA specimen, whereas the deposition angle and infill showed no effect on the flexural strength. He also concluded that layer thickness is the major contributing factor for computing the flexural strength of the sample. The results showed that with the increase in layer thickness the value of flexural strength changes from a higher to a lower value which is approximately three times smaller.

The experimental data also revealed that the infill density and deposition angle are dependent variables. The change in deposition angle indicates a larger effect when infill density is low.

The further studies illustrated that the flexural

strength yields are at a maximum when deposition angle and infill density lie near the points of 10% and 60°, respectively.

Antonio *et al.* studied the experimental characterization of PLA-fabricated parts [27]. He examined the tensile strength of the sample by changing the number of contours, layer thickness and build orientation. The results illustrated that due to anisotropic behavior, the fabricated parts are highly sensitive to the parameters used during processing. The ultimate tensile strength of the material is highly related to the infill orientation and the number of contours. As the infill orientation decreases the strength of the produced part decreases with the increase in layer thickness. This revealed that on increasing the number of the contours the fibre oriented in the longitudinal direction can withstand higher load.

He also concluded that tensile strength showed higher value with a larger number of contours and greater layer thickness. However, the lower value of tensile strength is the function of bonding between the fibre surface and the air gap. The study on elastic modulus showed that the maximum value is attained at the minimum value of infill orientation, and the maximum number of contours, which is due to the fibres that are oriented along the line in which parts are loaded. He also describes that a microscopic view of surface fracture showed that the ductile failure of the specimen occurs when the fibres are pulled until the yield point where the material separates from the plane which is normal to the direction of the force.

Gordon *et al.* demonstrated that the specimen constructed with an increasing number of contours have a higher range of tensile strength [28]. This is because all fibres are aligned in an orientation along the axis of force applied. With the increasing number of contours, the load is distributed and resisted by the line of contour rather than breaking the bond between the layers. It can be concluded that the rectilinear infill pattern shows the highest tensile strength. It is clear that infill density raster angle and build orientation are the most influential factors as far as tensile strength of the specimen is a concern. The tensile strength of the material is also affected by the chain alignment of the filament. The filament material extruded from the nozzle is also influenced by the functional group, the side chain and the chain orientation. Due to high environmental consideration biodegradable polymers such as polylactic acid are some of the most emerging polymers used in 3 D printers.

Research methodology

Mechanical characteristics, specifically the

tensile property is one of the basic parameters that need to be determined when dealing with FDM-processed parts. To perform the tensile test, a number of parameters are considered to get a logical and rational result. Due to the anisotropic properties of FDM parts, it is difficult to predict the results using linear mathematical models. From the literature review it is evident that every adjacent layer fabricated by FDM technique possesses a different property, hence the overall sample shows a nonlinear behavior. To overcome this problem curves using higher polynomial are constructed. The published literature shows that tensile strength can be influenced by the raster orientation and the number of contours while keeping other parameters constant. It is also observed that tensile strength can be affected by infill density till a certain point after which there is very less effect of infill density over tensile strength. So a mathematical model is calculated to determine the tensile strength of sample specimen that are manufactured using modified ASTM D638, in which the orientation of the model varies from 0° to 45° , and the number of the contours is 2, 3 and 4, keeping infill density at 25%.

Polylactic acid (PLA) is one of the most commonly used FDM materials after ABS. So a filament of PLA material of diameter 3.0 mm was used to fabricate specimen. The tensile strength of the feed sample was found to be 29 MPa. A Prusa Mendel i3 was used to prepare the samples. Considering the experimental setup used by Antonio *et al.*, the run sample was made according to the modified ASTM D638 type 1 standard. In Figure 13 the dog bone sample is the most commonly used specimen shape to determine tensile strength [27].

The Zwick/Roell ProLine table-top testing Z005 machine was employed for the destructive tensile testing of 54 samples with different combinations. The machine has its software, third generation test Xpert II testing software. The machine works on the manually gripping flat-jaws system, and automatically switches to the eco mode when not in use. The test was carried out at a rate of 2.4 mm/min. The machine has its database system where the data of each sample are saved.

Samples were manufactured using the methodology discussed. Three samples of each parameter were made in order to minimize error and get the best possible results. Samples were tested destructively as mentioned in the methodology. The experimental data of all samples are given in Tables 1 and 2. There are two variables considered; the variation of tensile strength concerning orientation and contour and second stress-strain analysis at constant raster angle.

The variation of tensile strength with respect to the orientation

Figure 14 shows the results of the tensile strength of different samples built at raster angle 0° , 15° , 30° , and 45° . Besides that two different infill patterns - concentric and honey comb structures - were also considered to study the tensile strength of the PLA sample. Fig. 14 depicts all trends of raster angle and tensile strength superimposed on the same plot.

Figure 15 depicts all trends of infill pattern (concentric and honey comb) superimposed on the same plot. It can be inferred from Figures 14, 15 and 16 that the change in raster angle causes significant variation in the tensile strength. With the increase in raster angle, the tensile strength increases with a specific number of contour and infill density of 25%. The tensile strength of the infill concentric pattern shows the highest strength with a maximum number of contours. The infill pattern highly influences the tensile strength of the sample manufactured.

The trend of tensile strength with respect to raster angle at a constant contour number 2 is shown in Figure 17. The graph depicts that the increase in build orientation from 0° to 30° results in an increase in tensile strength of the sample, however, when the material is made with the build orientation of 45° the tensile strength decreases. This phenomenon was thoroughly studied by Es-Said who observed the microscopic structure of the sample and determined that at 0° the filaments align themselves in the line of applied force.

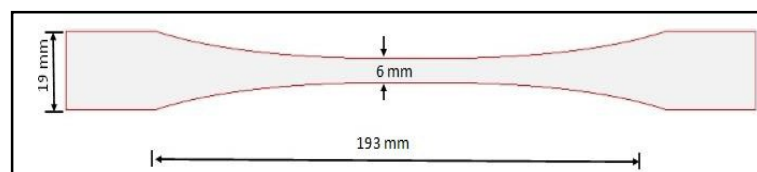


Fig. 13. ASTM D638 modified type 1 specimen [27].

Table 1. Tensile strength of the specimen

Raster angle		No. of contours		
		2	3	4
0°/-90°	I	20.7	28.1	62.7
	II	26.5	29.3	33.7
	III	25.3	30.6	25
15°/-75°	I	25.5	31	33.4
	II	24.6	33.3	37
	III	25.3	27.2	34.6
30°/-60°	I	28.1	34.6	31.5
	II	29.5	34.1	37.8
	III	26.2	32.2	38.8
45°/-45°	I	28.9	27.9	38.5
	II	24	33.2	37.5
	III	30.2	32.7	37.5
Concentric	I	25	34.6	39.9
	II	28.9	35.7	39.3
	III	29.2	35	39.7
Honey comb	I	21	30.6	36.1
	II	25.4	30.8	32.8
	III	24.2	28.3	34.9

Table 2. Average data

Raster angle	No. of contours		
	2	3	4
15°/-75°	25.13	30.50	35.00
30°/-60°	27.93	33.63	36.03
45°/-45°	27.70	31.27	37.83
Concentric	27.70	35.10	39.63
Honey comb	29.90	34.60	23.53

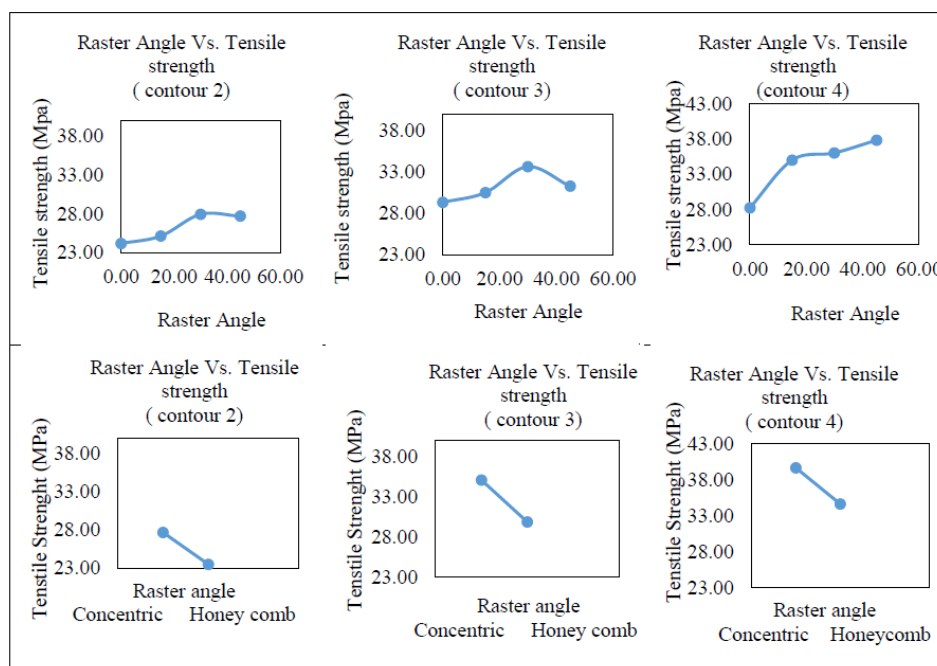


Fig. 14. Strength trends of number of contours 2, 3 and 4

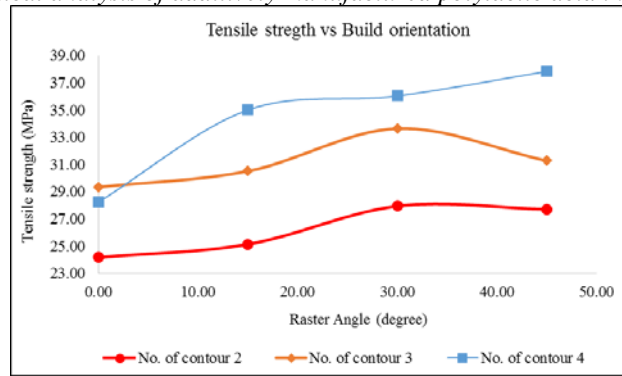


Fig. 15. Trends of contours superimposed

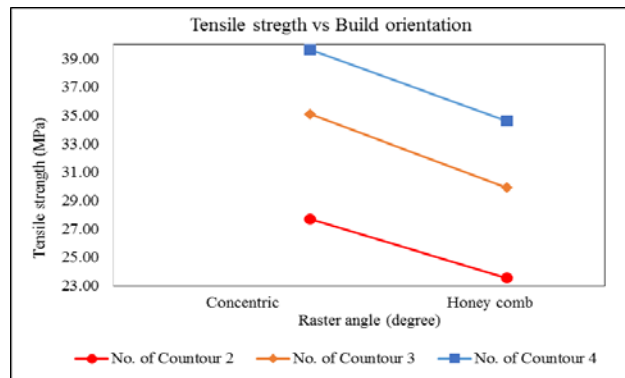


Fig. 16. Trends of all constant densities superimposed with build pattern concentric and honey comb

Number of contours 2 trend

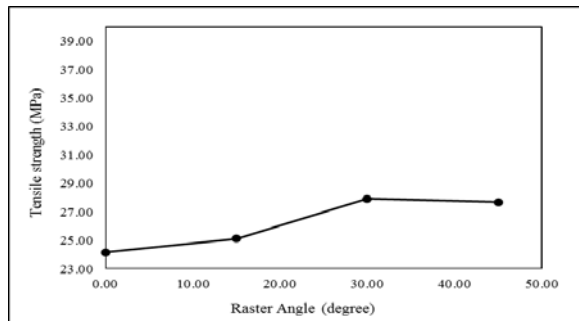


Fig. 17. The trend of tensile strength with respect to raster angle

The trend of tensile strength with respect to raster angle at a constant contour 2 is shown in Figure 17. The graph depicts that with the increase in build orientation from 0° to 30° results in an increase in tensile strength of the sample, however, when the material made with the build orientation of 45° the tensile strength decreases. This phenomenon was thoroughly studied Es-Said in which he studies the microscopic structure of the sample determine that at 0° the filaments align themselves in the line of applied force. It is also observed that at orientation 15° and 30°, the higher tensile strength is due to the high alignment of the filament, but reaching at angle 45° the transverse (90°) filament is more prominent, so the tensile

strength decreases [20]. Figure 18 shows the sample concentric pattern with a number of contours 2.

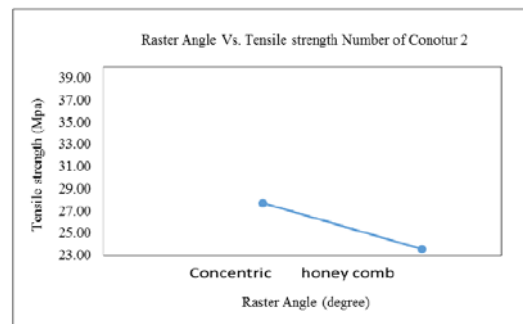


Fig. 18. The trend of tensile strength with a number of contours 2.

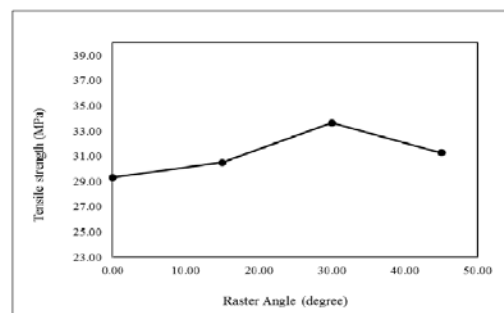


Fig. 19. The trend of tensile strength with respect to raster angle.

When the trend of tensile strength is drawn over the contour length of 3, the trend is same as it is for the tensile strength of a number of contour 2 as shown in Figure 19.

However, there lies an anomaly that shows that at 45° the tensile strength of the sample decreases, the reason of this decrease in tensile strength could be that in build orientation of 45°, delamination phenomenon is more prominent to the tensile load that could be beared by the axially oriented filament, hence, there is a decrease in tensile strength of the sample. Figure 20 shows the trend of tensile strength with a number of contours 3; the trend is the same as it was for 2 contours. The tensile strength is greater for the concentric pattern as it decreases for honey comb infill pattern.

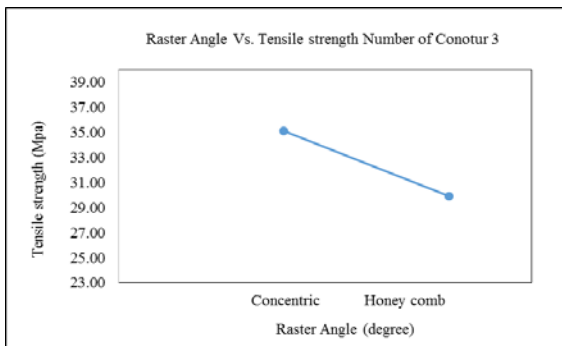


Fig. 20. The trend of tensile strength with a number of contours 3

Number of contours 4 trend

The trend of tensile strength with a contour number of 4 is shown in Figure 21. The strength of the sample increases with the increase in build orientation at a constant number of contours 4. This shows that with the number of contours 4 the tensile strength increases from 0° to 15° due to chain alignment of polymer filament.

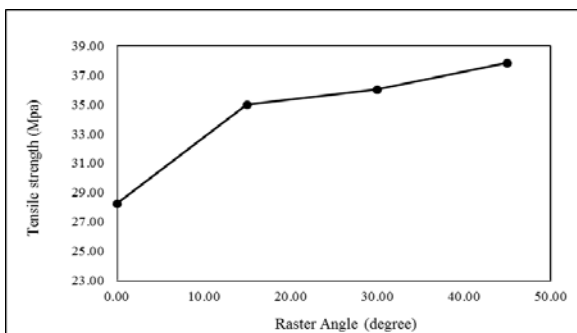


Fig. 21. The trend of tensile strength with respect to raster angle.

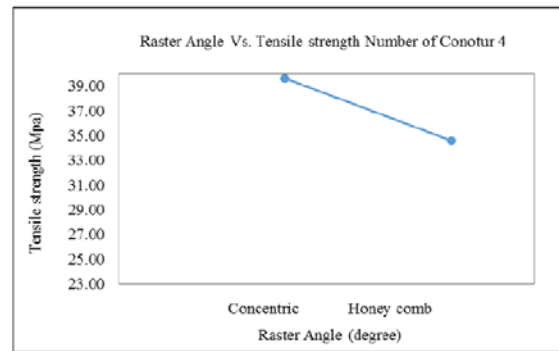


Fig. 22. The trend of tensile strength with a number of contours 4.

The trend pattern for 45° shows that with the increase in the number of contours the tensile strength increases. This is due to the fact that at 45° and number of contours 4 the load distribution is due to the contour since the filaments are arranged parallel to the direction of load. The axial 0° is prominent, hence the tensile strength increases [20].

It was found that the tensile strength of the concentric and honey comb structures is higher for concentric structure over honey comb as shown in Figure 22.

The tensile strength analysis of concentric and honey comb structures shows that with a number of contours 2, 3 and 4 concentric pattern shows higher strength as compared to honey comb structure. Figure 23 shows that in the concentric pattern filaments are along the direction of force, however in the concentric pattern the filaments are aligned in the direction perpendicular to the applied force, hence showing less tensile strength.



Fig. 23. Samples with honey comb and concentric pattern.

Variation of tensile strength with respect to the contour

The trend of tensile strength with respect to the number of contours is shown in Figure 24. The trend of strength increases with increasing the number of contours with a specific raster angle.

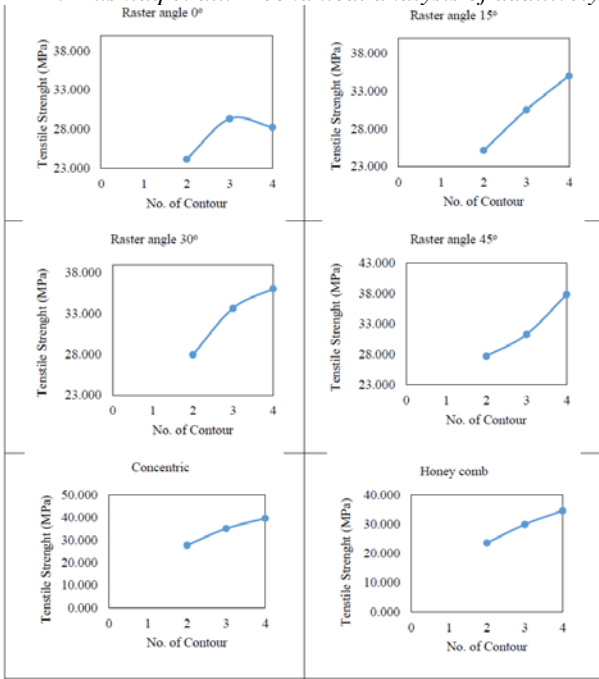


Fig. 24. The trend of tensile strength with build orientation 0°, 15°, 30°, 45°, concentric and honey comb

Figure 25 shows the superimposed results of all samples built with raster angle 0° to 45° with contour numbers 2, 3 and 4.

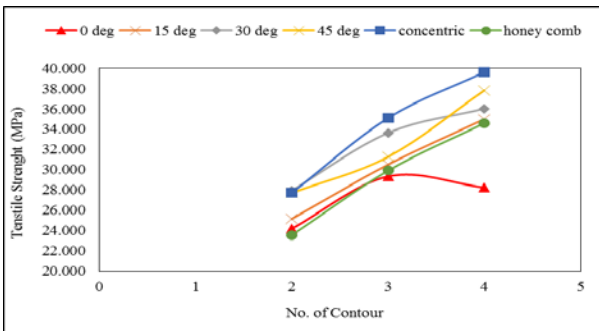


Fig. 25. The trend of tensile strength with build orientation 0°, 15°, 30°, 45°, concentric and honey comb

0/-90 Degrees trend

Figure 26 shows that as the number of contours increases from 2 to 3 the tensile strength increases with a build orientation of 0°. However, when a sample of 4 contours at 0° is analyzed, it shows a decrease in tensile strength of the sample.

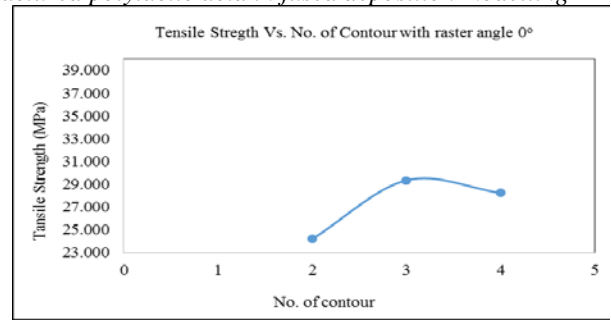


Fig. 26. The trend of tensile strength at 0°/-90°

15/-75 Degrees trend

Figure 27 shows the increase in tensile strength with increase in the number of contours because more filaments are aligned in the direction of the applied force increasing strength.

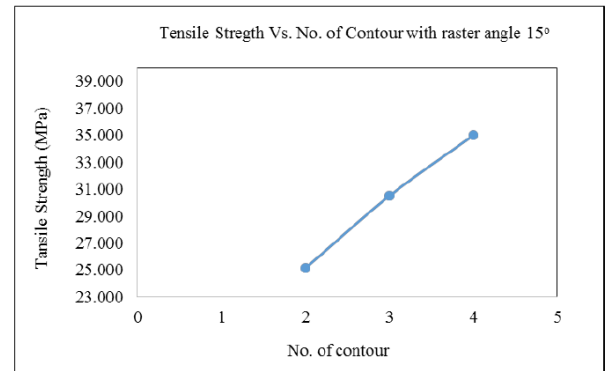


Fig. 27. The trend of tensile strength at 15°/-75°

30/-60 Degrees trend

The plot in Figure 28 shows the strength trend with an increase in the number of contours.

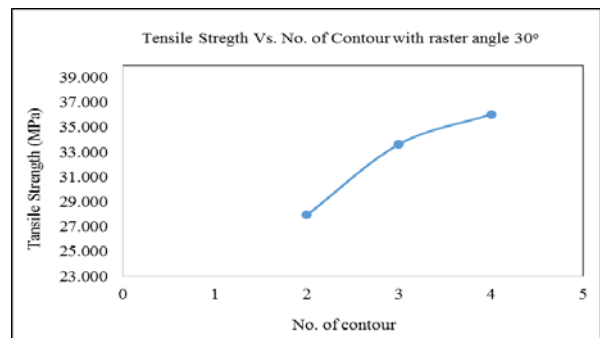


Fig. 28. The trend of tensile strength at 30°/-60°

45/-45 Degrees Trend

A similar trend is observed in tensile strength with increase in contour as compared to building orientation of 0°, 15° and 30° as shown in Figure 29.

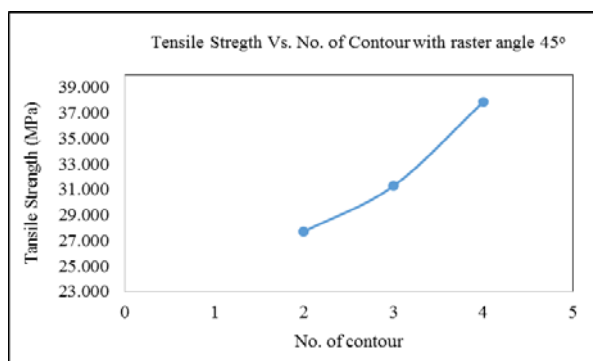


Fig. 29. The trend of tensile strength at 45⁰/-45⁰

Concentric pattern

The concentric pattern plot in Figure 30 shows that the pattern has the highest strength among all the samples studied. It is due to the infill pattern showing that maximum filaments during processing are aligned in the direction of applied force, hence, more load can be applied to the sample.

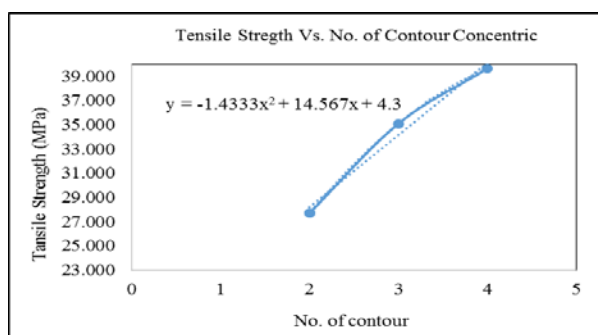


Fig. 30. The trend of tensile strength with a concentric pattern.

Honey Comb

The honey comb structure has a strength that lies in the range of 23 MPa to 35Mpa as shown in Figure 31. This is because in the honey comb structure the infill density can be the influential factor. The less the infill density, the structure will be the more spacious resulting in bigger voids. These voids would provide a weak point from where the sample can break resulting in lower tensile strength [14, 29].

Stress-strain analysis at constant raster angle

Stress-strain curve basically determines the change in length of the sample due to the application of load. The following trends were observed with the change on contours keeping

raster angle constant [30].

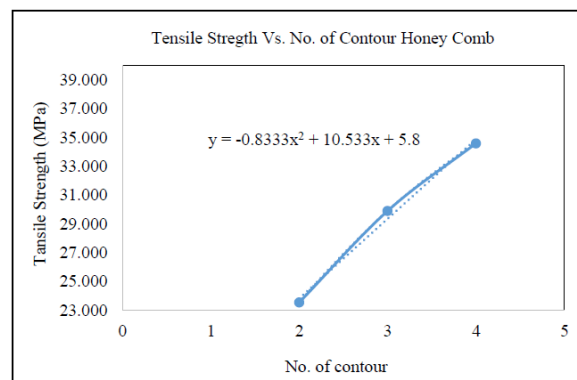


Fig. 31. The trend of tensile strength with honey comb pattern

Stress-strain curve with raster angle 0°

Figure 32 shows that the sample built with a number of contours 2 has withstood the highest load. Moreover, the sample built with a number of contours 3 has the least value of force tolerated. Similarly, the maximum elongation was experienced in the sample with 4 contours.

Stress-strain curve with raster angle 15°

It is observed in Figure 33 that with the increase in the number of contours at constant raster angle of 15° the sample could bear a higher force and could experience a stronger elongation.

Stress-strain curve with raster angle 30°

A similar trend was witnessed in the sample with constant raster angle of 30° as was observed in the part built with raster angle 15°, that with an increase in the number of contours there is an increase in load-bearing capacity of the sample and higher elongation is possible, see Figure 34.

Stress-strain curve with raster angle 45°

The change in elongation and is more prominent as the number of contour increase as shown in Figure 35. Similarly, the applied force noticeably increases with the number of contours.

Stress-strain curve with a concentric pattern

The analysis of the stress-stain curve of the concentric pattern (Figure 36) shows that initially at certain strain the sample with 2 contours have the tendency to tolerate more force, however, reaching a certain strain the sample with 3 contours can endure more force.

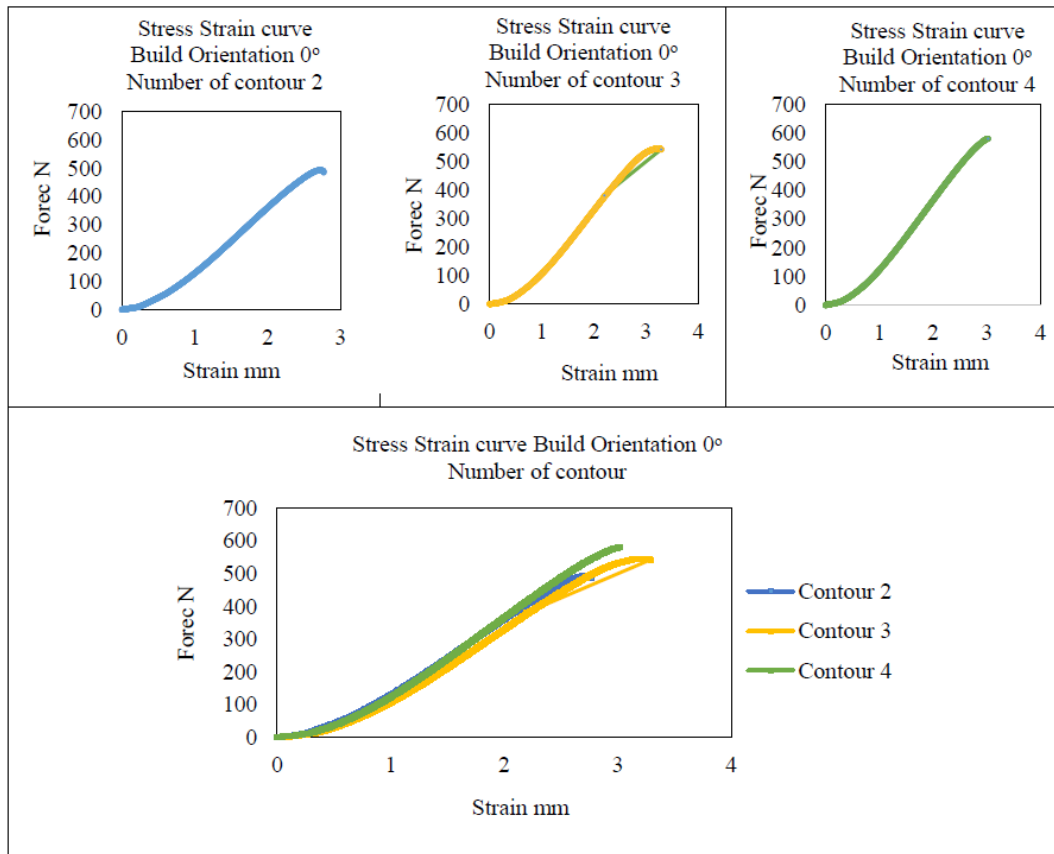


Fig. 32. Stress-strain curve at raster angle 0 °

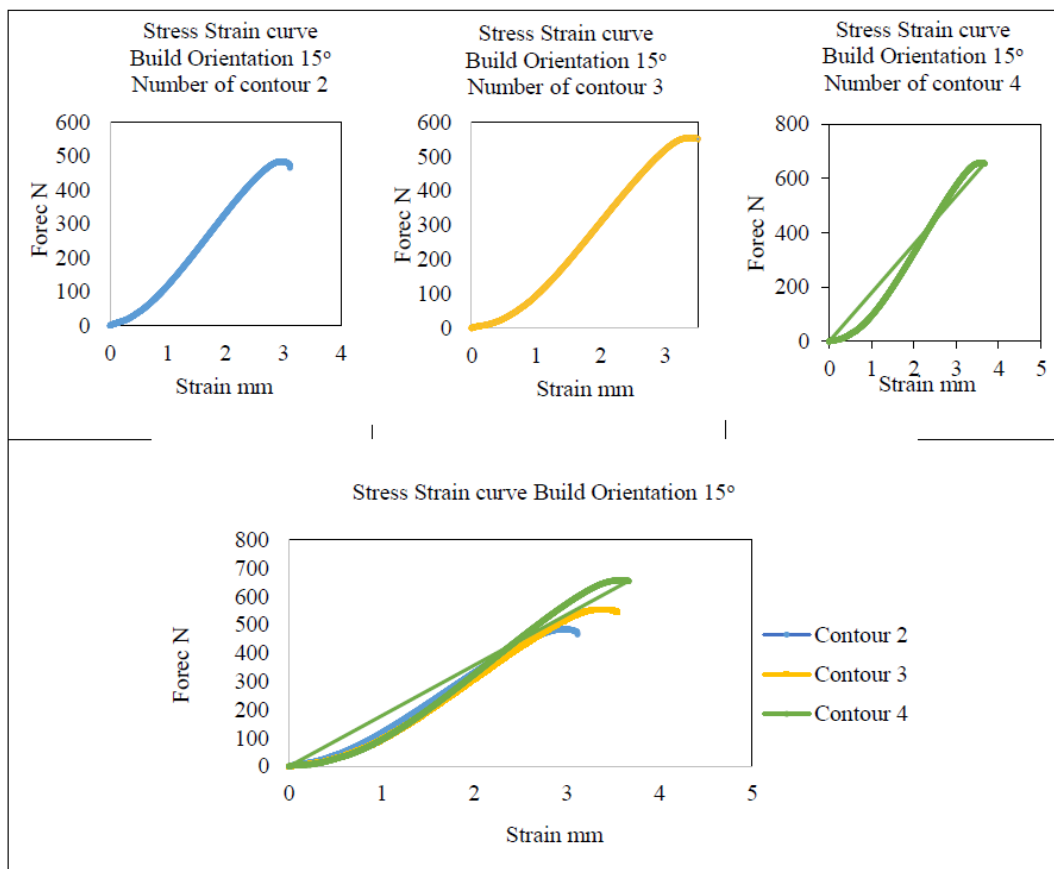


Fig. 33. Stress-strain curve at raster angle 15 °

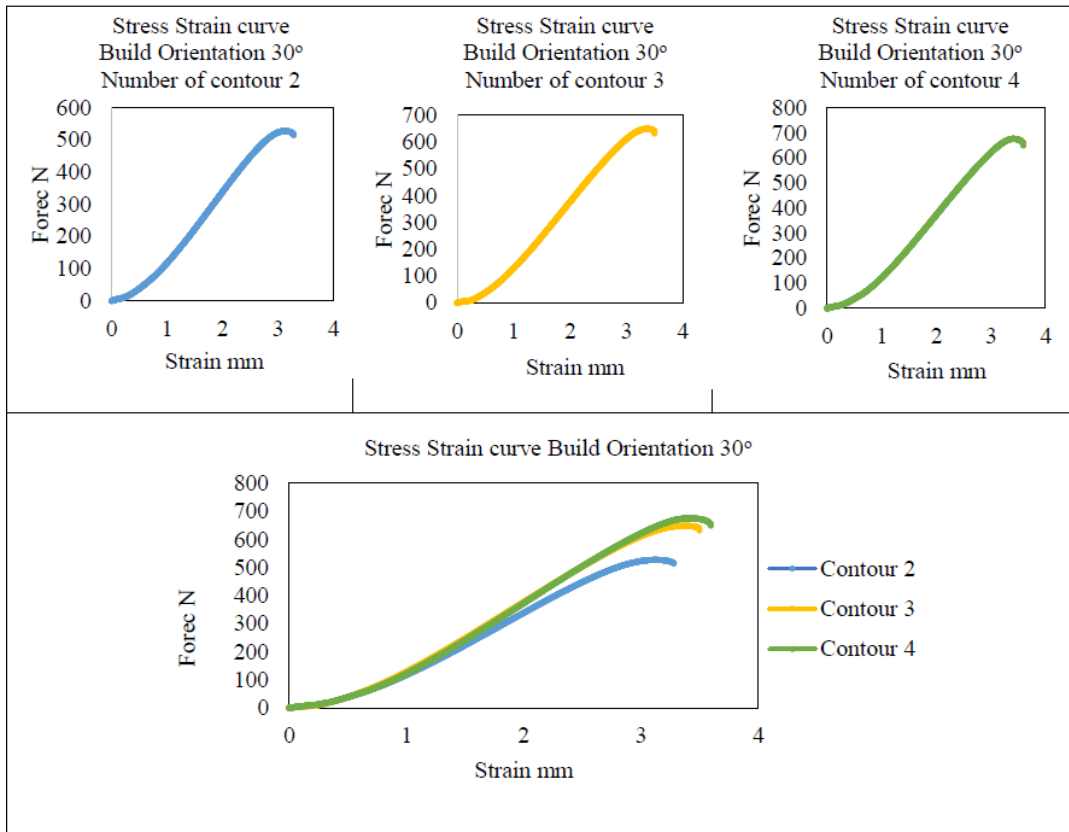


Fig. 34. Stress-strain curve at raster angle 30°

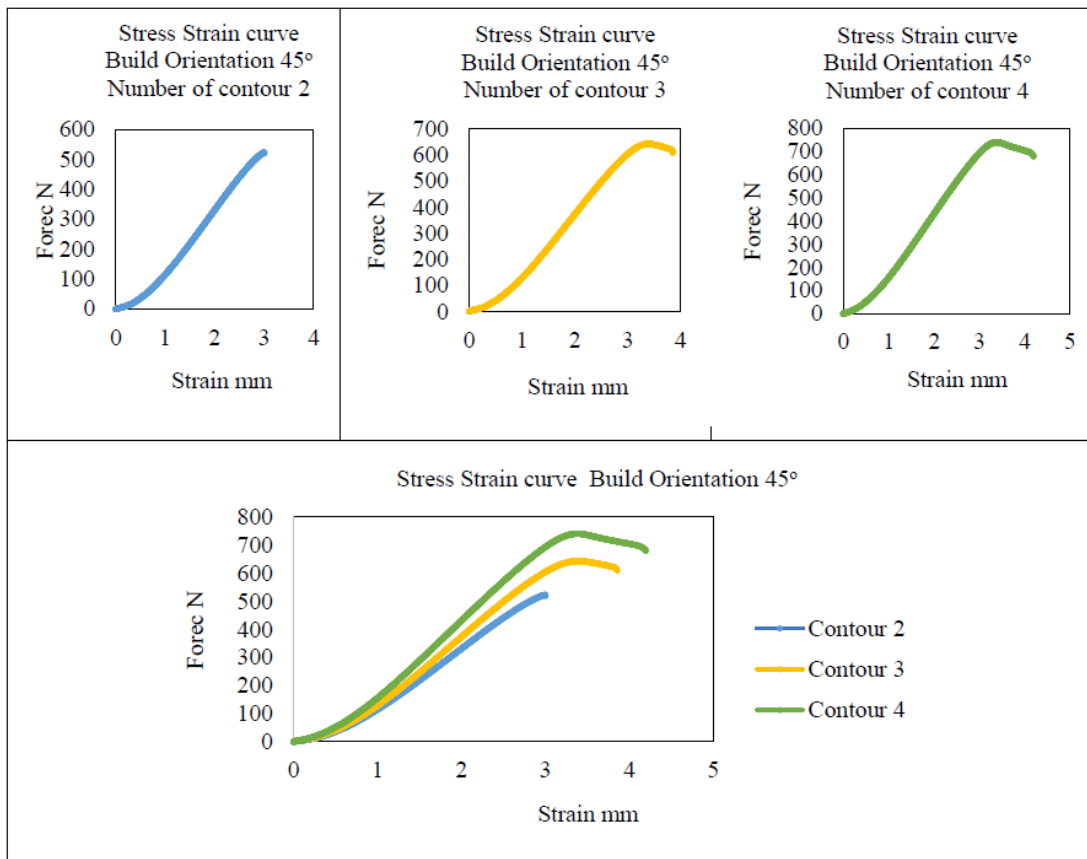


Fig. 35. Stress-strain curve at raster angle 45°

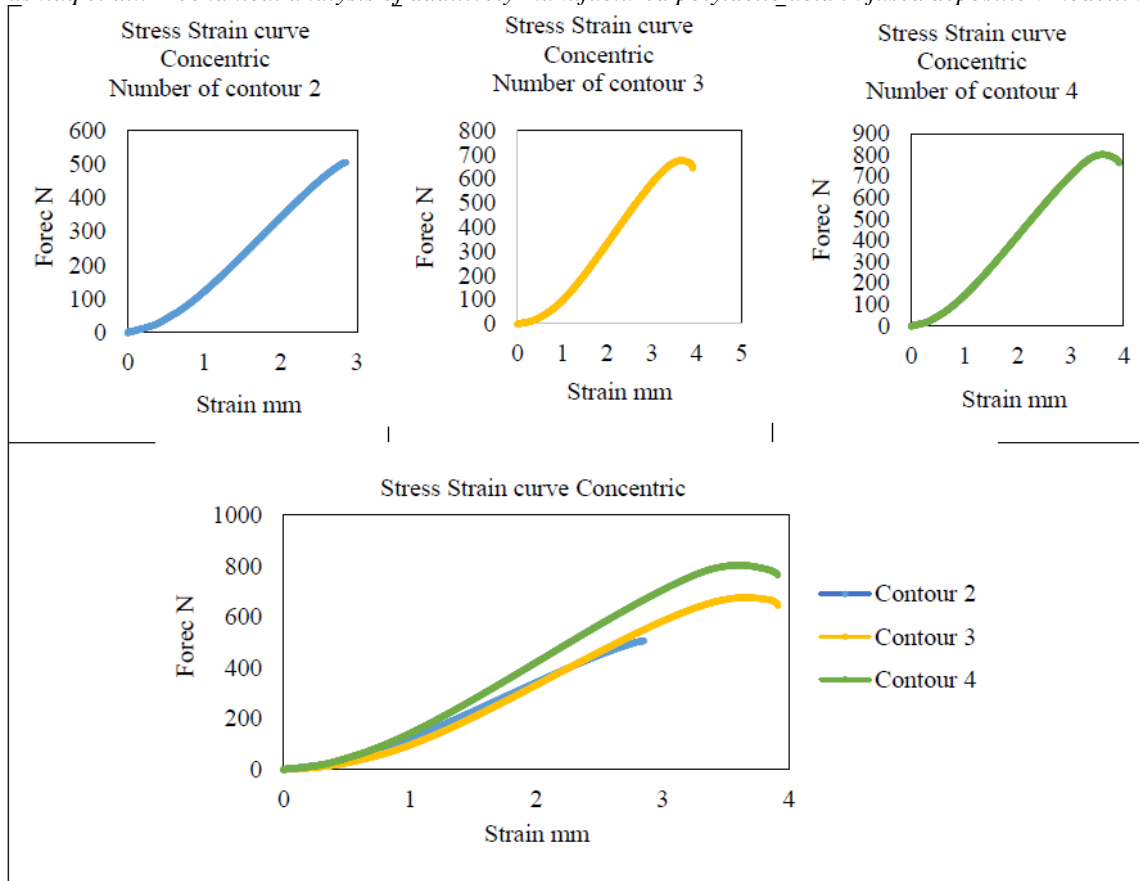


Fig. 36. Stress-strain curve of the concentric pattern

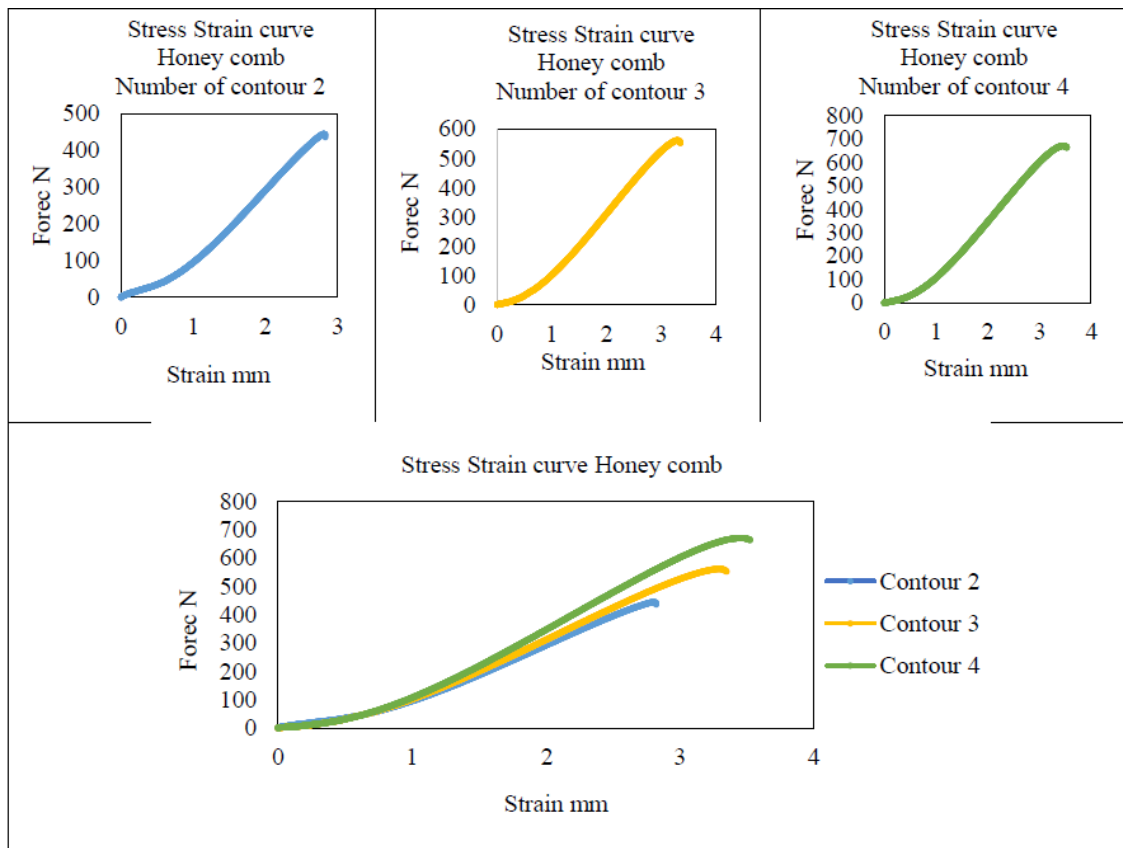


Fig. 37. Stress-strain curve of honey comb pattern

Figure 37 portrays the trend raster angle and different infill patterns are found to be related. In the infill pattern of honey comb the elongation and applied force increases with the number of contours.

The following three mathematical models were established, each for a different raster angle:

$$1. TS/Contours\ 2 = y = -0.0002x^3 + 0.0149x^2 - 0.1048x + 24.167$$

$$2. TS/Contours\ 3 = y = -0.0004x^3 + 0.021x^2 - 0.1537x + 29.333$$

$$3. TS/Contours\ 4 = y = 0.0003x^3 - 0.0272x^2 + 0.7867x + 28.233$$

where x is the raster angle $0^\circ \leq x \leq 45^\circ$

The following three mathematical models were established, with two different patterns: concentric and honey comb.

$$TS/Concentric = y = -1.4333x^2 + 14.567x + 4.3$$

$$TS/Honey\ Comb = y = -0.8333x^2 + 10.533x + 5.8$$

where x is the number of contours $2 \leq x \leq 4$

With the mathematical models for four different raster angles, there is a better understanding of how the FDM-manufactured objects of PLA material would behave under loading. The tensile strength equation could help to determine the tensile property of polylactic acid having different raster angle and build orientation.

CONCLUSION

The independent study project focused on the tensile strength of a sample by changing the process parameters. After a thorough review of the published literature it was concluded that raster angle and number of contours were the most important parameters to determine the tensile strength of manufactured parts. An open source Fused Deposition Modelling (FDM) machine with a custom-built variation was used in this ISP. The literature review showed that the tensile strength of the polylactic acid manufactured part using different build orientation with different raster angle at constant infill density needs to be determined. The results of this ISP depict that the parts built with concentric pattern show the highest tensile strength with a number of contours 2, 3 and 4. It can also be concluded that with an increase in the number of contours the tensile strength of the PLA sample increases with certain build orientation. The results also show that with an increase in build orientation from 0° to 45° there is an increase in tensile strength of the built sample. This study addressed the need for a mathematical model to

correlate the two process parameters, build orientation and raster angle with tensile strength along the layers.

Acknowledgement: The authors would like to acknowledge the Department of Polymer and Petrochemical Engineering, NED University of Engineering & Technology, Karachi, Pakistan for supporting this research work.

REFERENCES

1. Y. Huang, M. C. Leu, Report of NSF Additive Manufacturing Workshop, University of Florida, Gainesville, 2014, p. 1.
2. Bártolo, P. Jorge, I. Gibson, History of stereolithographic processes, in: Stereolithography, Springer, Boston, 2011, p. 37.
3. B. C. Gross, J. L. Erkal, S. Y. Lockwood, C. Chen, D. M. Spence, *Anal. Chem.*, **86**, 3240 (2014).
4. C. W. Hull (ed.), in: D.U.S.P.a.T. Office, U.S, 1986.
5. L. Novakova-Marcincinova, I. Kuric, *Manuf. and Ind. Eng.*, **11**, 24 (2012).
6. K. Serguei, E. Boillat, R. Glardon, P. Fischer, M. Locher, *Int. J. Mach. Tool Manuf.*, **44**, 117 (2004).
7. S. Bhandari, B. Regina, *Int. J. Comp. Sci. Inf. Tech. Res.*, **2**, 378 (2014).
8. H. J. Jee, E. Sachs, *Adv. Eng. Softw.*, **31**, 97 (2000).
9. J. G. Zhou, D. Herscovici, C. C. Chen, *Int. J. Mach. Tool Manuf.*, **40**, 362 (2000).
10. Ferrara, M. Herbert, International directory of company histories, in: J. P. Pederson (ed.) International directory of company histories, St. James Press, 2007.
11. Z. Moza, K. Kitsakis, J. Kechagias, N. Mastorakis, in: 14th International Conference on Instrumentation, Measurement, Circuits and Systems, Salerno, Italy, 2015.
12. A. Bagsik, V. Schöppner, *ANTEC*, **1**, 1 (2011).
13. A. Bagsik, V. Schöppner, E. Klemp, *Polymeric Materials*, **15**, 307 (2010).
14. F. Carrasco, P. Pagès, J. Gámez-Pérez, O. O. Santana, M. L. MasPOCH, *Polym. Degrad. Stab.*, **95**, 116 (2010).
15. J. F. Rodriguez, J. P. Thomas, J. E. Renaud., *Rapid Prototyping J.*, **6**, 175 (2000).
16. H.a.S. Executive, Controlling fume during plastics processing, The Health and Safety Executive, U.K, 2013, p. 1.
17. A. K. Sood, R. K. Ohdar, S. S. Mahapatra, *Mater. Des.*, **31**, 287 (2010).
18. S. H. Ahn, M. Montero, D. Odell, S. Roundy, P. K. Wright, *Rapid Prototyping J.*, **8**, 248 (2002).
19. J. Cantrell, S. Rohde, D. Damiani, R. Gurnani, L. DiSandro, J. Anton, A. Young, A. Jerez, D. Steinbach, C. Kroese, P. Ifju, *Rapid Prototyping J.*, **23**, 811 (2017).
20. O. S. Es-Said, J. Foyos, R. Noorani, M. Mendelson, R. Marloth, B. A. Pregger, *Mater. Manuf. Process*, **15**, 107 (2000).
21. M. Montero, S. Roundy, D. Odell, S.-H. Ahn, P. K.

- A. Mushtaq et al.: *Mechanical analysis of additively manufactured polylactic acid in fused deposition modelling* Wright, *Soc. Manuf. Eng.*, **10**, 1 (2001).
22. Q. Sun, G. M. Rizvi, C. T. Bellehumeur, P. Gu, *Rapid Prototyping J.*, **14**, 72 (2008).
 23. V. Vega, J. Clements, T. Lam, A. Abad, B. Fritz, N. Ula, O. S. Es-Said, *J. Mater. Eng. Perform.*, **20**, 978 (2010).
 24. A. K. Sood, R. K. Ohdar, S. S. Mahapatra, *J. Adv. Res.*, **3**, 81 (2012).
 25. R. A. Giordano, B. M. Wu, S. W. Borland, L. G. Cima, E. M. Sachs, M. J. Cima, *J. Biomater. Sci., Polym. Ed.*, **8**, 63 (1997).
 26. O. Lužanin, D. Movrin, M. Plančak, *J. Technol. Plast.*, **39**, 49 (2014).
 27. A. Lanzotti, D. Eujin Pei, M. Grasso, G. Staiano, M. Martorelli, *Rapid Prototyping J.*, **21**, 604 (2015).
 28. E. Fodran, M. Koch, U. Menon, *In Solid Freeform Fab. Proc.*, **1**, 419 (1996).
 29. A. Asaa, S. Abazary, A. Masomi, *Int. J. Curr. Eng. Tech.*, **3**, 81 (2013).
 30. W. Wu, P. Geng, G. Li, D. Zhao, H. Zhang, J. Zhao, *Materials*, **8**, 5834 (2015).

Synthesis, characterization, deoxyribonucleic acid interaction and antimicrobial studies of Schiff base binuclear transition metal complexes

K. Sivakumar¹, V. Chandrasekaran^{2*}

¹Department of Chemistry, V.S.B. Engineering College, Karur-639 111, Tamilnadu, India.

²Department of Chemistry, Government Arts College (A), Salem-636 007, Tamilnadu, India.

Received October 19, 2018; Revised September 5, 2019

In this paper, the ligand was prepared by using the organic compounds 3, 3'-dihydroxy benzidine and 3-amino coumarin. We have synthesised binuclear Schiff base complexes using the ligand and chloride salts of copper(II), nickel(II), manganese(II), zinc(II) and chromium(III). The type of the complexes was $[MLCl_4]$. The synthesized binuclear Schiff base complexes were characterized by elemental analysis, molar conductance, cyclic voltametry, UV-visible, IR, electron paramagnetic resonance and nuclear magnetic resonance spectra. Gel electrophoresis was used to study deoxyribonucleic acid cleavage. Copper and nickel binuclear complexes fully degraded the supercoiled plasmid deoxyribonucleic acid. The antibacterial activity of the binuclear metal complexes against the microbes *Escherichia coli*, *Klebsiella pneumoniae* and *Staphylococcus aureus* was studied by the disc diffusion method.

Keywords: 3, 3'-dihydroxy benzidine, 3-amino coumarin, infrared spectra, ultraviolet-visible spectra, electron paramagnetic resonance spectra, deoxyribonucleic acid

INTRODUCTION

Inorganic chemistry plays a vital role in electronics, pharmaceuticals, nuclear reactors, fertilisers, pesticides, polymers, semiconductors, solar cells, nano composites, photo catalysis, etc. The first-row transition metals such as copper, nickel, manganese, zinc and chromium show biological activity. In the 20th century, platinum complexes were used as anticancer agents. The ability of a metal complex to act as therapeutic agent is already discussed. Transition metals are used in bio synthesis. Complexes of transition metals show antitumor activity. Because of selective permeability, accumulation of transition metals in tumors is possible. In the past decade, a number of mononuclear complexes and their interaction with deoxyribonucleic acid were analyzed.

We have synthesized a novel Schiff base of the first row transition metal complexes which has many advantages compared with mononuclear complexes. Schiff base complexes are famous because of simple synthesis and formation of stable complexes with many transition metals. The intention of this study is to synthesize Schiff base transition metal complexes with organic ligands of the NNO type. Synthesized binuclear complexes play a vital role as anticancer [1,2], antimicrobial [3], antioxidant [4], antibacterial [5], antifungal [6], and anthelmintic [7] agents. Deoxyribonucleic acid interaction study is an important source to the development of reagents in biotechnology and

biomedical engineering. Transition metal complexes are cleaving deoxyribonucleic acid and can be used as therapeutic agents [8-10]. Ligands having nitrogen and oxygen can behave as effective chelating agents for transition metal ions [11, 12]. Antibacterial activity against microbes such as *Staphylococcus aureus*, *Klebsiella pneumoniae* and *Escherichia coli* was analysed [13].

EXPERIMENTAL

Description of equipment, materials, methods

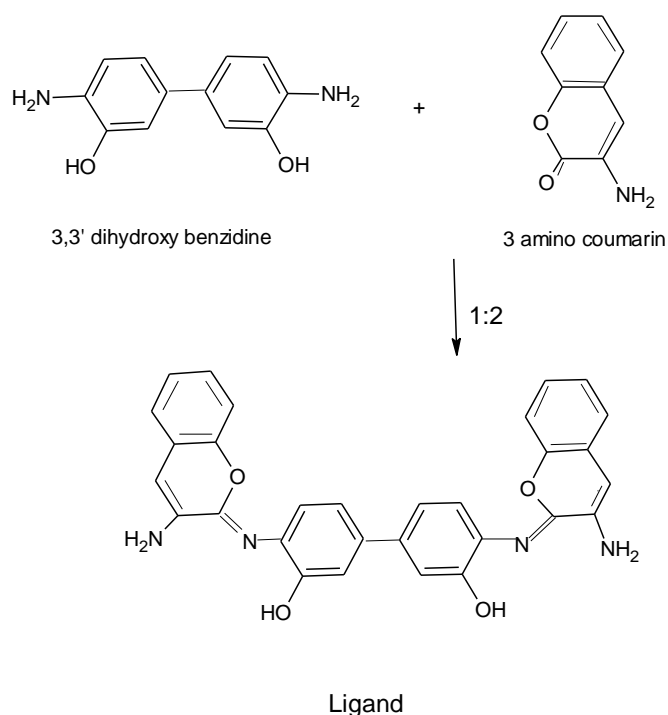
3,3'-Dihydroxy benzidine and 3-amino coumarin were obtained from Aldrich. Ethanol, DMSO and DMF solvents were used. Elemental analysis was performed by using a Carlo-Erba 1106 instrument. Molar conductances were calculated by using ELICO CM 185 conductivity bridge. The infrared spectra were collected on a Perkin Elmer FT-IR-8300 model spectrometer. Electronic absorption spectra in the UV-visible range were recorded on a Perkin Elmer Lambda-25 spectrometer between 200-700 nm. The voltammetric experiment was carried out with a CHI60 electrochemical analyzer. Electron paramagnetic resonance spectra were obtained on a Varian JEOL-JES-TE100 EPR spectrometer. The NMR spectrum was recorded on a Bruker Avance III HD nanobay spectrometer. The DNA interaction was monitored by the gel electrophoresis method. The disc diffusion technique was used for the antibacterial activity studies.

* To whom all correspondence should be sent:

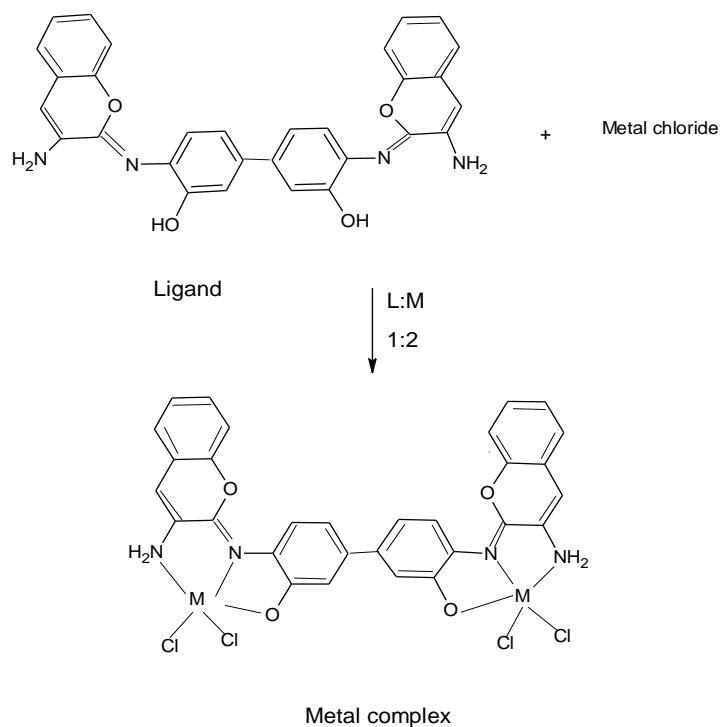
E-mail: chandru_v_m@yahoo.co.in

3,3'-Dihydroxy benzidine and 3-amino coumarin were mixed slowly with uniform stirring. Ethyl alcohol was used as a solvent. The organic

compounds were heated in a round-bottom flask fitted with condenser for two hours. Precipitate was collected after cooling at 36°C. It was filtered, washed with ethanol and desiccated (Scheme 1).



Scheme 1. Preparation of ligand



Scheme 2. Synthesis of binuclear metal complexes

Ligand and $\text{CuCl}_2 \cdot 2\text{H}_2\text{O}$ were mixed and refluxed for 2 hours. The mixture was chilled to 36°C . The prepared metal complex was collected, filtered and desiccated over fused CaCl_2 . Metal complexes of nickel(II), manganese(II), zinc(II) and chromium(III) were prepared in a similar way (Scheme 2).

RESULTS AND DISCUSSION

Elemental analysis

The results of the elemental analysis of the complexes are shown in Table 1. The 2:1 [M:L] ratio was confirmed from the data. The formula was ML , where M represents copper(II), nickel(II), manganese(II), zinc(II) and chromium(III) ions, while L represents ligand. Theoretical values and experimental values were more or less the same.

Molar conductance study

The binuclear complexes were dissolved in dimethyl formamide. Molar conductance values are presented in Table 1. It is confirmed that the molar conductivity of copper(II), nickel(II), manganese(II), zinc(II) and chromium(III) complexes was lying in the range of $12.26 - 15.74 \text{ Ohm}^{-1} \text{ cm}^2 \text{ mol}^{-1}$ (Table 1). Binuclear complexes are of non-ionic nature, i.e. chloride ions are not present inside the sphere.

Infrared (IR) spectra

The IR spectral bands in the range $3325-3335 \text{ cm}^{-1}$ belonged to $\nu(\text{N-H})$ of the coordinated amine group, which was further confirmed by the bands obtained in the range $470-488 \text{ cm}^{-1}$ corresponding to binding of metal and ligand, i.e. $\nu(\text{M-N})$. The bands obtained in the range $1592-1598 \text{ cm}^{-1}$ confirmed the presence of azomethine $\nu(\text{C=N})$ in all metal complexes. The far IR bands obtained in the range $344-355 \text{ cm}^{-1}$ were due to $\nu(\text{M-Cl})$ vibration [14]. The IR data are given in table 2.

Table 1. Elemental analysis of the metal complexes

Ligand/ Complexes	Mol. Weight	% C		% H		% N		μ_{eff} (B.M)	Λ_{M} (Ohm^{-1} $\text{cm}^2 \text{ mol}^{-1}$)
		Calc.	Exp.	Calc.	Exp.	Calc.	Exp.		
$(\text{C}_{30}\text{H}_{22}\text{O}_4\text{N}_4)$	502.84	71.71	71.80	4.41	4.52	11.14	11.08		
$[\text{Cu}_2(\text{C}_{30}\text{H}_{20}\text{O}_4\text{N}_4\text{Cl}_4)]$	769.76	46.85	46.94	2.62	2.73	7.28	7.35	1.56	12.26
$[\text{Ni}_2(\text{C}_{30}\text{H}_{20}\text{O}_4\text{N}_4\text{Cl}_4)]$	760.04	47.44	47.54	2.66	2.76	7.37	6.25	2.64	13.42
$[\text{Mn}_2(\text{C}_{30}\text{H}_{20}\text{O}_4\text{N}_4\text{Cl}_4)]$	752.54	47.92	47.85	2.68	2.59	7.45	7.40	5.60	15.74
$[\text{Zn}_2(\text{C}_{30}\text{H}_{20}\text{O}_4\text{N}_4\text{Cl}_4)]$	773.42	46.62	46.70	2.61	2.70	7.25	7.35		
$[\text{Cr}_2(\text{C}_{30}\text{H}_{20}\text{O}_4\text{N}_4\text{Cl}_4)]$	746.66	48.30	48.25	2.70	2.80	7.51	7.60		

Table 2. IR spectra of the binuclear complexes

Complex	(C=N) (cm^{-1})	NH_2 (cm^{-1})	(C=C) (cm^{-1})	(M-N) (cm^{-1})	(M-Cl) (cm^{-1})
$[\text{Cu}_2(\text{C}_{30}\text{H}_{20}\text{O}_4\text{N}_4\text{Cl}_4)]$	1592	3335	1515	470	344
$[\text{Ni}_2(\text{C}_{30}\text{H}_{20}\text{O}_4\text{N}_4\text{Cl}_4)]$	1598	3325	1518	473	347
$[\text{Mn}_2(\text{C}_{30}\text{H}_{20}\text{O}_4\text{N}_4\text{Cl}_4)]$	1597	3330	1522	477	350
$[\text{Zn}_2(\text{C}_{30}\text{H}_{20}\text{O}_4\text{N}_4\text{Cl}_4)]$	1594	3328	1526	482	352
$[\text{Cr}_2(\text{C}_{30}\text{H}_{20}\text{O}_4\text{N}_4\text{Cl}_4)]$	1595	3332	1530	488	355

Table 3. UV spectra of the Schiff base and its complexes

Binuclear Complexes	$\pi-\pi^*$ (nm)	$n-\pi^*$ (nm)	L-M CT (nm)	d-d (nm)
$[\text{Cu}_2(\text{C}_{30}\text{H}_{20}\text{O}_4\text{N}_4\text{Cl}_4)]$	276	325	412	659
$[\text{Ni}_2(\text{C}_{30}\text{H}_{20}\text{O}_4\text{N}_4\text{Cl}_4)]$	282	328	410	660
$[\text{Mn}_2(\text{C}_{30}\text{H}_{20}\text{O}_4\text{N}_4\text{Cl}_4)]$	287	312	382	640
$[\text{Zn}_2(\text{C}_{30}\text{H}_{20}\text{O}_4\text{N}_4\text{Cl}_4)]$	289	330	370	
$[\text{Cr}_2(\text{C}_{30}\text{H}_{20}\text{O}_4\text{N}_4\text{Cl}_4)]$	292	334	368	

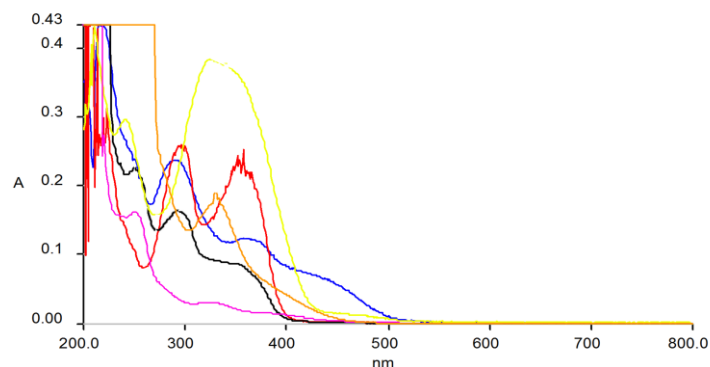


Fig. 1. UV spectra of the binuclear complexes. Yellow - $[\text{Mn}_2(\text{C}_{30}\text{H}_{20}\text{O}_4\text{N}_4\text{Cl}_4)]$, Red - $[\text{Cu}_2(\text{C}_{30}\text{H}_{20}\text{O}_4\text{N}_4\text{Cl}_4)]$, Indigo - $[\text{Cr}_2(\text{C}_{30}\text{H}_{20}\text{O}_4\text{N}_4\text{Cl}_4)]$; Blue - $(\text{C}_{30}\text{H}_{22}\text{O}_4\text{N}_4)$, Black - $[\text{Ni}_2(\text{C}_{30}\text{H}_{20}\text{O}_4\text{N}_4\text{Cl}_4)]$, Pink- $[\text{Zn}_2(\text{C}_{30}\text{H}_{20}\text{O}_4\text{N}_4\text{Cl}_4)]$

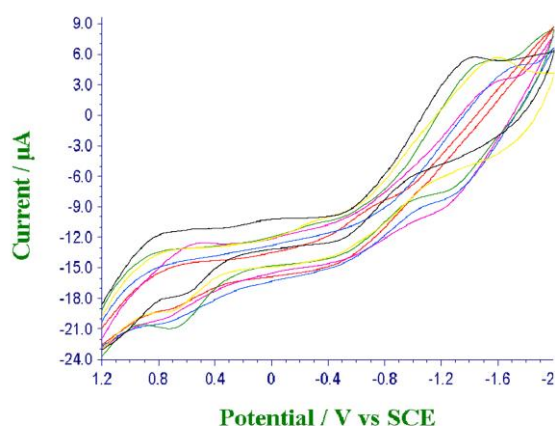


Fig. 2. Cyclic voltammograms of the Schiff base and its complexes. Black - $[\text{Cr}_2(\text{C}_{30}\text{H}_{20}\text{O}_4\text{N}_4\text{Cl}_4)]$, Green - $[\text{Mn}_2(\text{C}_{30}\text{H}_{20}\text{O}_4\text{N}_4\text{Cl}_4)]$, Yellow - $[\text{Zn}_2(\text{C}_{30}\text{H}_{20}\text{O}_4\text{N}_4\text{Cl}_4)]$, Pink- $[\text{Cu}_2(\text{C}_{30}\text{H}_{20}\text{O}_4\text{N}_4\text{Cl}_4)]$, Red- $(\text{C}_{30}\text{H}_{22}\text{O}_4\text{N}_4)$, Blue - $[\text{Ni}_2(\text{C}_{30}\text{H}_{20}\text{O}_4\text{N}_4\text{Cl}_4)]$

Ultraviolet-visible (UV-vis) spectral studies

The UV spectra are often very helpful in structural investigation. UV spectra of all complexes were obtained and show three main features. DMF medium was used. The intraligand charge transfer transition ($\pi \rightarrow \pi^*$) was confirmed by one or two peaks obtained in the range of 276–292 nm. The ligand-to-metal charge transfer transition was responsible for the peak in the range of 368–412 nm. Electronic spectra of the mononuclear nickel (II) complex show d-d transitions corresponding to Ni (II)- d^8 system in an octahedral field. The mononuclear copper (II) complex exhibits a distorted octahedral geometry because of low absorption peak at 530 nm and d-d transition and. Only one broad absorption peak obtained in the binuclear copper (II) and nickel(II) complex in the region 510–650 nm, which is due to one more metal ion present in a our synthesised complexes [15]. The UV spectral data was given in table 3.

Cyclic voltammetry (CV)

Metal character and deoxyribonucleic acid binding ability of the metal complexes were confirmed by an electrochemical method. Cyclic voltammetric technique was used to study the interaction between copper (II) complexes with DNA. The cyclic voltammograms (CV) of the complexes $[\text{Cu}_2(\text{C}_{30}\text{H}_{20}\text{O}_4\text{N}_4\text{Cl}_4)]$, $[\text{Ni}_2(\text{C}_{30}\text{H}_{20}\text{O}_4\text{N}_4\text{Cl}_4)]$, and $[\text{Mn}_2(\text{C}_{30}\text{H}_{20}\text{O}_4\text{N}_4\text{Cl}_4)]$ were obtained in DMF solution at a scan rate of 0.1 Vs^{-1} . The potential was fixed from 1.2 to -2.0 V . The cathodic wave (reduction) of the binuclear copper complex (Figure 2) gives redox properties to the own units. Thus, there was reduction of central Cu(II) to Cu(I) at -0.7920 V and irreversible copper reduction at -1.4832 V . The support of two one-electron reduction is observed for the binuclear copper complex, suggesting that the two copper ions have some sort of interaction with each other. Same results are obtained for the complexes $[\text{Ni}_2(\text{C}_{30}\text{H}_{20}\text{O}_4\text{N}_4\text{Cl}_4)]$ and $[\text{Mn}_2(\text{C}_{30}\text{H}_{20}\text{O}_4\text{N}_4\text{Cl}_4)]$ [16–18].

Electron paramagnetic resonance (EPR) spectra

The $[\text{Cu}_2(\text{C}_{30}\text{H}_{20}\text{O}_4\text{N}_4\text{Cl}_4)]$ complex was dissolved in DMF solvent. The solution was used in the EPR study. The EPR spectra of the $[\text{Cu}_2(\text{C}_{30}\text{H}_{20}\text{O}_4\text{N}_4\text{Cl}_4)]$ complex recorded in X-band frequency at room temperature and LNT with microwave frequency of 9.1 Ghz and magnetic field of 300 mT revealed the presence of Cu(II) ion. This spectrum confirms that a Cu(II) complex was formed. The spectrum has a g value of 2.32 mT. The shape of the spectrum and the g value indicates that Cu(II) complex structure is a cubically

distorted octahedral structure. There is no change in the LNT. The $[\text{Mn}_2(\text{C}_{30}\text{H}_{20}\text{O}_4\text{N}_4\text{Cl}_4)]$ complex was dissolved in DMF solvent. The solution was used in the EPR study. The EPR spectra of the $[\text{Mn}_2(\text{C}_{30}\text{H}_{20}\text{O}_4\text{N}_4\text{Cl}_4)]$ complex recorded at LNT in X-band with microwave frequency of 9.1 Ghz and magnetic field of 300 mT revealed the presence of Mn(II) ion. This spectrum confirms the formation of the Mn(II) complex. The spectrum has a g value of 2.01 mT. The shape of the spectrum and the g value indicate that Mn(II) complex structure is octahedral. No spectrum was obtained at 36°C [19, 20].

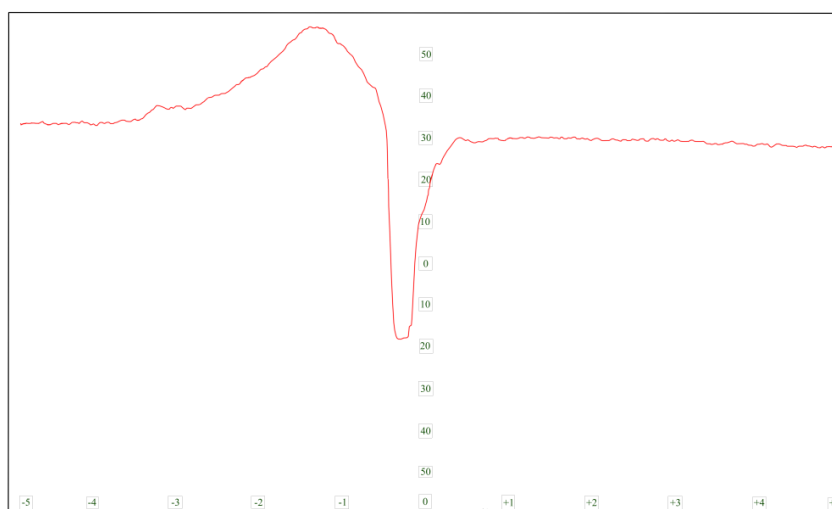


Fig. 3. EPR spectrum of the copper complex

$^1\text{H-NMR}$ spectrum and $^{13}\text{C NMR}$ spectrum

The ^1H and $^{13}\text{C-NMR}$ spectra were recorded on Bruker Avance III HD nanobay. DMSO- d_6 was used as a solvent. The spectrum of the uncomplexed Schiff base ligand was compared with that of the corresponding zinc complex. Expected signals were seen in the spectra. The spectra of the ligand were dependable with the proposed structure. A singlet corresponding to a single proton was observed in the range of δ 9.01 ppm attributed to the azomethine proton ($-\text{HC}=\text{N}$). The multiplet related to values δ 6.57 to 6.80 confirmed the presence of Ar-H. The study of the $^{13}\text{C NMR}$ spectrum of the zinc (II) complex confirmed that the resonances due to the carbon

atoms of the 3, 3'-dihydroxy benzidine and 3-amino coumarin showed irrelevant changes of complex formation. Expected signals are shown in the spectrum. The values of δ 39.29 to 40.55 confirmed the presence of amine (C-N). The presence of carbon-carbon double bond (C=C) is confirmed by the values of δ 112.33 to 117.24. The values of 130.28 to 144.67 were attributed to the presence of benzene ring (C-C). It was confirmed that coordination proceeded through the carbonyl oxygen and amino group to form azomethine. NON donor set donated electrons to zinc metal to form a coordination bond [21, 22]. Because of paramagnetic effects, no spectrum was obtained for other transition metal complexes.

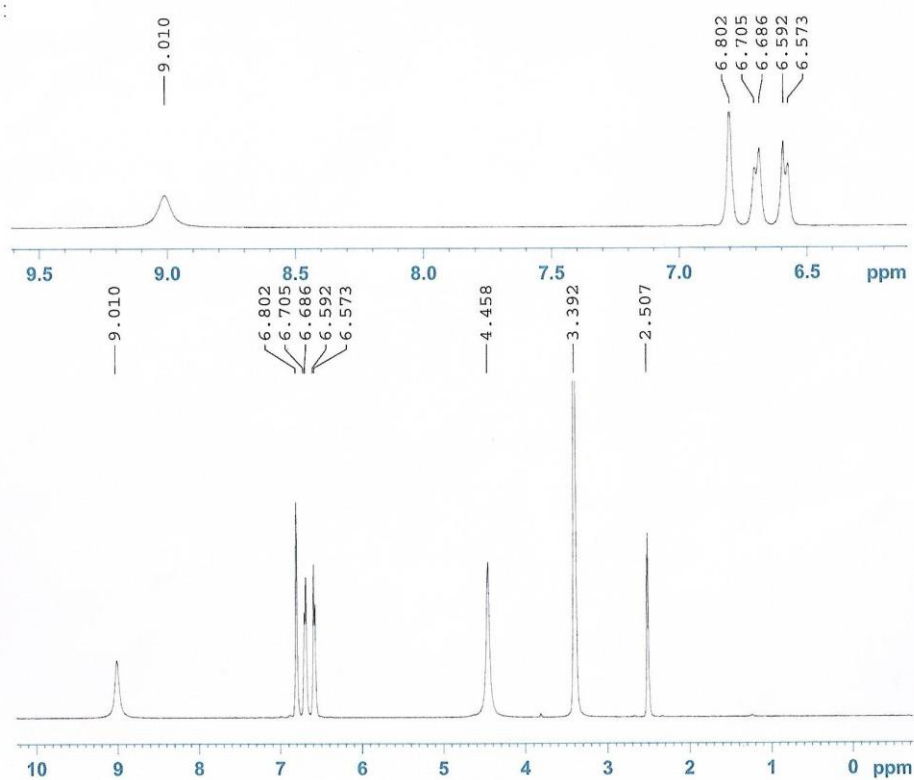


Fig. 4. ¹H NMR spectrum of the ligand

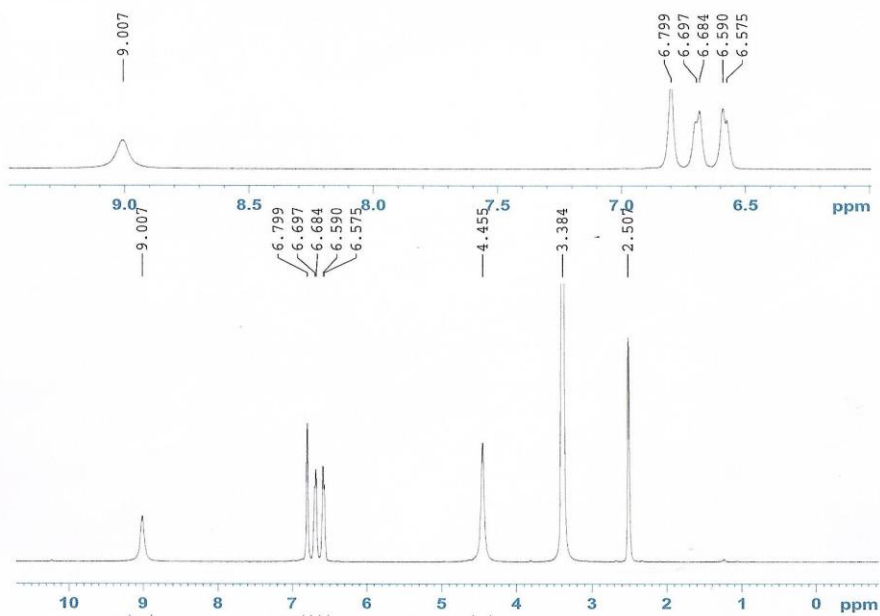


Fig. 5. ¹H NMR spectrum of the zinc complex

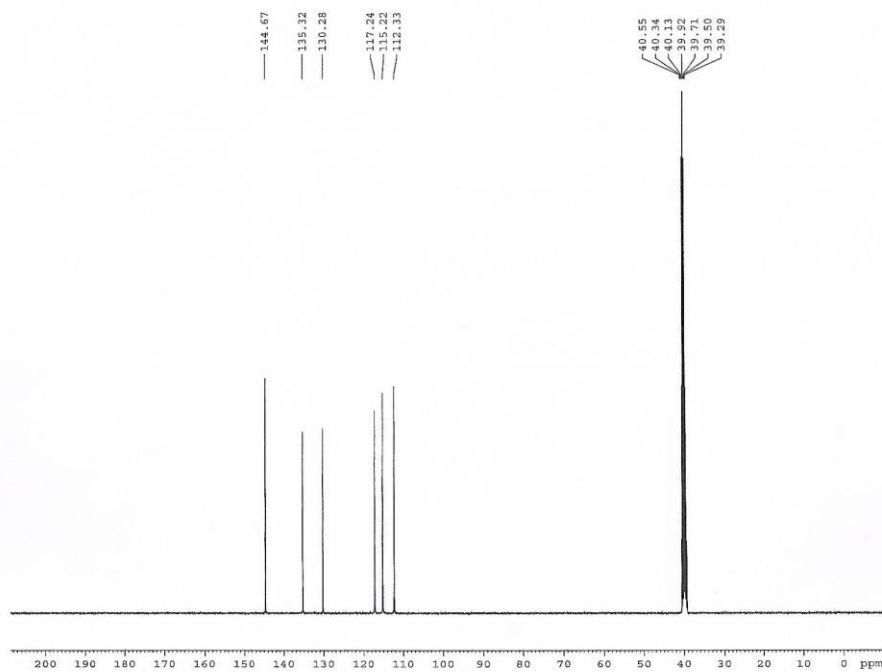


Fig. 6. ¹³C NMR spectrum of the ligand

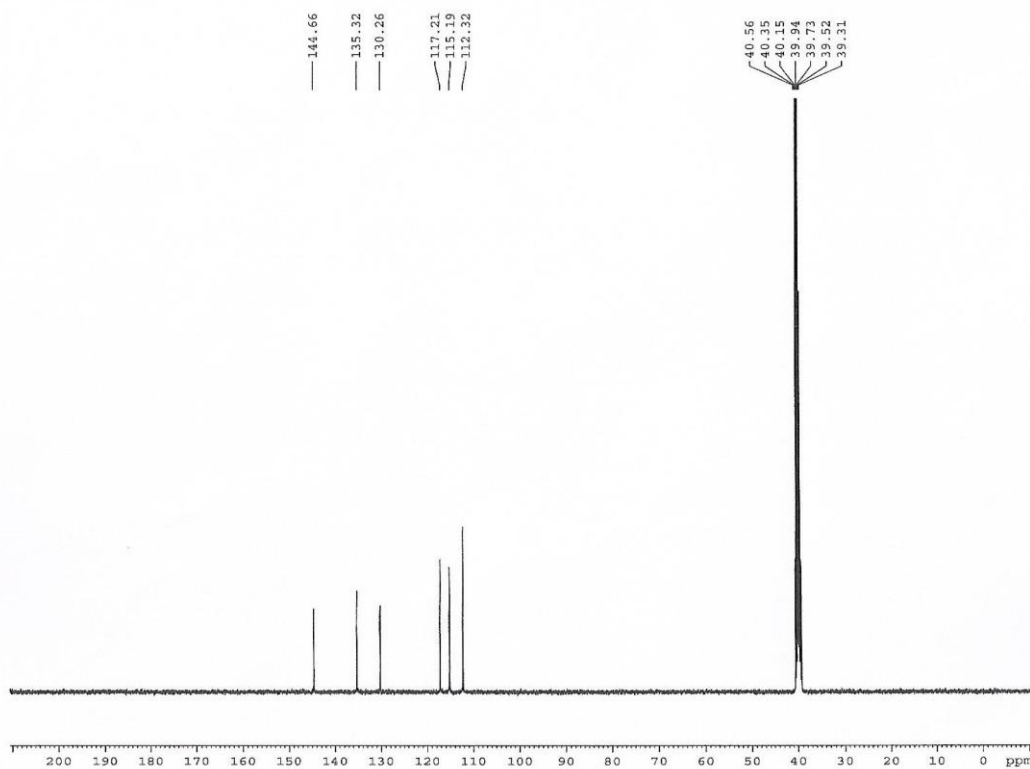


Fig. 7. ¹³C NMR spectrum of the zinc complex

Deoxyribonucleic acid (DNA) cleavage study

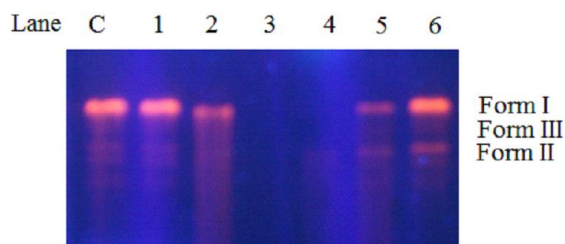


Fig. 8. Gel electrophoretic pattern of pUC18DNA induced by hydrogen peroxide and binuclear complexes: lane C: pUC18DNA alone; lane 1: ligand + hydrogen peroxide; lane 2: pUC18DNA + Mn binuclear complex + hydrogen peroxide; lane 3: pUC18DNA +Cu binuclear complex + hydrogen peroxide; lane 4: pUC18DNA +Ni binuclear complex + hydrogen peroxide; lane 5: pUC18DNA +Zn binuclear complex + hydrogen peroxide; lane 6: pUC18DNA +Cr binuclear complex + hydrogen peroxide.

Cleavage of plasmid pUC18 DNA. DNA cleavage study was analyzed by the electrophoresis method (Figure 8). While conducting electrophoresis for plasmid DNA, the migration for super coiled form was fastest (Form I). Supercoils became slower moving open circular forms if one strand was cleaved (Form II). A linear nicked form was generated and migrated in between if both strands were cleaved (Form III). The different binding affinity of the complex to DNA was the main factor for DNA cleavage efficiency of the complex. Purified DNA ligase was inhibited by metal chlorides [23]. There was no significant cleavage of DNA for ligand (lane 1) even though on long exposure time. Manganese binuclear complex (lane 2) in the presence of hydrogen peroxide at higher concentration showed cleavage activity. Super coiled DNA (Form I) was cleaved and converted to open circular form (Form II) by the manganese binuclear complex. When compared with other binuclear metal complexes, higher cleavage activity is shown by copper and nickel binuclear complexes in the presence of H_2O_2 (lanes 3&4). Copper and nickel binuclear complexes fully degraded the supercoiled plasmid DNA. If concentration was increased, it caused degradations. Formation of a redox couple of the metal ions and its behavior led to this degradation. The functional group -OH can cleave the DNA by combining with the hydrogen atom present in the deoxyribose sugar. Copper ions and H_2O_2 produced diffusible hydroxyl radical ($-OH$). It may damage DNA through Fenton type chemistry. Cleavage activity was shown by zinc and chromium binuclear complexes in the presence of H_2O_2 . Zinc and

chromium binuclear complexes in the presence of H_2O_2 (lanes 5&6) showed cleavage activity. Hence, supercoiled DNA (Form I) was converted to open circular form (Form II) [24].

Antimicrobial activity

Antimicrobial assay. Antibacterial activity of copper(II), nickel(II), manganese(II), zinc(II) and chromium(III) complexes was determined by the disc diffusion method. Streptomycin was used as the standard antibiotic. The prepared binuclear Schiff base complexes were tested against bacteria like *Staphylococcus aureus*, *Escherichia coli* and *Klebsiella pneumoniae* bacteria. Glass plates were initially sterilized in an autoclave and were kept inside an air purifier. The respective microbial culture was swabbed into the nutrient agar plates. Then the glass plates were kept inside the incubator at 36 °C for 25 h and the diameter was measured. Metal chelates displayed higher activity compared with the standard. The minimum inhibitory concentration (MIC) values of the synthesized complexes are indicated in table 4. From the results we understood that copper(II) and nickel(II) complexes exhibit high activity towards all microorganisms [25]. The order of bacterial growth inhibition capacity was: $Cu(II) > Ni(II) > Mn(II) > Zn(II) > Cr(III)$. The binuclear complexes had larger MIC values against growth of microorganisms compared with the standard. Chelation theory can be used to explain the improvement of activity of the copper binuclear complex. [26]. Low concentration of the compound (500 ppm) is good enough to bring out an effective inhibition against the chosen bacteria [27]. The activity of the complexes depends on size, charge distribution, shape of the metal ions. Mn(II) metal complexes showed moderate antibacterial property [28]. The Zn(II) complex exhibited low activity against the species [29]. The Cr(III) complex exhibited lower activity against microbes compared with the other metals [30].

CONCLUSION

From the molar conductance measurements, IR, UV, CV, EPR, and NMR spectra of the binuclear complexes, the above mentioned structure can be confirmed and complexes are octahedral. The molar conductance measurements revealed that the synthesized complexes are non-electrolytic in nature.

Table 4. Antibacterial activity of the binuclear complexes

Compounds	<i>K. pneumonia</i> (mm)				<i>E. coli</i> (mm)				<i>S. aureus</i> (mm)			
	Concentration ($\mu\text{g/ml}$)											
	25	50	75	100	25	50	75	100	25	50	75	100
[Cu ₂ (C ₃₀ H ₂₀ O ₄ N ₄ Cl ₄)]	11	14	16	19	12	12	16	18	11	14	18	19
[Ni ₂ (C ₃₀ H ₂₀ O ₄ N ₄ Cl ₄)]	11	12	15	18	12	14	15	17	10	12	17	18
[Mn ₂ (C ₃₀ H ₂₀ O ₄ N ₄ Cl ₄)]	12	13	14	17	11	14	14	16	11	13	16	17
[Zn ₂ (C ₃₀ H ₂₀ O ₄ N ₄ Cl ₄)]	10	11	12	14	11	12	12	14	11	12	13	14
[Cr ₂ (C ₃₀ H ₂₀ O ₄ N ₄ Cl ₄)]	10	10	11	13	10	11	11	13	10	11	13	13

The novel copper(II), nickel(II), manganese(II), zinc(II) and chromium (III) binuclear complexes were synthesized from 3,3'-dihydroxy benzidine and 3-amino coumarin containing NON donors set in different environments. The antibacterial activity of the binuclear Schiff base metal complexes against microbes *Escherichia coli*, *Klebsiella pneumoniae* and *Staphylococcus aureus* was studied by the disc diffusion method. Binuclear copper(II) and nickel(II) complexes have got higher cleavage activity when compared to manganese(II), zinc(II) and chromium (III) binuclear Schiff base metal complexes.

REFERENCES

- J. Qi, Y. Zhang, Y. Gou, Z. Zhang, Z. Zhou, X. Wu, F. Yang, H. Liang, *Mol. Pharmaceutics*, **13** (5), 1501 (2016).
- H. A. Ali, S. N. Omar, M. D. Darawsheh, H. Fares, *J. Coord. Chem.*, **69**, 1110 (2016).
- S. Sreedaran, K. S. Bharathi, A. K. Rahiman, K. Rajesh, G. Nirmala, L. Jagadish, V. Kaviyaran, V. Narayanan, *Polyhedron*, **27**, 1867 (2008).
- I. A. Ansari, M. F. Sama, Shahid, M. Ahmad, P. S. Nayab, A. Rahisuddin, A. Zafar, Z. Siddiqi, *J. Coord. Chem.*, **69**, 3336 (2016).
- S. A. Patil, T. Chetan, Prabhakara, M. Bhimashankar, Halasangi, S. Shivakumar, Toragalmath, P. S. Badami, *Spectrochim. Acta, Part A*, **137**, 641 (2015).
- Sh. L. Cravens, J. T. Stivers, *Biochemistry*, **55**, 5230 (2016).
- P. A. N. Reddy, B. K. Santra, M. Nethaji, R. Akhil, J. Chakravarty, *J. Inorg. Biochem.*, **98**, 377 (2004).
- S. Deepalatha, P. Sambasiva Rao, R. Venkatesan, *Spectrochim. Acta, Part A*, **64**, 178 (2006).
- U. M. Rabie, A. S. A. Assran, M. H. M. Abou-El-Wafa, *J. Mol. Str.*, **872**, 113 (2008).
- J. Parr, A. M. Z. Slawin, *Inorganica Chimica Acta*, **303**, 116 (2000).
- J. Lv, T. Liu, S. Cai, X. Wang, L. Liu, Y. Wang, *J. Inorg. Biochem.*, **100**, 1888 (2006).
- A. Ray, S. Banerjee, S. Sen, R. J. Butcher, G. M. Rosair, M. T. Garland, S. Mitra, *Struct. Chem.*, **19**, 209 (2008).
- A. A. A. Emara, O. M. I. Adly, *Trans. Met. Chem.*, **32**, 889 (2007).
- S. S. Tajudeen, G. Kannappan, *Indian J. Adv. Chem. Sci.*, **4**(1), 40 (2016).
- M. Sivasankaran Nair, D. Arish, T. Johnson, *J. Saudi Chem. Soc.*, **20**, S591 (2016).
- D. Basumatary, A. Kumar, R. A. Lal, *Intern. J. Adv. in R. & Tech.*, **2**, 11 (2013).
- I. Owsik, B. N. Kolarz, J. Jezierska, *Catalysis Letters*, **107**(3-4), 197 (2006).
- M. Bera, P. K. Nanda, U. Mukhopadhyay, D. Ray, *J. Chem. Sci.*, **116**(3), 151 (2004).
- H. Sahebalzamani, S. Ghammamy, K. Mehranic, F. Salimic, *Der Chemica Sinica*, **1**, 39 (2010).
- D. N. Tai, N. D. Thanh, P. D. Nam, H. T. Duc, *J. of Chem.*, **45**, 642 (2007).
- M. A. Neelakantan, F. Rusalraj, J. Dharmaraja, S. Johnsonraja, T. Jeyakumar, M. S. Pillai, *Spectrochimica Acta, Part A*, **71**, 1599 (2008).
- N. Sengottuvelan, D. Saravanakumar, M. Kandaswamy, *Polyhedron*, **26**, 3825 (2007).
- M. A. Neelakantan, F. Rusalraj, J. Dharmaraja, S. Johnsonraja, T. Jeyakumar, M. S. Pillai, M. Sridhar, *Spectrochim. Acta, Part A*, **71**, 1599 (2008).
- S. Prasad, P. Jayaseelan, P. R. Rajavel, *Intern. J. Pharm. & Tech.*, **2**, 694 (2010).
- M. A. Riswan Ahamed, R. S. Azarudeen, M. N. Kani, *Bioinorg. Chem and Appl.*, Article ID 764085 (2014).
- R. C. Maurya, P. Bohre, S. Sahu, M. H. Martin, A. K. Sharma, *Arab. J. Chem.*, **9**, S54 (2016).
- S. A. Aleaghil, E. Fattahy, B. Baei, M. Saghali, H. Bagheri, N. Javid, E. A. Ghaemi, *Intern. J. Adv. Biotech. Res. (IJBR)*, **7**, 1569 (2016).
- G. Sridhar, I.M. Bilal, D. Easwaramoorthy, S. Kutti Rani, B. Siva Kumar, C. S. Manohar, *J. Braz. Chem. Soc.*, **28** (5), 756 (2017).

Manufacturing of artificial core based on transparent soil technology: A preliminary experimental study on various grains and pore fluids

R. Song¹, Y. Wang^{1*}, J. J. Liu^{1, 2*}

¹ School of Geoscience and Technology, Southwest Petroleum University, Chengdu, 610500, Sichuan, P. R. China

² Institute of Rock and Soil Mechanics, Chinese Academy of Sciences, Wuhan, 430071, Hubei, P. R. China

Received October 25, 2018, Revised July 9, 2019

Artificial cores are more representative than natural cores on heterogeneity in laboratory core analysis. This paper presents a new method to prepare transparent cores based on transparent soil. A preliminary experiment is carried out to determine the optimal combination of different grains and pore fluids. The basic parameters of mineral oil used in this paper are tested including the refractive index RI value, density, and dynamic viscosity. The relations between RI value, pH value, viscosity, density and concentration of calcium bromide solution are obtained as well. The results indicate that the RI and density of calcium bromide solution increase with the increase in concentration, whereas pH and viscosity decrease with the concentration. The effect of temperature on RI value increases with the increase in calcium bromide solution concentration. When the particle size of silica gel ranges from 49.7 to 74.5 μm and the concentration of calcium bromide solution reaches 62%, the prepared mixed system will achieve the highest transparency.

Keywords: Artificial core; Transparent soil; Fluid flow; Geotechnical engineering; Petroleum

INTRODUCTION

Core analysis plays an important role both in the petroleum industry and the geotechnical engineering field [1]. During laboratory testing on natural cores, the limitations lay on the weak representativity, strong heterogeneity, and low efficiency of drilling of cores, which greatly restrict the development of laboratory tests [2, 3].

What's more, the opacity of natural and artificial samples makes it impossible to directly capture the internal processes in the sample. Computerized tomography (CT) technology [4, 5] and microfluidics model [6, 7] have been used to capture the inner rock structure and flow process. However, the view size of these pore scale tests is too small when compared to mesoscale experiment field application, compared to mesoscale experiments operated on the core samples.

Laboratory experiment conducted on physical models manufactured from transparent soil has been regarded as a new tool for visual technique in geotechnical engineering. The earliest study on transparent soils can be traced back to 1982. Allersma studied the stress-strain relationship under the single-shear condition with a model made of broken glass [8]. Mannheimer studied the non-Newtonian fluid flow by using a transparent slurry [9]. After that, researchers have conducted fruitful work on preparation, engineering properties and applications of transparent soil [10, 11].

Previous studies on the physical and mechanical properties of the consolidated samples were performed, and the results indicated that the mechanical properties of these samples are similar to those of the weak cemented natural rock-soil mass [12, 13]. In the literature, researchers mainly focused on the mechanical and deformation characteristics of transparent soil [14-18].

In this paper, we test the RI value and basic physical parameters of mineral oil. Meanwhile, the basic parameters of calcium bromide solution with different concentration are obtained as well, including RI value, pH value, density, and dynamic viscosity. Different combinations of grains and pore fluids are evaluated to achieve optimal transparency. The work conducted in this study presents a theoretical basis for further manufacturing of transparent artificial cores.

EXPERIMENTAL

Materials and methods

The artificial core is manually manufactured under a given pressure in a mold of specific shape with a certain proportion of grain and binder. According to the manufacturing process and different type of binder, the artificial core can be divided into three categories including cementation of quartzite and colophony, cementation of aluminum phosphate and filling tube of quartz sand [19-21], as shown in Fig. 1.

* To whom all correspondence should be sent:

E-mail: wangyao0927@126.com or

liujj0906@163.com

Transparent soil is generally synthesized by two materials, i.e. grains and pore fluids which have a similar RI value to each other. In the early stage, the amorphous silica powder and silica gel were the most common grain material for transparent soil preparation [10]. More types of new materials were then used as grains including fused silica [14], hydrogel (which was renamed Aquabeads) [22], and Laponite [23]. The pore fluids used in transparent soil mainly include mineral oil (a mixed system of liquid paraffin and normal alkanes), calcium bromide solution and sucrose solution. [24, 25]. The physical properties and corresponding pore fluids to different grain materials in literature are summarized, as shown in Table 1.

According to a previous study [12], fused quartz and glass sand contain more impurities and

are relatively less transparent compared to silica gel. Silica gel is selected as the grain material in this study with a corresponding RI value ranging from 1.41-1.46, and the matching pore fluids are mineral oil and calcium bromide solution. The silica gel used in this study is prepared by the Qingdao Bangkai High-tech Inc.

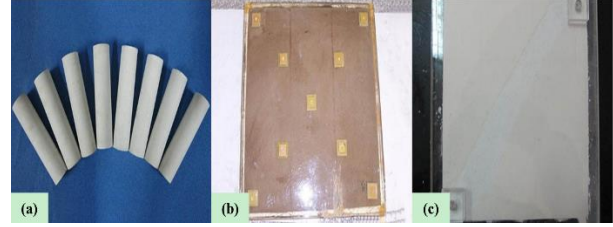


Fig. 1. Various types of artificial core (a) cementation of colophony; (b) cementation of aluminum phosphate; (c) filling tube of quartz sand.

Table 1. Physical properties of different grain material and matching pore fluids

Grain categories	Amorphous silica powder	Silica gel	Fused silica	Hydrogel (Aquabeads)	Laponite
RI	1.442	1.442	1.458	1.333	1.336
Saturated unit weight (kN/m ³)	9.4-16	11-14	13.4-16.4	10	10
Drained friction angle	19°-36°	29°-42°	44°-59°	—	—
Drained cohesion (kPa)	20-44	0	0	—	—
Compression index	1.6-3	—	0.34-0.54	0.1-0.15	16.6-20.6
Hydraulic conductivity (cm/s)	2.3×10 ⁻⁷ — 2.5×10 ⁻⁵	1.5×10 ⁻⁴ — 7×10 ⁻³	1.3×10 ⁻⁵ — 2.1×10 ⁻⁵	7×10 ⁻² — 6×10 ⁻⁸	5×10 ⁻⁹ — 1.6×10 ⁻⁶
Intrinsic permeability (Darcy)	0.015-0.16	1-45	24-40	—	—
Matching pore fluid	Mineral oil or calcium bromide solution		Mineral oil or sucrose solution (or STSI)	Water	Water

RESULTS AND DISCUSSION

General manufacturing process

The manufacturing process of the transparent core consists of three steps, i.e. the preparation of a mixed system of grain and pore fluid, molding and vacuuming of mixed system, and consolidation of mixed system. It should be noted that air bubbles must be removed from the mixed system to ensure the transparency of the core.

In addition, the pressure should be loaded step by step until the maximum load during the consolidation process.

Laboratory test of mineral oil

The mineral oil is composed of two alkanes with different RI values, which generally depend on the RI value of the selected grain material. There are four types of alkanes selected and tested in this study, including liquid paraffin, 2#, 5#, and 10# white oil. Different types of white oil are

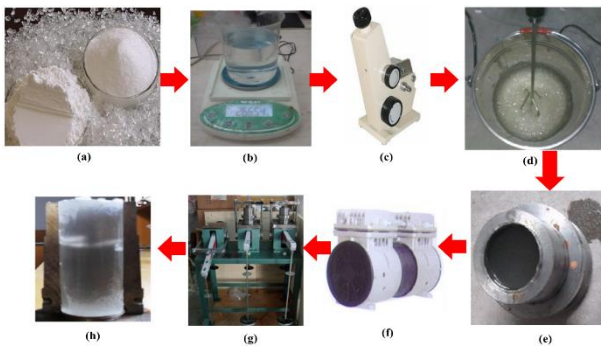


Fig. 2. General work-flow of the manufacturing process: (a) grain material; (b) pore fluid; (c) 2WJ type refractometer; (d) mixed system; (e) molding; (f) vacuuming; (g) consolidation; (h) removing of mold.

Generally, the RI value increases with viscosity at the same temperature. The test results of the four types of alkanes are listed in Table 2.

The RI value of a mixed system with two component liquids can be calculated by [26]:

$$\frac{(V_1 + V_2)}{n} = \frac{V_1}{n_1} + \frac{V_2}{n_2} \quad (1)$$

where, n is the RI value of the mixed system, n_1 and n_2 are the RI values of the component liquids, and V_2 is the volume fraction of the component liquids.

Table 2. Test results of mineral oil

Name	Refractive index	Density (kg/m ³)	Dynamic viscosity (m ² /s)
Liquid paraffin	1.4586	860-905	6-8
2# white oil	1.4205	816	2.8
5# white oil	1.4329	820	4.8
10# white oil	1.4485	828	9.8

Laboratory test of calcium bromide solution

The anhydrous calcium bromide used in this paper is prepared by Tianjin Guangfu Fine Research Institute. The molecular formula is CaBr₂, and the molecular weight is 199.89. It is white, granular or crystalline with strong hygroscopicity, easy deliquescence, and slight decomposition. The density, melting point and boiling point are 3.35 g/cm³, 730 °C, and 806-812 °C, respectively. It is soluble in water,

ethanol, and acetone, but is insoluble in ether and chloroform. It will turn yellow when stored in air for a long period and will decompose into bromine and calcium oxide at high temperature. The main technical parameters of CaBr₂ are listed in Table 3.

As is shown in Fig. 3, the RI values of calcium bromide solution are tested at various concentrations at room temperature conditions. It can be seen that the concentration of calcium bromide solution has a great effect on RI value which linearly increases with concentration. Besides, the test results are compared with the literature and are in good agreement [27].

Table 3. Technical parameters of CaBr₂

CaBr ₂ (%)	Chloride (%)	Sulfate (%)	Metal (ppm)	Insoluble (%)
≥ 96.0	≤ 1.0	≤ 0.02	≤ 5.0	≤ 1.0

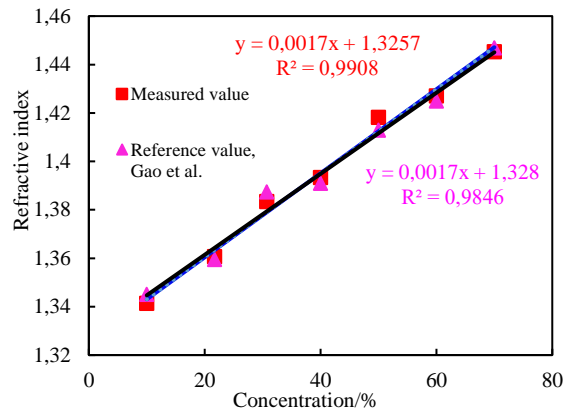


Fig. 3. Relationship between concentration and RI

Parameters such as density, pH value and dynamic viscosity of calcium bromide solution with different concentrations were tested as well, and the results are shown in Fig. 4.

Both density and viscosity increase with the concentration of calcium bromide solution, whereas pH decreases and shows acidic values.

The RI values of solutions of different concentration were determined at various temperatures, and the results are shown in Fig. 5. It is found that the RI value is insensitive to the temperature at low concentration. The sensitivity to temperature slightly increases with concentration, and the maximum increase is achieved at 40% concentration.

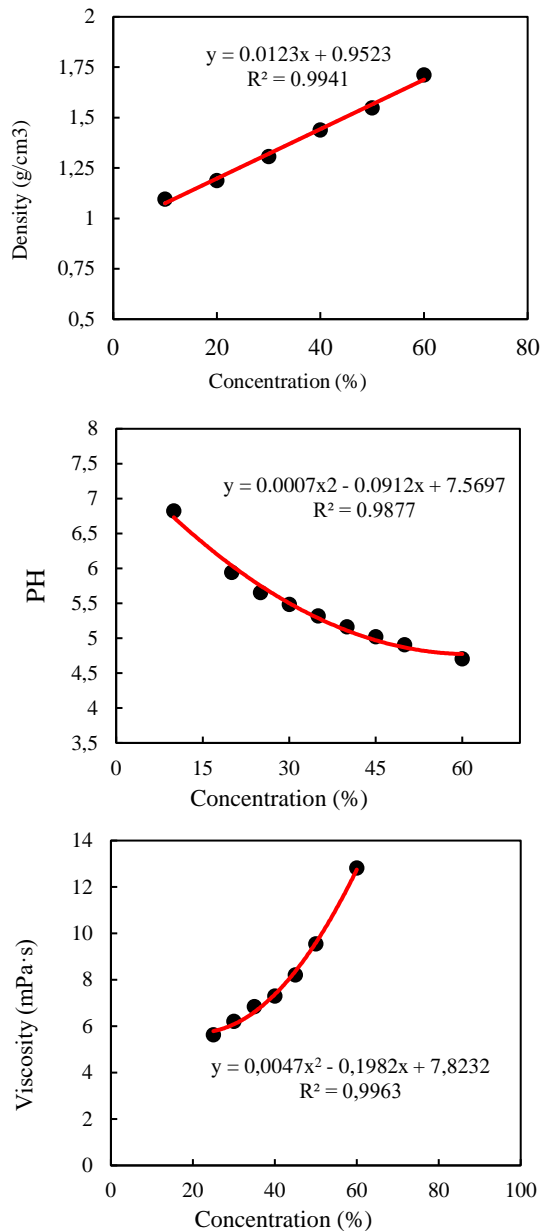


Fig. 4. Relationships between concentration & density, pH value, and viscosity.

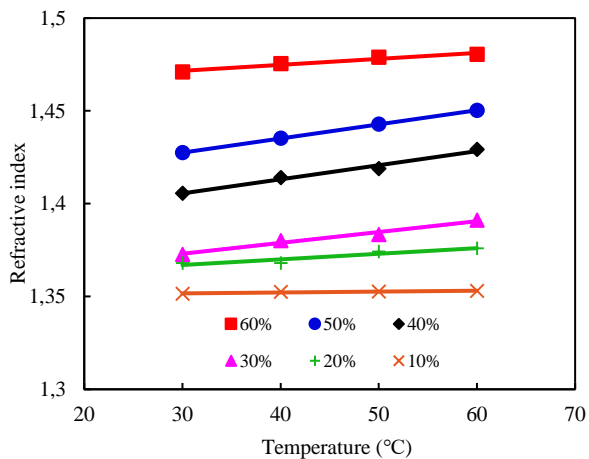


Fig. 5. Relationship between temperature and RI at various concentrations.

In summary, there is a good correlation between RI value and concentration of calcium bromide solution, and the RI value generally ranges from 1.34 to 1.47. The results indicate that calcium bromide solution is an ideal pore fluid material for transparent soil manufacturing, for it can satisfy a wide range of RI requirements. Considering the acidic alternation property of calcium bromide solution at high concentration, the mineral oil should be a better alternative selected in those cases when the experimental process is highly dependent on the chemical properties of the material.

Effect of particle size and concentration on sample transparency

The mixed systems of silica gel and mineral oil are prepared with four different types of particle size, as shown in Fig. 6. Four kinds of specifications of particle size including 1490 μm, 124.2 μm, 49.7 μm and 9.93 μm are used in this study.

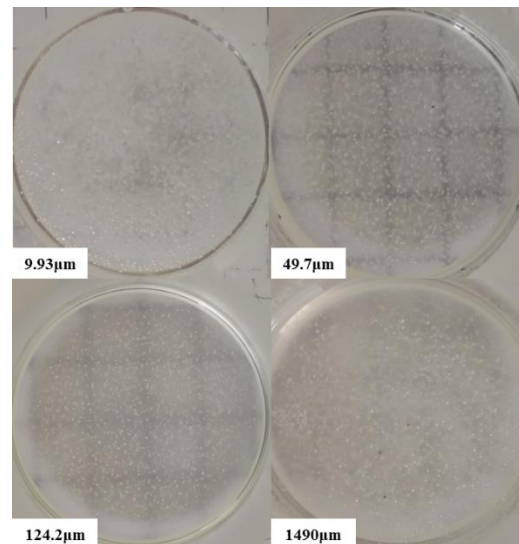


Fig. 6. Transparent mixed system of silica gel and mineral oil

In Fig. 6, it can be noted that the second group with particle size of 49.7 μm has relatively better transparency. The transparency decreases with the increase or decrease of particle size. When the particle size is too small, there will be more impurities which can significantly reduce the transparency of the mixed system. In addition, a large number of tiny air bubbles will be immersed in the mixed system during the molding and consolidation operation. On the other side, when the particle size is too large, segregation occurs easily between particles and pore fluids during the consolidation process, which can significantly reduce the transparency and strength of the final

cores. Currently, there are no products with a purity of 95% for a given particle size in the market. Therefore, the silica gel with particle size ranging from 49.7 to 74.5 μm was selected as the grain material in this study, and the corresponding RI values range from 1.41 to 1.46.

Calcium bromide solution was used as a pore fluid in this study to manufacture transparent soil at four levels of concentration including 56%, 60%, 62%, and 65%. Silica gel with particle size of 47.9 μm was added into the calcium bromide solution until saturation, and the mixed systems are shown in Fig. 7. Among the four mixed systems, the sample with 62% concentration has relatively good transparency.

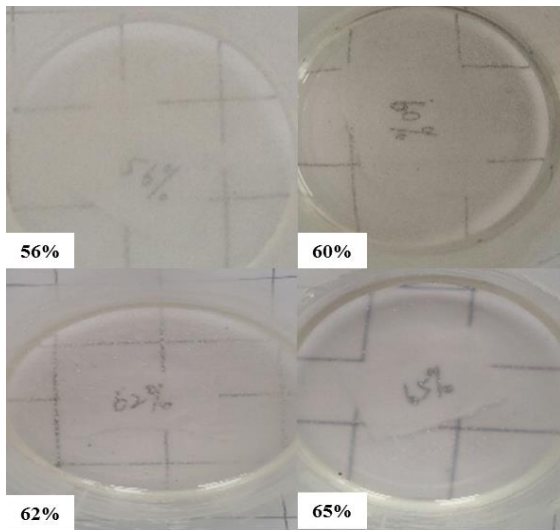


Fig. 7. Transparent mixture manufactured by calcium bromide solution with different concentrations.

Pressure sensors, flowmeter, and measuring ruler are utilized in the experiment to monitor the changes of pressure and flux inside the transparent sample. Meanwhile, the flow pattern could be imaged by multiple cameras which are arranged at different positions around the experimental setup, including front, side, and bottom of the sample box. These might be most helpful to realize the 3D analysis of the flow field during the test.

According to previous studies [28, 29], the transparent soil material not only has similar properties from the perspective of strength and deformation but also hydraulic property similar to some types of natural soil. By changing raw materials and operating conditions, transparent oil samples with different types of porosity, mechanical properties, and pore structure can be prepared. Then the samples can be adopted to conduct fluid flow experiments. A simple flow experimental setup was developed to model the 2D flow, as shown in Fig. 8.

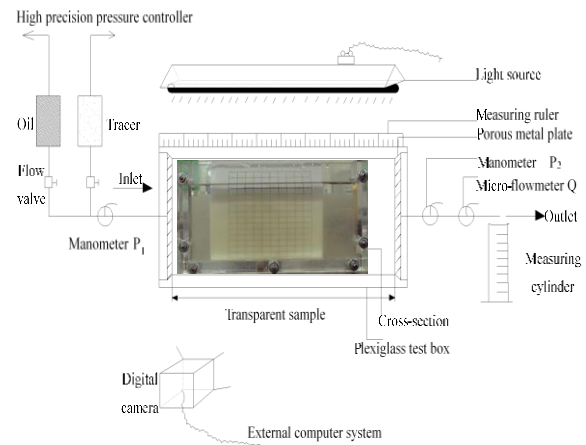


Fig. 8. 2D flow experimental setup used for transparent soil.

CONCLUSION

In this paper, a new technology was proposed to prepare transparent samples in combination with artificial core and transparent soil technique. Several groups of grain materials and corresponding pore fluids were tested to determine the optimal combinations of different materials.

The basic physical parameters such as RI value, density, dynamic viscosity, and pH value were obtained both for mineral oil with a different combination of alkane compounds, and calcium bromide solution with different concentrations. The pH value of the mineral oil is more stable than that of the calcium bromide solution. Nevertheless, the calcium bromide solution has a wider range of RI values.

The effect of temperature on RI value is also studied. The results indicated that the general trend of the RI value of calcium bromide solution increases with temperature, especially at high concentrations. However, mineral oil is less sensitive to temperature.

The mixed systems of grains and pore fluids were prepared for further study. As a key indicator of the transparent sample, the effect of particle size and solution concentration on the transparency of the mixed system were quantitatively investigated. The results indicated that the silica gel of particle size ranging from 49.7-74.5 μm and calcium bromide solution with a concentration of 62% will lead to relatively higher transparency of the mixed system.

Conflict of Interests: The authors declare that there is no conflict of interest regarding the publication of this manuscript.

Acknowledgements: This paper was financially supported by the National Science and Technology Major Project of China (Grant No. 2017ZX05013-001-002). Meanwhile, we appreciate the help in experimental work provided by the Experimental Center of the College of Chemistry and Chemical Engineering at Southwest Petroleum University.

REFERENCES

1. W. L. Liang, *Petro. Instruments*, **22**, 72 (2008).
2. Z. Z. Wang, R. H. Wang, H. Qiu, *Geophys. Prospecting Petro.*, **52**, 150 (2015).
3. F. Y. Li, S. L. Yang, W. L. Gao, *Sci. Tech. Eng.*, **13**, 685 (2013).
4. Y. Wang, R. Song, J. J. Liu, *J. Contamin. Hydro.*, **225**, 103, 499 (2019).
5. R. Song, J. J. Liu, M. M. Cui, *Int. J. Heat Mass Trans.*, **109**, 705 (2017).
6. M. X. Yu, W. Y. Zhu, H. Q. Song, *J. Liaoning Tech. Uni. (Nat. Sci. Ed.)*, **32**, 1646 (2013).
7. A. Chatenever, J. C. Calhoun Jr, *J. Pet. Technol.*, **4**, 149 (1952).
8. H. Allersma, Proceedings of the: IUTAM Symposium on Deformation and Failure of Granular Materials, Publ. Rotterdam: A. A. Balkema, 1982.
9. R. Mannheimer, *Tech. Today*, **3**, 2 (1990).
10. M. Iskander, J. Y. Liu, S. Sadek, *J Geotech. Geoenviron. Eng.*, **128**, 262 (2002a).
11. M. Iskander, S. Sadek, J. Y. Liu, *Int. J. Phys. Model Geomech.*, **2**, 13 (2002b).
12. M. Iskander, *Modeling with Transparent Soil* (1st edn.), Springer Press, New York, (2010).
13. J. Y. Liu, Visualization of 3-D deformation using transparent soil models, Ph.D. Thesis, Polytechnic Uni., New York, 2003.
14. S. Sadek, Soil structure interaction in transparent synthetic soils using digital image correlation. Ph.D Thesis, Polytechnic Uni., New York, 2002.
15. Y. X. She, *Site Invest. Sci. Tech.*, **6**, 7 (2005).
16. Y. H. Li, Z. B. Lin, X. L. Qin, *J. China Uni. Mining Tech.*, **44**, 977 (2015).
17. G. Q. Kong, Z. H. Cao, H. Zhou, X. J. Sun, *Geotech. Testing J.*, **38**, 1 (2015).
18. G. Q. Kong, L. Liu, H. L. Liu, H. Zhou, *Chin. J. Rock Mech. Eng.*, **35**, 1140 (2013).
19. Y. F. Pi, *Sci. Tech. Eng.*, **10**, 7724 (2010).
20. X. G. Lu, Z. H. Gao, W. H. Yan, *Petro. Geology Oil Field Develop. Daqing*, **13**, 53 (1994).
21. Y. F. Pi, *Sci. Tech. Eng.*, **10**, 6998 (2010).
22. S. R. Fernandez, M. Iskander, K. Tabe, *Geotech. Letters*, **1**, 71 (2011).
23. J. Wallace, C. Rutherford, *Geotech. Testing J.*, **38**, 1 (2015).
24. M. Iskander, R. J. Bathurst, M. Omidvar, *Geotech. Testing J.*, **38**, 557 (2015).
25. J. Y. Liu, M. Iskander, *Canad. Geotech. J.*, **47**, 451 (2010).
26. T. M. Aminabhavi, *J. Chem. Eng. Data*, **29**, 54 (1984).
27. Y. Gao, W. H. Sui, J. Y. Liu, *Geotech. Testing J.*, **38**, 5 (2015).
28. J. Y. Liu, M. Iskander, S. Sadek, *Geotech. Testing J.*, **26**, 4 (2003).
29. J. J. Liu, Y. Wang, R. Song, Y. Sun, *The Open Civil Eng. J.*, **11**, 544 (2017).

Geochemical appraisal of Stefanets Member (Etropole Formation) from the eastern part of the West Forebalkan, Bulgaria

N. Botoucharov^{1*}, M. Stefanova^{2*}, St. Marinov²

Department of Geology, Paleontology and Fossil Fuels, Faculty of Geology and Geography, Sofia University "St. Kl. Ohridski" 15, Tsar Osvoboditel Blvd., 1504 Sofia, Bulgaria

Institute of Organic Chemistry with Centre of Phytochemistry, Bulgarian Academy of Sciences, Acad. G. Bonchev Str., Bl. 9, 1113 Sofia, Bulgaria

Received December 19, 2018 Accepted December 10, 2019

The study presents a geochemical appraisal of key well core samples from Stefanets Member (Etropole Fm.), from the eastern part of the West Forebalkan, Bulgaria. Extractable organic matter, i.e. "free" and "bound" bitumens, was characterized by geochemical methods. Biomarkers were tracked, quantified and correlated. Parameters calculated on the base of *n*-alkanes, regular isoprenoids, hopanes, steranes and aromatic hydrocarbon distributions have determined organic matter as "mature" – early to late mature. The plots of the ratios Pr/*n*C₁₇ vs. Ph/*n*C₁₈ in a diagram were situated on the demarking line for Type II to mixed Type II/III kerogen. The magnitudes of Pr/Ph ratios < 1.0 have argued for reductive conditions in the depositional palaeoenvironment. There were proofs for hydrocarbons expelling and their total lack in "free" bitumen of the "late mature" sample. All calculated biomarker parameters have indicated that hopanes and steranes have attained their epimer equilibria. According to S29 $\alpha\alpha$ S/(S+R) vs. H31 $\alpha\beta$ S/(S+R) correlation one of the studied samples has been located in the "oil widow" area. Methyl phenanthrene index (MPI-3) has confirmed high samples maturity as the calculated values were in the range of 2.0-5.3.

Results have demonstrated very good agreement between Rock Eval data, biomarker assemblages and set of calculated parameters.

Keywords: West Forebalkan, Stefanets Member, biomarker assemblage, maturity

INTRODUCTION

In the process of petroleum exploration it is imperative to define the source rocks of the basins and to assess their hydrocarbon generative potentials. Therefore, methods of organic geochemistry, i.e. Rock Eval and GC/MS, are commonly applied. In previous papers [1,2] an attempt has been made to evaluate by geochemical proxies the generative potential of Middle Jurassic Stefanets Member (Etropole Fm.) from the Central South Moesian platform margin. The present study was a continuation of our attempts to characterize Stefanets Member by geochemical methods and exploring near area – the eastern part of the West Forebalkan, Forebalkan unit (Fig. 1) [3]. The size of the area is about 240 km² between Iskar River to the east and Ogosta River to the northwest. Lower and Middle Jurassic series are not completely developed everywhere in the study area, but among them predominates the terrigenous-carbonate succession. Extractable portions of initial ("free bitumen) and demineralized ("bound" bitumen) samples were under consideration. A broad range of homologue series were quantitatively interpreted, i.e. linear, branched and cyclic alkanes, as well as a set of polycyclic aromatic hydrocarbons (PAHs). The biomarker assemblages

allowed characterization of palaeoenvironmental conditions of deposition and assessment of the generative potentials of the Stefanets Member (Etropole Fm.) from the eastern part of the West Forebalkan, Bulgaria.

Materials and methods

Six wells, located in the land of villages Galatin and Golyamo Peshtene were investigated in details. Ten well-core samples from Middle Jurassic Stefanets Member (Etropole Fm.), in depths from 1956.6 to 3866.5 m, were selected and analyzed. They are representative for the shallow part of the Early-Middle Jurassic paleo basin. Two of them (St-2 and St-7) were chosen as key samples for the area of study, because of their maturity in a range of "oil window". All geochemical parameters for the samples are given in the complex Table 1. The same protocol for "free" and "bound" bitumen isolation, fractionation and characterization as in the previous study [2] was kept.

The last generation Rock Eval 6 equipment was used for the evaluation of the organic matter and hydrocarbon generative potential. The GC-MS distributions and quantitative peaks interpretations gave us ground to calculate the following biomarker parameters: (i) CPI [4], Pr/Ph [5],

* To whom all correspondence should be sent:

E-mail: botnd@gea.uni-sofia.bg maia@orgchm.bas.bg

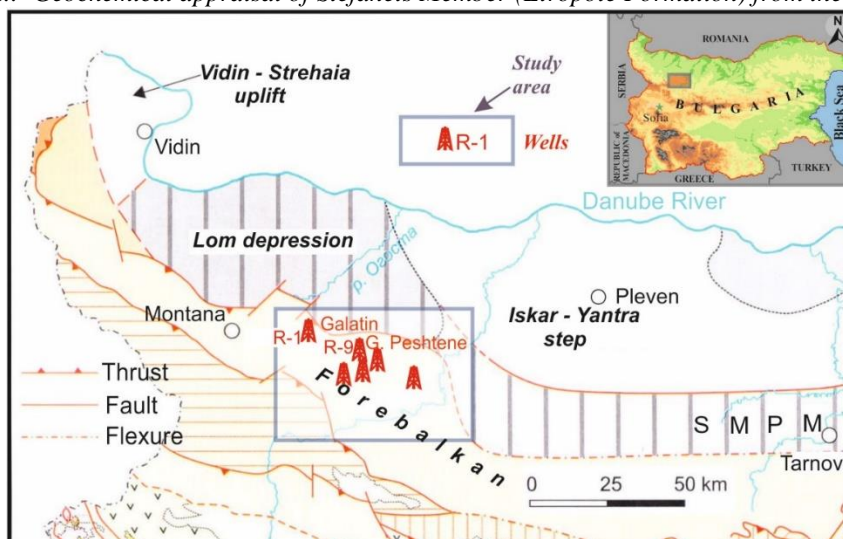


Fig. 1. Tectonic scheme of Central and North West Bulgaria with the location of the study area (after [3])

Pr/nC₁₇ vs. Ph/nC₁₈ [6] and P_{aq} [7] all for linear *n*-alkanes; (ii) biomarker ratios, i.e. hopanes, moretanes, steranes and diasteranes ratios [8] for cyclic alkanes; and (iii) methylphenanthrene index (MPI-3) [9] for aromatic hydrocarbons (PAHs).

RESULTS AND DISCUSSION

Major Rock Eval indices, yields of bitumens and their fractional compositions are shown in Table 1A. Extracted amounts were relatively low and this has reflected in high losses during fractionations. Better results were obtained only for the “free” bitumen of sample St-7, namely higher portion of oils compared to the sum of polar constituents (resins+asphaltenes) and reasonable loss of ~ 11 rel. %. The quantity of organic matter demonstrates its current condition after all transformations that have been carried out throughout the lithogenesis. TOC (wt. %) of the key samples shows fair to good hydrocarbon potential. T_{max} values characterize the maturity of the evaluated source rocks as early mature to late mature, according to the widely accepted scale [10].

Separations of *n*-alkanes are illustrated as histograms in Fig. 2. Therein are shown distributions of three samples as in “free” bitumen of sample St-2 *n*-alkanes were practically absent. Determined amounts of linear alkanes and geochemical parameters are summed in Table 1B. Herein only peculiarities will be denoted, namely absence of *n*-alkanes in St-2 “free” bitumen and a huge amount in the “bound” bitumen, 3304 µg/g TOC (Table 1B). The total lack of the shorter homologues (*n*C₁₅-*n*C₂₀) could be an indication that all low-molecular hydrocarbons have been expelled during organic matter transformation. This argument is supported by the value of S₂ lower than

2.5 mg HC/g rock and relatively high maturity of sample St-2.

n-Alkanes distributions of sample St-7 in Fig. 2 demonstrate some differences noticeable in the calculated values for ALC, TAR and P_{aq} parameter in Table 1B. In “bound” bitumens shorter members have decreased and ALC and TAR values have increased, giving a proof that attached alkanes were preferably of terrestrial origin. Regular isoprenoids were present only in sample St-7 (Table 1B). The cross plots of the ratios in a diagram Pr/nC₁₇ vs. Ph/nC₁₈ are situated on the demarking line for kerogen Type II and mixed Type II/III (Fig. 3). For comparison, the positions of the previously studied samples from the Stefanets Member (Etopole Fm.) from the Central South Moesian platform margin are indicated as well [2]. A certain similarity in the depositional environment for all samples studied is depicted, namely, deposition in reductive environment of mixed Type II/III toward Type II kerogen. The magnitudes of Pr/Ph ratios < 1.0 have also argued for reductive conditions in the depositional palaeoenvironment (Table 1B).

In their study of sedimentary input of submerged/floating fresh water aquatic macrophytes Ficken *et al.* [7] proposed the P_{aq} ratio to discriminate macrophytes and emergent terrestrial plants. It was able to distinguish macrophytes from terrestrial plants from the other supply. The following P_{aq} ranges have been proposed: 0.01-0.23 for terrestrial plant wax, whereas magnitudes in the range 0.48-0.94 were associated with submerged/floating species of macrophytes. P_{aq} values in Table 1B revealed mixed *n*-alkane supply, more precisely, from higher plant/macrophyte wax and algal or bacterial contributions.

Table 1. Complex geochemical characteristics of samples from the Stefanets Member (Etropole Fm.) from the eastern part of the West Forebalkan:

A. Rock Eval and bitumen data; B. Content of *n*-alkanes, distribution and geochemical parameters; C. Geochemical parameters based on hopanes and steranes distributions

A.

Sample	Rock Eval data							Bitumen							
	TOC	T _{max}	S ₁	S ₂	S ₃	HI	OI	Abbreviation	Yield		Fractional composition, %				
									%	mg/gTOC	Oils	Resins	Asph.	Loss	
St-2	1.235	456.5	0.03	0.23	0.31	18.5	25								
								"free"	0.02	18.4	16.1	21	32.3	30.6	
								"bound"	0.11	86.3	22.5	17.4	36	24.1	
St-7	0.71	440	0.045	0.38	0.42	53.5	59								
								"free"	0.05	68.5	65.2	14.3	9.1	11.4	
								"bound"	0.09	57.6	11.9	24.6	33.3	30.2	

B.

Sample	Bitumen	<i>n</i> -Alkanes content			Pr/Ph	Pr/ <i>n</i> C ₁₇	Ph/ <i>n</i> C ₁₈	Distribution, rel.%			CPI ⁽¹⁾	ALC ⁽²⁾	TAR ⁽³⁾	Paq ⁽⁴⁾
		[μg]	[μg/gTOC]	Total				short-	mid-	long-				
St-2														
	"free"	-	-	3304	-	-	-	-	-	-	-	-	-	
	"bound"	1255.5	3304		-	-	-	0	10.8	89.2	1.05	29.5	0.27	
St-7														
	"free"	47.4	216.5	278.6	0.89	0.23	0.27	42.9	32.1	25	1.19	22.2	0.67	0.65
	"bound"	13.6	62.1		0.76	0.39	0.33	11.3	15.3	73.4	1.26	27.5	8.14	0.23

C.

Sample	Bitumen	Hopane ratios					Sterane ratios		
		Ts/Tm	Hopane Ratio ⁽⁵⁾	Moretane Ratio ⁽⁶⁾	H31αβ S/(S+R)	H32αβ S/(S+R)	S29ααS(S+R) ⁽⁷⁾	Diasterane Ratio ⁽⁸⁾	S29 ββ/(αα+ββ) ⁽⁹⁾
St-7									
	"free"	1.29	0.63	0.16	0.56	0.57	0.52	0.61	0.37
	"bound"	1.32	0.68	0.14	0.58	0.58	n.d.	n.d.	n.d.

⁽¹⁾CPI - Carbon Preference Index; $CPI = \frac{\sum(C_{23} \div C_{31})_{odd} + \sum(C_{25} \div C_{33})_{odd}}{2\sum(C_{24} \div C_{32})_{even}}$; ⁽²⁾ALC - "average" length of carbon = $S(C_n \times n) / \sum(C_n)$; *n* - carbon number; *C_n* - relative content; ⁽³⁾TAR (Terrestrial to Aquatic Ratio) = $\frac{\sum(nC_{27} + nC_{29} + nC_{31})}{\sum(nC_{15} + nC_{17} + nC_{19})}$; ⁽⁴⁾Paq (Ratio of aquatic to terrestrial input) = $\frac{nC_{23} + nC_{25}}{nC_{23} + nC_{25} + nC_{29} + nC_{31}}$; Ts - 18α(H)22,29,30-Trisnorneohopane; Tm - 17α(H)22,29,30-Trisnorhopane; ⁽⁵⁾Hopane ratio = H29αβ/H30αβ; ⁽⁶⁾Moretane ratio = H30βα/H30αβ; ⁽⁷⁾Sterane S/(S+R) ratio = S29ααS/(S+R); ⁽⁸⁾Diasterane ratio = Dia27βαS/(S+R); ⁽⁹⁾Sterane ratio = S29 ββ/(αα+ββ)

Emergent and submerged/floating plants should have contributed to kerogen formation.

Hopanes and steranes distributions were tracked only in sample St-7. As was already mentioned above, *n*-alkanes and cyclic alkanes were practically absent in sample St-2. This peculiarity was explained by the sample late maturity and possibility of hydrocarbons expelling. In Table 1C are shown geochemical parameters for sample St-7 calculated on the base on steranes and hopanes GC-MS distributions [8]. All hopanes signatures pointed to advanced sample maturity: (i) prevalence of Ts over Tm hopane, with Ts/Tm ratio ~ 1.3; (ii) epimer ratios for hopanes 22S/22R attested that the equilibrium has been attained, i.e. homohopane index H31 α β S/(S+R) of 0.56-0.58 and almost the same magnitude for H32 α β S/(S+R) of 0.57-0.58 were determined. Hence, based on this parameter the sample St-7 was mature, as for mature samples H31 α β S/(S+R) was in the range of 0.57-0.62 [8]; (iii) there were low amounts of moretanes (moretane ratio H30 β α /H30 α β 0.14-0.16), and a total lack of "bio" hopanes.

Data for steranes distribution for sample St-7 "free" bitumen are shown in Table 1C. The signature was strongly dominated by diasteranes. Recent studies have proved that maturation has tolerated steranes rearrangement to diasteranes. Respectively, the high value for the diasterane ratio 0.61 (Table 1C) attested high St-7 maturity. Some amounts of rearranged and regular steranes at a certain extent have co-eluted and it was not advisable to be correlated in a ternary diagram. However, data for sample St-7, steranes ratios S29 α α S/(S+R) and homohopanes H31 α β S/(S+R) (Table 1) were correlated and therein sample was located in the "oil window". Both samples studied were characterized by the presence of PAHs with 3-5 aromatic rings, i.e. condensed (phenanthrene, chrysene, pyrene, etc.) or coupled (phenyl-naphthyl and binaphthyl). Naphthalene and its alkylated homologues were absent, probably lost during separation and fractionation procedures due to their high volatility. Phenanthrene was the maximizing PAH in the mixture. Its methylated homologues were well recognizable (Fig. 4).

For their application as biomarkers Radke and Welte [9] have developed the methyl phenanthrene index (MPI). It is based on the distribution of the 2-, 3-, (9+4)- and 1-methyl phenanthrenes (Fig. 4). Principally during maturation their proportions have shown a progressive change. The maturity increase has resulted in the increase in 2- and 3-methyl phenanthrenes (thermodynamically more stable isomers at higher temperatures).

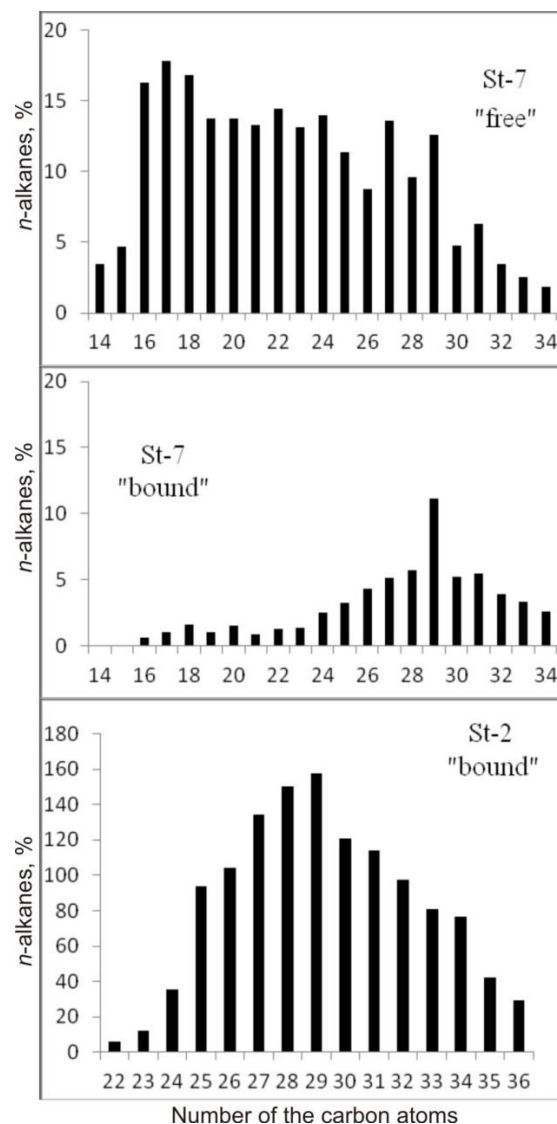


Fig. 2. Histograms of *n*-alkanes distributions

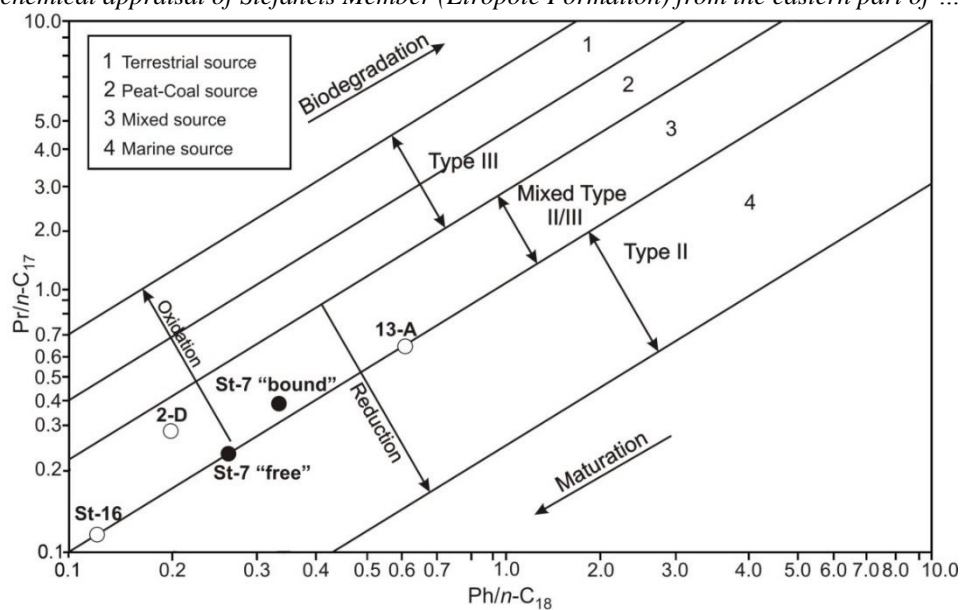


Fig. 3. Cross-plots Pr/nC_{17} vs. Ph/nC_{18} (positions of the previously studied samples [2] are also indicated in white dots)

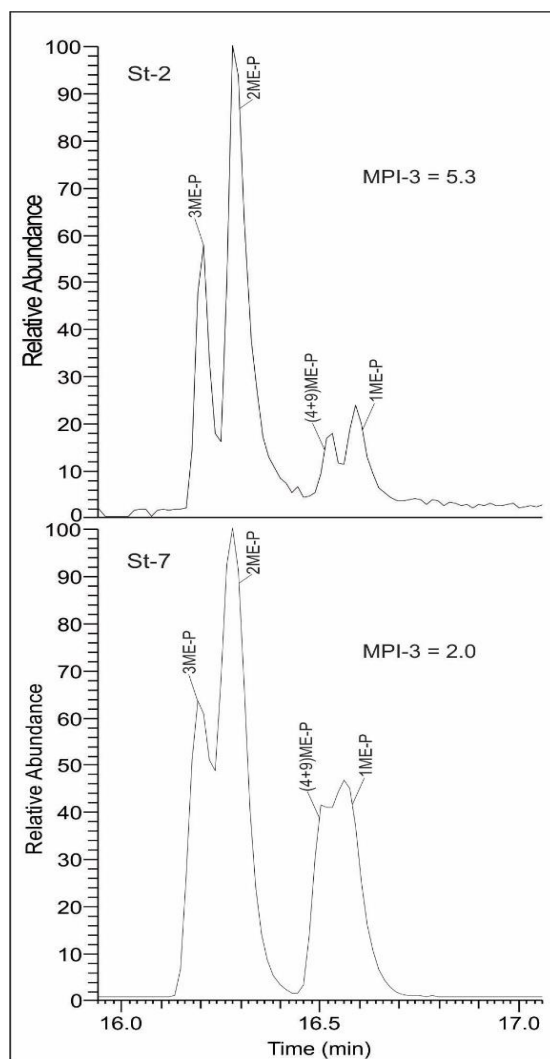


Fig. 4. Distributions of methyl phenanthrenes in samples according to SIM m/z 192 methyl phenanthrene index $MPI-3 = \frac{\Sigma (2-MeP + 3-MeP)}{\Sigma (4+9-MeP + 1MeP)}$

Respectively, higher values for MPI should be expected for the more mature samples. For the samples studied MPI-3 increases from 2.0 for St-2 to 5.3 for the “over mature” St-2. This result was in a very good agreement with the Rock Eval data as for St-2 was determined T_{\max} 456.5 °C - “late mature”.

CONCLUSIONS

Geochemical study of two core samples from Stefanets Member (Etropole Fm.) from the eastern part of the West Forebalkan, Bulgaria has revealed the following peculiarities: (i) good quantity of organic matter according TOC (wt. %); (ii) “free” bitumen was practically absent in St-2 sample, a hint for hydrocarbons migration (or expelling) during maturation; (iii) isoprenoids correlation gave ground to assume deposition in reductive palaeoenvironment of Type II to mixed Type II/III kerogen. The magnitudes of Pr/Ph ratios < 1.0 have also indicated reductive conditions in the palaeoenvironment; (iv) all biomarker parameters calculated on the base of hopanes, steranes and PAHs distributions have argued for relatively high maturity; (v) if figure the sterane S29 $\alpha\alpha$ S/(S+R) vs. homohopanes H31 $\alpha\beta$ S/(S+R) in a cross-plot diagram one of the studied samples is positioned in the “oil window” and for both samples could be assigned “fair to good” hydrocarbon generative potential.

Acknowledgement: Financial support by Sofia University “St. Kliment Ohridski”, Fund „Scientific research“, project №124/2014 is greatly acknowledged.

REFERENCES

1. N. Botoucharov, M. Stefanova, S. P. Marinov, B. Borisova, Rock Eval data of the Stefanets Member (Etropole Formation) from the Central South Moesian platform margin, Bulgaria, *C.R. Bulg. Acad. Sci.*, **68** (12), 1553 (2015).
2. N. Botoucharov, M. Stefanova, S. P. Marinov, B. Borisova, Biomarker assemblage of the Stefanets Member (Etropole Formation) from the Central South Moesian platform margin, Bulgaria, *C.R. Bulg. Acad. Sci.*, **69** (1), 57 (2016).
3. C. Dabovski, I. Zagorchev, in: Mesozoic Geology of Bulgaria, I. Zagorchev, C. Dabovski, T. Nikolov, (eds.) Acad. Press “Prof. Marin Drinov”, 2009, p. 13 (in Bulgarian).
4. E. Bray, E. Evans, Distribution of *n*-paraffines as a clue to recognition of source beds, *Geochimica et Cosmochimica Acta*, **22**, 2 (1961).
5. B. Didyk, B. R. T. Simoneit, S. Brassell, G. Eglinton, Organic geochemical indicators of paleoenvironmental conditions of sedimentation, *Nature*, **272**, 216 (1978).
6. D. Leythausen, Th. Schwarzkopf, The pristane/*n*-heptadecane ratio as an indicator for recognition of hydrocarbon migration effects, *Organic Geochemistry*, **10**, 191 (1986).
7. K. Ficken, B. Li, D. Swain, G. Eglinton, An *n*-alkane proxy for the sedimentary input of submerged/floating freshwater aquatic macrophytes, *Organic Geochemistry*, **31**, 745 (2000).
8. K. Peters, C. Walters, J. Moldowan, The Biomarker Guide, Second Edition, Vol. II, Biomarkers and Isotopes in Petroleum Systems and Earth History, UK, Cambridge University Press, 2005, p. 684.
9. M. Radke, D. H. Welte, Methylphenanthrene index (MPI): A maturity parameter based on aromatic hydrocarbons, in: Advances in Organic Geochemistry, M. Bjoroy (ed.), Wiley, Chichester, 1983, p. 504.
10. K. E. Peters, Guidelines for evaluating petroleum source rock using programmed pyrolysis, *AAPG Bulletin*, **70** (3), 318 (1986).

Synthesis, characterization, kinetic and thermodynamic evaluation from TG-DTA analysis of new nickel(II) mixed ligand complexes of bidentate salicylaldimine Schiff bases and 1,10-phenanthroline

S. Hamza Abbas*, H. Hamza Abbas, H. Kadhim Musa

Department of Chemistry, College of Science, University of Basrah, Basrah, 61004, Iraq

Received; Revised

New mixed-ligand complexes of nickel(II) ion with bidentate salicylaldimine ligands $\{[(2\text{-carboxyphenyl)imino}]\text{methyl}\}$ phenol; (L^1), $\{[(2\text{-hydroxyphenyl)imino}]\text{methyl}\}$ phenol (L^2), $\{[(2\text{-chlorophenyl)imino}]\text{methyl}\}$ phenol; (L^3) and $\{[(3\text{-methyl-2-chlorophenyl)imino}]\text{methyl}\}$ phenol; (L^4) with 1,10-phenanthroline; (L^5) were prepared by reacting NiCl_2 at an appropriate mole ratio of these ligands. The complexes were characterized by FT-IR, UV-Visible, ^1H NMR spectra, conductivity measurements and thermal analysis. The spectral data indicated that the salicylaldimine ligand is a monobasic bidentate ligand coordinated through NO donor atoms and 1,10-phenanthroline is a neutral bidentate ligand coordinated through NN donor atoms to the nickel(II) ion. The prepared complexes seem to have octahedral geometry of the general formula $[\text{NiL}^x(\text{L}^5)_2]\text{Cl}$ ($x=1-4$). The thermal behavior of the prepared compounds was studied using thermogravimetric (TG/DTA) analysis in static air. The obtained results show a continuous weight loss without any hydrated or coordinated water molecule losses, and the ligand molecules immediately decompose in consecutive steps.

Keywords: Schiff bases, Bidentate salicylaldimine ligand, Neutral bidentate ligand, Nickel(II) mixed ligand complex, Octahedral geometry complex, Thermogravimetric analysis.

INTRODUCTION

The complexes of mixed ligands have been widely investigated in solution and solid state [1]. Schiff bases and their metal complexes demonstrate a range of applications varying from catalysis to pharmaceuticals [2, 3]. The ternary transition metal complexes including an aromatic Schiff base and 1,10-phenanthroline have been extensively studied [4]; they are more stable compared with binary complexes so the steric effect and back donation have to be considered in defining the structure of the mixed ligand complexes [1]. Many studies have been done on the physico-chemical properties of various symmetrical Schiff bases and their transition metal complexes [5, 6], while few were done for the complexes of asymmetric Schiff bases and chelates with 1,10-phenanthroline, pyridine, and 2,2'-bipyridine ligands. The coordination of transition metals to different Schiff bases gives a series of novel complexes possessing a broad spectrum of bioinorganic applications and thermal stability [7], therefore a lot of mixed-ligand complexes including Schiff bases with heterocyclic bases have been reported due to their ability to enhance the biological activity and decrease the cytotoxicity of both the ligand and the metal ion on the host body [8, 9].

In this work, we report the synthesis, characterization and comparison of the thermal

decomposition behavior of the mixed ligand complexes of Ni(II) ion with salicylaldimine and 1,10-phenanthroline as bidentate ligands. The activation energy E_a and the thermodynamic parameters ΔS^* , ΔH^* and ΔG^* of the activated complexes were calculated by using the differential Freeman-Carroll equation. The molar conductivities show that the prepared complexes display electrolytic behavior due to the presence of one chloride ion outside of the coordination sphere [10].

EXPERIMENTAL

Materials

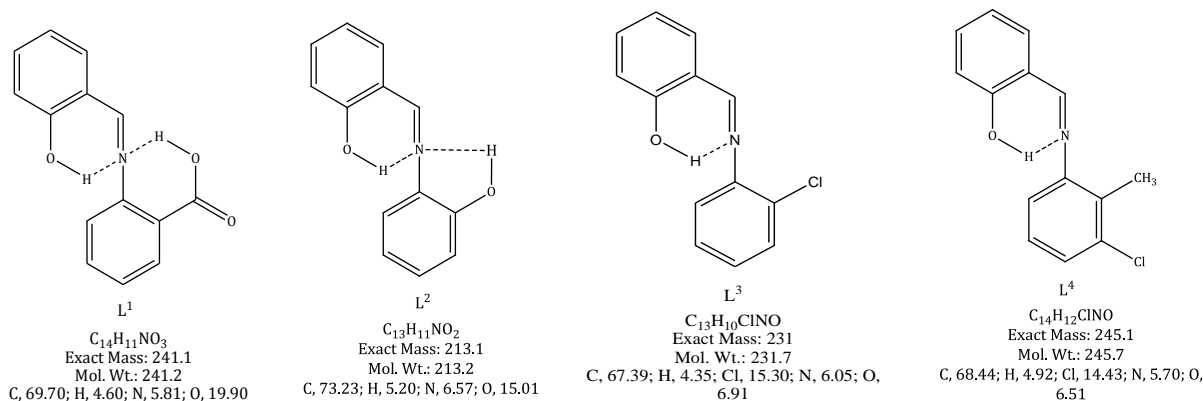
The starting materials were purchased from Fluka Chemicals Company and were used without further purification.

Synthesis of Schiff base ligands

The Schiff bases were prepared according to [11], by mixing 1.1 g, 1 mol of salicylaldehyde in 10 ml of ethanol with an equimolar quantity of substituted aniline, magnetically stirred with adding 2-3 drops of concentrated sulfuric acid, refluxed for 2 h and let overnight at room temperature. The obtained product was collected, recrystallized from hot ethanol, washed with ether and dried under vacuum at room temperature, Scheme 1.

* To whom all correspondence should be sent:

E-mail: salihhabbas@yahoo.ca



Scheme 1. The chemical structures of the ligands

Synthesis of complexes

The nickel(II) complexes were prepared as described in [11], by mixing an ethanolic solution of appropriate molar quantity of a Schiff base ligand (L^x ; $x=1-4$), 10 mmol with an ethanolic solution of Ni(II) chloride 10 mmol and refluxed for 3 h. To the mixture, an ethanolic solution of 1,10-phenanthroline 20 mmol was added and refluxed for an additional 1 h. The obtained product was collected, washed with ethanol, ether and dried under vacuum at room temperature.

Thermal study

TG/DTG of the four Schiff base ligands (L^x ; $x=1-4$) and their nickel(II) mixed ligand complexes with 1,10-phenanthroline were carried out to evaluate the thermal stability and characteristic parameters from the analysis of their thermograms.

RESULTS AND DISCUSSION

Infrared spectroscopy

Table 1. FT-IR spectral data (cm^{-1}) of the prepared compounds.

Compound	Ar-CH	CH=N	C-O	C=C
L^1	3070	1631	1246	1564
$[NiL^1(L^5)_2]Cl$	3076	1593	1240	1545
L^2	3047	1631	1274	1529
$[NiL^2(L^5)_2]Cl$	3059	1608	1290	1531
L^3	3066	1612	1276	1571
$[NiL^3(L^5)_2]Cl$	3055	1606	1295	1529
L^4	3075	1612	1276	1566
$[NiL^4(L^5)_2]Cl$	3050	1606	1327	1531

The FT-IR spectra of the prepared Schiff base ligands and their nickel(II) mixed ligand complexes

showed sharp and characteristic bands, as summarized in Table 1.

All Schiff base ligands (L^x ; $x=1-4$) show a medium intensity band at 1246, 1274, 1276 and 1276 cm^{-1} , respectively, due to $\nu(C-O)$ stretching frequency, which was shifted to higher frequency at 1260, 1290, 1295 and 1327 cm^{-1} , respectively, in the spectra of the complexes, indicating the coordination partnership of the oxygen atom [11, 12]. The high-intensity bands at 1620, 1631, 1612 and 1614 cm^{-1} , respectively, due to the azomethine group, were shifted to a lower frequency in the spectra of the complexes at 1593, 1612, 1604 and 1606 cm^{-1} , respectively, indicating the coordination of azomethine nitrogen atom to the central metal [14]. In addition, the $\nu(C-N)$ bending band of the 1,10-phenanthroline ligand that appeared at 1158 cm^{-1} was shifted to 1149-1153 cm^{-1} in the spectra of the complexes, indicating the coordination of the pyridine nitrogen atoms of 1,10-phenanthroline ligand to the central metal too [7]. Moreover, the spectra of the complexes showed new bands at 215-255 cm^{-1} due to $\nu(M-N)$ of 1,10-phenanthroline; L^5 and new bands at 420-432 cm^{-1} due to $\nu(M-N)$ and at 467-470 cm^{-1} due to $\nu(M-O)$ vibrations of the Schiff base ligands [15], these bands are out of the scale of the used instrument. So, it is easy to summarize that the salicylaldehyde Schiff base ligands are mononegative bidentate ligands and were coordinated to the nickel(II) ion *via* the phenolic oxygen atom and azomethine nitrogen atom, whilst the 1,10-phenanthroline ligand is a neutral bidentate ligand and was coordinated to the nickel(II) ion *via* its two pyridine nitrogen atoms, see Figs. 1, 2.

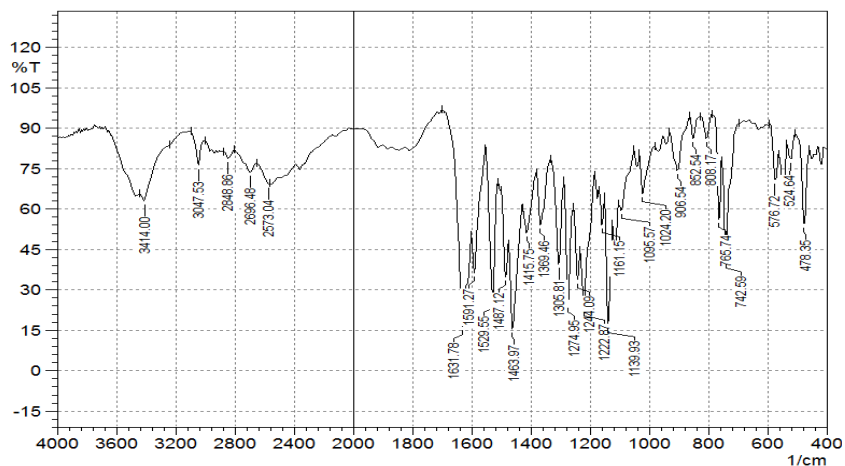


Figure 1. FT-IR of the ligand L².

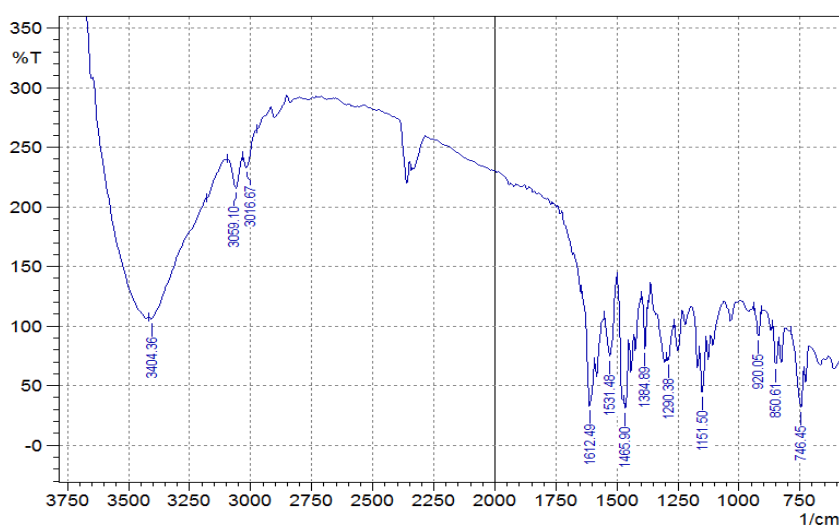


Figure 2. FT-IR of [NiL²(L⁵)₂]Cl complex.

Electronic spectra

The absorption band assignments of the Schiff base ligands (L^x; x=1-4) and of the nickel(II) mixed ligand complexes were clarified in three essential bands in the UV. region, see Figs. 3, 4.

The π - π^* transition of the imine group for the Schiff base ligands appears in the range of 225-272 nm. The π - π^* transition of the aromatic system for the ligands appears in the range of 255-325 nm and the n - π^* transition appears in the range of 335-420 nm, which were significantly affected by chelating [16]. The shifting of the n - π^* transition upon complexation may be attributed to charge transfer from the nitrogen or oxygen atoms of the ligands to the nickel(II) ion [17]. The electronic spectra of the present nickel(II) mixed ligand complexes showed three bands at 268-272 nm, 340-346 nm, and 420-446 nm, respectively, according to the three allowed transitions of the octahedral d^8 system in the 3F ground state [11], Scheme 2.

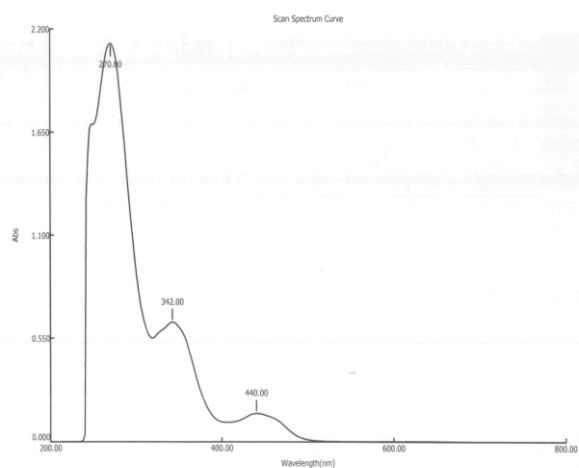


Figure 3. The UV spectrum of [NiL³(L⁵)₂]Cl.

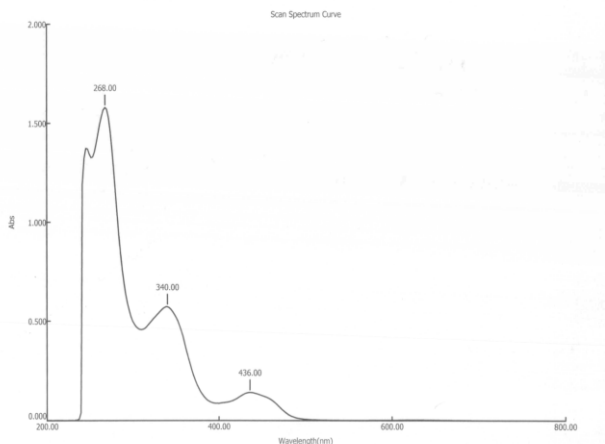
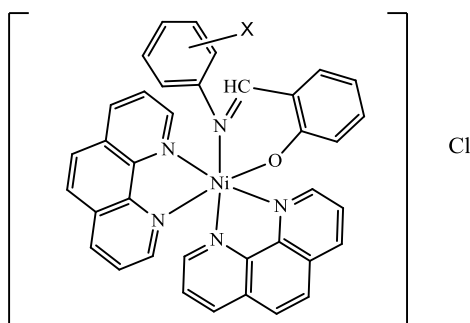


Figure 4. The UV. spectrum $[\text{NiL}^4(\text{L}^5)_2]\text{Cl}$ complexes.



X=L¹: 2-COOH, L²: 2-OH, L³: 2-Cl, L⁴: 2-CH₃-3-Cl

Scheme 2. The suggested octahedral structure of the prepared nickel(II) complexes, $[\text{NiL}^x(\text{L}^5)_2]\text{Cl}$, (x=1-4).

¹H NMR spectroscopy provides more information beside the identification groups in the structure of Schiff base ligands and nickel(II) mixed ligand complexes, showing an expected protons ratio, which is in agreement with previous work [6, 18]. The ¹H NMR spectra of Schiff base ligands (L^x; x=1-4) in DMSO-d⁶ (Fig. 5) display a distinctive signal at 8.96-10.25 ppm attributed to azomethine protons, which shifted downfield for the nickel(II) complexes, confirming the coordination of metal ion to the azomethine [14].

The phenolic protons always have a high chemical shift value δ , which confirms the intramolecular hydrogen bonding with the adjacent nitrogen atom [19]. The signals observed at 10.70-13.77 ppm are due to the phenolic -OH of the ligands. The multiple signals assigned to the aromatic protons of both rings were not affected by complexation. The number of peaks and the proton resonance of the Schiff base ligands completely differ upon complexation. The absence of proton signals of phenolic -OH and the downfield shift of the resonance of azomethine proton confirm the metal coordination with a phenolic oxygen atom and azomethine nitrogen atom of the Schiff base ligands [20].

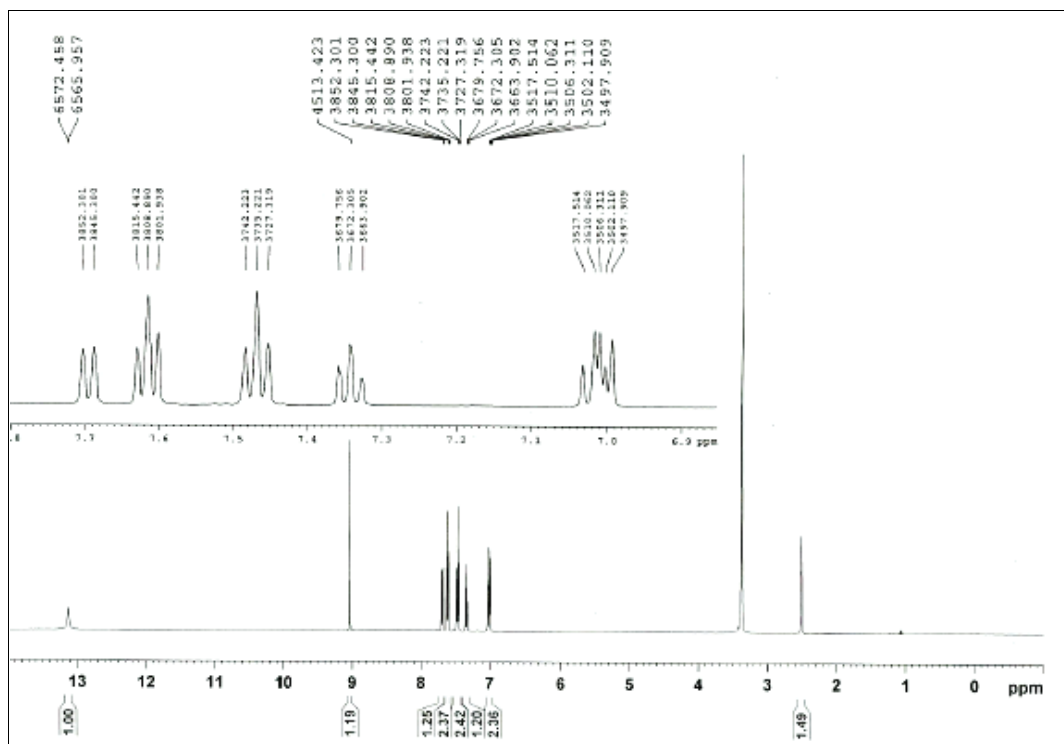


Figure 5. ¹H NMR spectra of the L³ ligand.

Thermal analysis

TG and DTA were used in this work as thermoanalytical methods to investigate the thermal stability, kinetic and thermodynamic characteristic parameters, see Figs. 6-14.

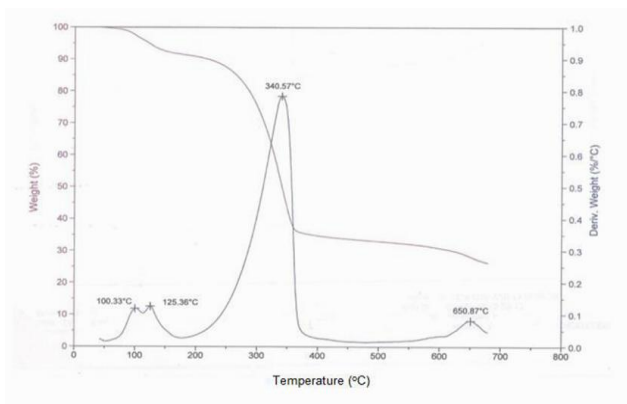


Figure 6. TG and DTA of L^5 .

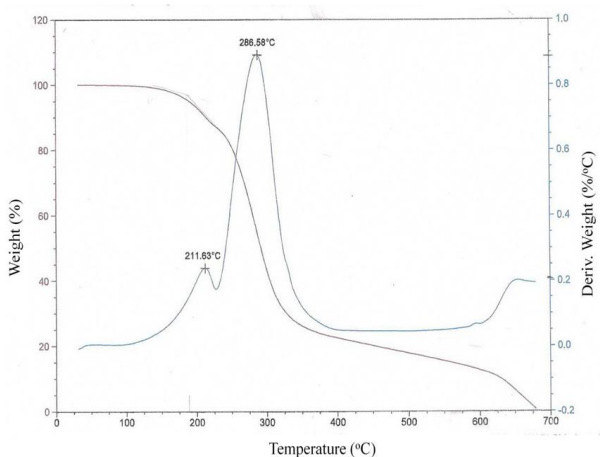


Figure 7. TG and DTA of L^1 .

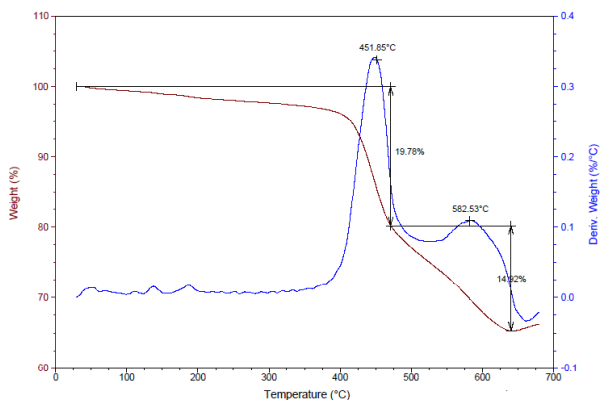


Figure 8. TG and DTA of $[NiL^1(L^5)_2]Cl$ complex.

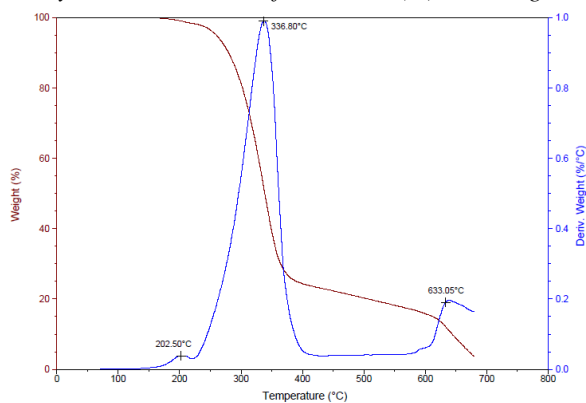


Figure 9. TG and DTA of L^2 .

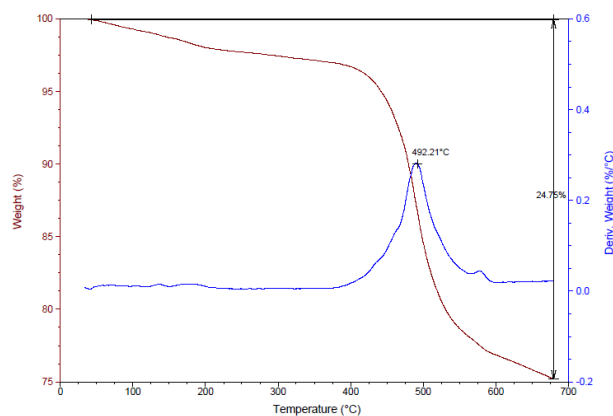


Figure 10. TG and DTA of $[NiL^2(L^5)_2]Cl$ complex.

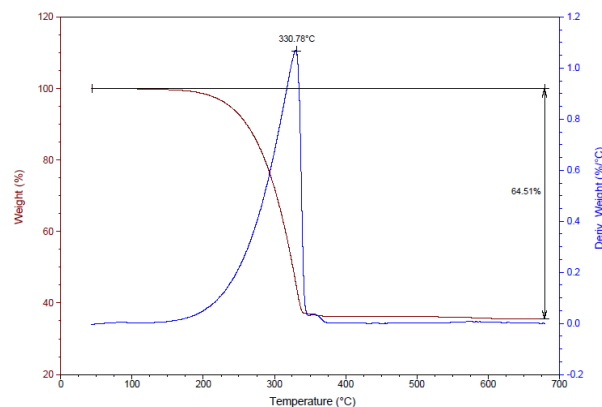


Figure 11. TG and DTA of L^3 .

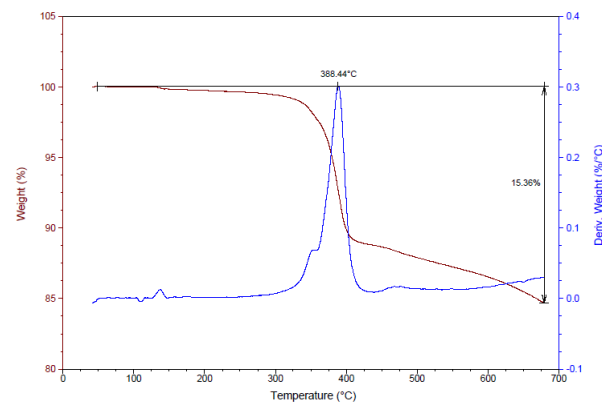


Figure 12. TG and DTA of $[NiL^3(L^5)_2]Cl$ complex.

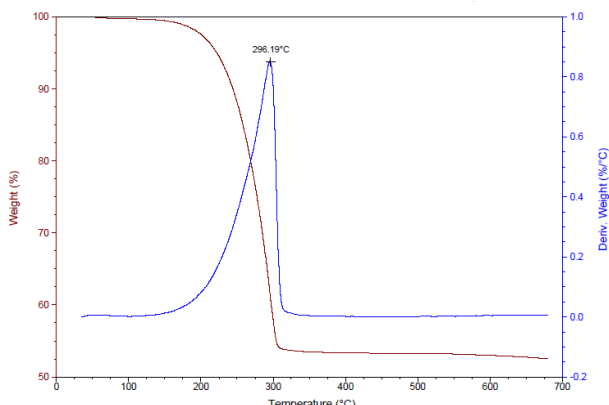


Figure 13. TG and DTA of L^4 .

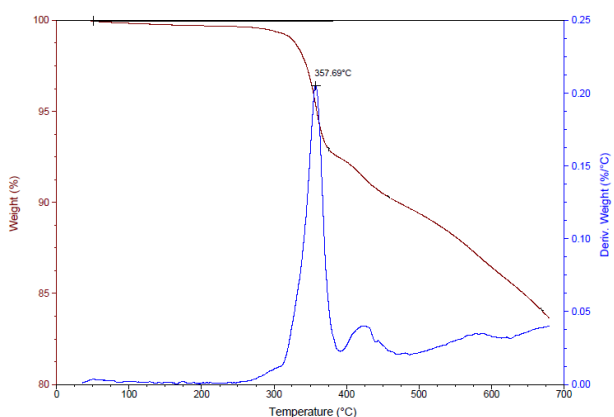


Figure 14. TG and DTA of $[NiL^4(L^5)_2]Cl$ complex.

The TG curves were mathematically analyzed by the differential Freeman-Carroll equation [21]. The kinetic parameters like activation energy; E_a for the dehydration and decomposition of 1,10-phenanthroline, Schiff base ligands and their nickel(II) complexes were calculated from the Arrhenius plot of the rate of decomposition; $\ln k$ versus $1/T_s$, E_a was calculated from the slope and the frequency factor; Z was defined from the obtained intercept. The thermodynamic parameters of the activated complexes are often calculated using the following equations:

$$\Delta S^* = 2.303 \log \left[\frac{Z h}{k_B T_s} \right] R$$

$$\Delta H^* = E_a - RT_s$$

$$\Delta G^* = \Delta H^* - T_s \Delta S^*$$

The peak temperature T_s is used in these calculations so that the values of ΔS^* , ΔH^* and ΔG^* are related to the highest rate of the process, as summarised in Table 2.

The negative values of ΔS^* indicate that the decomposition reactions proceed spontaneously and the low values of Z indicate that they were slow reactions in their nature [22]. According to the TG analysis, both the stability and decomposition temperature of the complexes were higher than those of the ligands. Usually, on pyrolysis the Schiff base complexes suffer volatilization leaving

a modest residue or decomposition to metal oxide [23].

The thermal decomposition process of the $[NiL^x(L^5)_2]Cl$ complexes involves two, one, one and three distinguished decomposition steps, respectively. The thermograms of these complexes point to their thermal stability up to 376, 426, 326 and 313 °C, respectively, indicating no moisture and solvent residue in these complexes. This fact was confirmed by the absence of the endothermic peak in 150-200 °C region of the DTA curves [24]. The sharp step due to the ligands decomposition takes place in the temperature range of 526-656, 426-559, 326-420 and 313-390 °C, respectively. Horizontal thermal curves were observed at 700-1000 °C. The percent weight of the residue corresponds to NiO as end product [25], Table 3. The relative thermal stability of the complexes is $3 < 4 < 1 < 2$ according to the decomposition temperature, while the E_a and Z values for the complexes are $1 < 2 < 3 < 4$ according to the crucial kinetic standards, which mostly differ from those defined by the thermal stability. The results of the thermal studies revealed that the complexes were more stable than the ligands through the thermal decomposition temperature by employing the formation of M-N and M-O coordination bond between the ligand and Ni(II) ion.

CONCLUSION

We have described the synthesis, spectroscopic and thermal properties of new nickel(II) mixed ligand complexes. The chemical structures were suggested based on FT-IR, UV-Visible, 1H NMR spectra, conductivity measurements and thermal analysis. The octahedral geometry of the general formula $[NiL^x(L^5)_2]Cl$ ($x=1-4$) was confirmed. The thermal properties of the prepared complexes were determined by thermogravimetric (TG/ DTA) analysis in static air and different thermodynamic parameters were obtained by using Freeman-Carroll equation.

Acknowledgements: We are grateful to Prof. Dr. Salah Alluaabi for help in thermal studies.

S. H. Abbas et al.: Synthesis, characterization, kinetic and thermodynamic evaluation of new nickel(II) mixed ligand...
Table 2. Thermal stability and thermodynamic parameters of ligands (L^x , $x=1-4$, L^5) and nickel complexes $[NiL^x(L^5)_2]Cl$.

Compound symbol	w_0 (mg)	T_s (k)	Temp. of 50% wt loss $^{\circ}C$	Rate of decomp. (%/min)	Chare cont. 625 $^{\circ}C$ (%)	Act. energy (E_a) (KJ/mol)	Temp. range ($^{\circ}C$)	Z	ΔH^* KJ/mol	ΔS^* KJ/mol	ΔG^* KJ/mol
L^1	20.3490	559.58	295	27.6	10.4	38.29	89-220	0.001	33.64	-305.75	171.13
$[NiL^1(L^5)_2]Cl$	22.7160	724.85	----	13.33	66	32.64	150-404	0.007	26.61	-312.138	226.2
L^2	39.365	609.80	337.04	29.62	14.19	62.88	180-263	0.015	57.76	-285.35	174.07
$[NiL^2(L^5)_2]Cl$	18.2870	765.21	----	7.6	76.33	38.29	203-433	0.038	31.9	-279.97	214.27
L^3	28.970	603.78	323.31	29.44	36.01	109.69	199-246	0.005	104.67	-294.87	178.17
$[NiL^3(L^5)_2]Cl$	16.1280	661.44	-----	7.56	85.99	100.33	246-344	0.023	94.83	-282.92	187.23
L^4	23.1980	589.19	-----	20.62	53.33	114.88	168-210	0.015	110.15	-285.31	76.917
$[NiL^4(L^5)_2]Cl$	20.2290	630.69	----	2.18	85.67	182.1	283-333	0.084	176.85	-271.75	171.57
L^5	24.1520	613.57	342.3	27.47	30.67	83.77	154-263	0.891	78.67	-271.04	166.39

Table 3. Thermoanalytical results TG and DTA of Ni(II) mixed ligand complexes.

Complex	Mwt	Initial wt w_0 (mg)	TG range ($^{\circ}C$)	Temp. of decomp. ($^{\circ}C$)	Mass loss estimation (calc.)%	Total mass loss estim. (calc.)%	Assignment	Residue (1000 $^{\circ}C$)
$[NiL^1(L^5)_2]Cl$ $C_{38}H_{26}ClN_5NiO_3$	694.8	22.716	376-526 526-656	451.81 582.51	19.78 (19.79) 14.92 (14.53)	34.70 (34.32)	$C_4H_8NO_2Cl$ and $C_{2.5}H_{11}N_4$	NiO+31.5C
$[NiL^2(L^5)_2]Cl$ $C_{37}H_{26}ClN_5NiO_2$	666.8	18.287	426-566	492.21	24.75 (25.71)	24.75 (24.71)	$C_2H_2ClN_5O$	NiO+35.5C
$[NiL^3(L^5)_2]Cl$ $C_{37}H_{25}Cl_2N_5NiO$	685.2	16.128	326-420	388.4	24.30 (24.22)	24.30 (24.22)	$H_{25}Cl_2N_5$	NiO+37C
$[NiL^4(L^5)_2]Cl$ $C_{38}H_{27}Cl_2N_5NiO$	699.3	20.229	313.5-390 390-476 476-630	357.69 425 583.25	10.45 (10.43) 5.06 (5.00) 8.60 (8.58)	24.11 (24.01)	$H_{27}Cl_2N_2$	NiO+38C

REFERENCES

1. D. Banerjee, Mixed-ligand complexes in coordination chemistry, New Delhi, Tata McGraw-Hill Publishing company Limited, 1993.
2. V. P. Daniel, B. *Spectrochim. Acta Part A*, **70**(2), 403 (2008).
3. N. G. Kandile, M. I. Mohamed, H. M. Ismaeel, *J. Enzyme Inhib. Med. Chem.*, **32**(1), 119 (2017).
4. M. A. Diab, A. Z. El-Sonbati, A. A. El-Bindary, S. M. Morgan, M. K. Abd El-Kader, *J. Mol. Liq.*, **218**, 571 (2016).
5. J. C. Lee, Y. K. Jeong, J. M. Kim, J. G. Kang, *Spectrochim. Acta Part A*, **124**, 256 (2014).
6. G. G. Mohamed, M. M. Omar, A. A. Ibrahim, *Eur. J. Med. Chem.*, **44**(12), 4801 (2009).
7. H. F. A. El-Halim, G. G. Mohamed, E. A. M. Khalil, *J. Mol. Struct.*, **1146**, Suppl. C, 153 (2017).
8. G. B. Bagihalli, P. G. Avaji, S. A. Patil, P. S. Badami, *Eur. J. Med. Chem.*, **43**(12), 2639 (2008).
9. A. K. Patra, M. Nethaji, A. R. Chakravarty, *J. Inorg. Biochem.*, **101**(2), 233 (2007).
10. W. J. Geary, *Coord. Chem. Rev.*, **7**(1), 81 (1971).
11. Y. Prashanthi, K. Kiranmai, I S. Kumar, V. K. Chityala, Shivaraj, *Bioinorg. Chem. Appl.*, 948534, 1 (2012).
12. K. Nakamoto, Infrared and Raman spectra of Inorganic and Coordination Compounds, 5th edn. New York, John Wiley and Sons, 1998.
13. H. F. Abd El-halim, M. M. Omar, G. G. Mohamed, *Spectrochim. Acta Part A*, **78**(1), 36 (2011).
14. P. P. Utthra, G. Kumaravel, N. Raman, *J. Mol. Struct.*, **1150**, 374 (2017).
15. G. G. Mohamed, M. M. Omar, A. M. M. Hindy, *Spectrochim. Acta Part A*, **62**(4), 1140 (2005).
16. S. Samal, R. R. Das, R. K. Dey, S. Acharya, *J. Appl. Polym. Sci.*, **77**(5), 967 (2000).
17. S. Samal, N. K. Mohapatra, S. Acharya, R. K. Dey, *React. Funct. Polym.*, **42**(1), 37 (1999).
18. W. H. Mahmoud, G. G. Mohamed, M. M. I. El-Dessouky, *J. Mol. Struct.*, **1082**, 12 (2015).
19. S. M. Lee, H. M. Ali, K. S. Sim, S. N. Abdul Malek, K. M. Lo, *Inorganica Chim. Acta*, **406**, 272 (2013).
20. R. Narain, *Res. J. Chem. Sci.*, **2**(4), 231 (2012).
21. L. Vlaev, N. Nedelchev, K. Gyurova, M. Zagorcheva, *J. Anal. Appl. Pyrolysis*, **81**(2), 253 (2008).
22. R. L. Blaine, H. E. Kissinger, *Thermochim. Acta*, **540**, 1 (2012).
23. M. Ikram, S. Rehman, Faridoon, R. J. Baker, H. U. Rehman, A. Khan, M. I. Choudhary, S. U. Rehman, *Thermochim. Acta*, **555**, 72 (2013).
24. S. Ilhan, H. Baykara, A. Oztomsuk, V. Okumus, A. Levent, M. Salih Seyitoglu, S. Ozdemir, *Spectrochim. Acta Part A*, **118**, 632 (2014).
25. M. H. Soliman, G. G. Mohamed, *Spectrochim. Acta Part A*, **91**, 11 (2012).

Flame atomic absorption determination of serum copper and zinc in disordered bone metabolism

R. Tomova^{1,2*}, S. Asenova¹, B. Atanasova³, K. Tzoneva⁴, M. Slavova^{5,6}

¹ Faculty of Pharmacy, Medical University of Pleven, Pleven, Bulgaria

² Faculty of Natural Sciences, Shumen University "Konstantin Preslavski", Shumen, Bulgaria

³ Faculty of Medicine, Medical University of Sofia, Sofia, Bulgaria

⁴ Department of Rheumatology, MBAL "Sveti Pantaleimon", Pleven, Bulgaria

⁵ Institute of Electrochemistry and Energy Sources, Bulgarian Academy of Science, Sofia, Bulgaria

⁶ Department of Machine Elements and Chemistry, Faculty of Transport Management, "Todor Kableshkov" University of Transport, Sofia, Bulgaria

Received March 11, 2019; Accepted August 20, 2019

This study presents the results from the atomic absorption analysis of the concentration of certain bone density-influencing microelements Zn and Cu in menopausal women with proven osteopenia or osteoporosis, and in a control group of menopausal women with normal bone density. In our preliminary measurements of copper and zinc levels we found no significant differences between patients with osteopenia and osteoporosis. That is why, we formed a new group of all patients with disturbances of the bone metabolism. We included the ratio copper/zinc as a new parameter. Serum samples were provided according to the requirements for quality assurance in pre-analytical phase of clinical laboratory testing. Serum Cu and Zn concentrations were measured by flame atomic absorption spectrometry (FAAS). Data about serum Cu and Zn and the ratio Cu/Zn in disordered bone metabolism were expressed as mean values \pm SD. Evaluation was done by analysis of variance with non-paired t-test between different groups with $P < 0.05$ for statistical significance. These preliminary observations only imply for slight tendency of increase in serum Cu in disordered bone metabolism. The tendency seems like more pronounced for osteoporosis than osteopenia. Serum Zn does not differ significantly. Intriguingly, the Cu/Zn ratio follows the same statistical model as serum Cu. This study is encouraging with a potential for serum Cu and Zn and the ratio Cu/Zn to serve as useful biomarkers in laboratory diagnosis and treatment monitoring of disordered bone metabolism, especially in more severe forms of osteoporosis. In any case, more detailed research with bigger numbers of individuals in the tested groups is necessary to provide convincing evidence in this direction.

Keywords: Atomic Absorption Analysis, Cu Serum Levels, Zn Serum Levels, Bone Density

INTRODUCTION

Osteoporosis is a topmost socio-economic disease with severe psychological and economic consequences not only for the affected individuals, but also for their families and society as a whole. In the European Union, annual expenditures for osteoporotic fractures aggregate 37 billion euro [1]. The loss of bone mass is more commonly observed in women. Typically, the onset is at the age of 40, with the beginning of menopause. To date, there are a number of known risk factors for the development of osteoporosis. Its pathogenesis is well-studied, and there are a number of medications available for its pathogenetic treatment [2].

This is not the case with the serum levels of certain microelements. In recent years, a number of researcher teams have directed their research towards studying these links.

The mechanism for achieving a better bone metabolism and for improving physical

impairments is yet unclear. Trace minerals such as Cu and Zn are important precursors for the biological process of bone health [3].

The serum levels of Cu, Zn and Ca were studied in postmenopausal women with osteoporosis ($n = 23$) and with osteopenia ($n = 28$). Considerably lower levels of Zn ($P = 0.001$) and Cu ($P = 0.05$) were detected. No statistically significant differences in serum levels were detected among osteoporotic patients [4].

Another trial included 50 participants (men and women with mean age 47.5 ± 5 years) with severe dental wear. Enamel biopsies showed reduced copper contents, which the authors associated with reduced mineral density of the spine. Copper deficit was seen as a potential factor for bone demineralization and dental wear [5].

Conflicting results were obtained from the measuring of serum levels of zinc and copper in 135 Iranian women. The mean levels of copper and zinc were 1.168 ± 0.115 and 1.097 ± 0.091 $\mu\text{g/mL}$ in the control group ($n = 51$, T-score ≥ -1); $1.237 \pm$

* To whom all correspondence should be sent:

E-mail: rtomova@mail.bg

0.182 and 1.127 ± 0.176 $\mu\text{g/mL}$ in patients with $1 > T\text{-score} > -1.7$; 1.463 ± 0.174 and 1.327 ± 0.147 $\mu\text{g/mL}$ in patients with $T\text{-score} < -1.7$. In this trial, higher serum levels of zinc and copper were measured in patients with reduced bone density than in the control group participants, even though the differences were insignificant [6].

The ratios between the levels of biogenic elements which are of metabolic importance are not yet fully understood. There are trials indicating a negative effect of high intakes of calcium and phosphorus (even from milk) on zinc absorption which has been demonstrated in adults and premature infants, as well as in animal models of human nutrition. The potential mechanisms by which calcium interferes with zinc absorption include competition for a divalent cation channel across the brush border membrane or calcium-stimulated excess loss of endogenous zinc. This type of interaction can be achieved in calcium to zinc ratio of 20:1 (in weight) to $\geq 50:1$. The serum level of zinc is an important factor for bone health, as 29% of the zinc in the body is part of the bone mineral and is a cofactor for a number of enzymes that participate in bone metabolism and collagen degradation [7].

In a one-year continuous measuring of serum zinc, magnesium, iron, and copper in 21 patients with primary osteoporosis treated with the anti-resorption drug denosumab it was found that denosumab can improve the metabolism of Zn. The serum level of Cu did not change until the 8th month of the trial, but it decreased in the 10th and 12th months [8]. Hence, during continuous treatment with medications affecting bone resorption, it is not enough to do a single measurement of the serum microelements, but it is necessary to follow the inter-mineral interactions and to establish the long-term effects of the medication.

The optimal serum level of Zn is $12 \div 2.4$ $\mu\text{mol/L}$ and the optimal serum level of Cu in women is $13.2 \div 24.3$ $\mu\text{mol/L}$ [9]. In order to prevent impairments in bone metabolism, the provision of the necessary Cu and Zn *via* supplements or *via* a nutritionist-prepared diet should be considered. The recommended daily intake for women is 0.90 mg Cu and 8 mg Zn. [10].

A number of trials are directed towards researching correlational micronutrient dependences. According to some authors, after continuous intake of zinc (50 mg/day or more), a copper deficit was found. The higher intake of zinc increases the synthesis of intestinal cell proteins known as metallothioneins. They bind the metals and disallow their absorption by the intestinal cells.

Metallothioneins have a higher affinity to copper than for zinc, hence higher levels of metallothioneins obtained due to an increase in zinc levels cause a decrease in copper absorption. On the other hand, higher doses of copper have not been found to affect the food status of zinc. No effect of copper supplements in humans has been established. The link between the serum levels of copper, zinc, iron, and oil-soluble vitamins A and E has also been studied. The increased intake of vitamin C also lowers the level of copper in the body. It has been found that the serum levels of zinc are strongly dependent on serum copper and iron [11].

Copper and zinc are essential microelements that play an important role in the human body as cofactors in a number of enzyme systems in the brain, muscles, bones, kidneys and liver. Copper participates in the synthesis of collagen and elastin. Cuproenzymes in the body act as antioxidants and prevent damage to the cells from free radicals. The daily intake of zinc is essential, as the body does not possess a system for its storage. There are data for low serum level of copper due to a high fructose diet [12]. Zinc is necessary for the catalyst activity of nearly 100 enzymes and for maintaining the immune system, protein syntheses, DNA-syntheses, and cell division. Zinc is responsible for the maintenance of taste and smell. Vegetarians typically have significantly lower doses of zinc intake. The zinc found in plant foods is in lower concentrations and is harder to assimilate. Zinc insufficiency presents itself with weakened immunity [10]. In some studies is reported that a lower zinc intake and lower serum concentrations of zinc are associated with disturbances of the metabolism [13]. There are publications in which a relation between serum levels of copper and zinc and the age at adults is reported [14, 15].

The important role of the microelements Cu and Zn and the non-equivocal trial results motivated us to conduct our own research, with the participation of patients from the region of Pleven.

MATERIALS AND METHODS

Study design

Included in the trial were 50 female patients settled into menopause (confirmed < 5 years ago), aged between 52 and 77 years (mean 59 years). In order to exclude the effect from any correlating risk factors such as tobacco smoking, coffee intake, motor activity, dieting, decreased levels of serum calcium and vitamin D, 24 out of these patients were specifically selected due to having this specific risk profile. Based on the T-score of

measuring their bone density via the method of Dual X-ray Absorption (DEXA), the patients were separated into three groups: osteoporotic (T-score < -2.5) – 12 patients; osteopenia (T-score between -1 and -2.5) – 6 patients and a control group with patients of normal bone density (T-score > -1/-6).

Biological specimen

Serum samples were provided according to the requirements for quality assurance in the pre-analytical phase of clinical laboratory testing. Venous blood was drawn by a standard collection procedure. Collection tubes with clot activator and gel separator were used. Serum was separated by centrifugation <1200 g for 10 min at room temperature and kept frozen in small Eppendorf tubes of 1.5 mL before the measurement. To avoid possible evaporation, the tubes were kept closed during the storage.

Quantitative determination

Serum Cu and Zn concentrations were measured by FAAS (Perkin-Elmer AAnalyst 300). The instrumental parameters are presented in Table 1.

Table 1. Instrumental parameters for Cu and Zn measurements in serum samples

Instrumental parameters	Analysis of serum Cu	Analysis of serum Zn
Wavelength, nm	324.8	213.9
Slit, nm	0.7	0.7
Light Source	Hollow Cathode Lamp HCL-Lumina	Electrode Discharge Lamp EDL
Current, mA	15	250/modulated on
Atomizer	Flame air-acetylene	Flame air-acetylene

Before the quantitative analysis, serum samples were diluted by distilled water with proven acceptable purity (1:3 for copper with total volume of 1.5 mL and 1:5 for zinc with total volume of 2.5 mL).

The measurement of both elements was based on routine 1-point calibration using an aqueous standard solution with known concentration (Cu 7.87 µmol/L and Zn 6.12 µmol/L), prepared by proper dilution with distilled water of the stock standard: Titrisol Copper Standard 1000 mg Cu as CuCl₂ in H₂O and Titrisol Zinc Standard 1000 mg Zn as ZnCl₂ in 0.06% HCL).

The quality of the patient results was guaranteed by the following: Internal Quality Control (IQC) and participation in External Quality Assessment (EQAS) programs. ICQ for serum Cu was applied using clinical assayed chemistry control material with declared value interval for atomic absorption and for serum Zn – using trace elements-certified reference material.

Statistical analysis

Data about serum Cu and Zn and the ratio Cu/Zn in disordered bone metabolism were expressed as mean values ± SD. Evaluation was done by analysis of variance with non-paired t-test between different groups with P < 0.05 for statistical significance.

RESULTS AND DISCUSSION

In our preliminary measurements of copper and zinc levels we found that there is not a significant difference between patients with osteopenia and osteoporosis. That is why we formed a new group of all patients with disturbances of the bone metabolism. We included the ratio copper/zinc as a new parameter.

Results

Serum zinc levels: The lowest mean level was found in the control group: 12.6 ± 2.7 µmol/L vs 13.6 ± 3.3 µmol/L in the osteopenia group and 13 ± 1.1 µmol/L in the osteoporotic group. However, there were no statistically significant differences between the measurements in the different groups (p = 0.73).

Serum copper levels: Again, the lowest mean level was found in the control group: 17.6 ± 2.6 µmol/L vs 19.5 ± 3.4 µmol/L in the osteopenia group and 20.2 ± 4.7 µmol/L in the osteoporotic group. However, once again there were no statistically significant differences between the measurements in the different groups (p = 0.25).

Serum copper/zinc levels: Again, the lowest mean level was found in the control group 1.4 ± 0.1 vs 1.6 ± 0.6 in the osteopenia group and 1.6 ± 0.3 in the osteoporotic group. The characteristics of the analytical performance are presented in Table 3.

Table 2. Grand Cu, Zn and Cu/Zn \pm SD

Parameter, $\mu\text{mol/L}$	Control group	Osteopenia group	Osteoporotic group	Mixed Group
Cu	17.6 \pm 2.6	19.5 \pm 3.4	20.2 \pm 4.7	19.9 \pm 4.2
Zn	12.6 \pm 2.7	13.6 \pm 3.3	13 \pm 1.1	13.2 \pm 2.3
Cu/Zn	1.4 \pm 0.1	1.6 \pm 0.6	1.6 \pm 0.3	1.6 \pm 0.5

Table 3. Analytical performance of the determination of Cu and Zn in serum by FAAS

Analytical Performance	Serum Cu	Serum Zn
Laboratory imprecision within one run (CV%)	3.0	4.0
Laboratory imprecision day-to-day variation (CV%)	4.0	7.4
Trueness (Bias%)	2.8	4.0

Table 4. T-test, $P < 0.05$ statistical significance

Parameter, $\mu\text{mol/L}$	Osteopenia vs controls	Osteoporosis vs controls	Osteoporosis vs osteopenia	Combined disordered group vs controls
Cu	0.3	0.25	0.76	0.23
Zn	0.62	0.73	0.64	0.62
Cu/Zn	0.54	0.25	0.95	0.4

The applied systems for detection and elimination of contaminating factors and direct measurement of Cu and Zn in serum by FAAS provide effective control of contamination. Standardized sample preparation in the pre-analytical phase is an aspect of quality assurance [16, 17].

Atomic absorption analysis is a reference method for determination of copper and zinc in biological specimens. The methods in the present study were validated. The calibration pointed linear mode for Cu up to 157 $\mu\text{mol/L}$ ($r = 0.999$) and up to 30 $\mu\text{mol/L}$ ($r = 0.999$) for Zn. The calibration curves for both elements were based on aqueous calibration solutions with concentrations chosen to fall into 3 intervals with clinical significance: pathologically low, interval of reference values, pathologically high [16].

The analytical characteristics (calibration procedure, imprecision in one run, day-to-day variation, trueness) as part of the whole standardized operated procedure are related to preliminary sample preparation and to the same atomic absorption measurement.

Comments

1. Higher mean values for serum copper in patients with disordered bone metabolism are more pronounced in osteoporosis. T-test points a difference between controls, osteopenia and osteoporosis: $P = 0.30$ osteopenia vs controls; $P = 0.25$ osteoporosis vs controls; $P = 0.76$ osteoporosis vs osteopenia. The difference between controls and combined disordered group (osteopenia + osteoporosis) is with $P = 0.23$. There is slight tendency for increasing serum copper in disordered

bone metabolism, more pronounced in osteoporosis than in osteopenia.

2. The statistical difference in serum Zn between the three groups and between controls and the combined disordered group is: (osteopenia + osteoporosis) with $P = 0.62$ osteopenia vs controls; $P = 0.73$ osteoporosis vs controls, $P = 0.64$ osteoporosis vs osteopenia and $P = 0.62$.

3. The statistical difference for the ratio Cu/Zn between the three groups and between controls and the combined disordered group is: $P = 0.54$ osteopenia vs controls; $P = 0.25$ osteoporosis vs controls, $P = 0.95$ osteoporosis vs osteopenia and $P = 0.4$ combined disordered group vs controls. These preliminary observations only imply for slight tendency of increasing in serum Cu in disordered bone metabolism. The tendency seems like more pronounced for osteoporosis than for osteopenia. Serum Zn does not differ significantly. Intriguingly, the ratio Cu/Zn follows the same statistical model as serum Cu.

This study is encouraging with a potential for serum Cu and Zn and the ratio Cu/Zn to serve as useful biomarkers in laboratory diagnosis and treatment monitoring of disordered bone metabolism, especially in more severe form of osteoporosis. In any case, more detailed research with bigger numbers of individuals in the tested groups is necessary to provide convincing evidence in this direction.

Visible from the results is that in the control group the mean level of serum zinc and copper was significantly lower than that of the patients with osteoporosis and osteopenia, even if the difference was not statistically significant. This can be explained by the fact that copper and zinc participate as cofactors in a number of enzyme

systems in bone metabolism. This might be the reason why the control group patients with normal bone metabolism did not possess these elements in high quantities in their serum, as they were engaged on an intracellular level. In order to find statistically significant results and to study this hypothesis, it will be necessary to increase the number of patients in all groups tested.

This is a preliminary investigation which will continue with extended numbers of patients. In case the found correlation is confirmed in future trials with a statistical significance of the results, the levels of copper and zinc will be able to be used as biomarkers for the efficiency of the bone metabolism.

High analytical reliability of the FAAS determination of Cu and Zn in serum, application of IQC schemes and successful participation in Trace Elements QAS programs provide evidence for guaranteed quality of the results. Such approach is a base for adequate clinical interpretations, also in the case of disordered bone metabolism.

REFERENCES

1. Tz. Petranova, I. Sheytanov, Y. Sheytanov, in: Osteoporoz. Eds., Steno Publishing House: Varna, Bulgaria. 2016, p 5.
2. J. Y. Reginster, N. Burlet, *Bone*, **38** (2), 4 (2016).
3. A. H. Alghadir, S. A. Gabr, E. S. Al-Eisa, M. H. Alghadir, *Clinical Interventions in Aging*, 11, 265 (2016).
4. M. Mahdavi-Roshan, M. Ebrahimi, A. Ebrahimi, *Clin. Cases in Mineral and Bone Metabol.*, **12**(1), 18 (2015).
5. T. Sierpiska, J. Konstantynowicz, K. Orywal, M. Golebeiwski, M. Szmitkowski, *Osteoporosis Int.*, **25**(2), 447 (2014).
6. N. Sadeghi, R. O. Mohammad, J. Behrooz, H. Mannan; B. Masoomeh, B. Abdolazim, S. Fatemeh, S. Sahereh, *J. Env. Health Sci. & Eng.*, **12**, 125 (2014).
7. S. A. Abrams, S. A. Atkinson, *The J. Nutrition*, **133**(9), 2994S (2003).
8. T. Suzuki, Y. Nakamura, H. Kato, *Nutrients*, **9**(8), 871 (2017)
9. K. Tsachev, Reference boundaries, Central Clinical Laboratory, MU, Sofia, 2004.
10. R. Tomova, K. Tzatchev, L. Boyanova, *Chemistry*, **19**(3), 189 (2017).
11. M. Angelova, S. Asenova, V. Nedkova, R. Koleva-Kolarova, *Trakia J. Sci.*, **9**(1), 88 (2011).
12. K. Gonoodi, A. Moslem, S. Darroudi, M. Ahmadnezhad, Z. Mazloum, M. Tayefi, S. A.T. Zadeh, S. Eslami, M. Shafiee, Z. Khashayarmanesh, H. M. Haghghi, G. A. Ferns, M. Ghayour-Mobarhan, *Clin. Biochem.*, **54**, 25 (2018).
13. J. Suliburska, S. Cofta, E. Gajewska, G. Kalmus, M. Sobieska, W. Samborski, Z. Krejpcio, S. Drzymala-Czyz, P. Bogdanski, *Eur. Rev. Med. Pharmacol. Sci.*, **17**, 2396 (2013).
14. G. Rakhra, D. Masih, A. Vats, S.K. Verma, V.K. Singh, R.T. Rana, V. Kirar, S.N. Singh, *Nutrition*, **43**, 75 (2017).
15. H. Yang, S. Lee, K. Han, B. Kang, S. Lee, K. Yoon, H.S. Kwon, Y.M. Park, *Diabete Metab.*, **41**, 282 (2015).
16. K. Tzatchev, Rationalization of Trace Elements Investigation in Clinical Laboratory, PhD Thesis, 1994, Medical faculty Sofia.
17. I. Ivanova, B. Atanasova, B. Petrova, S. Dragneva, L. Vladimirova, Z. Krastev, A. Kostadinova, A. Ivanova, K. Tzatchev, *Acta Med. Bulg.*, **XLII**, 49 (2015).

CO₂ capture on diethanolamine-grafted NaY zeolite

M. Tajbakhsh^{1*}, M. Fakhimi Abarghouei¹, H. Alinezhad¹, Kh. Niknam²

¹Department of Organic Chemistry, Faculty of Chemistry, University of Mazandaran, Babolsar, Iran

²Department of Organic Chemistry, Faculty of Chemistry, Persian Gulf University, Bushehr, Iran

Received March 25, 2019; Accepted September 8, 2019

In this study, NaY zeolite with molar ratio Si/Al=2.5 was chemically grafted with diethanolamine (DEA) and was characterized by XRD, IR, TGA, FE-SEM, EDAX, N₂-BET and CO₂-TPD. After grafting and changing in surface nature of NaY a significant increase in CO₂ adsorption capacity was registered. As the temperature raises the CO₂ adsorption capacity increases. The mechanism of CO₂ adsorption on NaY is usually a physical interaction, but it seems that after amine functionalization, the chemical mechanism is dominant for the interaction between CO₂ and amine groups. The adsorbents were characterized by CO₂-TPD technique. The results showed that the functionalized NaY zeolites have an excellent potential for CO₂ adsorption at high temperatures.

Keywords: NaY, diethanolamine, grafted amine, CO₂-TPD

INTRODUCTION

The concentration of CO₂ in the Earth's atmosphere is about 380 ppm, [1]. After Industrial Revolution an increase of approximately 110 ppm was registered [2]. The combustion of fossil fuels is the main source of energy for many years to come [3]. However, as more fossil fuels are combusted, the amount of greenhouse CO₂ emitted to the atmosphere will continue to increase, leading to global climate change from which we have already started seeing the consequences [4]. The development of CO₂ capture and separation technologies is the solution of this global problem. Aqueous amines have been used commercially for CO₂ removal in industries [5]. However, amine-based homogeneous chemical absorption as have disadvantages, including the need for a large equipment size and high regeneration energy [6]. Therefore, as an alternative selection, CO₂ capture with solid sorbents (heterogeneous adsorption) has attracted much attention in recent years [7,8]. Solid adsorbents are acceptable candidates because the significantly smaller heat capacities of solids may reduce the heat required for regeneration. In addition, solvent loss and corrosion problems resulting from the use of aqueous amines would be minimized if solid adsorbents were utilized instead [9]. Currently, aqueous amines are used industrially to separate CO₂ from gas mixtures with high CO₂ partial pressures like natural gas, but solid adsorbents are used to remove CO₂ from mixtures with very low CO₂ partial pressures. Amine-modified porous silica can be divided in two classes according to the different synthesis methods, namely impregnation and grafting.

For the impregnated adsorbents, high adsorption capacity for CO₂ can be achieved by loading a large amount of amines onto the support. However, weak interaction between amines and supports leads to poor thermal stability of these materials, which spoiled their application in practical processes [10]. By contrast, the grafted ones are more stable, due to the formation of chemical bonds between the surface silanols of silica and the aminosilanes. Mesoporous silicas and zeolites with different pore structures have been employed to synthesize various amine-grafted adsorbents [11,12].

Temperature-programmed desorption (TPD) is a sensitive technique for characterization of the interaction between adsorbed molecules and solid surface [13-15]. It is one of the most straightforward surface science experiments for the determination of the thermodynamic and kinetic parameters of a reaction and it can be a measure of the amount of chemisorption [16]. In this study after grafting NaY zeolite with diethanolamine we used CO₂-TPD technique to determine the chemisorbed amount of CO₂ on NaY and amine-functionalized NaY.

EXPERIMENTAL

Chemicals and reagents

Analytical grade CHCl₃, 3-(chloropropyl)-trimethoxysilane, diethanolamine were obtained from Merck Company (Germany). NaY nanozeolite with Si/Al=2.5 was purchased from Zeolyst Company (USA). Deionized water was used to prepare all solutions.

Instruments

The characterization of the crystal phase of the synthesized adsorbents was performed by means of

* To whom all correspondence should be sent:

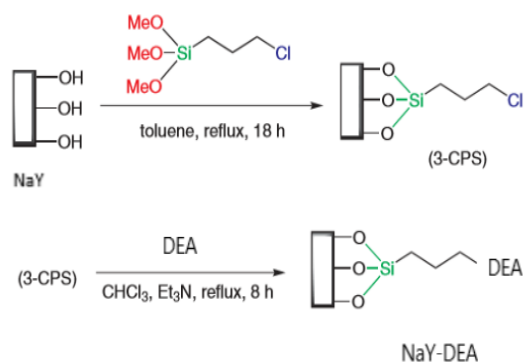
E-mail: tajbaksh@umz.ac.ir

X-ray diffraction (XRD) with the Philips 1830 instrument. The surface functional groups of the adsorbents were assessed using Fourier transform infrared spectroscopy (FTIR) (DIGILAB FTS 7000 spectrometer). Scanning electron microscopy FE-SEM (KYKY-EM 3200) was applied for investigating zeolites' morphology. Thermal program desorption of functionalized zeolites measured by Belcat-A. Micromeritics BET (Brunauer, Emmett and Teller) was used to measure the specific surface area of a sample comprising the pore size distribution.

Thermogravimetric analysis (TGA) of adsorbents was performed using the TGA 8000 Perkin Elmer instrument by scanning up to 800 °C with a heating rate of 10 °C/min.

Experimental methods

NaY zeolite and 3-(chloropropyl)-trimetoxysilane were used for synthesis of 3-CPS. The amine used for the modification of the adsorbents was diethanolamine (DEA) (Scheme 1).



Scheme 1. Preparation of functionalized NaY zeolite.

DEA was chemically grafted on NaY zeolites. Finally, the NaY zeolite powders were separated from the solution through filtration and were dried in an oven at 50-60 °C for 1 hour.

RESULTS AND DISCUSSION

The XRD patterns of NaY and DEA-grafted NaY zeolites are displayed in Fig. 1. The XRD patterns of the zeolite did not change significantly after the amine attachment, however, a decrease in the intensity of the signal located in the 6.0-6.5 range of the 2θ scale reported in the case of silica was attributed to the stress caused by the presence of the amines within the pores of the silica, in this case, of the NaY zeolite.

The FT-IR spectra of NaY and amine-grafted NaY samples are shown in Fig. 2.

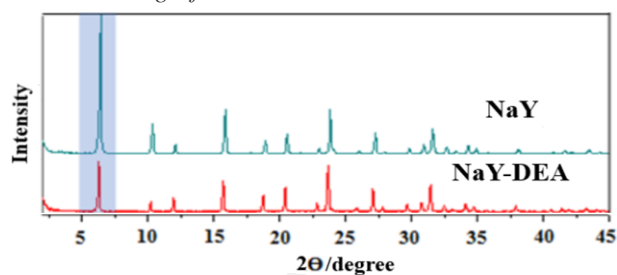


Figure 1. XRD patterns of NaY before and after amine grafting.

The amine-NaY spectra differed from those of pure NaY and showed several peaks. After modification of NaY, the adsorption peaks at 1500–1600 cm⁻¹ were related to the stretching vibrations of -NH₂. The absorption band at 2800–2900 cm⁻¹ shows the stretching of CH from the CH₂CH₂CH₂NH₂ groups. Therefore, the IR spectrum of the amine-modified NaY proved the absorption of amine inside the NaY channels.

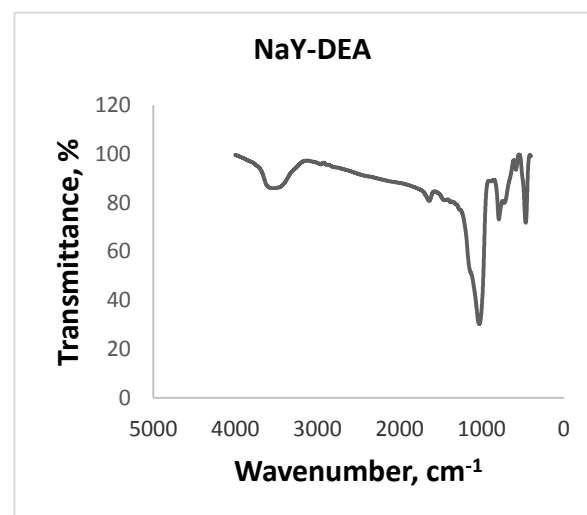
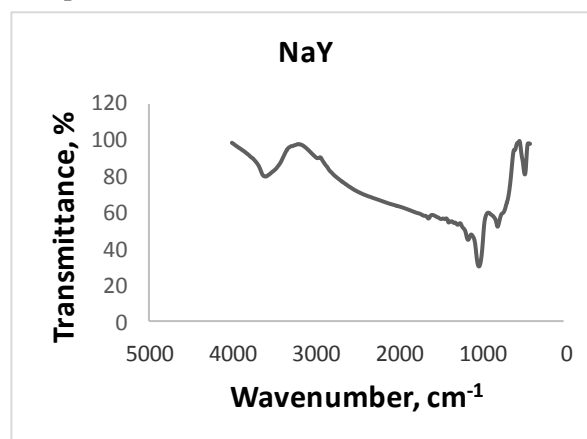


Figure 2. FT-IR spectra of NaY and NaY-DEA

Figure 3 represents the FE-SEM images corresponding to NaY, NaY-DEA with a magnification of 25 000 at 25 KV acceleration voltage. The outcome of FE-SEM showed that the NaY-DEA was grafted effectively by the amine

groups. The results of the EDAX analysis of NaY and NaY-DEA are shown in Table 1, confirming that the amines are successfully grafted.

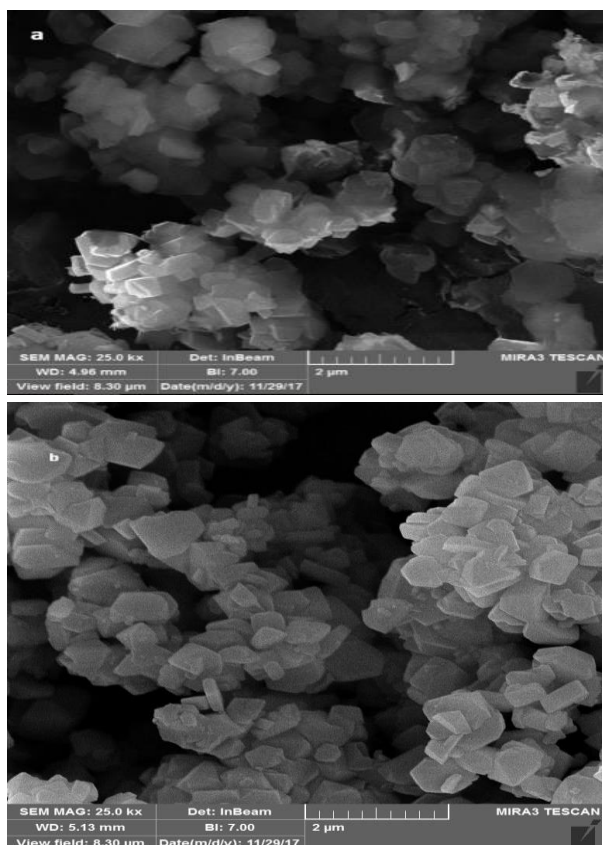


Figure 3. E-SEM images corresponding to (a) NaY, (b) NaY-DEA .

Table 1. EDAX information corresponding to NaY- and amine- modified NaY

Element	O Wt%	Na Wt%	Al Wt%	Si Wt%	N Wt%	C Wt%
Adsorbent						
NaY	61.42	6.18	7.76	24.64	0	0
NaY-DEA	37.44	6.01	7.76	22.92	2.64	23.23

Nitrogen physisorption is a technique which provides information about porous materials, like specific surface area and pore diameters. In physisorption tests, an activated porous or excellently divided solid is equilibrated with a permanent gas like nitrogen or a vapour at a fixed temperature [17,18].

The Barrett-Joyner-Halenda (BJH) technique on the basis of pore condensation phenomena is appropriate only for mesoporous or microporous materials (Fig. 4).

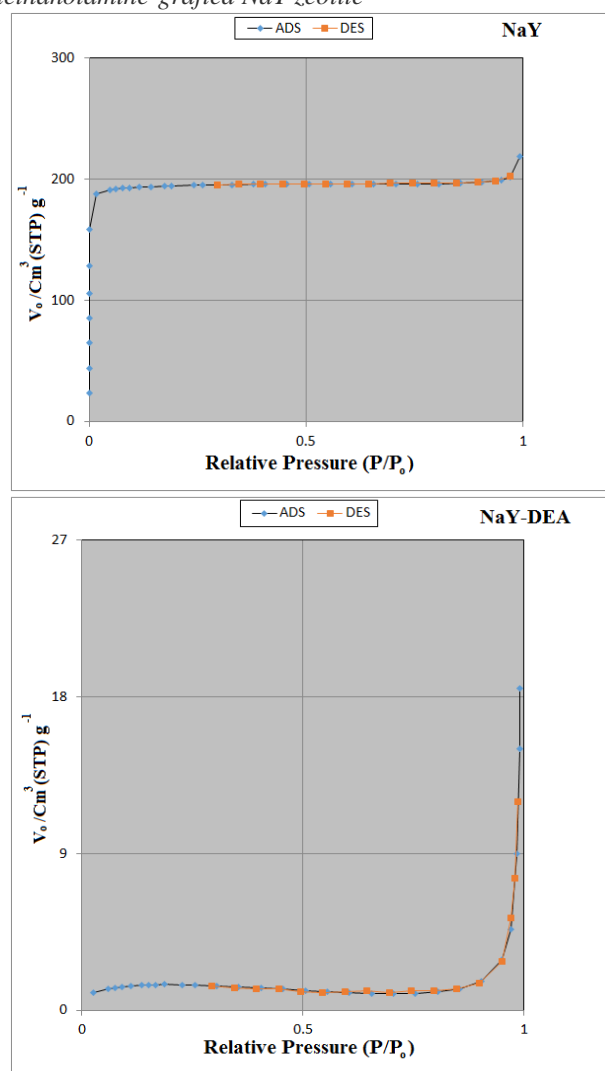


Figure 4. N₂ adsorption–desorption isotherms corresponding to NaY and amine-grafted NaY.

The structural features of the samples are represented in Table 2.

Table 2. Structural properties of NaY and amine-modified NaY

Adsorbent	BET Surface Area (m ² g ⁻¹)	Pore Volume (cm ³ g ⁻¹)	Mean Pore Diameter (nm)
NaY	810.64	0.336	1.658
NaY-DEA	5.45	0.025	18.384

Following the modification by the amine, the nitrogen adsorption isotherm becomes a straight line and the adsorbed volume reduces clearly. Furthermore, the BET surface area and pore volume are clearly reduced, which proves the occupation of the zeolite pores by amines.

To determine the amount of zeolite desorption a thermal desorption technique is suitable (Fig. 5).

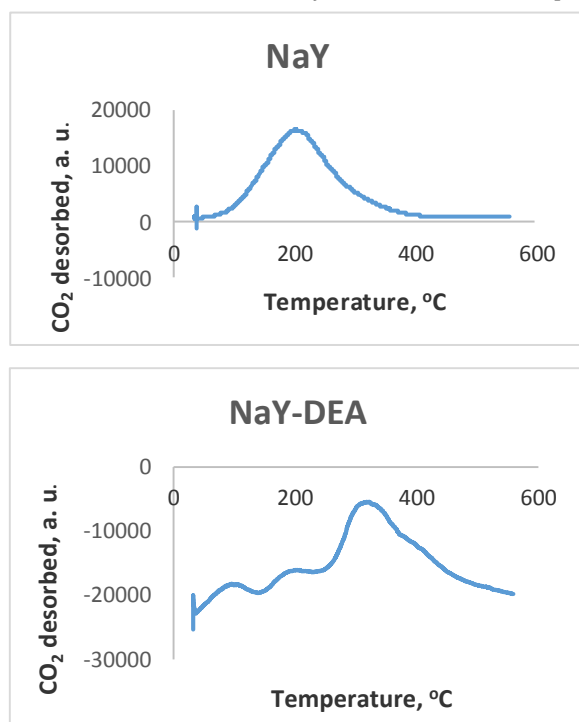


Figure 5. CO₂-TPD isotherms corresponding to NaY and NaY-DEA

The TPD-CO₂ technique was used for this study (Table 3).

Table 3. CO₂-TPD of NaY and amine-modified NaY

Adsorbent	Temp(°C)/CO ₂ desorption capacity(mmol/g)		
NaY	202°C	2.174	
NaY-DEA	94°C	202°C	320°C
	0.353	0.509	2.899

CO₂-TPD measurements were carried out to determine the chemisorbed amount of CO₂ on NaY and amine-functionalized NaY [19]. The adsorbent was first pre-treated at 120°C for 60 min in a He flow of 50 mL min⁻¹ then cooled to the desired temperature (50°C) before being saturated with CO₂ for 1 h at a rate of 5 mL min⁻¹. The CO₂-saturated samples were flushed with 50 mL min⁻¹ of He gas for 0.5 h to fully remove physically adsorbed CO₂. TPD program was then initiated by heating from the specific adsorption temperature (35 °C) to 380°C (for NaY) or 600°C (for NaY-DEA) at a rate of 0.1°C min⁻¹. The amount of desorbed CO₂ should be equal to the amount of CO₂ chemically adsorbed on the sample.

At low temperatures, physisorption is important and the adsorption capacity is directly proportional to the surface area of the adsorbent. With amines grafting, the surface area of zeolite was significantly reduced.

At high temperatures, chemical reactions occur between the amino groups and CO₂ to produce carbamate.

On the NaY zeolite CO₂ chemisorbed on the intrinsic Lewis basic sites is associated with the lattice oxygen in the NaY framework but in functionalized zeolite CO₂ can be chemically adsorbed on both the intrinsic basic sites in NaY and amine group. At low temperatures, CO₂ would diffuse quite slowly in amine-grafted adsorbents and its uptake would seem unusually low, whereas at high temperatures, the kinetics of the reaction becomes significant and the adsorption capacity increases with the temperature. These results showed that amine-functionalized NaY zeolites have excellent adsorption potential for CO₂ at high temperatures and can be employed in the process of CO₂ capture from flue gas which is performed at high temperatures.

CONCLUSIONS

In this study, NaY zeolite was functionalized with DEA. The samples were characterized by XRD, IR, TGA, FE-SEM, EDAX, N₂-BET and CO₂-TPD analyses.

The functionalized adsorbents were also evaluated for their CO₂ desorption capacities and it was observed that the functionalized zeolites desorb less than the pristine material at low temperatures, but their CO₂ uptake increases with a rise in the temperature. Therefore, it can be concluded that the mechanism of CO₂ adsorption on NaY is entirely a physical interaction process but appears mainly attributable to a chemical interaction after the amine modification. This suggests that the amine-grafted NaY zeolites can be employed in the process of CO₂ capture from flue gas which is performed at high temperatures.

Acknowledgement: The authors are thankful to University of Mazandaran, Persian Gulf University and Pardis Petrochemical Company for their financial support in this project.

REFERENCES

1. L. Krótki, A. Więclaw-Solny, M. Tatarczuk, A. Stec, D. Wilk, T. Śpiewak, T. Spietz, *Arab. J. Sci. Eng.*, **41**, 371 (2016).
2. H. Harde, *Global and Planetary Change*, **152**, 19 (2017).
3. F. Rezaei, A. A. Rownaghi, S. Monjezi, R. P. Lively, C.W. Jones, *Energy Fuels.*, **29**, 5467 (2015).
4. B. Niu, H. A. Loaiciga, Z.Wang, F. B. Zhan, S. Hong, *J. Hydrol.*, **519**, 966 (2014).

5. T.-L. Chew, A.L. Ahmad, S. Bhatia, *Advances in Colloid And Interface Science*, **153**(1), 43 (2010).
6. A. Veawab, P. Tontiwachwuthikul, A. Chakma, *Industrial & Engineering Chemistry Research*, **38**(10), 3917 (1999).
7. E. E. Ünveren, B. O. Monkul, S. Sanoglan, N. Karademir, E. Alper, *Petroleum*, **3**(1), 37 (2017).
8. H. A. Patel, J. Byun, C. T. Yavuz, *ChemSusChem.*, **10**(7), 1303 (2017).
9. Ch.-H. Yu, C.-H. Huang, Ch.-S. Tan, *Aerosol Air Qual. Res.*, **12**(5), 745 (2012).
10. A.Goeppert, S. Meth, G.K.S. Prakash, G.A. Olah, *Energy Environ. Sci.*, **3**, 1949 (2010).
11. M. J. Lashaki, A. Sayari, *Chemical Engineering Journal.*, **334**, 1260 (2018).
12. G Zhang, P. Zhao, L. Hao, Y. Xu, *Journal of CO2 Utilization*, **24**, 22 (2018).
13. A. Kotsifa, D.I. Kondarides, X.E. Verykios, *Appl. Catal. B.*, **72**, 136 (2007).
14. T. Nobukawa, K. Sugawara, K. Okumura, K. Tomishige, K. Kunimori, *Appl. Catal. B.*, **70**, 342 (2007).
15. K.-T. Wang, S. Nachimuthu, J.-Ch. Jiang, *Physical Chemistry Chemical Physics*, **20**(37), 24201 (2018).
16. Y. Yu, J. Mai, L. Wang, X. Li, Zh. Jiang, F. Wang, *Scientific Reports*, **4**, 5997 (2014).
17. JK. Sing, *Colloids Surfaces A: Physicochem. Eng. Asp.*, **187**, 3 (2001).
18. K. K. Unger, H. Reichert, *TrAC Trends Anal. Chem.*, **10**, 44 (1991).
19. Y. Yu, J. Mai, L. Wang, X. Li, Z. Jiang, F Wang, *Scientific Reports*, **4**, 5997 (2014).

Low-cost AEM water electrolysis with flat stainless steel electrodes

G. Borisov*, T. Dimitrov, D. Paskalev, E. Slavcheva

“Academician Evgeni Budevski” Institute of Electrochemistry and Energy Systems, Bulgarian Academy of Science, Sofia, Bulgaria

Received April 18, 2019; Revised June 6, 2019

The work presents a newly developed water electrolyser with AISI 316L stainless steel flat electrodes and anion exchanged membrane (AEM). The electrochemical behavior of AISI 316L is investigated in 25% KOH solution applying the methods of cyclic voltammetry and polarization curves. A single membrane electrode assembly (MEA) is prepared using the stainless steel flat sheets for both the cathode and anode and AB-PBI membrane. The MEA performance is tested by chronoamperometry at constant voltage 2.6 V. Finally, a small electrolyser stack with 4 MEAs is constructed and long-term electrolysis tests are performed. The stack with the AISI 316L electrodes demonstrates stable electrochemical behavior during 600 hours of operation and sustainable performance under a “start–stop” stress test procedure.

Keywords: Water electrolysis, stainless steel, stack measurements, anion exchange membrane

INTRODUCTION

The water electrolysis in cells with anion exchange membrane (AEMEC) is a new alternative for electrochemical production of clean hydrogen. The method offers several advantages in comparison to the classical alkaline water electrolysis such as higher current density, lower ohmic resistance, possibility to operate under high pressure, etc. It has also some benefits compared to the contemporary electrolysis cells with proton exchange membrane electrolyte (PEMEC), among which the most important are the enhanced kinetics of the partial electrode reactions, particularly of the oxygen evolution reaction, and the possibility to operate with non-noble catalysts which makes the technology much more cost efficient [1,2]. The main working unit for both AEM and PEM electrolysis cells is the membrane electrode assembly (MEA), consisting of two electrodes attached to and separated by a polymer electrolyte membrane [3,4]. The design and structure of the electrodes have strong influence on the energy efficiency and service life of the MEA. The electrodes typically have a complicated sandwich configuration with at least two sub-layers: gas diffusion layer (GDL) and catalytic layer (CL) [5]. The nature of the proceeding redox reactions in AEMEC allows the use of a metal mesh as gas diffusion layer. On the top of the GDL, usually highly active catalysts are spread out in the form of thin homogeneous catalytic layer. The catalysts for both partial reactions are mainly non-noble transition metals from the transition series of the periodic table and their alloys. Ni has demonstrated good catalytic properties concerning hydrogen

evolution reaction (HER), while in regard to the oxygen evolution reaction (OER), various Ni-alloys (with Mo, Co, Fe, P, etc.) in different ratios of the components are used [6-8].

Another major problem of AEM water electrolysis is the short life of the electrolyte membrane. The available commercial products are not capable to withstand elevated temperatures [9, 10]. Moreover, they are not stable at the high KOH concentrations required to ensure high ionic conductivity, respectively high energy efficiency of the AEMEC. Recently, the membranes based on poly-benzimidazole (PBI) such as AB-PBI or para-PBI are often used in various fuel cells applications showing good ionic conductivity [11,12]. The complication with this type of membranes is that the pre-conditioning procedure (doping of the polymer skeleton with electrolyte before usage) takes a lot of time and leads to problems with the mechanical preparation of the MEA.

In this work we have investigated stainless steel AISI 316L as potential suitable electrode material for both cathode and anode in AEMEC. This material is broadly used in the hydrogen combustion engines, as well as in the hydrogen-oxygen generators where the produced hydrogen and oxygen (molar ratio 2:1) are not separated. The steel contains about 10 – 14% of Ni and other doping elements and is resistant to corrosion in concentrated alkaline solution. Therefore, it was of interest to investigate its electrochemical activity toward electrolysis of water in AEMEC, as well as its stability at high voltages.

EXPERIMENTAL

The AISI 316L flat electrodes were sized and

* To whom all correspondence should be sent:

E-mail: gal.rusev@iees.bas.bg

shaped using a laser cutting machine. The geometric area of both cathode and anode was 5 cm². The first series of tests aimed to investigate the AISI 3016L electrochemical behavior in alkaline environment at room temperature. The electrolyte was an aqueous solution of potassium hydroxide (25 wt.% KOH). A three-electrode electrochemical cell with standard hydrogen reference electrode and Pt-wire counter electrode was used. The working area of the test electrode was 1 cm². The experiments were performed applying classical cyclic voltammetry and steady state polarization techniques.

In the second test series, anion exchange membrane was used as electrolyte. The experiments were carried out in a self-designed electrolysis cell, firstly in a single cell mode (fig. 1), and then in a small laboratory stack with 4 single cells (fig. 2).



Figure 1. Picture of a self-designed single AEM electrolysis cell



Figure 2. Picture of a small laboratory AEM electrolyser with 4 single cells

The cell/stack gaskets were made from a 4 mm thick oil-protective rubber. Cyclic voltammetry and quasi-steady-state polarization curves were recorded using Bank Electronics POS2 potentiostat/galvanostat. Long-term chronoamperometry tests were provided by means of power supply Voltcraft PPS – 1350 connected to photovoltaic panels.

RESULTS AND DISCUSSION

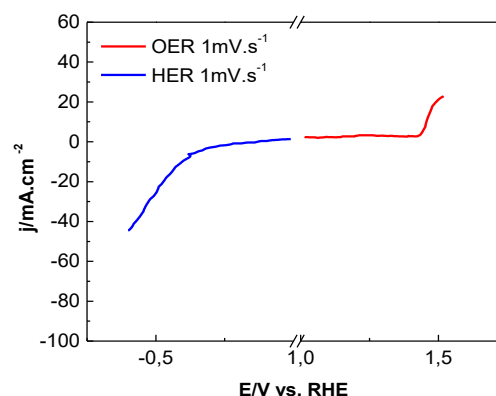


Figure 3. Cyclic voltammogram of AISI 316L stainless steel electrode in 25% KOH; potential range - 0.6V – 1.6 V (vs. RHE); scan rate 50 mV.s⁻¹

The cyclic voltammograms of AISI 326L flat electrode recorded in aqueous alkaline solution in the water window potential range are presented in fig. 3. Two well depicted current peaks are seen on the cathodic branch of the voltammogram. The first one which appears at about 1.2 V is related to reduction of oxygen. The second one (at about - 0.15 V) is much broader and is due to adsorption of hydrogen on the electrode surface. The hydrogen evolution reaction (HER) starts at -0.47 V and at the applied cathodic potential limit (-0.6 V) the current density reaches 50 mA.cm⁻². The reverse potential scan results in hydrogen desorption peak on the CV at 0.25 V and a broad shoulder in the potential range above 1.25 V, reflecting the formation of adsorbed oxygen-containing species on the electrode surface. The oxygen evolution reaction (OER) starts at 1.45 V, its rate increases rapidly and at the applied anodic potential limit (1.6 V) reaches 60 A.cm⁻². The electrochemical response of the stainless steel electrode does not change during the applied continuous potential cycling. The CVs recorded during the 2nd and 120th cycles are identical, indicating stability of the material under study at the chosen test conditions.

In order to assess more accurately the rate of both partial electrode reactions on the AISI 316L stainless steel electrode, quasi-steady-state polarization curves were recorded (Fig. 4).

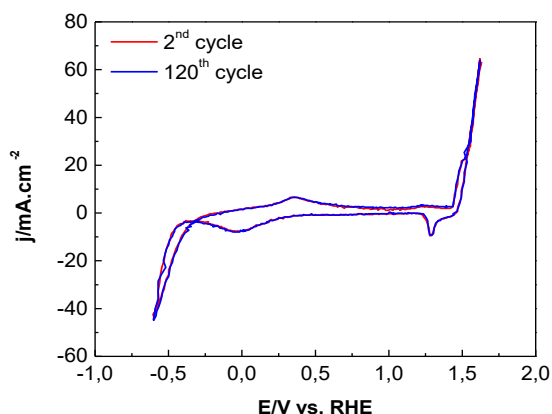


Figure 4. Polarization curves of AISI 316L stainless steel in 25% KOH; scan rate $1 \text{ mV}\cdot\text{s}^{-1}$

The cathode reaction of hydrogen evolution (in blue) starts at a potential of about -0.4 V and the current density reaches a value of $45 \text{ mA}\cdot\text{cm}^{-2}$ at a potential of -0.6 V . The oxygen evolution reaction (in red) starts at a potential of 1.4 V and the current density reaches a value of about $20\text{-}25 \text{ mA}\cdot\text{cm}^{-2}$ at 1.55 V . The further increase of the applied anodic potential leads to transport limitations and the current density reaches limited value.

The results obtained in 25% KON proved the efficiency and stability of AISI 316L as electrode material for electrochemical water splitting. Further, the stainless steel electrodes were integrated in a membrane electrode assembly using anion exchange membrane and tested in a single AEMEC (fig. 1).

Figure 5 presents the MEA performance at conditions of intensive oxygen evolution. A constant cell voltage of 2.6 V was applied for 8 h . Then the voltage was switched off and the cell was left at open circuit potential for another 8 h . The start-stop procedure known also as “stress-test” was repeated continuously in order to assess the long-term performance of the electrolysis cell. The results obtained demonstrated a stable electrochemical behavior for 70 h . When the voltage is switched-on, the current density reaches immediately a value of $0.4 \text{ A}\cdot\text{cm}^{-2}$ and stays constant during the whole test duration. The increase of the start-stop cycles does not lead to changes in the cell performance.

At low voltages the polarization curves of the MEAs differ essentially as those in the middle of the stack show lower current densities. At higher voltages the differences gradually disappear. At stack voltage of 12 V the performance of all 4 MEAs is nearly identical - cell voltage of 3.0 V and current density of about $0.3 \text{ A}\cdot\text{cm}^{-2}$. In order to investigate the stack performance during long term

operation, it was connected to a power supply Voltcraft PPS-1350 at constant stack voltage of 10.2 V .

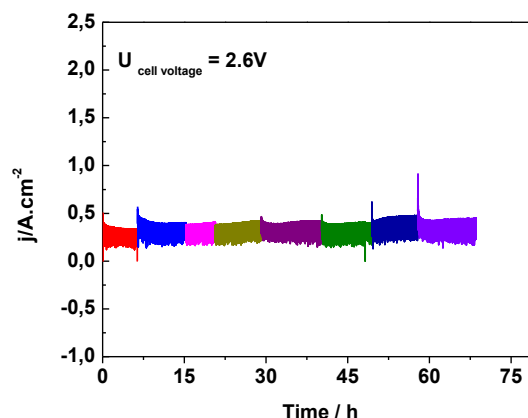


Figure 5. Long-term stress-test of a single AEMEC

The developed membrane assembly was extended in a small laboratory stack with 4 electrochemical cells connected in series (fig. 2). The performance of this small electrolyser was investigated by quasi-steady-state polarization tests. The recorded polarization curves of each single MEA and that of the whole stack are presented in figure 6.

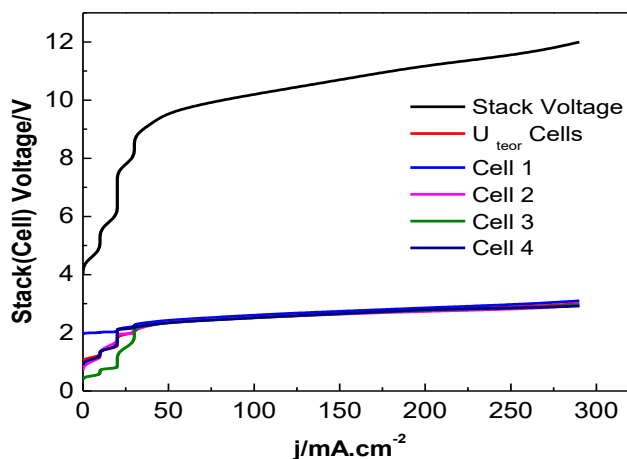


Figure 6. Polarization curves of a small laboratory AEMEC stack with 4 cells

The obtained results are presented in figure 7. For each single cell in the stack the current density reached value of about $50 \text{ mA}\cdot\text{cm}^{-2}$ and the measured voltage was 2.6 V . The electrolyser demonstrated stable electrochemical behavior for 600 h of operation.

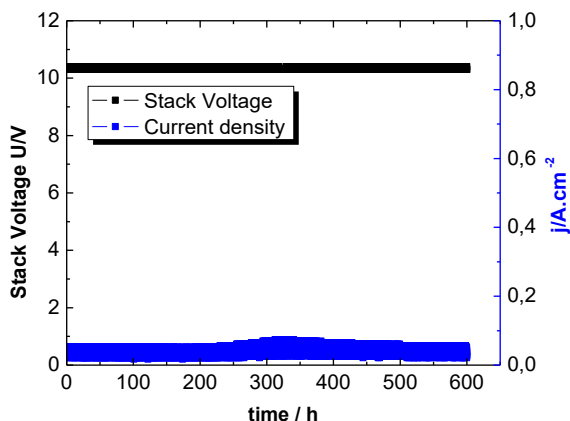


Figure 7. Long-term performance of electrolyser stack with 4 single cells

CONCLUSIONS

The AISI 316L stainless steel demonstrates moderate catalytic activity toward both HER and OER during electrochemical water splitting in electrolysis cell with anion exchange membrane. The material has an excellent stability under dynamic long-term test conditions and sustainable electrochemical behavior both in single AEMEC and when integrated in a stack. Further research on preparation of porous GDE based on AISI 316L stainless steel aimed to increase the active surface and efficiency of AEM electrolysis is in progress.

Acknowledgement: The research was funded by Bulgarian Science Fund, project KII-06-OIP04/3. The experiments were performed using equipment

REFERENCES

1. S. Marini, P. Salvi, P. Nelli, R. Pesenti, M. Villa, M. Berrettoni, G. Zangari, Y. Kiros, *Electrochim. Acta*, **82**, 384 (2012).
2. A. Manabe, M. Kashiwase, T. Hashimoto, T. Hayashida, A. Kato, K. Hirao, I. Shimomura, I. Nagashima, *Electrochim. Acta*, **100**, 249 (2013).
3. M. Prasanna, E.A. Cho, T.H. Lim, I.H. Oh, *Electrochim Acta*, **53**, 5434 (2008).
4. Z. Wang, Y. Nagao, *Electrochim Acta*, **129**, 343 (2014).
5. S. Park, J.-W. Lee, B.N. Popov, *J. Power Sources*, **163**, 357 (2006).
6. Z. Lu, W. Xu, W. Zhu, Q. Yang, X. Lei, J. Liu, Y. Li, X. Sun, X. Duan, *Chemical Communications*, **50**, 6479 (2014).
7. Y. Wang, G. Zhang, W. Xu, P. Wan, Z. Lu, Y. Li, X. Sun, *ChemElectroChem*, **1**, 1138 (2014).
8. U. Lačnjevac, B. M. Jović, V. D. Jović, *Journal of the Electrochemical Society*, **159**, D310 (2012).
9. D. R. Dekel, *J. Power Sources*, **375**, 158 (2018).
10. E. J. Park, Ch. B. Capuano, K. E. Ayers, Ch. Bae, *J. Power Sources*, **375**, 367 (2018).
11. G. Borisov, H. Penchev, K. Maksimova-Dimitrova, F. Ublekov, E. Lefterova, V. Sinigersky, E. Slavcheva, *Journal of Materials Letters*, **240**, 144 (2019).
12. H. Penchev, G. Borisov, E. Petkucheva, F. Ublekov, V. Sinigersky, I. Radev, E. Slavcheva, *Journal of Materials Letters*, **221**, 128 (2018).

Development and characterization of walnut shell and date seeds powder in low-density polyethylene

R. M. Khan¹, A. Mushtaq^{1*}, Z. U. Ali², S. Abbasi¹, R. N. Lodhi¹, S. M. ul Haq¹, S. A. Shakeel¹

¹*Polymer and Petrochemical Engineering Department, NED University of Engineering & Technology, Karachi, Sindh, Pakistan*

²*Chemical Engineering Department, NED University of Engineering & Technology, Karachi, Sindh, Pakistan*

Received May 21, 2019; Revised July 21, 2019

The demand for polymers in many applications has experienced steady growth over the years. This led to the evolution of different types of mixtures, blends, alloys, composites, and reinforced materials. Among the property-enhancing additives, fillers play a very prominent role. The aim of this study is to enhance the tensile and flexural strength of low-density polyethylene (LDPE) by incorporation of walnut shell powder and date seed powder. Both components added strength to the composite, and the combination often compensates for weaknesses in the individual components. Samples containing different weight fractions of the reinforcement were prepared through hot pressing by using a compression moulding process. Tensile strength resistance of an LDPE blend material to breaking under tension is decreased. So, the elongation decreases with fillers. Modulus resistance to flow, hardness and flexural strength are increasing in LDPE blend by adding fillers. There is no water absorption found neither by reinforcement nor by LDPE blend. So this composite can be used to make low-cost products or non-engineering products. As the prepared sample is biodegradable, it can be used in packaging material/disposable products.

Keywords: Low-density polyethylene; Walnut shell powder; Date seed powder; Moulding; Tensile strength; Flexural strength.

INTRODUCTION

In the world of polymers, composites have their charm and identity in connection with providing magnificent strength to the designed product. Moreover, when it comes to providing strength by reinforcing along with making the part cheaper, then what else would do better? A better way to explain this advantage is the strength to weight ratio. Distinctive materials have a diverse quality, that is, every material can take a diverse measure of the load for a similar volume (cross-sectional area) of the material [1].

The scope of this study is about a dispersion-strengthened composite using date seeds and walnut shell powder in the matrix phase of low-density polyethylene (LDPE). These two fillers are available in abundance and usually go to waste. Literature work shows that these natural fillers have a potential to provide strength to the material with which they are combined [1]. As LDPE is used in an enormous amount in the commodity to engineering applications, we can reduce its amount in the same part by reinforcing it with fillers, hence providing strength along with cost-effectiveness. A composite material is one made out of at least two components consolidated in a way that enables the materials to remain particular and recognizable. Van Suchetclan characterized the composite as at least two solid phases of heterogeneous material

which are in close contact with one another on a microscopic scale. The strengthening fibers can be cut, adjusted plaud in various approaches to influence the properties of the subsequent composite [2, 3].

Numerous composite materials are made of only two phases: the first phase is a matrix and second is a dispersed phase. The phase in a composite is completely surrounded by the other phase. The intention is to transfer stress to different phases and defend the phases from the environment. Composite materials are normally grouped by the kind of reinforcement they use. This reinforcement is embedded into the matrix that holds it together. The reinforcement is utilized to fortify the composite [4, 5]. For example, in a mud block, the mud is the matrix and straw is the reinforcement. Most common composites include short-fiber or random-fiber reinforcement, long-fiber or continuous-fibre reinforcement, flake reinforcement, particulate reinforcement, filler reinforcement.

The particulate composite comprises a composite material in which the filler materials are generally round. For example; in unreinforced concrete, cement is the matrix and the sand serves as a filler; for lead particles in a copper matrix both the matrix and the filler are metals. The dispersion is strengthened when materials are in little particles (usually less than 0.1 μm) of a hard yet inert phase

* To whom all correspondence should be sent:

E-mail: engrasimmushtaq@yahoo.com

uniformly distributed within a load-bearing matrix phase [6].

The matrix is usually a form of resin that retains the reinforcement in the preferred orientation. It defends the reinforcement from environmental and chemical attack, and bonds the reinforcement by which the applied loads can be efficiently transferred. Many composites, dependent on the thermoplastic for use in inside and outside building components, are presently produced from polyethylene both virgin and recycled. The polymer matrix is generally chosen on its intrinsic properties, product requisite, accessibility, cost and the manufacturers' awareness with the material. The polymeric matrices incorporate both thermo-setting and thermoplastic resins [6].

Fillers are solid additives to any polymer or other materials to enhance their physical properties and also some chemical properties. Including a cost-effective filler in the polymeric matrix can only be viable if it does not significantly alter the main characteristics of the matrix like mechanical properties. The use of natural reinforcement continues to generate interest especially for use in the plastic industry, for it is a renewable material and a biodegradable resource. The use of natural fibers in thermoplastic composites serves to improve the toughness and strength of the plastic [7].

Dates have been staple nourishment for the Middle East and part of south Asia for many years. Dates are oval or cylindrical with a diameter of 2-3 cm and 3-7 cm length, and the ripe range is dependent on the variety. The dates were also found to medicinal value; they cure a sore throat, cold, fever, and also can be used as cleansing powder. Dates are mostly consumed during fasting and other festivities. While the date is saturated with beneficial compounds for the skin, the effect of date seed particles reinforcement on the properties of polyester was discussed by Aleuo *et al.* They found out that as loading of the filler increases, tensile strength, impact strength and hardness increases while elongation decreases [8].

The effect of date seeds on the properties of natural rubber was also discussed by Abdullah *et al.* The results derived from their research were that tensile strength, hardness, density and Young modulus increases with increasing filler loading [9, 10]. The development and research activities in each country are mainly focused on the utilization of locally available resources of natural fibers. In general, the date palm plant consists of six distinctive potential sources of secondary waste that can be utilized for the production of natural fibers.

The effect of reinforcing date palm wood powder in LDPE based composites and its effect on the mechanical properties of composites was discussed by Marium *et al.* They found that with increasing filler content Young modulus increases, flexural strength is improved and the composite displays strong tendency to absorb water [9].

Walnut is an adaptable delicate rough medium with exceptional properties. It is ideal for a wide range of applications, like walnut shell blasting, cleaning, tumbling, filtration, polishing. It is also used in soaps and beauty care products. Walnut shells are fastidiously squashed and ground to standard mesh size that ranges from grainy grits to fine powder. The effect of walnut shell powder reinforcement in forming a composite was discussed by Rahul *et al.* They found a significant improvement in the tensile modulus and mechanical properties by adding walnut shell powder as reinforcement, a decrease in water absorption property. The grain size of the walnut shell powder can be diverse to enhance the mechanical properties [11].

METHODOLOGY

Powder LDPE grade FD0474 was obtained from Lotrene, Muntajat. Date seeds, walnut shells and their powders were bought from Pakistan. For making specimens for mechanical tests an injection molding setup arrangement of extruder is necessary for uniform mixing of (walnut shells+ date seeds) and LDPE powder. Date seeds and walnut shells powder were dried in an oven at 100°C for 1 hour to remove the moisture content.

Development of Enhanced LDPE Composite

Polymer resin was brought in very fine powder form instead of pellets form and mixing was done manually in dry form as shown in Figure 1. For mixing we used a plastic bottle, then added a specific amount of powder LDPE, walnut and date seeds powder and the bottle was shaken very well to ensure good mixing. In the mixture equal proportions of date seeds powder and walnut shell powder were added. The reinforcement was about 30 wt.%, when 15 wt.% of date seeds powder and 15 wt.% of walnut shell powder were added and similarly for 10 wt.% and 20 wt.% reinforcement as shown in Table 1. Above 30 wt of fillers were not used because as we increased filler amount above 30 wt.%, the sample had a rough surface and was not stable enough under normal conditions. The preparation of composites with different proportions is shown in Figure 2.

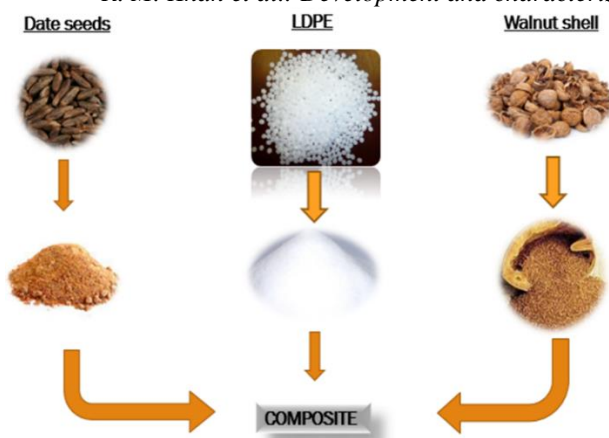


Fig 1. Mixing of LDPE with date seeds and walnut shells

Table 1. Different composition of composite

Samples	LDPE wt. %	Walnut shell wt.%	Date seed wt.%
1	100	-	-
2	90	10	-
3	90	-	10
4	90	5	5
5	80	10	10
6	70	15	15



Fig 2. Composite preparation with different proportions

Choose the type of mold that is tensile, compressive or flexural. Clean the mold surface to remove any film or grease particles. Then preheat the mold for about 5-8 min by placing it into the hot press machine jaws. After that fill the material manually with excess in order to have good flow behaviour so that there would be less number of voids. After filling the preheated mold, press it and again place in the hot press machine. Let the

material remain in heating mode for about 5-10 min at a temperature of about 130 degree Celsius and 120 bar pressure. When the temperature is about 140 degree Celsius close the heaters and open the cooling water supply so that it may lose some heat and cool down. Allow the mold to be cooled for about 5 min. Before taking out the mold release the pressure that you have applied in order to make it air tight. After this open the jaws and take out the mold and with the help of gloves take out the samples as shown in Figure 3. After that, weigh the samples and send them for testing. The best samples are chosen and on them different testing procedures are performed.

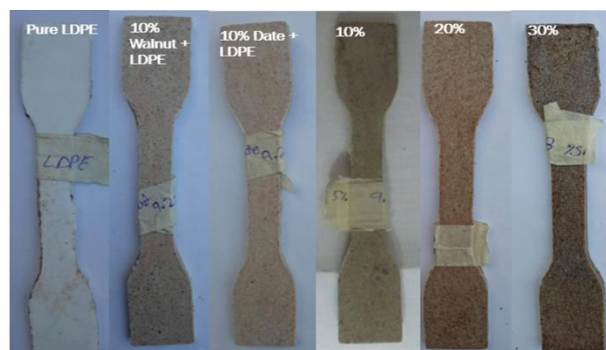


Fig. 3. Samples prepared of different composition

Characterization and Testing

The following techniques were used for characterization.

Stereomicroscopy test: The dissecting or stereoscopic microscope is an optical microscope modified for low magnification of a sample, usually using light mirrored from the surface of an object instead of transmitted through it [1]. Stereomicroscopy test was done to find out the dispersion of the particles in the matrix; this test gives enlarged pictures of the samples so that it could give us the dispersion of the particles. Take the sample which will be use for destructive testing. Place the sample under the microscope and adjust the height of the microscope. Fix the lens magnification according to the requirement and open the software and camera. Figure 4 shows the different composition of LDPE with walnut and date at 500× magnification.

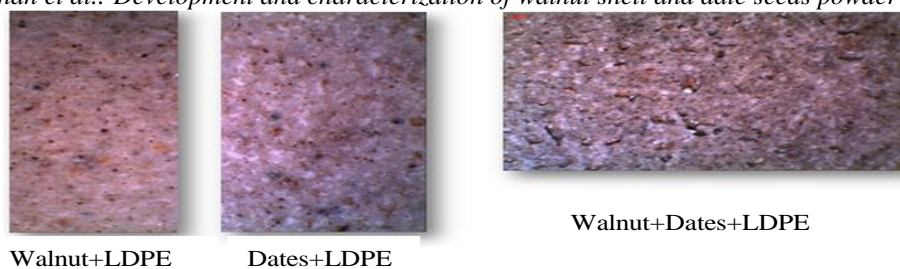


Fig. 4. Microscopic images of the samples

Tensile Test: The tensile test is an important test to check the properties of the composite. The tensile test gives us the mechanical properties of the composite materials. It is a destructive test which gives the maximum force which is composite can withstand under tensile loading and is determined by standard test method ASTM D638 [12]. The tensile test is performed on a dumbbell specimen. Universal testing machine is used for performing the tensile test. Cut or injection-mold the material into one of the five “dumbbell” shapes. The exact shape used will depend on material’s thickness, and rigidity. Load the sample in the tensile grips. Begin the test by separating the tensile grips at a constant rate of speed (20 mm per min). The test ends after breaking of the sample. The tensile strength is calculated by Eq. (1)

$$\text{Tensile strength} = F / (L * W) \quad (1)$$

where, F = maximum applied load at failure, L = gauge length, W =width of gauge area.

Flexural Test: The flexural test estimates the force required to bend a beam under three-point loading conditions. The data are commonly used to select materials for parts that will support loads without flexing. Flexural modulus is utilized as a sign of a material's firmness when flexed. Flexural strength is expressed as modulus of rupture in PSI and is determined by standard test method ASTM D790 [13]. For the testing procedure a specimen of long rectangular shape is used. The load is applied to the centre by the loading nose producing three-point-bending at a specified rate. The test is stopped when the sample reaches 5% deflection or breaks before 5%. For ISO 178, the test is stopped when the sample breaks. If the sample does not break, the test is continued as far as possible and the stress at 3.5% is reported. The result of max force is recorded. The flexural strength is calculated by Eq. (2)

$$\text{Flexural Strength} = \frac{3PL}{2wT^2} \quad (2)$$

where; ‘ P ’ denotes the load, ‘ L ’ represents the length of span, ‘ w ’ indicates the width of the specimen and ‘ T ’ is for the thickness of the specimen.

Water Absorption Test: Water absorption test was done because the composite contains date seeds powder and walnut shell powder both of which absorb water [14]. This test will give us the result how much the composite is absorbing water, as shown in Figure 5. This test involves a water pot and a circularly shaped specimen. First, the specimen is weighed before dipping it into the water. The specimen is left in the pot for 24 h, then it is removed from the pot and again weighed. The difference between the initial weight and final weight of the specimen will tell us how much water is absorbed.



Fig. 5. Water absorption

Hardness Test: Hardness test is done on the sample to check how much the prepared sample shows resistance towards penetration, which gives us a guideline for defining the application of the samples by using the shore D hardness test. A formed circular disk-shaped sample is used, which has a good surface finish as shown in Figure 6 [15]. Place the sample on the testing plate, lower the plunger so that the pin can penetrate in the sample and reading is noted on the meter.



Fig. 6. Sample for hardness testing

Biodegradation Test: This test was conducted to check the biodegradation ability of the samples. We

conducted this test on different samples of varying filler loading [1]. This test takes 2 months to complete. Weigh the sample before putting it and place three samples of different filler loading in a

pot. The pot must be filled with microorganism-rich soil and after about 2 months take out the sample from the pot and weigh it again as shown in Figure 7.



Fig. 7. Biodegradation sample placing

RESULTS AND DISCUSSION

Effect of Tensile strength, Modulus and Elongation in Enhanced LPDE Composite

Figure 8 shows a decrease in tensile strength with filler and this would be because of the poor interfacial bond between matrix and filler. Filler particles are just adhered on the matrix surface and work as a void weakening the sample. Moreover, when we use date seeds with LDPE the tensile strength decreases but when we use walnut shells with LDPE, its tensile strength decreases more than the first composition which shows that walnut particles have a weaker interfacial bond with LDPE [10]. Their max bearing force is also decreasing.

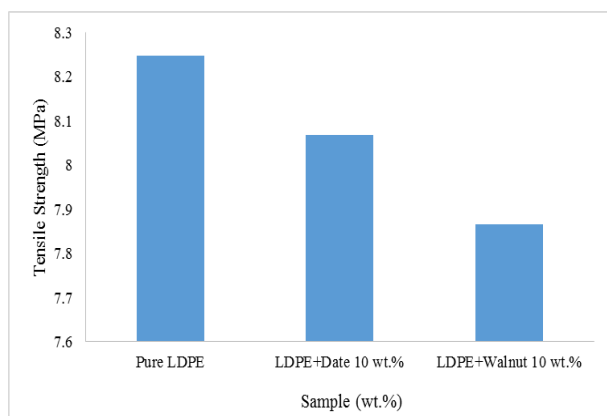


Fig. 8. Tensile strength of individual fillers

Figure 9 shows that by increasing the filler loading, tensile strength decreases. More the amount of filler, more voids are in the sample, which more weakens the sample. Drop in tensile strength is due to porosity, poor adhesion and poor interfacial interaction between both phases [16, 17].

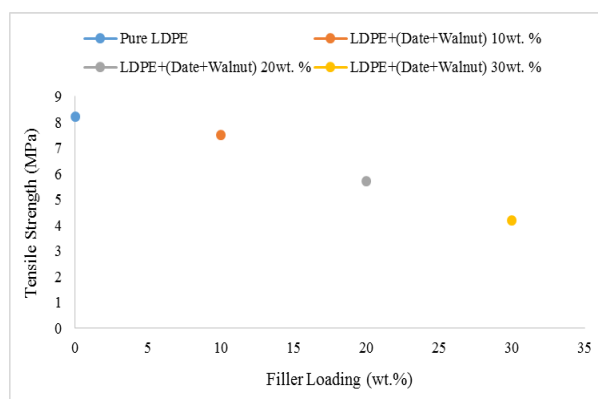


Fig. 9. Tensile strength of combined fillers

Figure 10 shows an increase in modulus with filler that would be due to the resistance shown by filler to LDPE chains to move. Walnut shells resist more than date seeds and this depends on particle size, shape and distribution in matrix [17].

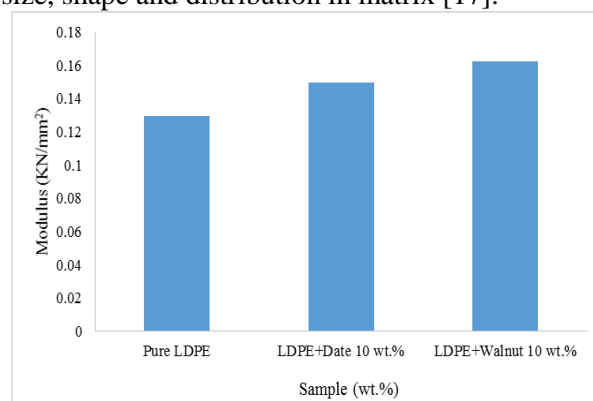


Fig. 10. Modulus of individual fillers

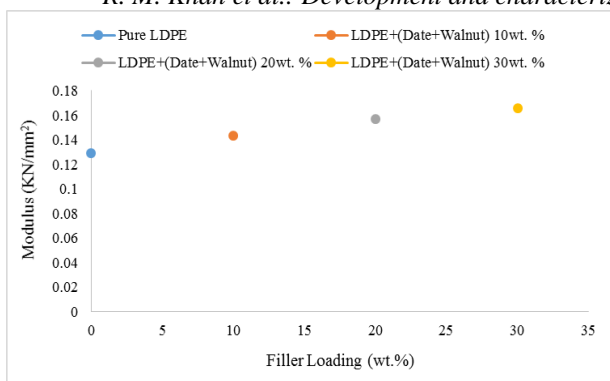


Fig. 11. Modulus of combined fillers

Figure 11 shows the increment in modulus as we increase the filler loading from 0% to 30% of both fillers. As modulus is a measure of the stiffness of a material, that is its resistance to extension. The higher the modulus of a material, the less it extends for a given force. This behaviour can be explained by the fact that adhesion occurred between the filler and the matrix which led to increased stiffness [17]. The LDPE with walnut shells and date seeds powder reinforcement displays a high elastic modulus. The highest value of the modulus was observed for the LDPE composites, attributable to higher strength, stiffness, and better interfacial bonding of fillers.

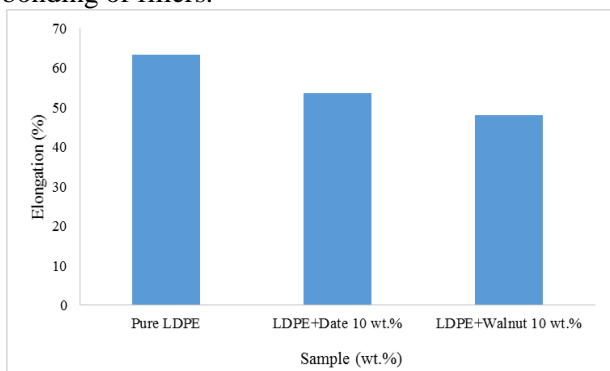


Fig 12. Elongation of individual fillers

Figure 12 shows that the elongation behaviour of LDPE decreases with date seeds and it decreases more with walnut shells due to the weaker interface existing among the composite components. That means, as we use a filler whether it is date seeds or walnut shells, it reduces the ductility of LDPE and moreover, makes the sample rigid [10, 18]. Elongation failure shows the ductility of materials, in other words, the amount of strain it can experience before failure in tensile testing and here the elongation decreases with fillers.

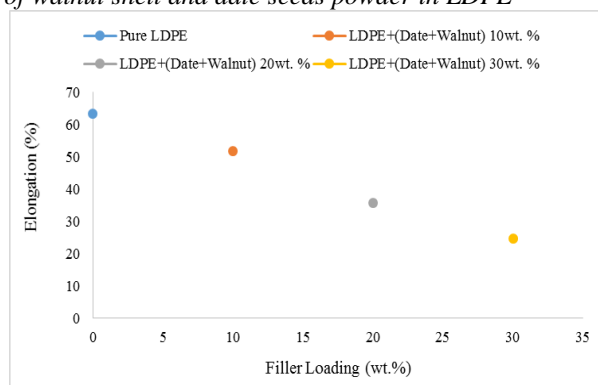


Fig. 13. Elongation of combined fillers

The elongation of the composite decreases with increase in particle concentration because there is adherence of the filler to the polymer phase which results in the reduction of the intermolecular bonds between the filler and matrix and it works for stiffening of the matrix chain. According to the literature, the percentage elongation decreases due to rigid fibres restraining matrix deformation persuading strength gain and brittleness of the resultant composites [17, 18].

Effect of Flexural Strength and Hardness in Enhanced LPDE Composite

As flexural strength expresses the rigidity of sample, in Figure 14 the flexural strength of LDPE increases with date seeds powder and it increases more when we take walnut shell powder with LDPE. This is happening because surface interaction increases due to flexural strength increase.

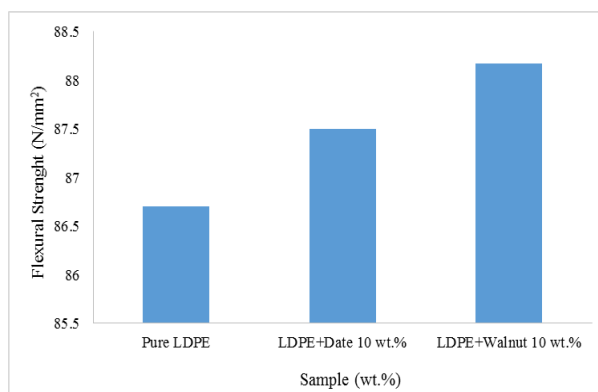


Fig 14. Flexural strength of individual fillers

Figure 15 shows an increase in flexural strength with increased filler loading as by the increase in the amount of filler the surface properties will increase due to good heat transfer at the surface of the mold. As a result, flexural strength and bending force increase. The reinforcement of both fillers in the LDPE led to a change in mechanical properties also depending on the temperature and running conditions. This is anticipated as a result of the high

modulus of both fillers [19]. However, all results proved that LDPE makes the interactions amongst the components stronger and this is proved by the solid-like behaviour of the composite at higher content of both fillers. The results obtained are in good agreement with previous literature concerning filler reinforced composite [19, 20].

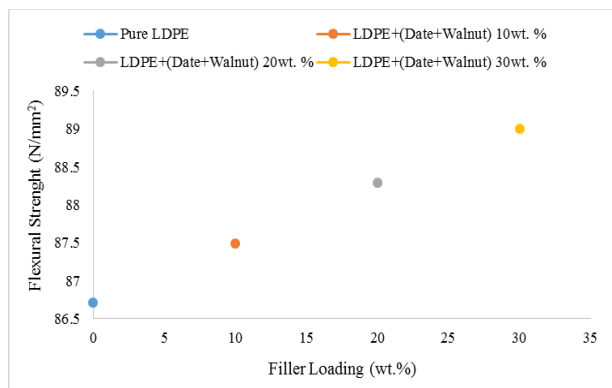


Fig 15. Flexural strength of combined fillers

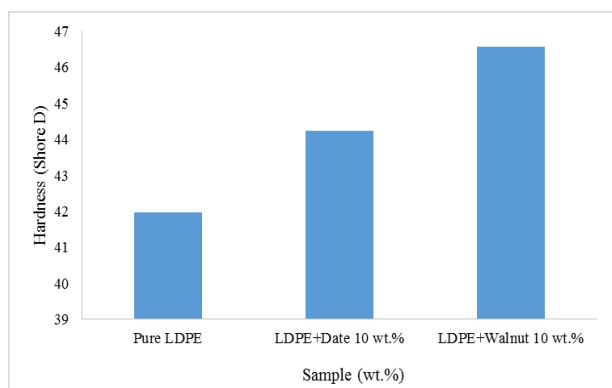


Fig. 16. Hardness of individual fillers



Fig. 17. Hardness of combined fillers

Hardness is a measure of material's resistance to surface indentation. In Figure 16, hardness is increasing by adding filler in the LDPE matrix. Moreover, there is not much change in effect/results of whether we use date seeds or walnut shells [2].

By increasing the filler loading from 0 wt.% to 30 wt.% the hardness of the composite is increasing as the filler enhances the surface property of

composite and resists deformation by penetration as shown in Figure 17. That means that combined reinforcement of date seeds and walnut shell powder increases the abrasion resistance of the sample, as well as the wear resistance (loss of material) [2, 21].

Effect of Water Absorption and Biodegradation in Enhanced LPDE Composite

As shown in Figure 18, both fillers are not water absorbing. They show negligible change in the water absorption test. Moreover, the change in weight would be because some water molecules adhere on the surface, as after drying the sample has the same weight as it had before the test. The date seeds (bio filler) can absorb the water a bit but here no change is seen that would be due to particle size or may be 24 h are not enough time to register water absorption. Whatever in this case, this composite hardly absorbs water which was also found in the literature [9].

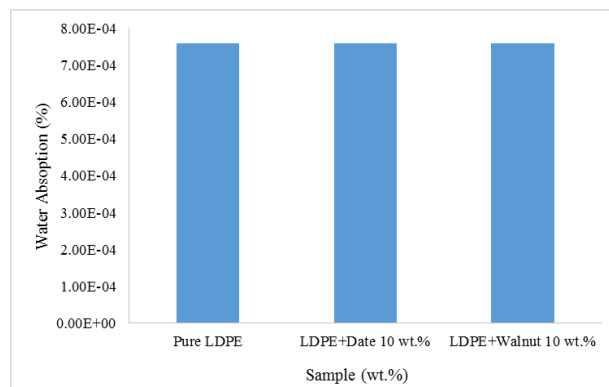


Fig. 18. Water absorption of individual fillers

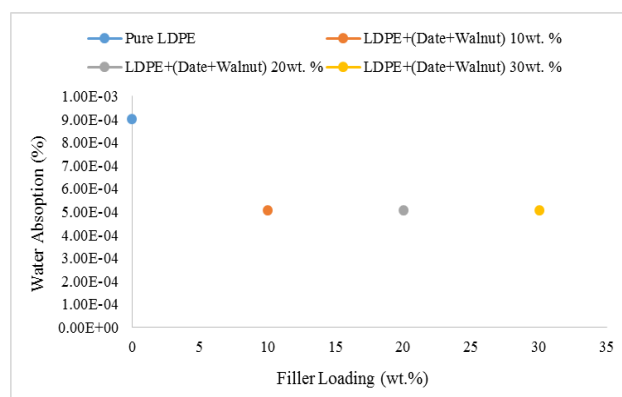


Fig. 19. Water absorption of combined fillers

Figure 19 shows that there is no difference in the weight of the sample before and after the test as there has been no water absorption by combined reinforcement of the composite even by changing the amount of fillers [9].

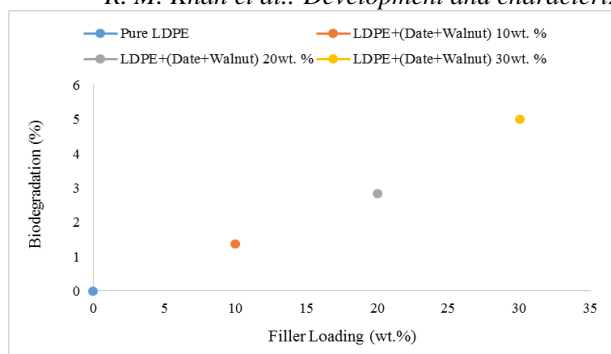


Fig. 20. Biodegradation of enhanced LDPE blend

Figure 20 shows the effect of biodegradation (deterioration) by reinforcement of date seeds and walnut shell powder. The use of biomass filler shows increased reduction in weight as biodegradation is the disintegration of reinforcement materials (date seeds and walnut shells) by bacteria, fungi, or other biological means [22]. Moreover, from 10 wt.% to 30 wt.% biodegradation increases. These are results of just 2 months. By increasing the time these results can be improved that means, biodegradation would increase.

CONCLUSION

The polymer matrix is generally chosen on its intrinsic properties, product requisite, accessibility, cost and manufacturers' awareness with the material. By increasing the proportion of dates and walnuts in LDPE, the tensile strength is getting decreased. On the other hand, the modulus shows a different trend, by increasing the proportion of both fillers, the trend goes high. The most appreciable results are related to the hardness of the composite, as the reinforcement is aiding in increasing the hardness of the composite with increased proportion. As both fillers used in the reinforcement are biomass fillers that is why the biodegradation test showed reduction in weight. So it is a huge advantage of using these fillers as reinforcing agents as they are making the sample biodegradable. There was no water absorption property found in the produced sample. So the sample will not absorb any moisture content. The future recommendation is to study combined reinforcement of walnut shells and date seeds in LDPE with a coupling agent and the effect of processing parameters.

Acknowledgement: The authors would like to acknowledge the Department of Polymer and Petrochemical Engineering, NED University of Engineering & Technology, Karachi, Pakistan for supporting this research work.

REFERENCES

1. A. Valdés, O. Fenollar, A. Beltrán, R. Balart, E. Fortunati, J.M. Kenny, M.C. Garrigós, *Polym. Degrad. Stab.*, **132**, 181 (2016).
2. S. Nitin, V.K. Singh, *J. Mater. Environ. Sci.*, **4**, 233 (2013).
3. S. Roudsari, S. Hamoush, S. Soleimani, T. Abu-Lebdeh, M. HaghighiFar, *Am. J. Eng. Appl. Sci.*, **1** (2018).
4. A. Valdés García, M. Ramos Santonja, A.B. Sanahuja, M.d.C.G. Selva, *Polym. Degrad. Stab.*, **108**, 269 (2014).
5. N.A. Sarsari, S. Pourmousa, A. Tajdini, *BioResources*, **11**, 6968 (2016).
6. D. Chandramohan, A.J. Presin Kumar, *Data Brief*, **13**, 460 (2017).
7. E.V. Bachtar, M. Rüggeberg, S. Hering, M. Kaliske, P. Niemz, *Mater. Struct.*, **50**, 247 (2017).
8. E. Rayón, S. Ferrandiz, M.I. Rico, J. López, M.P. Arrieta, *Int. J. Food Prop.*, **18**, 1211 (2014).
9. M.A. AlMaadeed, Z. Nógellová, M. Mičušík, I. Novák, I. Krupa, *Mater. Design*, **53**, 29 (2014).
10. S.A. Kolawole, D. Abdullahi, B.M. Dauda, U.S. Ishiaku, *Int. J. Sci. Res.*, **4**, 1412 (2015).
11. R. Khantwal, G. Gupta, R.S. Negi, *Int. J. Scient. Eng. Res.*, **7**, 179 (2016).
12. A.J. Mohammed, *Int. J. Sci. Tech.*, **3**, 18 (2014).
13. S.A. Rayabag, P.U. Raikar, S. Malagi, *Int. Adv. Res. J. Sci. Eng. Technol.*, **4**, 57 (2017).
14. Q. Zhang, Y. Li, H. Cai, X. Lin, W. Yi, J. Zhang, *Results Phys.*, **1**, 1 (2018).
15. P.C. Gope, V.K. Singh, D.K. Rao, *J. Reinf. Plast. Compos.*, **34**, 1075 (2015).
16. M. Doddamani, G. Parande, V. Manakari, I.G. Siddhalingeswar, V.N. Gaitonde, N. Gupta, *Mater. Perform. Char.*, **6**, 54 (2017).
17. C.B. Talikoti, T.T. Hawal, P.P. Kakkamari, D. M.S. Patil, *Int. Res. J. Eng. Tech.*, **2**, 721 (2015).
18. A. Selcuk, M. Tufan, T. Gulec, A. Temiz, *Int. Cauc. Fores.*, **1**, 947 (2013).
19. V.K. Singh, *Sci. Eng. Compos. Mater.*, **22**, 1 (2015).
20. S. Pashaei, S. Hosseinzadeh, *Iranian Chem. Commun.*, **5**, 138 (2016).
21. D.P.P. Rao, B.R. Kumar, *Int. J. Eng. Trend. Tech.*, **24**, 151 (2015).
22. W. Cheng, G. Liu, L. Chen, *Appl. Sci.*, **7**, 1 (2017).

Removal of caprylic acid impregnated on resins using organic solvents and water

M. A. P. Rocha¹, N. P. Merlo², M. R. Franco Júnior^{1*}, N. R. A. F. Rocha², W. A. Pereira²

¹ Federal University of Uberlândia, Chemical Engineering Faculty, PPG Biocombustíveis, Campus Santa Mônica, Uberlândia MG, Brazil

² Rio Verde University, Environmental Engineering Department, Fazenda Fontes do Saber, Rio Verde, Goiás, Brazil

Received May 7, 2019; Revised February 3, 2020

In this study, organic solvents and water were used to remove caprylic or octanoic acid from resins. The conventional batch method of stirring with a solvent-extractor produced a reasonable quantity of unbound acid in the liquid phase (0.00433–0.0772 g.L⁻¹). Removal characteristics were investigated with water, ethylene glycol (MEG), diethylene glycol (DEG), ethanol and butanol. For the anionic and cationic resins in both exposure times studied, the order of maximum removed amount was: using water (95%) > MEG (60%) ≈ DEG (50%)>ethanol(25%)>butanol (20%). On the other hand, the removal percentage was very low and similar in the mixed resin system. In spite of being soluble in alcohols, caprylic acid was a little removed from resins when attacked by them.

Keywords: caprylic acid; resins; DEG; MEG; exposure time.

INTRODUCTION

Regeneration and reusability of an adsorbent are highly appreciated in industry due to the factors of economy, environmental aspects and operational convenience. However, regeneration was not often employed in some cases because of the difficulty and inconvenience of the procedure. Recently, Punyapalakul *et al.* (2013) [1] found that the reused Plasma Arc Cured (PAC) resin had a significant loss of adsorption capacity, while functional silicas with better regeneration ability required a high-cost synthesis. In the case of adsorbent MIPs (Molecularly Imprinted Polymers), Yu *et al.* (2008) [2] obtained a satisfactory regeneration in a percentage of 95% for the adsorbent MIP, whereas the mixture of acetone and sodium hydroxide (NaOH) solution as regeneration solvent was not "green" or ecologically correct.

In relation to dry washing, some alternative commercial adsorbents have been discussed in recent research studies [3-5]. One of these adsorbents is the Purolite® PD206 resin, which has shown good performance in biodiesel purification [3]. The adsorption of biodiesel contaminants on PD 206 resin can occur in two ways: by ion exchange or by physical adsorption.

The regeneration of resins or adsorbents must be efficient to increase the removal of contaminants and the life time of the adsorbent material. In addition, the optimization of the regeneration methods is essential to increase the efficiency and economy of the dry washing processes.

Recently, Stapea *et al.* (2016) [6] published a work involving resins used in dentistry, in which a solvent, DMSO, was tested as a compound of new potential that could promote the adhesion of the hydrophilic resin to the dentin of the human tooth. In this case the researchers sought to improve the thermo-mechanical properties of the resin by introducing an organic solvent. Different concentrations of DMSO in water were employed in the study. According to Ekambaram *et al.* (2015) [7], in addition to influencing the mechanical and physical properties of resins, solvents have a great impact on resin-dentin bonding. In this sense, the second assertion of the researchers must be explored so that experimental studies can define a solvent that positively affects the bond that one wishes to strengthen or weaken.

Solubility data [8,9] have confirmed that caprylic acid has some solubility in water and is highly soluble in some organic solvents [8]. This fact encouraged the research on the possibility to extract this solute from Purolite resins employing pure organic compounds or water. Among available solvents, in this research we used diethylene glycol (DEG), monoethylene glycol (MEG), ethanol and butanol. Therefore, this work will be developed in considering the potentialities of the solvents by checking the removal of caprylic acid from three different resins. The experimental work will answer what solvent has affinity to caprylic acid and could be used with success to regenerate resins previously used in biodiesel production [10-13].

* To whom all correspondence should be sent:

E-mail: moilton@ufu.br

METHODOLOGY

The experimental procedure for desorption of caprylic acid using pure organic compounds or water will be described below. The experiment was similar to that used by Franco *et al.* [14]. Desorption experiment was performed using a 150-mL glass vessel placed on a magnetic stirrer. The pure solvent was weighed on a semi-analytical balance (SHIMADZU, AUW Series, $\pm 10^{-2}$ g). One gram of resin previously contaminated with caprylic acid was added to the vessel and the system was stirred at 300 rpm for about 15-30 min. After stirring, the equipment (IKA, RH Basic) was switched off and the solid-liquid mixture was decanted for a few minutes. Using a glass syringe, 15.0 mL of the decanted mixture was sampled and titrated with 0.01 N sodium hydroxide solution (V_{NaOH} , mL) with phenolphthalein as an indicator. Thus, the concentration of caprylic acid in the liquid phase can be determined by potentiometric titration with alkaline solution using a drop of phenolphthalein as indicator. In the literature the use of a mixture of ether and ethanol (1:1) as diluents of the sample to be titrated was recommended. In this case, for every 2 g of sample it is recommended to use 25 mL of dilution mixture. In this research, 15 mL of sample were collected in duplicate, so that the dilution can be initially dispensed. Different solvent extractors were used. The reagents available were of P.S. grade 99.5% purity and were purchased from Dinâmica Química Contemporânea LTDA. Anionic, cationic and mixed (Purolite) resins were contaminated by caprylic acid and submitted to regeneration treatment taking into account the following parameters: type of resin, exposure time and type of solvent. The experiments were conducted at controlled temperature using a thermostatic bath, as well as at room temperature.

Solid Sample Preparation

Ten grams of resin were weighed into a beaker and two drops of caprylic acid measured with microsyringe (Hamilton; 100 μL) were added. The mass of added acid (0.0552 ± 0.0030 g) to the resin can be measured by knowing its density, as well as by using an analytical balance. The vial (VIDROLABOR®) containing the contaminated solid was shaken in a centrifuge for a given period of time, about one hour. The sample remained at rest according to the contact time to be tested. This exposure time varied from 14 to 170 hours, or more. After this period the sample was used for the desorption tests. After the treatment, the liquid

sample was titrated and the results were presented for the desorption of caprylic acid from anionic, cationic and mixed resins. The effect of the exposure time of the resin to the acid can be observed. All experiments were conducted at room temperature (25-27°C).

Tables and Figures illustrate the results for the regeneration studies of anionic, mixed and cationic resins. Most of the titration analyzes were done in duplicate or triplicate with δ being the standard deviation. The mass (m) and final acid concentration in the liquid mixture is given by $C \pm \delta$ in g.L^{-1} .

As the exposure time of octanoic acid with the resin increases, the desorption of this solute turns to be more difficult. This is extremely disadvantageous for the process of regeneration. Tests with all resins used in the biofuels line should be carried out using organic solvents and water. The final concentration of the acid in solution (C , g.L^{-1}) will allow to obtain the mass of extracted acid. It is believed that some resins, if contaminated with this acid, after 24 h of exposure, cannot be regenerated. Only a solid phase evaluation can define its possible re-use in adsorption processes.

RESULTS AND DISCUSSION

The comparison among five solvents (water, ethanol, butanol, MEG and DEG) for acid-contaminated resin treatment was carried out doing blank tests as an initial study. Solvents permeated the resin and acid will be desorbed from the pores and then, dissolved in the liquid phase. Acid molecules that were not desorbed will stay on the resin surface during this process and connect to each other.

The acid removal performance of solvents was examined by doing experimental blank tests with the clean (not used) resin as it could contain some acid that belongs to the fresh resin. As it can be seen from Table 1, MEG and DEG extract a higher amount of acid from the resins. Results show that all solvents remove an amount of acid which can influence the final results of removing. In Table 1, 15 mL of sample was titrated and then the volume of NaOH solution (0.01 mol/L) used can confirm that there is some acid removed which is not caprylic acid.

In order to exemplify the removal results, together with the concentration and final mass levels of acid in the liquid phase ($C_{\text{Liq}}^{\text{ac}}$, $m_{\text{Liq}}^{\text{ac}}$), and residual mass of acid in the solid $m_{\text{Res}}^{\text{ac}}$, it was chosen to present the data for the tests with the anionic resin (Table 2).

Table 1. Volume of the NaOH solution (mL) used for titration of a sample in the blank extraction process of 1.0 g of original resin.

Solvent	Resin		
	Mixed	Cationic	Anionic
water	0.25	0.35	0.25
MEG	1.55	1.45	0.95
DEG	1.2	1.45	1.35
ethanol	0.55	0.65	0.55
butanol	0.35	0.55	0.55

Table 2. Results for the removing of caprylic acid from the anionic resin exposed to the contaminant for 170 hours.

Solvent	$C_{Liq.}^{ac.}/g.L^{-1}$	$m_{Liq.}^{ac.}/g$	$m_{Res.}^{ac.}/g$
water	0.0527±0.005	0.00264	0.00271±0.0004
MEG	0.0772±0.006	0.00390	0.00148±0.0002
DEG	0.0167±0.003	0.00082	0.00460±0.0005
ethanol	0.00935±0.001	0.00047	0.00489±0.0007
butanol	0.00432±0.001	0.00011	0.00510±0.0008

Table 3. Results for the removing of caprylic acid from the cationic resin exposed to the contaminant for 170 hours.

Solvent	$C_{Liq.}^{ac.}/g.L^{-1}$	$m_{Liq.}^{ac.}/g$	$m_{Res.}^{ac.}/g$
water	0.0671±0.006	0.0034	0.00398±0.0003
MEG	0.0627±0.006	0.0032	0.00219±0.0002
DEG	0.0094±0.0008	0.0005	0.00399±0.0003
ethanol	0.0577±0.005	0.0029	0.00244±0.0002
butanol	0.0072±0.0007	0.00036	0.00230±0.0002

Table 4. Results for the removing of caprylic acid from the mixed resin exposed to the contaminant for 170 hours.

Solvent	$C_{Liq.}^{ac.}/g.L^{-1}$	$m_{Liq.}^{ac.}/g$	$m_{Res.}^{ac.}/g$
water	0.0193±0.003	0.00096	0.00438±0.0003
MEG	0.0526±0.008	0.00265	0.00271±0.0002
DEG	0.0236±0.004	0.00120	0.00420±0.0003
ethanol	0.0094	0.00048	0.00487±0.0004
butanol	0.0094	0.00047	0.00487±0.0005

Note that alcohols are unsuitable for removal of caprylic acid from resins; water and MEG are the most recommended ones. Figs. 1 and 2 show the effect of time exposure on the acid removal ability. The influence of the dielectric constant on caprylic acid removal ability is shown in Figs. 1 and 2. Thus, the x-axis contains dielectric constant data for butanol (17.1), ethanol (24.3), diethylene glycol (31.7), monoethylene glycol (41.2) and water (76.7), respectively. Comparing the two exposure

times (14 h and 170 h), it is clear that the results of acid removal are different. We believe that it is because, as Fig. 2 shows, the caprylic acid will be much stickier at high contact time of solute and resin.

Also, the influence of the solvent is clear for the cases studied. It is noted that water acted as the most appropriate solvent to remove the solute from all resins and that butanol, which has a lower dielectric constant, was unsuitable for the process.

Summing up, the removal efficiency depended largely on the solvent type and less on the exposure time.

From Fig. 1, none of the solvents proved to be suitable for recovering the mixed resin, which should probably be discarded after to its use. Also, results in Fig. 1 are presented for two experiments which were carried out using the same resin. Fig. 2 shows that the exposure time of the resin to the acid influences the percentage of removal from the resin, so that lower removal values are observed when the exposure time is eleven times greater. In the two exposure times, a similar behavior of the solvents, regarding the removal, is observed for the three resins studied. Solvents with higher dielectric constant are more suitable for removal of caprylic acid.

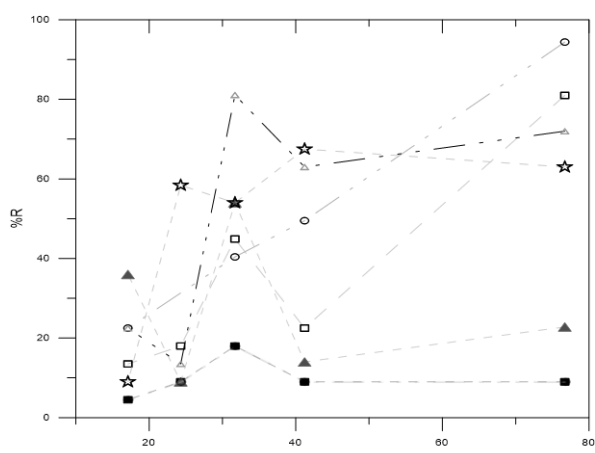


Fig. 1. Removal of caprylic acid as a function of dielectric constant of extractor solvent. (14 hours of exposure). (type of resin: ○☆ Anionic; ■▲ Mixed; □△ Cationic)

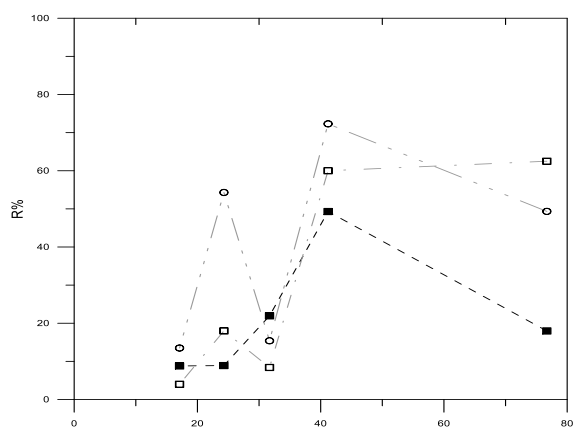


Fig. 2. Removal of caprylic acid as a function of dielectric constant of extractor solvent. (170 hours of exposure). (type of resin: ○ Anionic; ■ Mixed; □ Cationic)

Although the removal results using MEG and DEG solvents showed pronounced variation for the

experiments with 170 h of contamination, water continues to be the best solvent, when comparing the costs of the removing process. What is clear from the removal measurements is that for all the resins impregnated with acid, alcohols are not recommended as solvents.

CONCLUSIONS

Among all solvents employed, water was the most suitable solvent to remove caprylic acid from the solid phase. On the other side, the use of alcohols to clean resins contaminated with caprylic acid is not recommended.

As the time of contact of resin with the acid increases, the removal of the acid from the resin through the use of extractor solvents becomes more difficult.

Acknowledgement: This research was partially supported by the Rio Verde University (Proposal approved in CHAMADA INTERNA 02/2018 – PRPI/UniRV – Scholarship of N. A. F. Rocha)

REFERENCES

1. P. Punyapalakul, K. Suksomboon, P. Prarat, S. Khaodhiar, *Sep. Sci. Technol.*, **48**, 775 (2013).
2. Q. Yu, S. Deng, G. Yu, *Water Res.*, **42**, 3089 (2008).
3. M. Berrios, R. L. Skelton, *Chem. Eng. J.*, **144**, 459 (2008).
4. K. Suppalakpanya, S. B. Ratanawilai, C. Tongurai, *Applied Energy*, **87**, 2356 (2010).
5. Z. J. Predojevic, *Fuel*, **87**, 3522, (2008).
6. T. H. S. Stapea, A. Tezvergil-Mutluaya, M. M. Mutluaya, L. R. M. Martins, R. L. do Prado, E. C. G. Pizic, L. Tjaderhane, *Journal of the Mechanical Behavior of Biomedical Materials*, **64**, 220 (2016).
7. M. Ekambaram, C. K. Y. Yiu, J. P. Matinlinna, *Int. J. Adhes.*, **57**, 22 (2015).
8. K. T. Tan, M. M. Gui, K. T. Lee, A. R. Mohamed, *J. Supercritical Fluids*, **53**, 82 (2010).
9. S. Budavari, *The Merck Index: An Encyclopedia of Chemicals, Drugs, and Biologicals*, 12th edn., Merck, ISBN 0911910123, 1996.
10. D. R. Lide, *CRC Handbook of Chemistry and Physics*, 70th edn., Boca Raton (FL), CRC Press, 1990.
11. P. Valle, A. Velez, P. Hegel, G. Mabe, E. A. Brignole, *J. Supercritical Fluids*, **54**, 61 (2010).
12. M. M. Gui, K. T. Lee, S. Bhatia, *J. Supercritical Fluids*, **49**, 286 (2009).
13. J. M. Marchetti, V. U. Miguel, A. F. Errazu, *Renewable and Sustainable Energy Reviews*, **11**, 1300 (2007).
14. M. R. Franco Júnior, N. R. A. F. Rocha, W. A. Pereira, N. P. Merlo, *Bulg. Chem. Commun.*, **51**(3), (2019).

Investigation and optimization of a novel MAHB reactor for COD and lignin removal and methane production using response surface methodology (RSM) and artificial neural network (ANN)

S. R. Hassan¹, I. Dahlan^{2*}

¹Faculty of Bioengineering and Technology, Universiti Malaysia Kelantan, Jeli Campus, 17600, Jeli, Kelantan, Malaysia

²School of Chemical Engineering, Universiti Sains Malaysia, Engineering Campus, Seri Ampangan, 14300 Nibong Tebal, Pulau Pinang, Malaysia

Received July 10, 2019, Revised January 7, 2020

In this study, response surface methodology (RSM) and artificial neural network (ANN) were used to investigate and optimize COD and lignin removal and methane production rate in a novel modified anaerobic hybrid baffled (MAHB) reactor treating recycled paper mill effluent (RPME). Both feeding COD concentration and hydraulic residence time (HRT) are recognized as the two most important factors that affect COD and lignin removal and methane production rate. RSM analysis gives an optimum condition with HRT of 3.93 days and feeding COD concentration of 3020.88 mg L⁻¹ that yield COD removal efficiency of 97.42 %, lignin removal efficiency of 59.59 % and methane production rate of 8.07 L CH₄ day⁻¹ with desirability value of 0.897. From the analysis using ANN, results show a good agreement between experimental and ANN outputs for COD removal, lignin removal and methane production rate with R² values of 0.970, 0.9906 and 0.9545, respectively. These demonstrated that RSM and ANN were effective to assess and optimize the MAHB reactor system for COD and lignin removal and methane production, which provides a promising guide to further improvement of the system for potential applications.

Keywords: Modified anaerobic baffled reactor, Recycled paper mill effluent, RSM, ANN, Anaerobic digestion.

INTRODUCTION

The rise in environmental concerns related with the production of energy with CO₂ mitigation policies has renewed the interest in anaerobic digestion technologies. Anaerobic digestion (AD) is a series of bacteria events that convert organic matter in wastewater to methane (CH₄) and carbon dioxide (CO₂) that occurs in the absence of oxygen (O₂). This process has advantages in biogas recovery and waste stabilization. It has also been proven as a competent process in green technology for disposing crop residue, food waste, sewage sludge and animal manure [1,2]. Methane is a rich source of renewable energy which contributes to environmental conservation and sustainability by replacing the fossil fuel. This in turn govern the wide use of AD as an attractive means for paper mill wastewater treatment all around the globe while more and more new process configurations were developed [3].

The production of methane will be higher when several responses are combined in an optimized condition that will enhance the conversion process of organic matters. Among the factors that affect the methane fermentation are hydraulic retention time (HRT) and feeding COD concentration. If the process does not fall into the suitable range of optimized parameters, there is a tendency for

potential toxicity and digester failure. Mostly, the previous studies optimized the optimum conditions for COD and lignin removal and biogas production by the conventional method by changing one factor at a time. This is a method in which a single factor is varied while all the other factors are kept fixed at a specific condition. It is time consuming, laborious and difficult to reach the optimal conditions due to ignoring the interactions between variables. Hence, in this study D-optimal design of response surface methodology (RSM) and artificial neural network (ANN) are used as a beneficial technique for a statistical and mathematical process modeling and optimizing due to a more practical approach compared to the other as it arises from an experimental methodology. The results enable highlighting interactive effects among the variables and, eventually, it depicts the overall effects of the parameters on the process [4].

Several researchers described the application of RSM in wastewater treatment studies for multidisciplinary design of optimization study. Chou et al. [5] used CCD design of RSM to identify the optimum COD solubilization condition while treating palm oil mill effluent whereas Halim et al. [6] applied RSM based on central composite rotatable design to optimize the transesterification of waste cooking oil using continuous packed-bed reactor by manipulating two main variables which are substrate flow rate and packed-bed

* To whom all correspondence should be sent:

E-mail: chirvan@usm.my

height. The results illustrated the effects of the operating variables along with their interactive effects on the responses. For better accuracy of the predicted model obtained by D-optimal design, artificial neural network (ANN) analysis was used. Previous study also showed that ANNs were successfully used to model the results of COD and lignin removal and biogas production with an expanded granular sludge-bed (EGSB) reactor [7] and an upflow anaerobic sludge blanket reactor (UASB) [8]. Holubar et al. [9] also used ANNs to control and model methane production from anaerobic continuously stirred tank reactors under different organic loading rates.

In the present study, a novel MAHB reactor was developed where each modified baffle has its own characteristics (form/shape) to facilitate a better contact and greater mixing of wastewater and anaerobic microorganisms [10]. This novel MAHB is a combination of regular suspended-growth and fixed biofilm systems. Furthermore, the treatment of this recycled paper mill effluent (RPME) is rarely studied using ABR. With RSM and ANN, the interactions of influencing parameters on COD

and lignin removal, as well as methane production rate can be evaluated. Thus, the main objective of this research is to explore the interaction and to investigate and optimize a novel MAHB reactor for COD and lignin removal and methane production rate using response surface methodology (RSM) and artificial neural network (ANN) by developing an active methanogens biomass in treating RPME.

MATERIAL AND METHODS

The schematic diagram of the laboratory-scale MAHB reactor is shown in Figure 1. The basic design of the MAHB reactor is rectangular in shape that contains five compartments which are separated by a modified vertical baffle. The reactor has a total effective volume of 58 L. Polypropylene ring packings are used as media for supporting the biofilm formation and these packing materials are located at the undersurface of compartments 2 and 3. Sampling ports are present on the top of each compartment and the reactors are maintained at a constant temperature of $35 \pm 0.2^\circ\text{C}$. Samples were collected from each compartment for analysis together with the effluent.

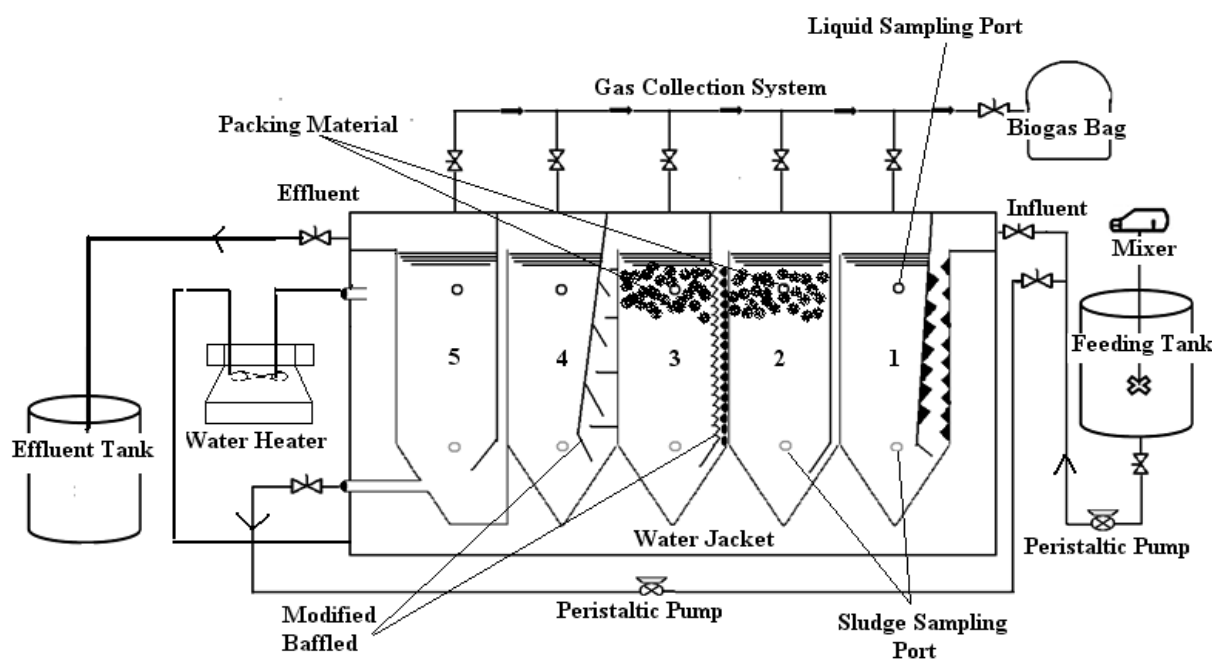


Figure 1. Schematic diagram of the modified anaerobic hybrid baffled reactor

Bioreactor operation

The inoculum used for seeding was anaerobic granular sludge (10% v/v) taken from the anaerobic pond of Malpom Industries Berhad, which was mixed with 750 mg L^{-1} COD of RPME taken from Muda Paper Mills Sdn Bhd. The characteristics of RPME used and the startup of MAHB reactor have been reported previously [11]. The steady-state

performance was evaluated at different influent COD concentrations ($1000\text{--}5000 \text{ mg L}^{-1}$) and hydraulic retention times (HRT) of 1-7 days. Variation of $\pm 5\%$ in effluent COD concentration at each condition was considered as the criterion for steady-state conditions. COD was measured using the spectrophotometer DR-2800 according to the reactor digestion method [12], while biogas composition was determined using Shimadzu GC-

FID with propack N column. Carrier gas was helium set at a flow rate of 50 ml min⁻¹, column temperature of 28°C, detector temperature of 38°C and injector temperature of 128°C. The lignin concentration was determined using DR-2800 spectrophotometer (HATCH model) by the tyrosine method. Triplicate samples were collected for each parameter reading to increase the precision of the results, and only the average value was reported throughout this study.

Experimental design and optimization

The statistical software Design-Expert 6.0 (Stat Ease Inc. Minneapolis, USA) was used to determine the optimal combination of parameters equivalent to the optimized responses achieved. D-optimal design of RSM was used in the optimization of COD and lignin removal and methane production rate from anaerobic digestion of RPME. The hydraulic retention time (HRT) and feeding COD concentration were chosen as the factors and the experimental ranges used are shown in Table 1. According to the design, a total of 12 runs of experiments were performed (Table 2). For optimal point prediction, experimental data were fitted with a second-order polynomial model. The adequacy of the model was evaluated by analysis of variance (ANOVA) and coefficient of determination, R². The model describes the interaction among the parameters influencing the response by varying them concurrently. For ANN, a narrower range of 3 – 5 days for HRTs and 2500 – 4500 mg L⁻¹ for feeding COD concentration was used. This ANN was done to investigate whether the data obtained fit well with the data from RSM and to achieve better values of performances in terms of responses.

Table 1. Experimental ranges and levels of the factors used

Factors	Range	
	-1	1
Hydraulic retention time/ HRT (days), x_1	1	7
Feeding COD concentration (mg L ⁻¹), x_2	1000	5000

Table 2. Factors used for interaction study by D-optimal design of RSM

Run	Hydraulic retention time/HRT (days),	Feeding COD concentration (mg L ⁻¹),
	x_1	x_2
1	4	1000
2	1	5000
3	1	5000
4	1	3000
5	1	1000
6	7	3000
7	4	3000
8	7	1000
9	7	5000
10	1	1000
11	4	5000
12	7	5000

All data used in RSM and ANN were taken during steady-state process for each experimental condition. Eighty one data points from 27 different continuous experiments were used as shown in Table 3. The 81 sample sets were split into training (80%), validation (10%) and testing (10%) data sets. The ranges for input and output data used to perform ANN optimization study are shown in Table 4.

A feed forward network with two hidden layers was used in this study which is trained using a backpropagation algorithm by means of Levenberg-Marquardt (LM) method. A two-layer ANN with sigmoidal transfer function was used for both hidden neurons and the input and output neurons.

RESULTS AND DISCUSSION

Response surface analysis regression

Two variables, namely hydraulic retention time (HRT) and feeding COD concentration were coded as x_1 and x_2 , respectively. The three responses - COD removal, lignin removal and methane production rate were denoted as Y_1 , Y_2 and Y_3 , respectively. The responses in coded terms are summarized in Table 5.

Table 3. Experimental conditions

Type of wastewater	No of batches	No of data points	HRT (days)	Influent COD (mg L ⁻¹)
RPME	27	81	3 -5	2500 – 4500

Table 4. Range of input and output parameters used in ANN

Parameters	Minimum	Maximum	Units
HRT	3	5	days
Influent COD	2500	4500	mg L ⁻¹
Methane production rate	0	8.09	L CH ₄ day ⁻¹
COD removal	0	97	%
Lignin removal	0	60	%

Table 5. Results of response surface design analysis

Run	Variables		Responses			
	x_1 (day)	x_2 (mg L ⁻¹)	Y_1 (%)	Y_2 (%)	Y_3 (L CH ₄ day ⁻¹)	Y_3 (L CH ₄ gCOD ⁻¹ day ⁻¹)
1	4	1000	95.41	51.16	4.903	4.90
2	1	5000	94.28	43.13	4.354	0.87
3	1	5000	94.45	45.81	4.116	0.82
4	1	3000	95.45	49.47	7.362	2.45
5	1	1000	94.20	42.67	5.317	5.32
6	7	3000	95.86	49.62	6.817	15.85
7	4	3000	97.93	62.83	8.475	11.30
8	7	1000	94.29	45.00	3.403	3.40
9	7	5000	94.41	40.54	5.097	7.18
10	1	1000	94.46	42.67	5.646	5.65
11	4	5000	95.59	49.23	5.231	4.18
12	7	5000	94.18	45.87	5.197	7.32

As can be seen, Y_1 gives values of ≥ 92.18 %, Y_2 gives a value of ≥ 40.54 % and Y_3 gives a value of ≥ 3.403 L CH₄ day⁻¹. All responses were then analysed to investigate the interaction and to predict the optimum values. The experimental data were analysed and results indicated that the models are greatly significant with very low probability values (<0.0001 - <0.0074) which signifies that independent variables model terms were significant at 95% confidence level.

(a) *Effect of independent variables on COD removal.* COD removal efficiency was found to be a function of hydraulic retention time, (HRT) and feeding COD concentration. The feeding COD concentration affects the removal efficiencies since the substrate-to-microorganism ratio is affected by the feeding COD concentration. The experimental results show that COD removals are between 94 - 98 % in the range of COD concentrations and HRT studied. These results indicate that the MAHB reactor had a higher ability to resist shocking load at high COD concentrations. The compartmentalization of the MAHB reactor offered good phase separation that is able to convert substrate in depth, which acts as a main contributor

to the high COD removal in this system. Multiple regression analysis was applied on the experimental data and the results are fitted with second order polynomial equation. The relationship between COD removal and the two variables in coded terms is shown in Equation (1):

$$Y_1 = 97.42 + 0.013x_1 + 0.032x_2 - 1.51x_1^2 - 1.66x_2^2 - 1.934E-004x_1x_2 \quad (1)$$

where Y_1 is COD removal (response) in percentage, x_1 and x_2 are coded terms for feeding COD concentration (mg L⁻¹) and hydraulic retention time (days), respectively. The results using analysis of variance (ANOVA) for COD removal responses are as tabulated in Table 6. The *F-values* and *p-values* are used to measure the degree of significance of each coefficient. Larger *F-values* and smaller *p-values* denote higher significance of the corresponding coefficients. *P-values* less than 0.0500 indicate significant model terms. In this case, the square effects of HRT (x_1^2) and feeding COD concentration (x_2^2) were significant in terms of the model. The model *F-values* of 20.52 and *p-values* less than 0.0010 indicate significant model terms.

Table 6. ANOVA results for COD removal responses

Model term	Coefficient estimate	Standard error	F-value	p-value
Intercept	97.42	0.26	20.52	0.0010
x_i	0.013	0.12	0.012	0.9165
x_2	0.031	0.12	0.071	0.7984
x_1^2	-1.51	0.24	40.80	0.0007
x_2^2	-1.66	0.24	49.53	0.0004
x_1x_2	-0.0001934	0.14	0.000001993	0.9989

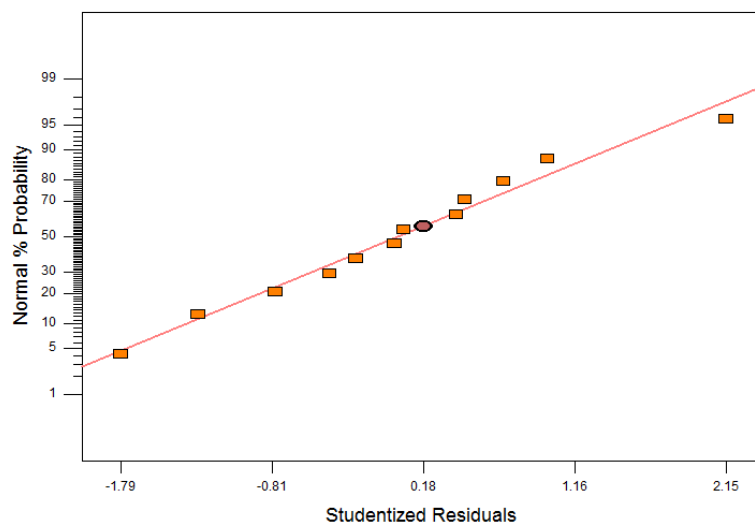


Figure 2. COD removal plot of normal probability with respect to HRT and feeding COD.

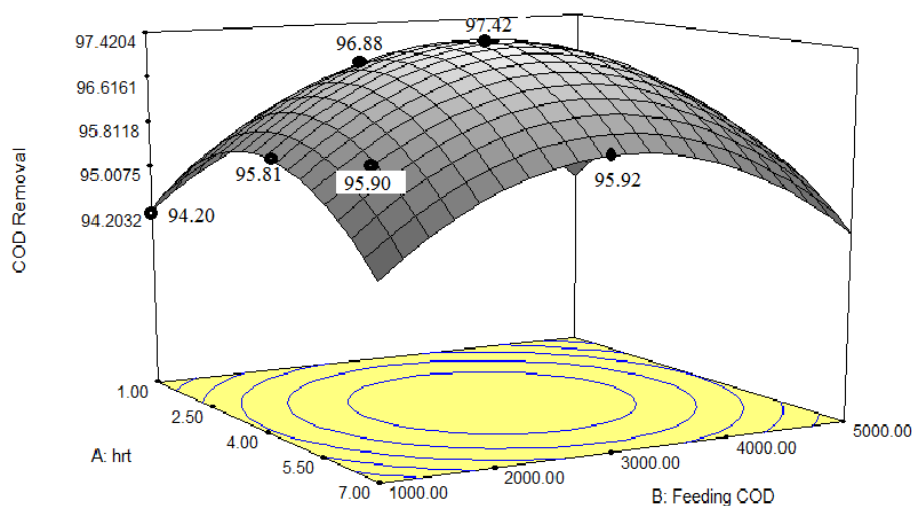


Figure 3. COD removal 3D plots predicted with respect to HRT and feeding COD.

Figure 2 shows the normal probability plot of residuals for COD removal which can be used to indicate whether the standard deviation of actual and predicted responses follows the normal distribution. The figure shows that all residuals are near to a straight line and no severe sign of abnormality of the experimental data is denoted.

This suggests that the underlying error is normally distributed. A portrayal of the 3D plot of COD removal with respect to the two variables is shown in Figure 3. Results indicate that the two variables influence the response as defined earlier.

As shown in Figure 3, as the variables (HRT and feeding COD concentration) increase, an increase

in the response is achieved. Then, as the optimum condition is achieved (highest peak of removal efficiency), a reduction in responses is noted once the variables are further increased. Based on Figure 3, an increase in HRT from 1 to 4 days and in feeding COD concentration from 1000 to 3000 mg L⁻¹ caused a remarkably high COD removal, (95 – 96%). The interaction of variables towards responses can be explained through the contour plot. Variable x_1 is fixed at 4 days to analyse the effect of increasing x_2 towards Y_1 . As can be seen, as the values of x_2 increase from 1000 to 2000 mg L⁻¹, the response Y_1 shows an increment from 95.81 % to 96.88 %. Further increase of x_2 gives an optimum value of Y_1 of 97.42 %. However, as x_1 further increases to 5000 mg L⁻¹, a slight reduction of Y_1 is noticed. The reduction of responses at higher x_2 was mainly attributed to the greater toxicity to methanogens in the long run. This is due to the low biodegradability of the microorganisms that cause acid accumulation, which affects the activity of some bacteria and contributes to deteriorate the effect on the reactor performance [13]. For a fixed variable x_2 at 3000 mg L⁻¹, an increment of x_1 from 1 to 4 days shows an increment in Y_1 from 95.90 to 97.42 %. However, further increments of x_1 to 7 days show a reduction in value of Y_1 of 95.92 %. From the interaction of contour plots, it is clearly seen that the maximum value of the predicted COD removal efficiency is 97.42 % at HRT of 4 days and feeding COD concentration of 3000 mg L⁻¹, whereas the minimum predicted response (95.73%) was achieved at HRT of 4 days and feeding COD of 1000 mg L⁻¹.

(b) *Effect of independent variables on lignin removal.* ANOVA results for lignin removal are as shown in Table 7.

Table 7. Regression analysis using D-optimal response surface methodology

Model term	Coefficient estimate	Standard error	F-Value	p-Value
Intercept	59.6	1.93		
x_i	0.18	0.91	0.04	0.8463

(c) *Effect of independent variables on methane production rate.* One important factor that indicates better microbial activities inside the MAHB reactor is the production of biogas, specifically methane gas. High methane production indicates that the methanogenic bacteria are in good activity and consume the substrate inside to produce methane.

x_2	-0.15	0.91	0.026	0.8772
x_1^2	-8.43	1.78	22.41	0.0032
x_2^2	-7.79	1.78	19.11	0.0047
x_1x_2	-0.84	1.03	0.67	0.4458

From the results, the square effect, x_1^2 and x_2^2 shows significant model terms of the response. Linear effect (x_1 and x_2) and two level interaction (x_1x_2) have probability values > 0.05 which are not significant. This is because the extracellular enzymes required for de-polymerization of lignin need molecular oxygen, and their oxidative reactions would not be anticipated under anaerobic conditions. However, results indicate that both variables do not contribute to the production of the particular extracellular enzymes. The model for coded factors of lignin removal is shown in Equation (2):

$$Y_2 = 59.60 + 0.18x_1 - 0.15x_2 - 8.43x_1^2 - 7.79x_2^2 - 0.84x_1x_2 \quad (2)$$

Figure 4 shows a contour plot with respect to the variables. From the contour plots, it can be seen that the response increases as the HRT is close to 4 days and feeding COD is 3000 mg L⁻¹.

For the fixed variable x_2 at 3000 mg L⁻¹, an increment of x_1 from 1 to 4 days shows an increase in Y_2 from 50.98 to 59.60 %. However, further increments of x_1 to 7 days show a reduction in the value of Y_1 of 51.35 %. The interaction of variables towards responses can be explained through the contour plot. Once the variable x_1 is fixed at 4 days and x_2 increases from 1000 to 3000 mg L⁻¹, the response Y_2 shows an increment from 51.96 to 59.60 %. With further increase of x_2 to 5000 mg L⁻¹, a slight reduction of Y_2 is noticed. From the interaction of contour plots, it is clearly seen that the maximum value of the predicted lignin removal efficiency is 59.60 % at HRT of 4 days and feeding COD concentration of 3000 mg L⁻¹, whereas the minimum predicted response (42.49 %) was achieved at HRT of 1 day and feeding COD of 1000 mg L⁻¹. This indicates that intermediate values of both HRT and feeding COD concentration yield a good performance in removing lignin.

The results for ANOVA of methane production are shown in Table 8.

P-value greater than 0.0500 indicates that the model terms are not significant. From the analysis, x_1 , x_1^2 , x_2^2 and x_1x_2 are significant model terms. The coded factors model for lignin removal is shown in Equation (3):

$$Y_3 = 8.06 - 0.30x_1 + 0.14x_2 - 0.77x_1^2 - 2.79x_2^2 + 0.76x_1x_2 \quad (3)$$

Figure 5 shows the predicted versus actual plot for methane production with R² value of 0.9798 which demonstrates a reasonable degree of correlation between experimental and predicted

values. The contour plots of the quadratic model for methane production with respect to HRT (x₁) and feeding COD (x₂), within the space design are shown in Figure 6.

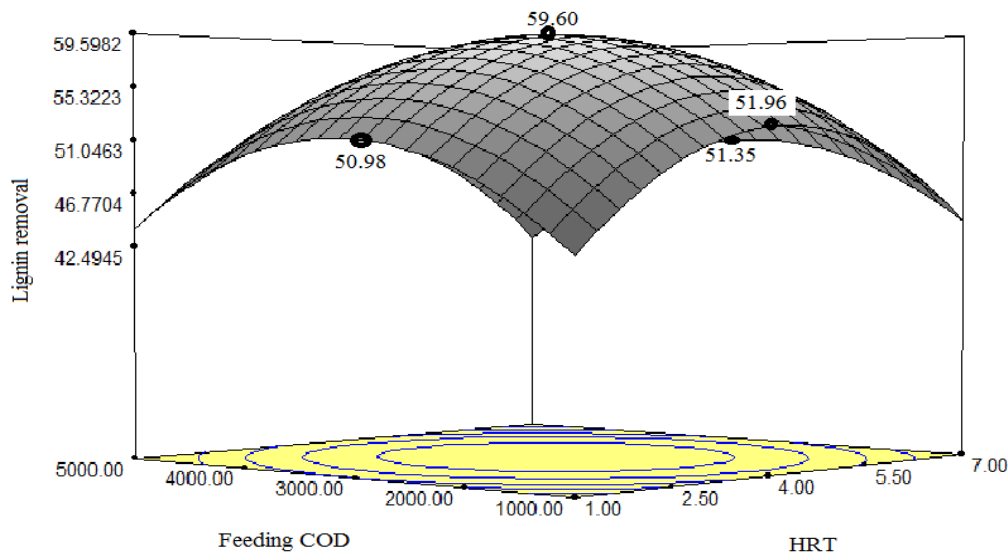


Figure 4. 3D plot with respect to HRT and feeding COD.

Table 8. Regression analysis using D-optimal response surface methodology

Model term	Coefficient estimate	Standard error	F-Value	p-Value
Intercept	8.06	0.20	58.10	0.0001
x ₁	-0.30	0.09	9.950	0.0197
x ₂	0.14	0.09	2.270	0.1823
x ₁ ²	-0.77	0.19	17.23	0.0060
x ₂ ²	-2.79	0.19	226.55	0.0001
x ₁ x ₂	0.76	0.11	49.97	0.0004

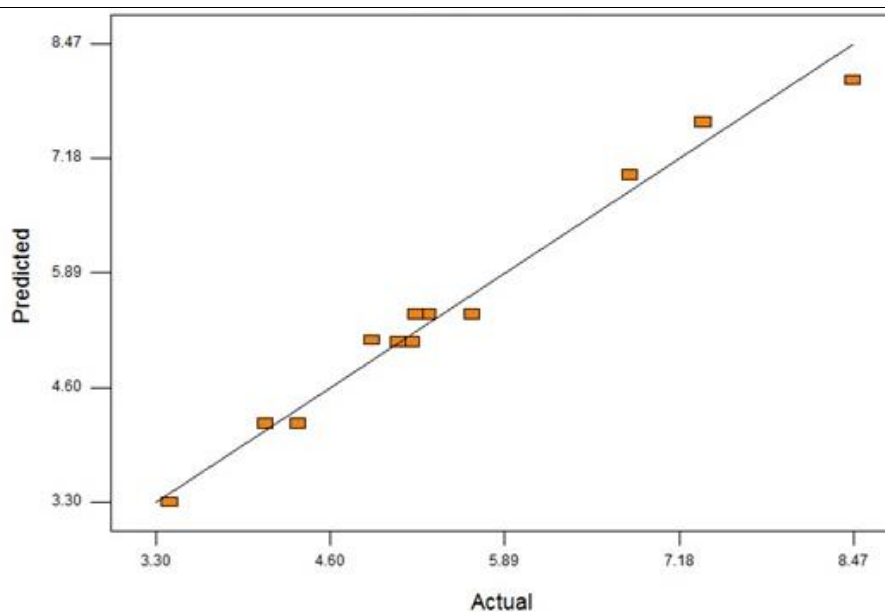


Figure 5. Predicted vs actual values plot for methane production rate.

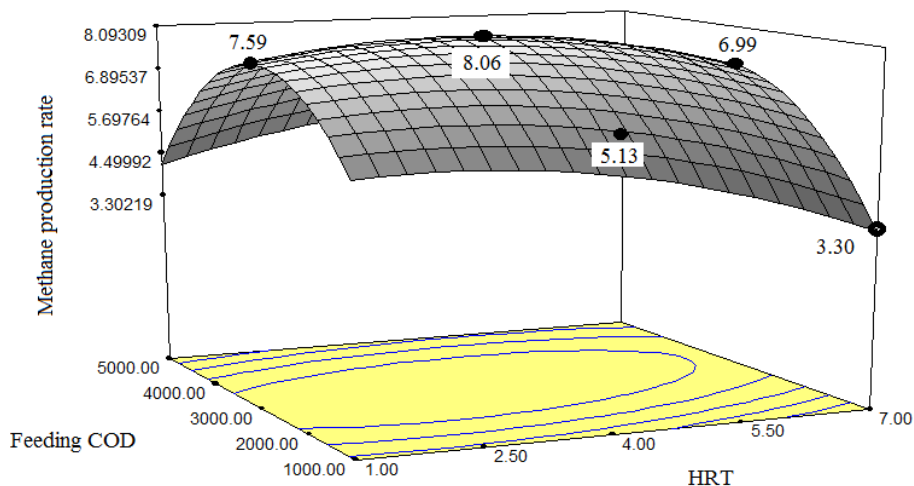


Figure 6. Response surface and counter plots for methane production rate with respect to HRT and feeding COD.

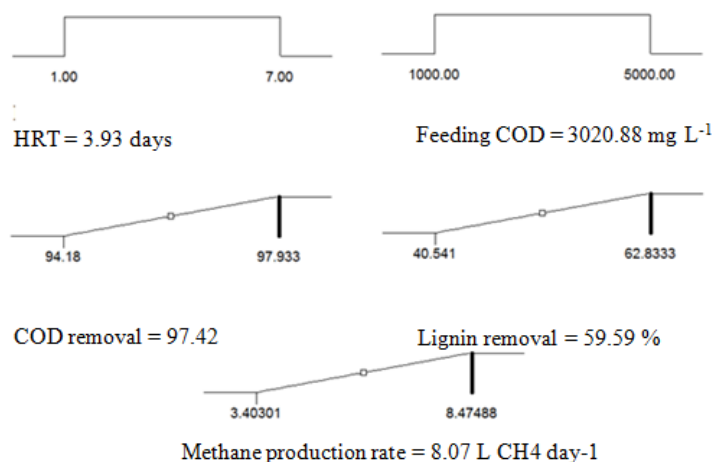


Figure 7. Desirability ramp for numerical optimization of four goals, namely the initial solution pH, initial lead ion concentration, biomass dosage and lead removal.

As can be seen, at fixed variable x_2 at 3000 mg L⁻¹ and increment of x_1 from 1 to 4 days there is an increase in Y_3 from 7.59 to 8.06 L CH₄ day⁻¹. However, a further increment of x_1 to 7 days shows a reduction in the value of Y_1 to 6.997 L CH₄ day⁻¹. For the variable x_1 , once the variable is fixed at 4 days and x_2 is increased from 1000 to 3000 mg L⁻¹, the response Y_3 shows an increment from 5.13 to 8.06 L CH₄ day⁻¹. Further increase of x_2 to 5000 mg L⁻¹ shows a slight reduction of Y_3 . From the interaction of contour plots, it is clearly seen that the maximum value of the predicted methane production rate is 8.06 L CH₄ day⁻¹ at HRT of 4 days and feeding COD concentration of 3000 mg L⁻¹, whereas the minimum predicted response (3.30 L CH₄ day⁻¹) is achieved at HRT of 7 days and feeding COD of 1000 mg L⁻¹. Intermediate feed strength (3000 mg L⁻¹) and HRT (4 days) gave an optimum condition in terms of organic load and feed flow rate that permitted the biomass or

microbes inside to become contact to the substrate to digest it and produce methane. The interaction indicated that HRT and feeding COD concentration played a significant role in methane production in the reactor.

(d) *Optimization using desirability function.* There are various options for the data that can be set during this optimization including minimizing, maximizing, setting to exact values or setting the data within the range of study. The shape of particular desirability function was adjusted by assigned weight to each goal, then combined into an overall desirability function. Figure 7 shows the desirability ramp for optimization of five goals, namely HRT, feeding COD concentration, COD removal, lignin removal and methane production rate. The maximum desirability function was set within a range of HRT from 1 to 7 days, feeding COD concentration from 1000 to 5000 mg L⁻¹, and maximize level of COD removal efficiency (97.93%), lignin removal efficiency (62.8%) and

methane production rate ($8.47 \text{ L CH}_4 \text{ day}^{-1}$). The best local maximum found was at HRT of 3.93 days, feeding COD concentration of $3020.88 \text{ mg L}^{-1}$, COD removal efficiency of 97.42 %, lignin removal efficiency of 59.59 % and methane production rate of $8.07 \text{ L CH}_4 \text{ day}^{-1}$ with desirability value of 0.897. The obtained desirability value indicates that the estimated function signifies the desired conditions and experimental model. Interaction of variables towards MAHB reactor performance in terms of COD removal, lignin removal and methane production rate was successfully investigated. From the RSM result, ANN analysis was then used to compare the results (analysis) using ANN in order to check whether the data fit well with the actual data and predict the optimum performance of the MAHB reactor in treating RPME. The results are further discussed in the following section.

Analysis of COD and lignin removal and methane production using neural network

In the present study, the experimental data were compared with the predicted optimum data obtained from RSM analysis to evaluate the ANN ability. The experimental data were chosen from the RSM analysis. Three different data set were used for fitting purpose which are 54 data for training process, 81 data for validation and 36 data for testing. Mean square error (MSE) and regression R^2 values were used to evaluate the performance and validation of ANN. Figure 8 shows the regression plot of neural network generated by ANN toolbox. As can be seen, the R values for all training, validation and testing sets were 0.99996, 0.99989 and 0.9998, respectively. This indicates that the ANN gave good agreement between the outputs and predicted values. The correlation between outputs and predicted values indicates that higher R values represent closer interaction while zero R

indicates random interaction. In training process, the weights of the ANN were adjusted in order to minimize the values of MSE. From the regression plots (Figure 8), it can be seen that R values were closer to 1 which suggests that the predicted values from the ANN analysis have a linear correlation with experimental data. Hence, it can be concluded that the ANN toolbox is a good indicator in predicting the outcome of the COD removal efficiency, methane production rate and lignin removal efficiency from the MAHB reactor.

Figure 9 shows the MSE *versus* epochs for training, validation and testing. The ANN fitting revealed that the smallest MSE obtained was 0.34249 at an epoch of 7. The correlations between experimental data and output predicted by ANN using ANN toolbox are shown in Figure 10. As can be seen, a good agreement between experimental and ANN outputs was achieved for all outputs of COD removal, lignin removal and methane production rate with R^2 values of 0.970, 0.9906 and 0.9545, respectively. Table 9 summarizes the optimum predicted COD removal efficiency, lignin removal efficiency and methane production rate using RSM and ANN toolbox.

Results show that predicted COD removal efficiency are 97.42 and 98.16 %, lignin removal efficiency - 59.59 and 77.29 % and methane production rate - 8.07 and 8.34 L day^{-1} for RSM and ANN, respectively. The predicted values for COD removal, lignin removal and methane production for both RSM and ANN are most likely to be similar to the actual values. This also indicates that the validation and fitting using ANN toolbox yield close optimum predicted results as compared to the predicted results previously obtained using RSM.

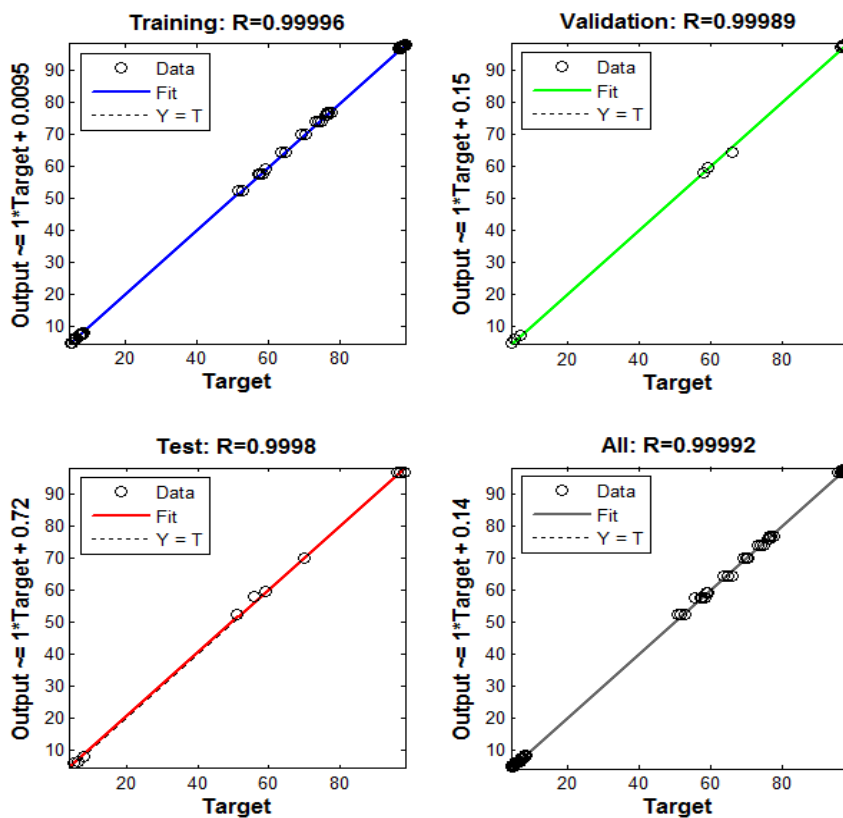


Figure 8. Regression plots of the neural network model.

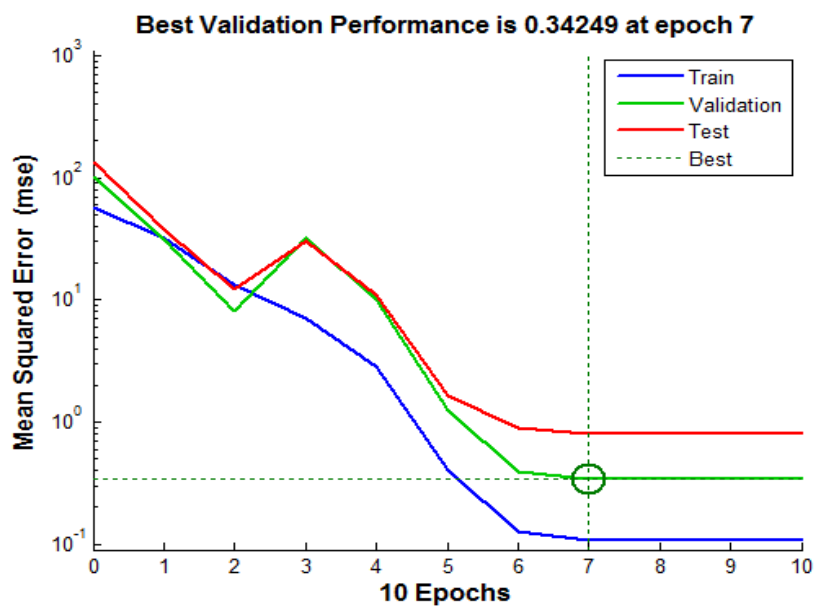


Figure 9. Training, validation, and test square mean errors for Levenberg-Marquardt algorithm

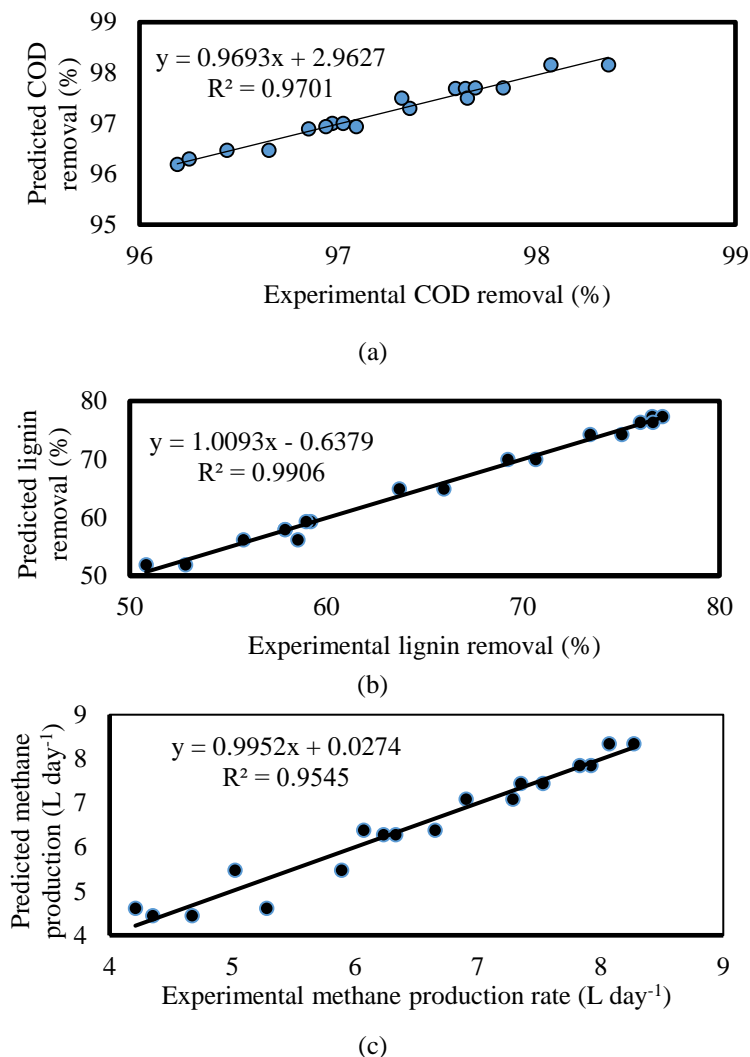


Figure 10. Correlation between experimental and predicted ANN data for (a) COD removal efficiency, (b) lignin removal efficiency and (c) methane production rate

Table 9. Optimum predicted output obtained by RSM and ANN

	COD removal	Lignin removal	Methane production rate (L day ⁻¹)
RSM	97.42	59.59	8.07
ANN	98.16	77.29	8.34
R ²	0.970	0.990	0.954

CONCLUSIONS

The HRT and feeding COD concentration variables showed significant effects towards the increase of responses. Intermediate HRT and COD concentrations significantly enhanced the COD and lignin removal and also gave the highest methane production rate. The predicted COD removal efficiency was 97.42 and 98.16 %, lignin removal was 59.59 and 77.29 % and methane production rate was 8.07 and 77.29 L day⁻¹ for RSM and ANN, respectively, which indicates that the predicted values for both methods are most likely to be

similar to the actual values. This designates that the validation and fitting using ANN toolbox yield close optimum predicted results to those predicted by RSM. Higher R² values achieved demonstrated that both methods could be efficiently used for the prediction of COD and lignin removal and methane production by anaerobic digestion of RPME using MAHB reactor.

Acknowledgement: The authors wish to acknowledge the financial support from the Universiti Sains Malaysia (RU-I A/C.1001/PJKIMIA/814148) and MyBrain15 Scholarship (KPM (B) 870204115782).

REFERENCES

1. X. Li, L. Li, M. Zheng, G. Fu, J. S. Lar, *Energy Fuels*, **23**(9), 4635 (2009).
2. C. Wan, Q. Zhou, G. Fu, Y. Li, *Waste Manag.*, **31**, 1752 (2011).
3. Q. Chen, MSc Thesis, University of Missouri, Columbia, USA, 2010.
4. D. Bas, I. H. Boyaci, *J. Food Eng.*, **78**(3), 836, (2007).
5. K. W. Chou, I. Norli, A. Anees, *Bioresour. Technol.*, **101**(22), 8616 (2010).
6. S. F. A. Halim, A. H. Kamaruddin, W. J. N. Fernando, *Bioresour. Technol.*, **100**(2), 710 (2009).
7. W-Q. Guo, N-Q. Ren, Z-B. Chen, B-F. Liu, X-J. Wang, W-S. Xiang, J. Ding, *Int. J. Hydrogen Energy*, **33**, 7397 (2008).
8. Y. Mu, H-Q. Yu, *Int. J. Hydrogen Energy*, **32**(15), 3308 (2007).
9. P. Holubar, L. Zani, M. Hager, W. Froschl, Z. Radak, R. Braun, *Water Res.*, **36**, 2582 (2002).
10. S. R. Hassan, H. M. Zwain, I. Dahlan, *J. Adv. Sci. Res.*, **4**(1), 7 (2013).
11. S. R. Hassan, H. M. Zwain, N. Q. Zaman, I. Dahlan, *Environ. Technol.*, **35**(3), 294 (2013).
12. A. M. Jirka, M. J. Carter, *Anal Chem.*, **47**(8), 1397 (1975).
13. A. P. Buzzini, E. C. Pires, *Bioresour. Technol.*, **98**(9), 1838 (2007).

Determination of an effective immunogenic peptide against *Acinetobacter baumannii*

E. Valipour*

Department of Molecular Biology and Genetics, Faculty of Arts and Sciences, Zonguldak Bulent Ecevit University, Zonguldak, Turkey

Received July 15, 2019; Accepted October 7, 2019

Nosocomial infections caused by *Acinetobacter baumannii* are a growing clinical problem. *A. baumannii* biofilm-associated protein (Bap) is necessary for mature biofilm formation on medically relevant surfaces and pathogenicity. In this research, conserved regions of the Bap were determined using various programs. The epitope rich segments of the conserved regions were detected. Two fragments (151AA and 172AA) were selected as peptide fragments that were rich in the aspect of leaner and structural B-cell epitopes, CD4 T-cell epitopes and MHC binding sites. The two peptides were linked to each other by a linker peptide and were named as AC peptide. The codon usage and GC contents of the nucleotide sequences coding the AC peptide were optimized. MHC-II binding predictions were done by consensus method that showed the average of immunogenicity score, combined score, and median percentile to be 92.63, 46.18 and 15.22, respectively. Antigenic peptide prediction by Kolaskar and Tongaonkar method and by VAXIGENE program showed the average antigenic propensity for this peptide as 1.0281 and 0.8656, respectively. This immunogenic peptide can be used as a valuable tool to detect the *A. baumannii* and to defend against nosocomial infection caused by the strain.

Keywords: *Acinetobacter baumannii*, immunogenicity, biofilm, nosocomial, design

INTRODUCTION

Acinetobacter baumannii is a non-motile aerobic gram-negative bacillus strain [1]. Nosocomial infections caused by *Acinetobacter baumannii* are serious problems in intensive care units. Urinary tract, soft-tissue, skin and wound infection, secondary meningitis, bloodstream infections are caused by *A. baumannii* [2]. *A. baumannii* strains are perilous because they are resistant to many antibiotics such as trimethoprim-sulfamethoxazole, tetracyclines, betalactams (including carbapenems), fluoroquinolones and aminoglycosides. Therefore, that is a serious problem that needs to be solved promptly by the international health care community [3]. Up to now, biofilm associated protein of the strains, auto-transporter, outer membrane proteins, capsular polysaccharide, and whole cell was used to raise antiserum against *A. baumannii*. All of the antigens showed to be a potential vaccine against the strains. The methods have some disadvantages including protection limitation and high cost. Up to now, there is no vaccine against *A. baumannii*, therefore, there is a serious need for more research to find a better vaccine candidate having the least disadvantage [4, 5]. Yet more research and works are needed to discover all factors involved in epidemicity and virulence of *A. baumannii*. To make infection in a host, the bacterial strain essentially needs to attach to host's epithelial cells and colonize them.

Acinetobacter species usually adhere and colonize on human mucosal membrane and skin even for some weeks which shows that the adherence of the strain is an essential factor in pathogenicity [6]. In addition, many researchers discovered that the strain with high capability to make biofilm has high ability to adhere to epithelial cells [7]. *A. baumannii* to be able to make a biofilm on epithelial cells requires a biofilm-associated protein (Bap) [8, 9]. Inactivation of the biofilm-associated protein caused a decrease in biofilm formation and a decrease in adherence ability of the strain to human epithelial cells. The antibody against biofilm-associated protein inhibits the strain from binding to the epithelial cells. The proteins are expressed at the cell surface of Bap [10]. Therefore this study aimed to design new and effective antigenic recombinant peptide from Bap against *A. baumannii*.

MATERIAL AND METHODS

Primary sequence analysis

Sequences related to Bap were selected from clusters in Uniprot database at <http://www.uniprot.org>. To find the Bap family proteins a cluster with 50% sequence identity levels was selected. Some members of the cluster were subjected to multiple sequence alignments by MUSCLE at www.ebi.ac.uk/Tools/psa/emboss_needle/ using [11]. The alignment was visualized

* To whom all correspondence should be sent:
E-mail: Va.cell@yahoo.com

E. Valipour: Determination of an effective immunogenic peptide against Acinetobacter baumannii

and edited by Jalview program (<http://csbg.cnb.csic.es/PB/E1120>) [12]. The program of Compared at <http://bioinf4.cs.ucl.ac.uk:3000/compred> was used to annotate disorders and detect homolog domains. InterProScan online software at <http://www.ebi.ac.uk/Tools/pfa/iprscan/> was used to detect homology within the PROSITE database [13]. The conserved regions of the protein were subjected to further analysis.

Antigenicity prediction of the selected region

T-Cell Epitope was predicted by NetTepi1 program (<http://www.cbs.dtu.dk/services/NetTepi/>) SYFPEITHI program (<http://www.syfpeithi.de>), Immune Epitope Database and Analysis Resource (IEDB) (<http://www.immuneepitope.org>) and <http://imed.med.ucm.es/Tools/antigenic.pl> [14, 15]. DNASTar program (V5.0) (<http://www.dnastar.com>), SYFPEITHI program (<http://www.syfpeithi.de>), ProPred (<http://www.imtech.res.in/raghava/propred/index.html>) and IEDB (<http://tools.immuneepitope.org>) were used to determine MHCII binding regions [16]. B-Cell Epitopes were predicted by BCPreds (<http://ailab.cs.iastate.edu/bcpreds/index.html>), ABCpred (<http://www.imtech.res.in/raghava/abcpred/>), DNASTar (V5.0) (<http://www.dnastar.com>) and conformational epitopes by Seppa program (<http://lifecenter.sgst.cn/seppa>), BEpro (<http://pepito.proteomics.ics.uci.edu/cgi-bin/BEpro.cgi>) and DiscoTope Server (<http://www.cbs.dtu.dk/services/-DiscoTope>) [17, 18]. Regions of proteins that are rich in the aspect of linear and conformational epitopes can be used as vaccine candidates. Therefore two segments of the Bap protein were selected to join together to make an immunogenic protein.

Further scrutiny

The gene sequence encoding the selected amino acid sequences was retrieved from the NCBI website; GC content and codon usage were evaluated according to *E. coli* expression system by the programs at <http://eu.idtdna.com>, <http://www.genscript.com> and <http://www.jcat.de/>

websites [19]. One of the most important factors for protein production is mRNA structure and stability. Therefore, the structure and stability of mRNA to be transcribed from the gene fragment was analyzed and controlled by <http://rna.tbi.univie.ac.at/cgi-bin/RNAfold.cgi> [20]. Protein stability and solubility were analyzed by <http://web.expasy.org/protscale/> and <https://protein-sol.manchester.ac.uk/>, respectively. After that, the construct was subjected to antigenic evaluation by the programs mentioned above.

RESULTS

Primary sequence analysis

The proteins having protein ID (UniProt) of G2JKC0, A0A3B0GRS0, B0VEF9, A0A3B0GRS0, UPI000A394F5F, B0LHN4 were selected from a cluster with 50% sequence identity. They are large proteins with tandem repeat modules. Alignment of these proteins revealed the conservation of several locations in sequences, mainly repeat modules. Within these conserved regions, two specific regions were selected based on PSI-BLAST search against a non-redundant protein database.

Immunogenic regions selection

Two regions (151AA and 172AA) were selected as peptide fragments that were rich in the aspect of leaner and structural B-cell epitopes, CD4 T-cell epitopes and MHC binding sites. The two peptides were linked to each other by a linker peptide (EAAAKEAAAKEAAK) (Table 1) and were named AC peptide. The AC peptide coding gene sequence was extracted from *Acinetobacter baumannii* biofilm-associated protein (Bap) (GenBank: EU117203.1) and subjected to codon usage optimization and RNA structure analysis. The distribution of codon usage frequency along the length of the construct is very important. After codon usage optimization the initial CAI value (0.284) of the construct increased to 1.0 and initial GC-content (44.27) changed to 54.27 (Fig. 1).

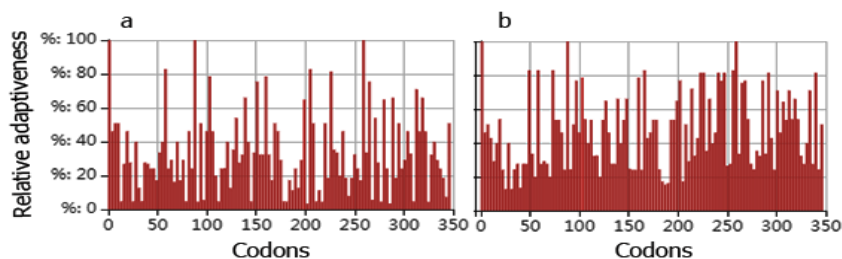


Fig. 1. Codon usage optimization. **a** shows the relative adaptiveness of the AC sequence before optimization; **b** represents that after optimization. The codon usage of this sequence was optimized due to the codon usage of *E. coli* k12 strain.

E. Valipour: Determination of an effective immunogenic peptide against Acinetobacter baumannii
Table 1. A: AS peptide sequence that was made from regions of BAP having high antigenicity; B: The gene sequences coding AS peptide.

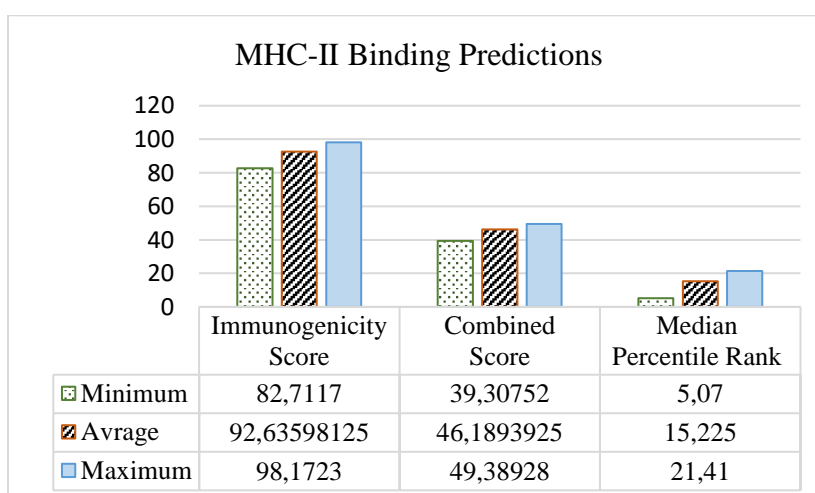
```

>A
MTATDAAGNVGTDGTVVTVDTAAPNTAGVTFTIDSVTADNVINASEAAGNVTTITGVLKNI
PADATNTAVTVVINGVTYNATVDKTAGTWTVSVPGSLVADADKTIDAKVTFTDAAGNSS
TVNDTQIYTLDTAAPAAPVIDPVNGTDPITGEAAAKEAAAKEAAAKNDAGEVDVVTPTTV
ISEVNGQPVVADGTSITGTYGTLVINLDGSYTYTPTASAAGVGQTDQFTYTLTDPVTGDT
AQANLNIQLSSVKAVDNVVTAEINPEPLLVAADDVALGSSTYLAAVSLAGLDLQLLGNDAI
EFTVDPNREGTATFTFDAVITADLLSDYAIVVQKFDEATGQWVSIGGT

>B
ATGACTGCAACAGATGCAGCAGGTAACGTAGGTACAGATACAGGTGTTGTGACAGTTGAT
ACAGCTGCTCCAAATACAGCTGGCGTTACCTTTACGATTGACTCAGTAACAGCTGACAAT
GTGATTAATGCATCAGAAGCAGCAGGTAATGTCACGATTACTGGTGTCTGAAAAACATT
CCAGCAGATGCGACTAACACGGCCGTTACAGTTGTTATTAATGGGGTAACTTATAATGCA
ACGGTAGATAAAACAGCAGGCACGTGGACAGTAAGTGTGCCGGGTAGTGGTTTGGTTGCT
GATGCAGATAAAACGATTGATGCTAAAGTAACGTTTACAGATGCAGCAGGTAATAGCAGC
ACTGTTAACGATACGCAAATTTATACATTAGACACAGCTGCTCCTGCAGCGCCAGTAATC
GACCCAGTTAACGGGACAGACCCAATTACAGGTGAAGCAGCAGCAAAGAAGCAGCAGCA
AAAGAAGCAGCAGCAAAAAATGATGCAGGTGAGGTAGATGTTGTAACCTCCAACAACAGTT
ATAAGTGAGGTTAATGGTCAGCCTGTTGTAGCAGATGGCACGAGCATCACTGGTACTTAC
GGTACATTAGTGATCAACCTGGATGGTTCATACACTTATACGCCTACTGCTAGTGCGGCA
GGTGTAGGACAAACAGATCAGTTTACCTATACCTTAACTGATCCTGTAACCTGGTGATACG
GCTCAAGCAAACCTCAATATTCAATTGAGCTCTGTGAAAGCTGTGGATAATGTTGTAAC
GCAGAAATCAACCCAGAACCCTGCTAGTTGCAGATGATGTTGCTCTAGGCAGTTCAACT
TACCTTGCAGCAGTATCGTTAGCTGGTCTGGACTTACAATTGCTTGGTAACGACGCAATT
GAGTTTACTGTTGATCCAAACCGGAAGGTACAGCAACGTTACATTTCGATGCGGTAATC
ACAGCAGATTTACTCAGTGATTATGCGATTGTTGTTTCAGAAATTTGATGAAGCAACAGGC
CAATGGGTATCGATCGGTGGTACT

```

Table 2. The MHC-II binding predictions done by the ElliPro program.



The free energy of the thermodynamic ensemble of the RNA from the construct was -329.77 kcal/mol. The centroid secondary structure had minimum free energy of -276.70 kcal/mol.

Instability index (II) of the protein was computed to be 8.57 and predicted scaled solubility was 0.761.

E. Valipour: Determination of an effective immunogenic peptide against Acinetobacter baumannii

The AC peptide was converted to PDB format using the LOMETS program [21]. The model showed Cov Norm value of 0.95 and a Z score of 1.71. The model was also analyzed by I-TASSER that showed Tm-score of 0.914, RMSD value of 1.42, IDEN value of 0.281 and Cov value of 0.950. In this analysis, the protein having PDB accession number of 4p99A was reference protein.

Sequence-based epitope prediction of the AC peptide

VAXIGENE program showed the Overall antigenicity prediction for the target peptide to be 0.8656. In this analysis, the threshold was 0.4. Antigenic Peptide Prediction at <http://imed.med.ucm.es/Tools/antigenic.pl> showed the average antigenic propensity for this peptide to be 1.0281. MHC-II Binding Predictions were done by consensus methods that showed the average of immunogenicity score, combined score, and median percentile to be 92.63, 46.18 and 15.22 respectively (Table 2). CD4 T cell immunogenicity prediction of the target peptide by Predicting Antigenic Peptides in <http://imed.med.ucm.es/Tools/antigenic.pl> showed the average antigenic propensity for this protein as 1.0292 (Fig. 2).

The antigenicity was determined using the method of Kolaskar and Tongaonkar [22]. Analysis of Linear B Cell Epitope by BepiPred-2.0 showed an average score of 0.477, a minimum score of -0.007 and a maximum score of 1.803 (Fig. 3).

Structure-based b-cell epitope prediction of the AC peptide

In linear B cell epitopes predicted by ElliPro, the highest score is related to the first 29 amino acids 'TATDAAGNVGTDGVTVDTAAPNTAGVT' with a score of 0.848. The region starting from 282 to 320 'QLLGNDIAIEFTVDPNREGTATFTFDVAVITADLLSDYAIV' showed a score of 0.764 and the minimum score (0.583) was related to the region starting from 93 to 105 (PGSGLVADADKTI). Discontinuous B cell epitopes predicted from the 3D structure of a protein by ElliPro are shown in Table 3. The server showed 6 regions that involve in conformational epitopes. The region made from residues (1-29, 54-88 and 112-117) showed the maximum score (0.732) and residues of Q:P137, Q:A162, Q:A163, Q:A164, Q:K165, Q:D167, Q:A168, Q:G169, Q:E170, Q:V171, Q:D172, Q:V173, Q:V174 showed the minimum score (0.539).

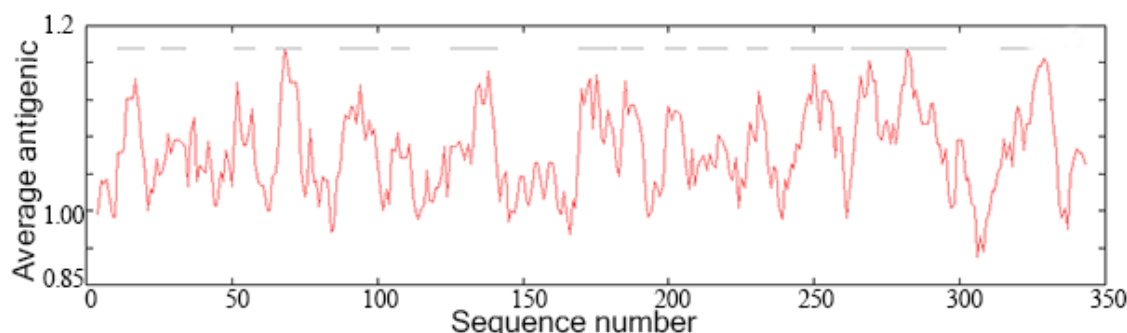


Fig. 2. CD4 T cell immunogenicity prediction of the target peptide by the IEDB program that showed a reasonable immunogenicity

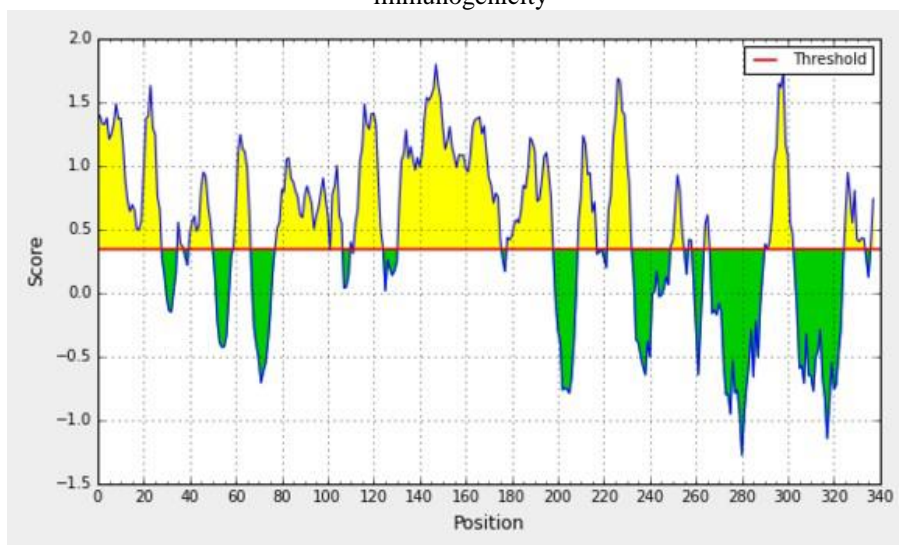


Fig. 3. Analysis of Linear B Cell Epitope by BepiPred-2.0 that showed an average score of 0.477, a minimum score of -0.007 and a maximum score of 1.803

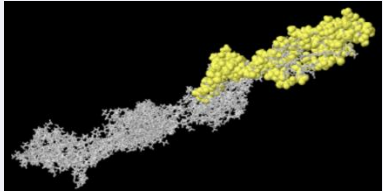
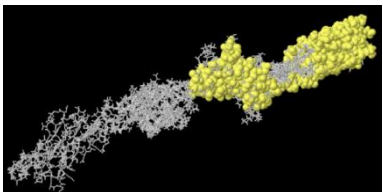
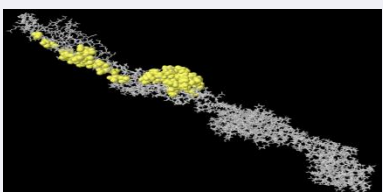
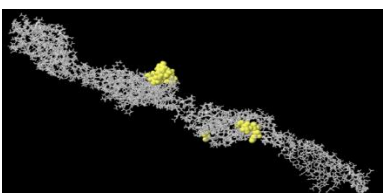
DISCUSSION

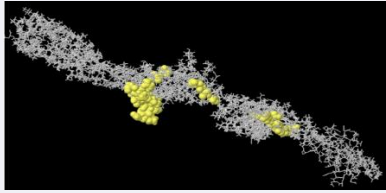
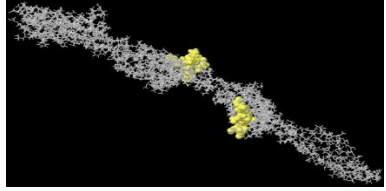
The UniRef (UniProt Reference Clusters) provides clustered sets of sequences from the UniProt Knowledge base (UniProtKB) and selected UniProt Archive records to obtain complete coverage of sequence space at several resolutions while hiding redundant sequences [23]. Therefore, in this research the cluster with 50% sequence identity level was used to find the members of Bap family. There is a significant correlation between high protein expression level and codon adaptation index (CAI). If the CAI value is high the expression level is high. The CAI value of 1.0 was considered as an ideal value and the CAI value of >0.8 was considered as a good value for protein expression in a host cell [19]. In addition, the GC present has a significant effect on the expression. The ideal percentage range of GC content is between 30% and 70%. In this research, after codon usage optimization the CAI value (0.284) of the construct increased to 1.0 and GC content (44.27) changed to 54.27. The free energy of the thermodynamic ensemble of the RNA from the construct was -329.77 kcal/mol. The instability index (II) was computed to be 8.57. A protein whose instability index is smaller than 40 is predicted as stable, a value above 40 predicts that the protein may be unstable [24]. Predicted scaled solubility of the protein was 0.761. The scaled solubility value (QuerySol) is the predicted solubility. The population average for the experimental dataset (PopAvrSol) is 0.45, and therefore any scaled solubility value greater than 0.45 is predicted to have a higher solubility than the average soluble *E.coli* proteins and any protein with a lower scaled solubility value is predicted to be less soluble [25]. The centroid secondary structure had minimum free energy of -276.70 kcal/mol. The AC peptide was converted to PDB format using the LOMETS program [21]. The model showed a Cov Norm value of 0.95 and a Z score of 1.71. The root-mean-square deviation (RMSD) value indicates how closely two structures (target protein and reference protein) are related. The value less than 3\AA shows that our protein is a novel fusion protein. Also, the RMSD value more than 3\AA indicates a lower accuracy and quality of the modeling. In that condition, the TM-score is more significant. Template modeling (TM) score value of more than

0.5 shows a model having almost acceptable topology [26]. Confidence score (C-score) is usually in the range of (-5, 2). The higher value shows the confidence of the model. The C-value of our protein was 0.950 showing high confidence. These results showed that our protein 3D structure was correctly predicted [4]. If a pathogen has sufficient binding domain to a major histocompatibility complex (MHC) it can elicit a high-level response of the immune system [27]. For MHC-II binding predictions, the mean of the area under the curve (AUC) value was usually ranged from 0.697 to 0.813. The consensus method having AUC value of (0.896, - 0.05) is a good method for prediction [28]. In this research MHC-II binding predictions were done by consensus methods. In this part, the consensus method of IEDB was used. The method is a combination of Sturniolo, CombLib, SMM-align, and NN-align. The server is a good tool for prediction of T- helper cell (allele independent) immunogenicity of the population [29]. In this method, the lower percentile value shows a high affinity [29, 30]. CD4 T cell immunogenicity prediction of the target peptide by Predicting Antigenic Peptides in <http://imed.med.ucm.es/Tools/antigenic.pl> showed the average antigenic propensity for this protein to be 1.0292. This tool uses the method of Tongaonkar and Kolaskar to predict antigenic parts of the peptide [22]. The accuracy of the data reported by this tool is almost 75%. Analysis of Linear B Cell Epitope by BepiPred-2.0 showed an average score of 0.477, a minimum score of -0.007 and a maximum score of 1.803. The BepiPred-2.0 tool uses a random forest algorithm to predict B-cell epitopes from crystal structures [31] In this research, the BepiPred-2.0 was used to predict the B-cell epitopes from antigen sequences. ElliPro predicts linear and discontinuous antibody epitopes based on a protein antigen's 3D structure. The prediction of epitopes by this tool was determined by the PI (Protrusion Index) value. The residue that has a large value of PI is more accessible to solvent. Discontinuous epitopes are defined by PI values and are clustered based on the distance R (in \AA) between residue's centers of mass. The larger R is associated with larger discontinuous epitopes being predicted [32].

E. Valipour: Determination of an effective immunogenic peptide against Acinetobacter baumannii

Table 3. Discontinuous B cell epitopes predicted from the 3D structure of the protein by ElliPro.

No.	Residues	Number of residues	Score	3D structure
1	Q:T1, Q:A2, Q:T3, Q:D4, Q:A5, Q:A6, Q:G7, Q:N8, Q:V9, Q:G10, Q:T11, Q:D12, Q:T13, Q:G14, Q:V15, Q:V16, Q:T17, Q:V18, Q:D19, Q:T20, Q:A21, Q:A22, Q:P23, Q:N24, Q:T25, Q:A26, Q:G27, Q:V28, Q:T29, Q:G54, Q:V55, Q:L56, Q:K57, Q:N58, Q:I59, Q:P60, Q:A61, Q:D62, Q:A63, Q:T64, Q:N65, Q:A79, Q:T80, Q:D82, Q:K83, Q:T84, Q:A85, Q:G86, Q:T87, Q:W88, Q:T112, Q:D113, Q:A114, Q:A115, Q:G116, Q:N117	56	0.738	 A 3D molecular model of a protein structure with a specific region highlighted in yellow, representing the predicted B cell epitope.
2	Q:V244, Q:D245, Q:N246, Q:V247, Q:V248, Q:T249, Q:A250, Q:E251, Q:I252, Q:N253, Q:P254, Q:E255, Q:P256, Q:L257, Q:L258, Q:V259, Q:A260, Q:D261, Q:D262, Q:V263, Q:A264, Q:L265, Q:G266, Q:S267, Q:S268, Q:T269, Q:Y270, Q:L271, Q:A272, Q:A273, Q:V274, Q:S275, Q:L276, Q:A277, Q:G278, Q:Q282, Q:L283, Q:L284, Q:G285, Q:N286, Q:D287, Q:A288, Q:I289, Q:E290, Q:F291, Q:T292, Q:V293, Q:D294, Q:P295, Q:N296, Q:R297, Q:E298, Q:G299, Q:T300, Q:A301, Q:T302, Q:F303, Q:T304, Q:F305, Q:D306, Q:A307, Q:V308, Q:I309, Q:T310, Q:A311, Q:D312, Q:L313, Q:L314, Q:S315, Q:D316, Q:Y317, Q:A318, Q:I319, Q:V320, Q:V321, Q:Q322, Q:G335, Q:G336, Q:T337	79	0.716	 A 3D molecular model of a protein structure with a specific region highlighted in yellow, representing the predicted B cell epitope.
3	Q:V70, Q:V71, Q:I72, Q:N73, Q:G74, Q:V75, Q:T76, Q:Y77, Q:P93, Q:S95, Q:G96, Q:V98, Q:A99, Q:D100, Q:A101, Q:D102, Q:K103, Q:T104, Q:I105, Q:D106, Q:A107, Q:K108, Q:N122, Q:I126	24	0.584	 A 3D molecular model of a protein structure with a specific region highlighted in yellow, representing the predicted B cell epitope.
4	Q:T175, Q:G197, Q:T198, Q:Y199, Q:G200, Q:T201	6	0.573	 A 3D molecular model of a protein structure with a specific region highlighted in yellow, representing the predicted B cell epitope.

No.	Residues	Number of residues	Score	3D structure
5	Q:E182, Q:V183, Q:N184, Q:G185, Q:Q186, Q:P187, Q:V188, Q:V189, Q:A190, Q:G210, Q:G212, Q:Q213, Q:T214, Q:Q237, Q:L238, Q:S239	16	0.54	
6	Q:P137, Q:A162, Q:A163, Q:A164, Q:K165, Q:D167, Q:A168, Q:G169, Q:E170, Q:V171, Q:D172, Q:V173, Q:V174	13	0.539	

Conflict of interest. There is no conflict of interest associated with the present manuscript.

REFERENCES

1. A. Howard, M. O'Donoghue, A. Feeney, R. D. Sleator, *Virulence*, **3**, 243 (2012).
2. D. G. Moriel, S. A. Beatson, D. J. Wurpel, J. Lipman, G. R. Nimmo, D. L. Paterson, M. A. Schembri, *PLoS ONE*, **8**, e77631 (2013).
3. A. Y. Peleg, H. Seifert, D. L. Paterson, *Clin. Microbiol. Rev.*, **21**, 538 (2008).
4. E. Z. Hosseingholi, I. Rasooli S. L. M. Gargari, *Acta Biotheor.*, **62**, 455 (2014).
5. L. V. Bentancor, A. Routray, C. Bozkurt-Guzel, A. Camacho-Peiro, G. B. Pier, T. Maira-Litrán, *Infect. Immun.*, IAI, 06096 (2012).
6. J. C. Lee, H. Koerten, P. Van den Broek, H. Beekhuizen, R. Wolterbeek, M. Van den Barselaar, T. Van der Reijden, J. Van der Meer, J. Van de Gevel, L. Dijkshoorn, *Res. Microbiol.*, **157**, 360 (2006).
7. H. W. Lee, Y. Koh, J. Kim, J. C. Lee, Y. C. Lee, S. Y. Seol, D. T. Cho, J. Kim, *Clin. Microbiol. Infect.*, **14**, 49 (2008).
8. K. A. Brossard, A. A. Campagnari, *Infect. Immun.*, **80**, 228 (2012).
9. Y. Fattahian, I. Rasooli, S.L.M. Gargari, M.R. Rahbar, S.D.A. Astaneh, J. Amani, *Microb. Pathog.*, **51**, 402 (2011).
10. E. De Gregorio, M. Del Franco, M. Martinucci, E. Roscetto, R. Zarrilli, P. P. Di Nocera, *BMC Genomics*, **16**, 933 (2015).
11. R. C. Edgar, *Nucleic Acids Res.*, **32**, 1792 (2004).
12. A. M. Waterhouse, J. B. Procter, D. M. Martin, M. Clamp, G. J. Barton, *Bioinformatics*, **25**, 1189 (2009).
13. F. Sefid, I. Rasooli, A. Jahangiri and H. Bazmara, *Acta Biotheor.*, **63**, 129 (2015).
14. R. E. Soria-Guerra, R. Nieto-Gomez, D. O. Govea-Alonso, S. Rosales-Mendoza, *J. Biomed. Inform.*, **53**, 405 (2015).
15. Y. Yang, W. Sun, J. Guo, G. Zhao, S. Sun, H. Yu, Y. Guo, J. Li, X. Jin, L. Du, *Human Vaccines & Immunotherapeutics*, **11**, 795 (2015).
16. S. Pahil, N. Taneja, H. R. Ansari, G. Raghava, *PLoS ONE*, **12**, e0180505 (2017).
17. R. L. M. Guedes, C. M. F. Rodrigues, N. Coatnoan, A. Cosson, F. A. Cadioli, H. A. Garcia, A. L. Gerber, R. Z. Machado, P. M. C. Minoprio, M. M. G. Teixeira, *Genomics*, **111**(3),407 (2018).
18. R. C. Russi, E. Bourdin, M. I. Garcia, C. M. I. Veaute, *Biomedical Journal*, **41**, 109 (2018).
19. E. Valipour, M.-L. Moosavi, J. Amani, S. Nazarian, *World J. Microbiol. Biotechnol.*, **30**, 1861 (2014).
20. B. Hamidi, F. Ebrahimi, A. Hajizadeh, H. K. Alikhani, *Eur. J. Exper. Biol.*, **2**, 1154 (2012).
21. S. Wu, Y. Zhang, *Nucleic Acids Res.*, **35**, 3375 (2007).
22. A. Kolaskar, P. C. Tongaonkar, *FEBS Lett.*, **276**, 172 (1990).
23. B. E. Suzek, H. Huang, P. McGarvey, R. Mazumder, C. H. Wu, *Bioinformatics*, **23**, 1282 (2007).
24. E. Gasteiger, C. Hoogland, A. Gattiker, M. R. Wilkins, R. D. Appel, A. Bairoch, in: *The Proteomics Protocols Handbook*, Springer, 2005, p. 571.
25. T. Niwa, B.-W. Ying, K. Saito, W. Jin, S. Takada, T. Ueda, H. Taguchi, *Proceedings of the National Academy of Sciences*, **106**, 4201 (2009).
26. J. Xu, Y. Zhang, *Bioinformatics*, **26**, 889 (2010).
27. M. N. Davies, D. R. Flower, *Drug Discov. Today*, **12**, 389 (2007).
28. M. Marmion, M. Parviainen, M. Luoto, R. K. Heikkinen, W. Thuiller, *Divers. Distrib.*, **15**, 59 (2009).
29. S. Paul, C. S. L. Arlehamn, T. J. Scriba, M. B. Dillon, C. Oseroff, D. Hinz, D. M. McKinney, S. C. Pro, J. Sidney, B. Peters, *J. Immunol. Methods*, **422**, 28 (2015).
30. S. K. Dhanda, E. Karosiene, L. Edwards, A. Grifoni, S. Paul, M. Andreatta, D. Weiskopf, J. Sidney, M. Nielsen, B. Peters, *Frontiers in Immunology*, **9** (2018).
31. J. Garnier, *J. Mol. Biol.*, **120**, 97 (1978).
32. J. Ponomarenko, H.-H. Bui, W. Li, N. Fusseder, P. E. Bourne, A. Sette, B. Peters, *BMC Bioinformatics*, **9**, 514 (2008).

Trifunctionalized allenes. Part V. Competitive electrophilic cyclization and cycloisomerization of 4-phosphorylated 5-hydroxy-5-methylhexa-2,3-dienoates

I. E. Ismailov, I. K. Ivanov, V. Ch. Christov*

Department of Chemistry, Faculty of Natural Sciences
Konstantin Preslavsky University of Shumen, 115 Universitetska St., 9712 Shumen, Bulgaria

Received July 30, 2019, Revised August 20, 2019,

Dedicated to Professor Dr. Toru Minami of the Kyushu Institute of Technology, Tobata, Kitakyushu, Japan on the occasion of his 80th anniversary

The interest is focused on the reactions of 4-phosphorylated 5-hydroxy-5-methylhexa-2,3-dienoates with protected or unprotected hydroxy groups involving 5-*endo-trig* cyclizations. Reactions with electrophiles result in mixtures of the 2,5-dihydro-1,2-oxaphosphole-5-carboxylates and the 5-phosphoryl-furan-2(5*H*)-ones by competitive electrophilic cyclization due to the neighboring phosphonate (phosphine oxide) and the carboxylate groups participation. 4-Phosphorylated 5-hydroxy-5-methylhexa-2,3-dienoates were smoothly transformed into the corresponding 4-phosphoryl-2,5-dihydrofuran-2-carboxylates by using 5 mol % of a silver salt as a catalyst in the 5-*endo-trig* cycloisomerization reaction.

Keywords: 4-Phosphorylated 5-hydroxy-5-methylhexa-2,3-dienoates, electrophilic cyclization, 2,5-dihydro-1,2-oxaphospholes, furan-2(5*H*)-ones, silver-catalyzed cycloisomerization, 2,5-dihydrofurans.

INTRODUCTION

Allenes have broad applications in modern synthetic chemistry due to their nature adaptable as building blocks [1-5]. They have provoked interest in scientists for years due to their unique cumulene structure and atypical biological activities. Allenes are considered to be key subunits in a variety of natural products and pharmaceutical molecules [2,5,6]. Phosphorylated allenes, allenyl phosphonates and phosphine oxides, are a very important class of allene-containing, extremely versatile reagents in organic chemistry, especially for the preparation of structurally diverse organophosphorus compounds and phosphorus heterocycles [7-12].

The study on the reactions of phosphorylated allenes (phosphonates, phosphinates, and phosphine oxides) with electrophilic reagents proves that reactions proceed with cyclization of the allenic system bearing phosphoryl group (O=P-C=C=C) to give heterocyclic compounds in most cases depending on the structure of the starting allenic compound, as well as on the type of the electrophile [13-21]. It means that the reaction of electrophilic reagents with dialkyl allenyl phosphonates [13-21] or allenyl phosphine oxides [22-24] leads to 2,5-dihydro-1,2-oxaphospholes or/and 2,1- or/and 2,3-adducts or a mixture of them, depending on the degree of substitution at the C¹ and C³ atoms of the allenic system, the nature of these substituents, and the type of the reagents.

Furan-2(5*H*)-ones (γ -lactones) are important intermediates in organic synthesis [25-27] and much attention has been paid to the development of efficient and diverse synthetic methods for construction of this five-membered ring system. α -Allenecarboxylic acids and their esters, disubstituted on the γ -carbon atom, underwent electrophilic attack on the central atom and ring closure to furan-2(5*H*)-ones when treated with electrophile [28-40]. Among these, cyclization involving allenecarboxylic acids and their derivatives, the so-called lactonization reaction, is one of the most efficient pathways [28-40].

It is the transition metal-catalyzed cyclization of functionalized allenes bearing a nucleophilic center that has attracted considerable attention in recent years [41]. Particularly, the cyclization reactions of allenols catalyzed by Ag(I) [42-45], Hg(II) [46,47], Pd(0) [48-50], Pd(II) [51,52], or Ru(III) [53-60] have become quite useful methodologies for the synthesis of five- or six-membered oxygen-containing heterocycles. Krause's group has reported a highly efficient and stereoselective synthesis of 2,5-dihydrofurans by Au(I)- and Au(III)-catalyzed cycloisomerization of α -hydroxyallenes [63-65]. The method of choice, however, is the use of transition metal catalysts, since this combines high reactivities and excellent yields with a tolerance to many functional groups.

Intramolecular cyclization of the diethylphosphono-substituted α -allenic alcohols in the presence of AgNO₃ [61] and CuCl₂ [62] yielded

* To whom all correspondence should be sent:

E-mail: vchristo@shu.bg

Our long-standing research program focuses on the synthesis [66] and the development of efficient cyclization reactions of trifunctionalized allenes. More specifically, our attention is drawn to 4-phosphorylated 5-hydroxyhexa-2,3-dienoates as 1,1,3-trifunctionalized allenes that comprise a phosphoryl, an ethoxycarbonyl and a hydroxymethyl group. The applications of these groups as temporary transformers of chemical reactivity of the allenic system in the synthesis of heterocyclic compounds are of particular interest. These molecules are considered to be a combination of an allenephosphonate or allenyl phosphine oxide, an allenecarboxylate and a hydroxyallene and they are supposed to have different reactivity profiles in cyclization reactions. In a continuation to our communications [67-72] on the synthesis and cyclization reactions of the bifunctionalized allenes, in this paper we present recent results of our studies dedicated towards the electrophilic cyclization and cycloisomerization reactions of a library of 4-phosphorylated 5-hydroxyhexa-2,3-dienoates, which strongly improve the scope of this method for synthesis of heterocyclic compounds.

EXPERIMENTAL

General Information

All new synthesized compounds were purified by column chromatography and characterized based on NMR, IR, mass, and microanalytical data. NMR spectra were recorded on a Bruker Avance II+600 (^1H at 600.1 MHz, ^{13}C at 150.9 MHz, ^{31}P at 242.9 MHz) spectrometer for solutions in CDCl_3 . All ^1H and ^{13}C NMR experiments were performed referring to the signal of internal TMS and ^{31}P NMR experiments were measured referring to the signal of external 85% H_3PO_4 . J values are given in hertz. IR spectra were recorded with an FT-IRafinity-1 Shimadzu spectrophotometer. Elemental analyses were carried out by the Microanalytical Service Laboratory using Vario EL3 CHNS(O). HRMS were recorded on a Thermo Scientific Q Exactive hybrid quadrupole-orbitrap mass spectrometer. Column chromatography was performed on Kieselgel F₂₅₄60 (70-230 mesh ASTM, 0.063-0.200 mm, Merck). CH_2Cl_2 was distilled over CaH_2 . Reactions were carried out in oven-dried glassware under an argon atmosphere and exclusion of moisture. All compounds were checked for purity on TLC plates Kieselgel F₂₅₄ 60 (Merck).

Diphenyl disulfide and sulfuryl chloride in dichloromethane were used to prepare benzenesulfonyl chloride which was distilled *in vacuo* (bp 80-81 °C/20 mm Hg) [80]. All other chemicals used in this study were commercially available and were used without additional purification unless otherwise noted. The starting 4-phosphorylated 5-hydroxyhexa-2,3-dienoates **1-4** were prepared according to earlier reported procedure [66].

General Procedure for the Reactions of the 4-Phosphorylated 5-Hydroxy-5-methylhexa-2,3-dienoates **1-4** with Electrophilic Reagents

To a solution of the 4-phosphorylated 5-hydroxyhexa-2,3-dienoates with protected (**1** or **2**) or unprotected (**3** or **4**) hydroxy group (3.0 mmol) in dry dichloromethane (10 mL) at -20 °C was added dropwise under stirring a solution of electrophilic reagent (sulfuryl chloride, bromine, benzenesulfonyl chloride or benzeneselenenyl chloride) (3.6 mmol) in the same solvent (10 mL). The reaction mixture was stirred at the same temperature for 3 hours (**5** and **6**) and 5 hours (**7** and **8**) at room temperature. After evaporation of the solvent, the residue was purified by column chromatography on silica gel with ethyl acetate/hexane. The pure products **5-8** had the following properties:

Methyl 4-bromo-2-isopropoxy-3-(1-methyl-1-tetrahydro-2H-pyran-2-yloxyethyl)-2-oxo-5-phenyl-2,5-dihydro-1,2-oxaphosphole-5-carboxylate (5a). Yellow oil, yield: 41%. Eluent for TLC: ethyl acetate:hexane = 1:4, R_f 0.43; IR (neat, cm^{-1}): 1024 (C-O-P), 1123 (C-O-C), 1269 (P=O), 1439, 1494 (Ph), 1578 (C=C), 1723 (C=O). ^1H NMR (600.1 MHz): δ 1.27 (t, $J=6.8$ Hz, 3H, MeCH_2O), 1.32 (d, $J=6.1$ Hz, 3H, Me_2CHO), 1.40-1.72 (m, 6H, OTHP), 1.60 (d, $J=10.6$ Hz, 3H, Me_2C), 3.69-3.82 (m, 2H, OTHP), 4.07-4.18 (m, 1H, Me_2CHO), 4.19 (q, $J=6.8$ Hz, 2H, MeCH_2O), 4.72-4.76 (m, 1H, OTHP), 7.45-7.64 (m, 5H, Ph). ^{13}C NMR (150.9 MHz): δ 13.9 (CH_3), 21.2 (CH_2), 23.9 ($J=7.8$, 2CH_3), 25.5 (CH_2), 31.8 ($J=7.9$, 2CH_3), 33.0 (CH_2), 62.5 (CH_2), 64.4 (CH_2), 66.6 ($J=5.1$, CH), 77.8 ($J=6.0$ Hz, C), 93.4 ($J=9.8$ Hz, C), 94.1 ($J=5.0$ Hz, CH), 127.1-136.4 (Ph), 134.5 ($J=51.4$ Hz, C), 136.6 ($J=153.5$ Hz, C), 169.9 ($J=8.1$ Hz, C). ^{31}P NMR (242.9 MHz): δ_P 31.2. HRMS (ESI): m/z calcd for $\text{C}_{22}\text{H}_{31}\text{BrO}_7\text{P}$ $[\text{M}+\text{H}]^+$ 518.3551, found 518.3573. Anal. Calcd for $\text{C}_{22}\text{H}_{30}\text{BrO}_7\text{P}$: C 51.08, H 5.84. Found: C 51.14, H 5.88.

Diisopropyl [3-bromo-2-(1-methyl-1-tetrahydro-2H-pyran-2-yloxyethyl)-5-oxo-4-phenyl-2,5-

dihydrofuran-2-yl]-phosphonate (6a). Light yellow oil, yield: 28%. Eluent for TLC: ethyl acetate:hexane = 1:4, R_f 0.65; IR (neat, cm^{-1}): 1117 (C-O-C), 1271 (P=O), 1441, 1489 (Ph), 1619 (C=C), 1747 (C=O). ^1H NMR (600.1 MHz): δ 1.26 (dd, $J=6.1$ Hz, $J=6.2$ Hz, 6H, Me_2CHO), 1.39-1.63 (m, 6H, OTHP), 1.61, 1.74 (ss, 6H, Me_2C), 4.62-4.79 (m, 1H, Me_2CHO), 3.54-3.77 (m, 2H, OTHP), 4.91-4.97 (m, 1H, OTHP), 7.44-7.80 (m, 5H, Ph). ^{13}C NMR (150.9 MHz): δ 21.0 (CH_2), 24.1 ($J=7.8$, 2CH_3), 25.4 (CH_2), 27.2 ($J=8.0$, CH_3), 28.1 ($J=8.0$, CH_3), 32.3 (CH_2), 64.2 (CH_2), 72.3 ($J=5.0$ Hz, CH), 84.3 ($J=9.7$ Hz, C), 93.3 ($J=4.6$ Hz, CH), 97.4 ($J=137.7$ Hz, C), 127.1-129.6 (Ph), 140.5 ($J=50.4$ Hz, C), 146.3 ($J=7.9$ Hz, C), 169.8 ($J=7.8$ Hz, C). ^{31}P NMR (242.9 MHz): δ_p 15.7. Anal. Calcd for $\text{C}_{24}\text{H}_{34}\text{BrO}_7\text{P}$: C 52.85, H 6.28. Found: C 52.80, H 6.24.

Methyl 3-(1-hydroxy-1-methyl-ethyl)-2-isopropoxy-2-oxo-5-phenyl-4-phenylsulfenyl-2,5-dihydro-1,2-oxaphosphole-5-carboxylate (5b). Orange oil, yield: 40%. Eluent for TLC: ethyl acetate:hexane = 1:4, R_f 0.36; IR (neat, cm^{-1}): 1018 (C-O-P), 1267 (P=O), 1438, 1490 (Ph), 1580 (C=C), 1722 (C=O), 3411 (OH). ^1H NMR (600.1 MHz): δ 1.21 (d, $J=6.1$ Hz, 6H, Me_2CHO), 1.31 (t, $J=7.1$ Hz, 3H, MeCH_2O), 1.48 (d, $J=10.5$ Hz, 6H, Me_2CH), 2.75 (s, 1H, OH), 4.18 (q, $J=7.1$ Hz, 2H, MeCH_2O), 4.51-4.71 (m, 1H, Me_2CHO), 7.09-7.61 (m, 10H, 2Ph). ^{13}C NMR (150.9 MHz): δ 13.8 (CH_3), 21.2 ($J=7.8$, 2CH_3), 32.4 ($J=8.0$, 2CH_3), 62.4 (CH_2), 71.5 ($J=4.9$ Hz, CH), 74.8 ($J=9.8$ Hz, C), 95.0 ($J=9.9$ Hz, C), 124.9-139.0 (2Ph), 141.5 ($J=98.5$ Hz, C), 155.8 ($J=15.0$ Hz, C), 167.7 ($J=7.8$ Hz, C). ^{31}P NMR (242.9 MHz): δ_p 33.6. Anal. Calcd for $\text{C}_{23}\text{H}_{27}\text{O}_6\text{PS}$: C 59.73, H 5.88. Found: C 59.79, H 5.91.

Diisopropyl [2-(1-hydroxy-1-methylethyl)-5-oxo-4-phenyl-3-phenylsulfenyl-2,5-dihydrofuran-2-yl]-phosphonate (6b). Yellow oil, yield: 27%. Eluent for TLC: ethyl acetate:hexane = 1:4, R_f 0.58; IR (neat, cm^{-1}): 1125 (C-O-C), 1272 (P=O), 1441, 1493 (Ph), 1620 (C=C), 1748 (C=O), 3424 (OH). ^1H NMR (600.1 MHz): δ 1.29 (dd, $J=6.3$ Hz, $J=6.1$ Hz, 6H, Me_2CHO), 1.49, 1.63 (ss, 6H, Me_2C), 4.14 (s, 1H, OH), 4.63-4.78 (m, 1H, Me_2CHO), 7.11-7.94 (m, 10H, 2Ph). ^{13}C NMR (150.9 MHz): δ 24.1 ($J=8.0$, 2CH_3), 27.4 ($J=7.8$, CH_3), 28.1 ($J=7.8$, CH_3), 72.4 ($J=4.6$ Hz, CH), 80.9 ($J=10.1$ Hz, C), 95.6 ($J=140.2$ Hz, C), 125.3-136.9 (2Ph), 131.7 ($J=7.8$ Hz, C), 163.2 ($J=14.7$ Hz, C), 168.8 ($J=7.9$ Hz, C). ^{31}P NMR (242.9 MHz): δ_p 15.5. HRMS (ESI): m/z calcd for $\text{C}_{25}\text{H}_{32}\text{O}_6\text{PS}$ $[\text{M}+\text{H}]^+$ 491.5577, found 491.5590. Anal. Calcd for $\text{C}_{25}\text{H}_{31}\text{O}_6\text{PS}$: C 61.21, H 6.37. Found: C 61.28, H 6.32.

5-Methoxycarbonyl-3-(1-methyl-1-tetrahydro-2H-pyran-2-yloxyethyl)-2,2,5-triphenyl-4-phenylselenenyl-2,5-dihydro-1,2-oxaphosphol-2-ium Chloride (7a). Orange oil, yield: 48%. Eluent for TLC: ethyl acetate:hexane = 1:4, R_f 0.36; IR (neat, cm^{-1}): 1119 (C-O-C), 1437, 1493 (Ph), 1578 (C=C), 1721 (C=O). ^1H NMR (600.1 MHz): δ 1.29 (t, $J=6.8$ Hz, 3H, MeCH_2O), 1.39-1.49 (m, 6H, OTHP), 1.63 (s, 6H, Me_2C), 3.67-3.84 (m, 2H, OTHP), 4.11-4.20 (m, 2H, MeCH_2O), 4.96-5.03 (m, 1H, OTHP), 6.83-8.31 (m, 20H, 4Ph). ^{13}C NMR (150.9 MHz): δ 14.0 (CH_3), 21.4 (CH_2), 25.7 (CH_2), 27.9 ($J=7.7$ Hz, 2CH_3), 32.7 (CH_2), 62.4 (CH_2), 64.0 (CH_2), 86.7 ($J=10.2$ Hz, C), 95.8 ($J=4.6$ Hz, CH), 99.2 ($J=9.9$ Hz, C), 110.8-140.2 (4Ph), 138.1 ($J=49.8$ Hz, C), 170.3 ($J=14.1$ Hz, C), 177.1 ($J=7.8$ Hz, C). ^{31}P NMR (242.9 MHz): δ_p 82.4. Anal. Calcd for $\text{C}_{37}\text{H}_{38}\text{ClO}_5\text{PSe}$: C 62.76, H 5.41. Found: C 62.82, H 5.45.

5-(Diphenylphosphinoyl)-5-(1-methyl-1-tetrahydro-2H-pyran-2-yloxyethyl)-3-phenyl-4-phenylselenenyl-5H-furan-2-one (8a). Yellow oil, yield: 26%. Eluent for TLC: ethyl acetate:hexane = 1:4, R_f 0.63; IR (neat, cm^{-1}): 1125 (C-O-C), 1173 (P=O), 1437, 1488 (Ph), 1621 (C=C), 1747 (C=O). ^1H NMR (600.1 MHz): δ 1.34-1.64 (m, 6H, OTHP), 1.55, 1.72 (ss, 6H, Me_2C), 3.54-3.77 (m, 2H, OTHP), 4.90-4.96 (m, 1H, OTHP), 7.41-7.95 (m, 20H, 4Ph). ^{13}C NMR (150.9 MHz): δ 21.2 (CH_2), 25.9 (CH_2), 25.8 ($J=8.1$ Hz, CH_3), 26.9 ($J=8.1$ Hz, CH_3), 64.1 (CH_2), 86.3 ($J=10.2$ Hz, C), 93.5 ($J=4.6$ Hz, CH), 99.7 ($J=139.4$ Hz, C), 126.6-132.0 (4Ph), 141.4 ($J=50.1$ Hz, C), 150.6 ($J=7.9$ Hz, C), 170.4 ($J=7.8$ Hz, C). ^{31}P NMR (242.9 MHz): δ_p 15.2. HRMS (ESI): m/z calcd for $\text{C}_{36}\text{H}_{36}\text{O}_5\text{PSe}$ $[\text{M}+\text{H}]^+$ 658.6018, found 658.6079. Anal. Calcd for $\text{C}_{36}\text{H}_{35}\text{O}_5\text{PSe}$: C 65.75, H 5.36. Found: C 65.82, H 5.41.

4-Chloro-3-(1-hydroxy-1-methyl-ethyl)-5-methoxycarbonyl-2,2,5-triphenyl-2,5-dihydro-1,2-oxaphosphol-2-ium Chloride (7b). Yellow oil, yield: 47%. Eluent for TLC: ethyl acetate:hexane = 1:4, R_f 0.39; IR (neat, cm^{-1}): 1439, 1492 (Ph), 1580 (C=C), 1726 (C=O), 3389 (OH). ^1H NMR (600.1 MHz): δ 1.23 (t, $J=6.8$ Hz, 3H, MeCH_2O), 1.69 (s, 6H, Me_2C), 4.10-4.20 (m, 2H, MeCH_2O), 5.64 (s, 1H, OH), 6.90-8.24 (m, 15H, 3Ph). ^{13}C NMR (150.9 MHz): δ 13.9 (CH_3), 34.7 ($J=7.8$ Hz, 2CH_3), 62.3 (CH_2), 73.4 ($J=9.8$ Hz, C), 100.7 ($J=10.2$ Hz, C), 106.9-136.7 (3Ph), 137.1 ($J=50.1$ Hz, C), 158.2 ($J=39.7$ Hz, C), 167.9 ($J=7.8$ Hz, C). ^{31}P NMR (242.9 MHz): δ_p 85.1. HRMS (ESI): m/z calcd for $\text{C}_{26}\text{H}_{26}\text{Cl}_2\text{O}_4\text{P}$ $[\text{M}+\text{H}]^+$ 504.3614, found 504.3637. Anal. Calcd for $\text{C}_{26}\text{H}_{25}\text{Cl}_2\text{O}_4\text{P}$: C 62.04, H 5.01. Found: C 61.97, H 4.95.

4-Chloro-5-(diphenylphosphinoyl)-5-(1-hydroxy-1-methyl-ethyl)-3-phenyl-5H-furan-2-one (8b). Yellow oil, yield: 27%. Eluent for TLC: ethyl acetate:hexane = 1:4, R_f 0.64; IR (neat, cm^{-1}): 1119 (C-O-C), 1180 (P=O), 1435, 1488 (Ph), 1622 (C=C), 1745 (C=O), 3409 (OH). ^1H NMR (600.1 MHz): δ 1.55, 1.70 (ss, 6H, Me_2C), 5.59 (s, 1H, OH), 7.33-7.86 (m, 15H, 3Ph). ^{13}C NMR (150.9 MHz): δ 27.4 ($J=7.8$ Hz, CH_3), 28.3 ($J=7.8$ Hz, CH_3), 80.0 ($J=10.2$ Hz, C), 100.7 ($J=139.4$ Hz, C), 127.3-132.4 (3Ph), 144.3 ($J=7.9$ Hz, C), 155.1 ($J=10.1$ Hz, C), 168.0 ($J=8.1$ Hz, C). ^{31}P NMR (242.9 MHz): δ_p 16.5. Anal. Calcd for $\text{C}_{25}\text{H}_{22}\text{ClO}_4\text{P}$: C 66.30, H 4.90. Found: C 66.26, H 4.96.

Procedure for Silver-catalyzed Cycloisomerization of the 4-Phosphorylated 5-Hydroxy-5-methylhexa-2,3-dienoates 3 and 4.

Method A: Silver perchlorate (0.15 mmol) was added to a solution of the 4-phosphorylated 5-hydroxy-5-methylhexa-2,3-dienoate **3** or **4** (3.0 mmol) in dry dichloromethane (10 mL). The mixture was stirred at room temperature in the dark for 7 hours (in case of **3**) and 9 hours (in case of **4**). Saturated sodium chloride solution was added to precipitate the silver ions. The product was extracted by chloroform. The organic layer was dried over anhydrous sodium sulfate. After evaporation of the solvent, the residue was chromatographed on a column with a mixture of ethyl acetate and hexane as an eluent to give the pure products **9** as oils.

Method B: The 4-phosphorylated 5-hydroxy-5-methylhexa-2,3-dienoate **3** or **4** (3.0 mmol) is dissolved in 40:60 water/acetone (10 mL) containing calcium carbonate (1 mmol) and silver nitrate (0.3 mmol). The mixture was stirred at room temperature in the dark for 12 hours (in case of **3**) and 15 hours (in case of **4**). The product was taken up in diethyl ether and the ether solution was washed with saturated sodium chloride solution. The organic layer was dried over anhydrous magnesium sulfate. After evaporation of the solvent, the residue was chromatographed on a column with a mixture of ethyl acetate and hexane as an eluent to give the pure products **9** as oils, which had the following properties:

Methyl 4-(diisopropylphosphoryl)-5,5-dimethyl-2-phenyl-2,5-dihydrofuran-2-carboxylate (9a). Yellow oil, yield: 83% (*Method A*), 61% (*Method B*). Eluent for TLC: ethyl acetate:hexane = 1:4, R_f 0.50; IR (neat, cm^{-1}): 1122 (C-O-C), 1267 (P=O), 1438, 1489 (Ph), 1624 (C=C), 1721 (C=O). ^1H NMR (600.1 MHz): δ 1.54, 1.63 (ss, 6H, Me_2C), 3.66 (d, $J=10.7$ Hz, 6H, 2MeO), 3.81 (s, 3H, MeO),

7.16 (d, $J=10.5$ Hz, 1H, =CH), 7.20-7.84 (m, 5H, Ph). ^{13}C NMR (150.9 MHz): δ 28.4 ($J=7.9$ Hz, CH_3), 28.8 ($J=7.9$ Hz, CH_3), 52.4 ($J=14.6$ Hz, 2 CH_3), 53.2 (CH_3), 89.7 ($J=9.8$ Hz, C), 90.5 ($J=7.7$ Hz, C), 126.4-139.6 (Ph), 138.5 ($J=21.7$ Hz, C), 142.5 ($J=7.8$ Hz, CH), 169.4 ($J=4.0$ Hz, C). ^{31}P NMR (242.9 MHz): δ_p 16.6. HRMS (ESI): m/z calcd for $\text{C}_{20}\text{H}_{30}\text{O}_6\text{P}$ [$\text{M}+\text{H}$] $^+$ 397.4224, found 397.4303. Anal. Calcd for $\text{C}_{20}\text{H}_{29}\text{O}_6\text{P}$: C 60.60, H 7.37. Found: C 60.54, H 7.40.

Methyl 4-(diphenylphosphinoyl)-5,5-dimethyl-2-phenyl-2,5-dihydrofuran-2-carboxylate (9b). Colourless oil, yield: 84% (*Method A*), 64% (*Method B*). Eluent for TLC: ethyl acetate:hexane = 1:4, R_f 0.46; IR (neat, cm^{-1}): 1122 (C-O-C), 1173 (P=O), 1442, 1493 (Ph), 1623 (C=C), 1726 (C=O). ^1H NMR (600.1 MHz): δ 1.50, 1.58 (ss, 6H, Me_2C), 3.78 (s, 3H, MeO), 7.20-7.84 (m, 15H, 3Ph), 7.35 (d, $J=10.5$ Hz, 1H, =CH). ^{13}C NMR (150.9 MHz): δ 27.3 ($J=7.8$ Hz, CH_3), 27.9 ($J=7.8$ Hz, CH_3), 52.8 (CH_3), 91.3 ($J=9.7$ Hz, C), 92.0 ($J=7.6$ Hz, C), 126.3-140.5 (3Ph), 143.5 ($J=20.9$ Hz, C), 144.4 ($J=8.1$ Hz, CH), 169.0 ($J=4.2$ Hz, C). ^{31}P NMR (242.9 MHz): δ_p 82.5. Anal. Calcd for $\text{C}_{26}\text{H}_{25}\text{O}_4\text{P}$: C 72.21, H 5.83. Found: C 72.26, H 5.90.

RESULTS AND DISCUSSION

Synthesis of the 4-phosphorylated 5-hydroxy-5-methylhexa-2,3-dienoates 1-4

We applied a convenient, efficient, atom-economical and regioselective four-step method to achieve a range of the 4-phosphorylated 5-hydroxy-5-methylhexa-2,3-dienoates **1-4** [66]. The allenylphosphonates **1** and **3** and allenyl phosphine oxides **2** and **4** isolated in preparative amounts allowed us to study its chemical behavior in the reactions with electrophilic reagents and the silver-catalyzed cycloisomerization reactions. The present paper is a recent part of our long-term objective to investigate both the scope and the limitations of the electrophilic cyclization and cycloisomerization reactions of the trifunctionalized allenes, namely the phosphorylated hydroxyallenecarboxylates.

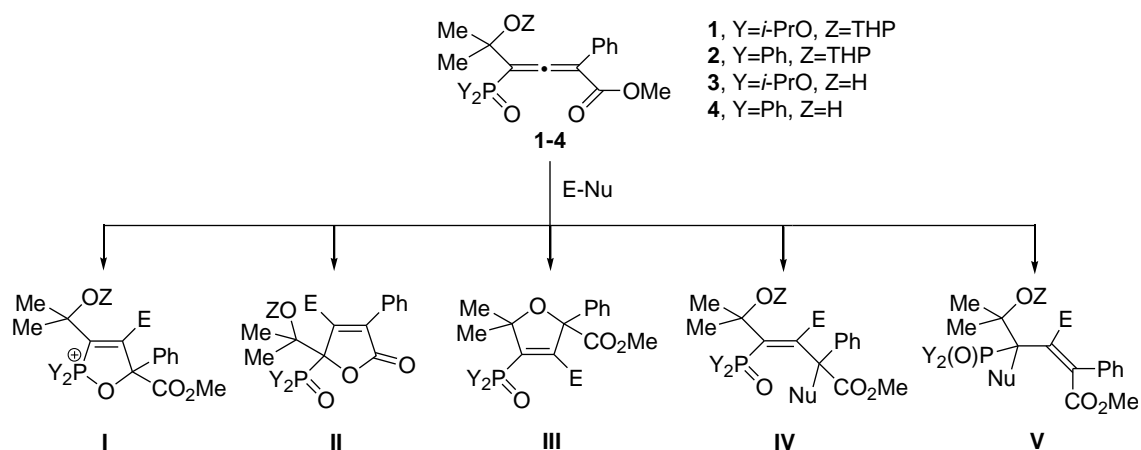
Competitive Electrophilic Cyclization of the 4-phosphorylated 5-hydroxy-5-methylhexa-2,3-dienoates 2 and 4

It is necessary to draw attention to the fact that conceptually three distinct modes of cyclization of the 4-phosphorylated 5-hydroxyhexa-2,3-dienoates **1-4** are possible. They depend on the electrophilic atom that forms a new bond with the central carbon of the allenic system, which seems likely [13-24,73-78]. It is evident that these pathways are closely connected with the intramolecular

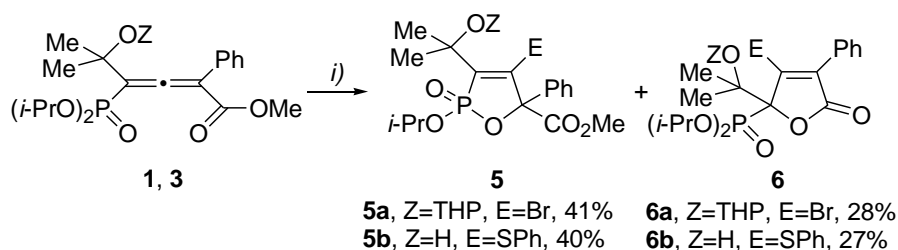
I. E. Ismailov et al.: Trifunctionalized allenes. Part V. Competitive electrophilic cyclization and cycloisomerization ...

neighboring group participation of the phosphoryl, ethoxycarbonyl and/or the hydroxymethyl groups as internal nucleophile(s) in the final step of the cyclization. Besides the 5-*endo-trig* cyclizations [79] to the 2,5-dihydro-1,2-oxaphosphole-5-carboxylates **I**, the 5-phosphoryl-furan-2(5*H*)-ones **II** or the 4-phosphoryl-2,5-dihydrofuran-2-carboxylates **III**, the electrophilic addition might afford the 2,3-adducts **IV** and/or the 2,1-adducts **V** (Scheme 1). We started the present study with the reaction of the 4-(dimethoxyphosphoryl)-5-hydroxy-5-methylhexa-2,3-dienoates with protected (**1**) or unprotected (**3**) hydroxy group with bromine or benzenesulfonyl chloride (Scheme 2). We conducted the reactions under the optimized reaction conditions determined in the similar reactions of the bifunctionalized allenes [67,68,70] – solvent CH₂Cl₂ at -20 °C using 1.0 *equiv* of the

allenephosphonate and 1.2 *equiv* of the electrophilic reagent. We have to say that the reaction under this set of standard reaction conditions in the favored 5-*endo-trig* mode affords mixtures of the 2-oxo-2,5-dihydro-1,2-oxaphosphole-5-carboxylates **5** and 5-oxo-2,5-dihydrofuran-2-ylphosphonates **6** at the ratio 1.48:1 and 1.46:1 by competitive electrophilic cyclization of the 4-phosphorylated 5-hydroxy-5-methylhexa-2,3-dienoates **1** and **3** with the neighboring group participation of phosphonate and carboxylate groups in the cyclization in very good overall yields (69 and 67%). To outline the general terms of this methodology, the reaction of the 4-(diphenylphosphinoyl)-5-hydroxy-5-methylhexa-2,3-dienoates with protected and unprotected hydroxyl group **2** and **4** with benzeneselenenyl chloride or sulfonyl chloride was investigated.

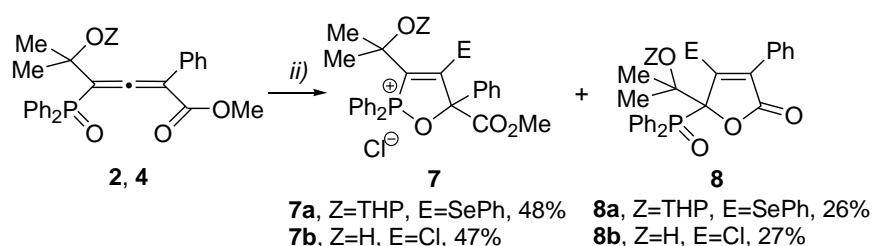


Scheme 1. Probable products of the reaction of the 4-phosphorylated 5-hydroxy-5-methylhexa-2,3-dienoates **1-4** with electrophilic reagents



Reagents and Conditions: i) Br₂ or PhSCL (1.2 eq), CH₂Cl₂, -20 °C, 3 h, rt, 5h, stirring, column chromatography.

Scheme 2. Synthesis of the 2-oxo-2,5-dihydro-1,2-oxaphosphole-5-carboxylates **5** and the 5-oxo-2,5-dihydrofuran-2-ylphosphonates **6** by electrophilic cyclization of the 4-phosphorylated 5-hydroxy-5-methylhexa-2,3-dienoates **2** and **4**.



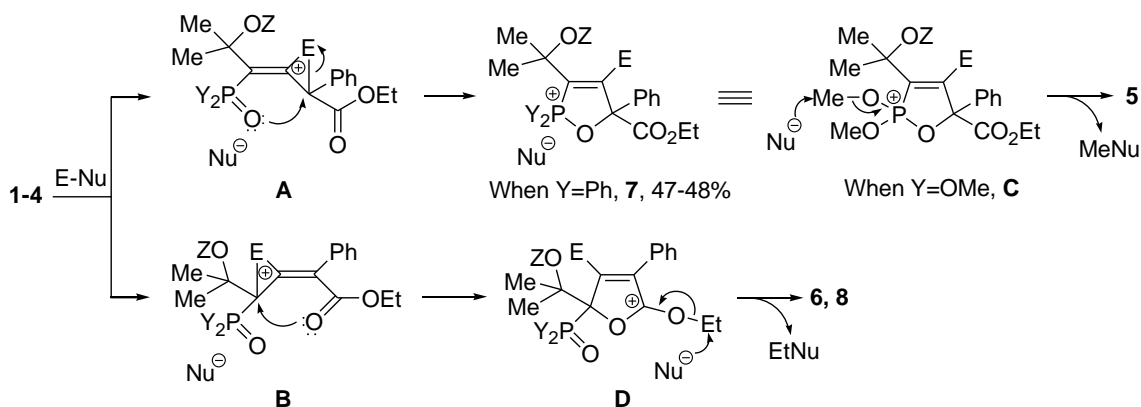
Reagents and Conditions: ii) PhSeCl or SO₂Cl₂ (1.2 eq), CH₂Cl₂, -20 °C, 3h, rt, 5h, stirring, column chromatography.

Scheme 3. Synthesis of the 5-carbonylated 2,5-dihydro-1,2-oxaphosphol-2-ium chlorides **7** and the 5-phosphorylated furan-2(5*H*)-ones **8** by electrophilic cyclization of the 4-phosphorylated 5-hydroxy-5-methylhexa-2,3-dienoates **2** and **4**.

Surprisingly, once we applied the current standard conditions to the 1,1,3-trifunctionalized allenes comprising a phosphine oxide, an ethoxycarbonyl and a hydroxymethyl group such as **2** and **4** (Scheme 3), the interaction afforded mixtures of the 5-ethoxycarbonyl-2,5-dihydro-1,2-oxaphosphol-2-ium chlorides **7** and 5-(diphenylphosphinoyl)-furan-2(5*H*)-ones **8** in overall yields (74% and 74%) at the ratio 1.74:1 and 1.85:1. These reaction pathways may be interpreted as a result of the neighboring phosphine oxide and ethoxycarbonyl groups participation as the internal nucleophiles in the favored 5-*endo-trig* mode cyclization.

The simplest - although by no means unique - mechanistic rationale for this reaction based on available literature data [13-24,73-78] and on our recent results [67,68,70] is depicted in Scheme 4. The starting point is the attack of the electrophile (Cl^+ , Br^+ , S^+ or Se^+) on the most nucleophilic atom of the allenic system of π -bonds (central C^3 -atom) with formation of the cyclic onium (chloronium, bromonium, thiiranium or seleniranium) ions **A** and **B** after attack on both C^2 - C^3 - and C^3 - C^4 -double

bonds. Then the ions **A** and **B** are easily transformed into the more stable five-membered cyclic ions **C** (the isolated compounds **7** in the case of the phosphine oxides **2** and **4** ($\text{Y}=\text{Ph}$)) and **D** via the attachment of the oxygen atom of the phosphonate and carboxylate functionality. Further, the intermediates **C** undergo nucleophilic attack on the MeO group and elimination of methyl halide (MeNu) affording the final cyclic products **5** (when Y is OMe). Analogously, the ions **D** transform in the furan-2(5*H*)-ones **6** and **8** after nucleophilic attack on the EtO group and elimination of ethyl halide (EtNu). Formation of the cyclic products **5-8** can be considered in terms of the assumption of concurrent attacks of the external nucleophiles (phosphoryl and carboxyl groups) on the cyclic three-membered onium ion **A** and **B**. When $\text{Y}=\text{Ph}$ (starting compounds are phosphine oxides **2** and **4**), the reaction stops in the stage of formation of the cyclic phosphonium salts **7**, since in this case the stabilization by elimination of methyl halide (second stage of an Arbuzov-type rearrangement) and formation of products with tetracoordinated phosphorus is impossible [17,19,21-24].



Scheme 4. A rationale for the reaction of the 4-phosphorylated 5-hydroxyhexa-2,3-dienoates **1-4** with electrophilic reagents.

Obviously, this mechanistic rationale could be explained by the assumption of favorable *trans* arrangement of the electrophile and the internal nucleophile (phosphoryl or carboxyl groups) and *anti*-attack of the internal nucleophiles Nu on the onium ions **A** and **B**. This is supposed to arise from attacks on the allenic C^2 - C^3 - and C^3 - C^4 -double bonds *anti* to the phosphoryl and carboxyl groups, respectively.

The above mentioned explanation should account for the results on the study of the reactions of other trifunctionalized allenes with electrophilic reagents. Further work in this area shall focus on exploiting and extending the synthetic utility of the

trifunctionalized allenes for the preparation of different heterocyclic systems by application of the electrophilic cyclization methodology.

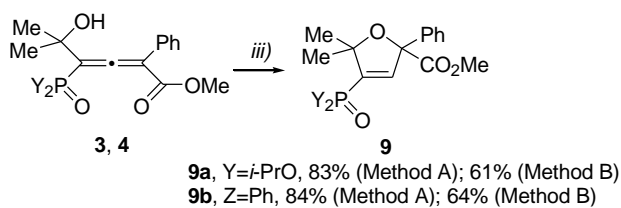
Silver-catalyzed cycloisomerization of the 4-phosphorylated 5-hydroxy-5-methylhexa-2,3-dienoates 3 and 4

In addition to the above mentioned preparation of 2,5-dihydro-1,2-oxaphosphole-5-carboxylates **5** and **7** and the 5-phosphoryl-furan-2(5*H*)-ones **6** and **8** by electrophilic cyclization of the 4-phosphorylated 5-hydroxy-5-methylhexa-2,3-dienoates **1-4** due to the phosphonate (phosphine oxide) or carboxylate neighboring group

I. E. Ismailov et al.: Trifunctionalized allenes. Part V. Competitive electrophilic cyclization and cycloisomerization ...

participation in the 5-endo-trig mode cyclization, the next step in our study was to explore the possibilities of the cycloisomerization reaction of the above 4-phosphorylated 5-hydroxy-5-methylhexa-2,3-dienoates **3** and **4** in the presence of silver salts as catalysts. We conducted the reaction under the optimized reaction conditions determined earlier in the similar reactions of the phosphorylated (α -hydroxy)- [69,71] and (β -hydroxy)-allenes [71,72] – solvent methylene chloride, 5 mol % catalyst and room temperature. The reaction occurred *via* a 5-endo-trig cyclization to give the 4-phosphoryl-2,5-dihydrofuran-2-carboxylates **9** (Scheme 4).

The results are explicit enough – a catalytic 5-endo-trig cycloisomerization occurs and the hydroxy group participates as an internal nucleophile to give the 4-phosphoryl-2,5-dihydrofuran-2-carboxylates **9** in good yields in the silver-catalyzed cycloisomerization reaction of the 4-phosphorylated 5-hydroxy-5-methylhexa-2,3-dienoates **3** and **4**.



Reagents and Conditions: iii) *Method A:* AgClO₄ (5 mol %), CH₂Cl₂, rt, stirring in the dark 7 h (for **9a**) and 9 h (for **9b**), work-up (NaCl, CHCl₃, Na₂SO₄), column chromatography; *Method B:* 40:60 water/acetone with CaCO₃ (1 mol %), AgNO₃ (10 mol %), rt, stirring in the dark 12 h (for **9a**) and 15 (for **9b**), work-up (Et₂O, NaCl, MgSO₄), column chromatography.

Scheme 4. Synthesis of 4-phosphorylated 2,5-dihydrofuran-2-carboxylates **9** by silver-catalyzed cycloisomerization of the 4-phosphorylated 5-hydroxy-5-methylhexa-2,3-dienoates **3** and **4**.

CONCLUSIONS

In conclusion, we have developed the competitive electrophilic cyclization and silver-catalyzed cycloisomerization reactions of 4-phosphorylated 5-hydroxypenta-2,3-dienoates, which provided an efficient route to 2,5-dihydro-1,2-oxaphospholes, 5-phosphorylated furan-2(5*H*)-ones and 4-phosphorylated 2,5-dihydrofurans which are produced as a result of the participation of the neighboring phosphonate (phosphine oxide), carboxylate or hydroxy groups as internal nucleophiles in the 5-endo-trig cyclization processes. Due to the convenient operation and mild conditions, the ready availability of the reagents and catalysts, the good yields and the

usefulness of the heterocyclic compounds prepared, the cyclization reactions may show potential and will be useful in their application in target-oriented synthesis. The successful synthesis of these compounds opens a new access to novel heterocyclic molecules with interesting properties, as well as a broad range of biological activities.

Acknowledgements: Financial support by the Research Fund of the Konstantin Preslavsky University of Shumen under Projects Nos. RD-08-158/2018 and RD-08-94/2019 is gratefully acknowledged.

REFERENCES

- H. F. Schuster, G. M. Coppola, *Allenes in Organic Synthesis*, Wiley, New York, 1984.
- Modern Allene Chemistry, N. Krause, A. S. K. Hashmi (eds.) Wiley-VCH, Weinheim, 2004.
- M. Brasholz, H.-U. Reissig, R. Zimmer, *Acc. Chem. Res.*, **42**, 45 (2009).
- S. Ma, *Acc. Chem. Res.*, **42**, 1679 (2009).
- S. Yu, S. Ma, *Angew. Chem., Int. Ed.*, **51**, 3074 (2012).
- A. Hoffmann-Röder, N. Krause, *Angew. Chem., Int. Ed.*, **43**, 1196 (2004).
- F. Yu, X. Lian, S. Ma, *Org. Lett.*, **9**, 1703 (2007).
- F. Yu, X. Lian, J. Zhao, Y. Yu, S. Ma, *J. Org. Chem.*, **74**, 1130 (2009).
- P. Li, Z.-J. Liu, J.-T. Liu, *Tetrahedron*, **66**, 9729 (2010).
- N. Xin, S. Ma, *Eur. J. Org. Chem.*, 3806 (2012).
- P. Fourgeaud, J.-N. Volle, J.-P. Vors, Y.-A. Bekro, J.-L. Pirat, D. Virieux, *Tetrahedron*, **72**, 7912 (2016).
- I. Essid, C. Laborde, F. Legros, N. Sevrain, S. Touil, M. Rolland, T. Ayad, J.-N. Volle, J.-L. Pirat, D. Virieux, *Org. Lett.*, **19**, 1882 (2017).
- C. M. Angelov, *Zh. Obshch. Khim.*, **50**, 2448 (1980).
- C. M. Angelov, N. M. Stoianov, B. I. Ionin, *Zh. Obshch. Khim.*, **52**, 178 (1982).
- C. M. Angelov, C. Z. Christov, *Synthesis*, 664 (1984).
- F. Yu, X. Lian, J. Zhao, Y. Yu, S. Ma, *J. Org. Chem.*, **74**, 1130 (2009).
- C. M. Angelov, *Phosphorus, Sulfur*, **15**, 177 (1983).
- N. G. Khusainova, A. N. Pudovik, *Russ. Chem. Rev.*, **56**, 564 (1987).
- I. V. Alabugin, V. K. Brel, *Russ. Chem. Rev.*, **66**, 205 (1997).
- S. Ma, *Acc. Chem. Res.*, **42**, 1679 (2009).
- V. K. Brel, *Heteroatom. Chem.*, **17**, 547 (2006).
- C. M. Angelov, C. Z. Christov, B. I. Ionin, *Zh. Obshch. Khim.*, **52**, 264 (1982).
- N. G. Khusainova, L. V. Naumova, E. A. Berdnikov, A. N. Pudovik, *Zh. Obshch. Khim.*, **52**, 1040 (1982).

- I. E. Ismailov et al.: Trifunctionalized allenes. Part V. Competitive electrophilic cyclization and cycloisomerization ...
24. D. D. Enchev, C. M. Angelov, E. Krawchik, A. Skowronska, J. Michalski, *Phosphorus, Sulfur, Silicon*, **57**, 249 (1991).
 25. Y. S. Rao, *Chem. Rev.*, **64**, 353 (1964).
 26. Y. S. Rao, *Chem. Rev.*, **76**, 625 (1976).
 27. D. W. Knight, *Contemp. Org. Synth.*, 287 (1994).
 28. E. P. Kohler, W. J. Whitcher, *J. Am. Chem. Soc.*, **62**, 1489 (1940).
 29. G. Asknes, P. Froyen, *Acta Chem. Scand.*, **22**, 2347 (1968).
 30. G. Kresze, W. Runge, E. Ruth, *Liebigs Ann. Chem.*, **756**, 112 (1972).
 31. S. Musierowicz, A. Wroblewski, H. Krawczyk, *Tetrahedron Lett.*, 437 (1975).
 32. G. Kresze, L. Kloimstein, W. Runge, *Liebigs Ann. Chem.*, 979 (1976).
 33. G. B. Gill, M. S. H. Idris, *Tetrahedron Lett.*, **26**, 4811 (1985).
 34. K. Shingu, S. Hagishita, M. Nakagawa, *Tetrahedron Lett.*, 4371 (1967).
 35. S. Ma, S. Wu, *Tetrahedron*, **55**, 12137 (1999).
 36. S. Ma, S. Wu, *Tetrahedron Lett.*, **42**, 4075 (2001).
 37. S. Ma, F. Pan, X. Hao, X. Huang, *Synlett.*, 85 (2004).
 38. C. Fu, S. Ma, *Eur. J. Org. Chem.*, 3942 (2005).
 39. G. Chen, C. Fu, S. Ma, *Tetrahedron*, **62**, 4444 (2006).
 40. C. Zhou, Z. Ma, Z. Gu, C. Fu, S. Ma, *J. Org. Chem.*, **73**, 772 (2008).
 41. R. Zimmer, C. U. Dinesh, E. F. A. Hhan, *Chem. Rev.*, **100**, 3067 (2000).
 42. L.-I. Olsson, A. Claesson, *Synthesis*, 743 (1979).
 43. S. S. Nikam, K. H. Chu, K. K. Wang, *J. Org. Chem.*, **51**, 745 (1986).
 44. J. A. Marshall, C. A. Sehon, *J. Org. Chem.*, **60**, 5966 (1995).
 45. J. A. Marshall, R. H. Yu, J. F. Perkins, *J. Org. Chem.*, **60**, 5550 (1995).
 46. J. -J. Chilot, A. Doutheau, J. Gore, *Tetrahedron Lett.*, **23**, 4693 (1982).
 47. R. Gelin, S. Gelin, M. Albrand, *Bull. Soc. Chim. Fr.*, 1946 (1972).
 48. K. Uemura, D. Shiraiishi, M. Noziri, Y. Inoue, *Bull. Chem. Soc. Jpn.*, **72**, 1063 (1999).
 49. S.-K. Kang, T.-G. Baik, A. N. Kulak, *Synlett.*, 324 (1999).
 50. S.-K. Kang, T. Yamaguchi, S.-J. Pyun, Y.-T. Lee, T.-G. Baik, *Tetrahedron Lett.*, **39**, 2127 (1998).
 51. S. Ma, W. Gao, *Tetrahedron Lett.*, **41**, 8933 (2000).
 52. S. Ma, W. Gao, *J. Org. Chem.*, **67**, 6104 (2002).
 53. E. Yoneda, T. Kaneko, S.-W. Zhang, K. Onitsuka, S. Takahashi, *Org. Lett.*, **2**, 441 (2000).
 54. B. M. Trost, A. B. Pinkerton, *J. Am. Chem. Soc.*, **121**, 10842 (1999).
 55. A. Hoffmann-Roder, N. T. Krause, *Org. Biomol. Chem.*, **3**, 387 (2005).
 56. R. A. Widenhoefer, X. Han, *Eur. J. Org. Chem.*, 4555 (2006).
 57. A. S. K. Hashmi, G. J. Hutchings, *Angew. Chem. Int. Ed.*, **45**, 7896 (2006).
 58. E. Jimenez-Nunez, A. M. Echavarren, *Chem. Commun.*, 333 (2007).
 59. D. J. Gorin, F. D. Toste, *Nature*, **446**, 395 (2007).
 60. N. Bongers, N. Krause, *Angew. Chem. Int. Ed.*, **47**, 2178 (2008).
 61. V. K. Brel, *Synthesis*, 463 (1999).
 62. V. K. Brel, E. V. Abramkin, *Mendeleev Commun.*, **12**, 64 (2002).
 63. A. Hoffman-Roder, N. Krause, *Org. Lett.*, **3**, 2537 (2001).
 64. N. Krause, A. Hoffman-Roder, J. Canisius, *Synthesis*, 1759 (2002).
 65. C. Deutsch, B. Gockel, A. Hoffmann-Roder, N. Krause, *Synlett.*, 1790 (2007).
 66. I. E. Ismailov, I. K. Ivanov, V. C. Christov, *Bulg. Chem. Commun., Special Edition B*, **49**, 33 (2017).
 67. I. K. Ivanov, I. D. Parushev, V. C. Christov, *Heteroatom Chem.*, **25**, 60 (2014).
 68. I. E. Ismailov, I. K. Ivanov, V. C. Christov, *Molecules*, **19**, 11056 (2014).
 69. V. C. Christov, I. E. Ismailov, I. K. Ivanov, *Molecules*, **20**, 7263 (2015).
 70. H. H. Hasanov, I. K. Ivanov, V. C. Christov, *Phosphorus, Sulfur, Silicon*, **193**, 611 (2018).
 71. H. H. Hasanov, I. K. Ivanov, V. C. Christov, *Phosphorus, Sulfur, Silicon*, **193**, 797 (2018).
 72. H. H. Hasanov, I. K. Ivanov, Christov, V. C. *Heteroatom. Chem.*, **28**, e21357 (2017).
 73. P. B. D. De la Mare, R. Bolton, *Electrophilic Addition to Unsaturated Systems*, Elsevier, Amsterdam, The Netherlands, 1966, p. 250.
 74. M. C. Caserio, *Selectivity in Addition Reactions of Allenes*, in: *Selective Organic Transformations*, B. S. Thyagarajannm (ed.), John Wiley & Sons, New York, NY, 1970, p. 239.
 75. P. B. D. De la Mare, R. Bolton, *Electrophilic Addition to Unsaturated Systems*, Elsevier, Amsterdam, The Netherlands, 1982, p. 317.
 76. T. L. Jacobs, *Electrophilic Addition to Allenes*, in: *The Chemistry of the Allenes*, S. R. Landor (ed.), Academic Press, New York, 1982, Vol. 2, p. 417.
 77. W. Smadja, *Chem. Rev.*, **83**, 263 (1983).
 78. S. Ma, *Ionic Addition to Allenes*, in: *Modern Allene Chemistry*, N. Krause, A. S. K. Hashmi (eds.), Wiley-VCH, Weinheim, Germany, 2004, Vol. 2, p. 595.
 79. J. E. Baldwin, *Chem. Commun.* 734 (1976).
 80. H. Lecher, F. Holschneider, *Ber. Dtsch. Chem. Ges.*, **57**, 755 (1924).

Synthesis of poly-(alkyleneterephthalate-co-alkylenephosphate)s and their blends with a linear polyurethane

V. Mitova, N. Koseva*, Z. Todorova, P. Tuleshkov, K. Troev

Institute of Polymers, Bulgarian Academy of Sciences, 1113 Sofia, Bulgaria

Received July 25, 2019; Revised August 13, 2019

Polyphosphoesters present a family of synthetic biodegradable polymers that are recognized as attractive candidates for biomaterials development. Novel poly(alkyleneterephthalate-co-alkylenephosphate)s were prepared from 1,4-bis(2-hydroxyethyl)terephthalate, poly(tetrahydrofuran) (average $M_n \sim 650$) as diol co-monomers in a polycondensation process with ethyl dichlorophosphate and terephthaloyl chloride. ^1H , $^{31}\text{P}\{\text{H}\}$ and ^{31}P NMR spectral data were used for elucidation of the copolymer structure and composition. Products with varying ratios of the phosphate units to the phthalate segments from 1.5 to 4 and number average molar masses in the range of 4500 g/mol to 6800 g/mol were synthesized. Their film-forming properties were enhanced *via* blending with linear polyurethane. The blended materials displayed T_g values and relative hydrophobicity dependent on the content of the phosphate segments. The established trends in structure-properties relationship could be used for design of biomaterials with targeted applications.

Keywords: polyphosphoesters, copolymers, polymer blends, NMR, DMA

INTRODUCTION

The development of novel biomedical technologies such as tissue engineering, drug delivery, regenerative medicine, nanomedicine, etc. requires versatile biodegradable materials as a platform to build on. The complexity and the broad range of applications pose the need for fabrication of new polymers with tailored structure and functionalities. Some of the inherent properties of polymeric biomaterials that can affect their performance include material composition, molecular weight, solubility, hydrophilicity/hydrophobicity, water absorption, degradation, etc. Since 1960s when the first synthetic poly(glycolic acid) based sutures were implemented, extensive research on design of biodegradable polymer materials based on polyesters, polyurethanes, polyanhydrides, poly(alkyl cyanoacrylate)s, polymer blends or composites has been carried out [1].

Polyphosphoesters (PPEs) present a family of synthetic biodegradable polymers with a variety of attractive properties [2]. The common structural characteristics of the PPEs are the phosphoester bonds that link the building units of the polymer backbone. Therefore, they have been recognized as attractive candidates for biomaterials manufactured as polymers susceptible to both hydrolytic and enzymatic degradation under physiological conditions [3]. The physico-chemical properties of these polymers can be adjusted by varying either the backbone building units or side chains structure [4-6]. PPE polymers have been successfully used

for controlled drug and gene delivery [7-10].

The synthetic flexibility of polyphosphoesters allows for the development of copolymers with structural versatility. The polycondensation is a widely studied method to synthesize polyphosphoesters. The reaction proceeds between diols and diesters of H-phosphonic acid, phosphoric dihalides, or phosphoric acid. The biodegradable polylactofate was obtained by bulk or solution polycondensation of dihydroxy(oligolactide) with ethyl dichlorophosphate and the product composition was thoroughly analyzed [11]. The glass transition temperature of the copolymers was found to be inversely proportional to the weight percentage of the phosphoester segment. The copolymers were also found to be more hydrophilic due to the presence of ethylphosphate groups in the backbone.

PPEs derived from bis(2-hydroxyethyl)terephthalate (BHET) and ethyl dichlorophosphate (ECP) with addition of terephthaloyl chloride (TC) as a chain extender were obtained and studied in the preparation of microspheres or conduits [12, 13]. Biocompatibility studies indicated that these PPEs (P(BHET/ECP/TC)) were non-toxic but the implanted devices underwent fragmentation and partial rupture.

Linear polyurethanes (PUs) are an important class of thermoplastic elastomers, which consist of an alternating flexible component (macrodiol) called soft segment, and a stiff component derived from diisocyanate and a chain extender, called hard segment. The nature of hydrogen bonding in the hard segment causes a strong mutual attraction leading to formation of hard and soft segment

* To whom all correspondence should be sent:

E-mail: koseva@polymer.bas.bg

domains. Hard domains act as thermoreversible physical crosslinks and provide for the thermoplastic and elastomeric characteristics of the PU. Therefore, their molecular structure affords a combination of mechanical flexibility and chemical stability that captured the attention of researchers in the field of biomaterials [14, 15].

The aim of the present investigation is the synthesis of poly(alkyleneterephthalate-co-alkylenephosphate)s as new members of the PPE family. The results on their preparation and structural characterization applying NMR technique are reported. To improve PPE film-forming properties and manipulate their physico-chemical characteristics blends with linear polyurethane were prepared and tested.

EXPERIMENTAL

Materials and Methods

Terephthaloyl chloride (TC), 1,4-bis(2-hydroxyethyl) terephthalate (BHET), poly(tetrahydrofuran) (PTHF, average Mn~650), 4-dimethylaminopyridine (DMAP), ethyl dichlorophosphate (ECP), chloroform, tetrachloroethane were purchased from Sigma-Aldrich. Linear polyurethane (PU) with terminal hydroxyl groups and dynamic viscosity 1800 mPa.s (15 % solution in butan-2-one at 23 °C) was kindly supplied by Specialty Polymers Ltd. (Bulgaria). PTHF, BHET and tetrachloroethane were dried prior to use.

Synthetic procedures

Synthesis of poly(alkyleneterephthalate-co-alkylenephosphate)s.

The poly(alkyleneterephthalate-co-alkylenephosphate)s were synthesized following a procedure reported by Mao *et al.* [16] with some modifications. The quantities of the starting monomers in the reaction feed mixture are listed in Table 1. DMAP was used as catalyst in equivalents to the sum of the diols moles. The general procedure used is as follows. Under an argon stream, a two-neck round-bottom flask fitted with a condenser and a dropping funnel was charged with a solution of BHET, PTHF and DMAP in 10 mL tetrachloroethane. The mixture in the flask was cooled down to – 15 °C. A solution of ECP in 5 mL of tetrachloroethane was added dropwise to the flask through the funnel. Following the addition of the ECP, the mixture was stirred first at room temperature for 3 h and then at 45 °C for 6 h. Then the mixture was cooled to room temperature and a solution of TC in 5 mL of tetrachloroethane was added to the flask. The temperature was gradually brought up to 50 °C and allowed to react for 12 h, followed by heating at 65°C for additional 2 h. The mixture was cooled down to room temperature, washed three times with saturated NaCl solution and once with distilled water. The organic layer was concentrated and quenched with ether. The precipitate was dried under vacuum at 40°C overnight to give a copolymer as a white solid. The yield of poly(alkyleneterephthalate-co-alkylenephosphate)s varied between 60% and 65%. The obtained products were assigned as PTPm/n, where m/n was the molar ratio of TC to ECP.

Table 1. Content of the starting monomers in the reaction feed mixture.

Product code	Monomers' content in the reaction feed mixture			
	BHET	PTHF	ECP	TC
PTP4/6	1.5 g	0.4261 g	0.6399 g	0.5316 g
	5.89×10^{-3} moles	0.66×10^{-3} moles	3.93×10^{-3} moles	2.62×10^{-3} moles
PTP3/7	1.5 g	0.4261 g	0.7467 g	0.399 g
	5.89×10^{-3} moles	0.66×10^{-3} moles	4.58×10^{-3} moles	1.96×10^{-3} moles
PTP2/8	1.5 g	0.4261 g	0.907 g	0.266 g
	5.89×10^{-3} moles	0.66×10^{-3} moles	5.75×10^{-3} moles	1.31×10^{-3} moles

Preparation of films from poly(alkyleneterephthalate-co-alkylenephosphate)s-polyurethane blends. Solutions of poly(alkyleneterephthalate-co-alkylenephosphate)s (PTPn/m) and PU in chloroform (0.50 g in 3 ml) were mixed and stirred for 15 min. Then the mixed solutions were casted in PTFE molds and air dried. The films were additionally dried under reduced pressure overnight. A PU film was prepared by casting of PU solution (1.0 g in 6 ml chloroform) and dried under the same conditions.

For contact angle measurements thin polymer films were obtained on glass slides by spin-coating of 7 % solutions in chloroform.

Characterization techniques

NMR spectroscopy. ^1H , ^{31}P and $^{31}\text{P}\{\text{H}\}$ NMR spectra of the synthesized copolymers were recorded on a Bruker Avance II+600 MHz instrument in tetrachloroethane- d_2 at a temperature of 293 K.

Contact angle measurements. The water contact angle of the polymeric films was determined using an Easy Drop DSA20E Krüss GmbH apparatus (Germany). A drop of deionized water (10 μL) was deposited on the surface of the films. Images for temporal evolution of the contact angle value were taken. The average value of the contact angle was determined based on 20 different measurements for each sample.

Dynamic mechanical analysis. The measurements were performed on DMA Q 800 instrument (TA Instruments) in iso-force mode. Specimens with approximate dimensions of $17 \times 7 \times 0.26$ mm were cut off from the prepared films of the PTPm/n-PU blends and PU. Force of 0.5 N was applied to the specimens that were cooled down to -80 °C and held for 3 min. Then displacement (in μm) and relaxation modulus were measured as a function of temperature which increased at a rate of 3 °C/min until displacement reached 2000 μm .

RESULTS AND DISCUSSION

Synthesis and NMR characterization of poly(alkyleneterephthalate-co-alkylenephosphate)s

The polycondensation process of the two diols (BHET and PTHF) and the two acid chlorides (ECP and TC) was performed as a two-step process. At the first step the diols were condensed with ECP and the obtained oligomers were reacted with TC. This reaction scheme reduces the probability for long polyterephthalate blocks to be obtained in the copolymer backbone due to higher reactivity of TC compared to ECP. It was reported by Mao *et al.* [16] that the addition of both chlorides at the same time to the reaction feed resulted in a copolymer displaying a high melting point (above 180 °C) and decreased solubility, especially for ratios $\text{TC:ECP} \geq 0.25$. The reaction scheme is presented in Fig. 1 and the mole ratio of the reactants is given in Table 2. The diols in mole ratio $\text{BHET:PTHF} = 9$ (mass ratio $\text{BHET:PTHF} = 3.5$) and DMAP in equivalents to the sum of the diols moles were dissolved in tetrachloroethane. Preliminary experiments proved tetrachloroethane to be a better solvent for the resulting copolymer than dichloromethane or chloroform. The solution was cooled to -15 °C and ECP was added drop-wise. The reaction proceeded at room temperature for 3 h and at 45 °C for 6 h. When ECP was exhausted (detected by NMR) the second chloride was added followed by stirring at elevated temperatures up to 65 °C for a total of 14 h. The entire synthetic experiment was performed under dry argon atmosphere. The isolated and purified product was structurally characterized applying ^1H , ^{31}P and $^{31}\text{P}\{\text{H}\}$ NMR technique.

Three copolymers were synthesized applying different ratios between TC and ECP. It was proved by the NMR data that the composition of the obtained copolymers was close to the ratio of the starting monomers in the reaction mixture (Table 2).

Table 2. Composition of the reaction feed mixture and of the obtained copolymer.

Product code	Reaction feed mixture		Copolymer composition*		M_n^* , g/mol
	Mole ratio BHET:PTHF	Mole ratio TC:ECP	Phthalate units: phosphate units	Phthalate units: PTHF units	
PTP4/6	9:1	4:6	1:1.5	12.9:1	4500
PTP3/7	9:1	3:7	1:2.3	11.8:1	5600
PTP2/8	9:1	2:8	1:3.9	10.5:1	6800

*Values were calculated on the basis of the ^1H NMR data for the copolymer products.

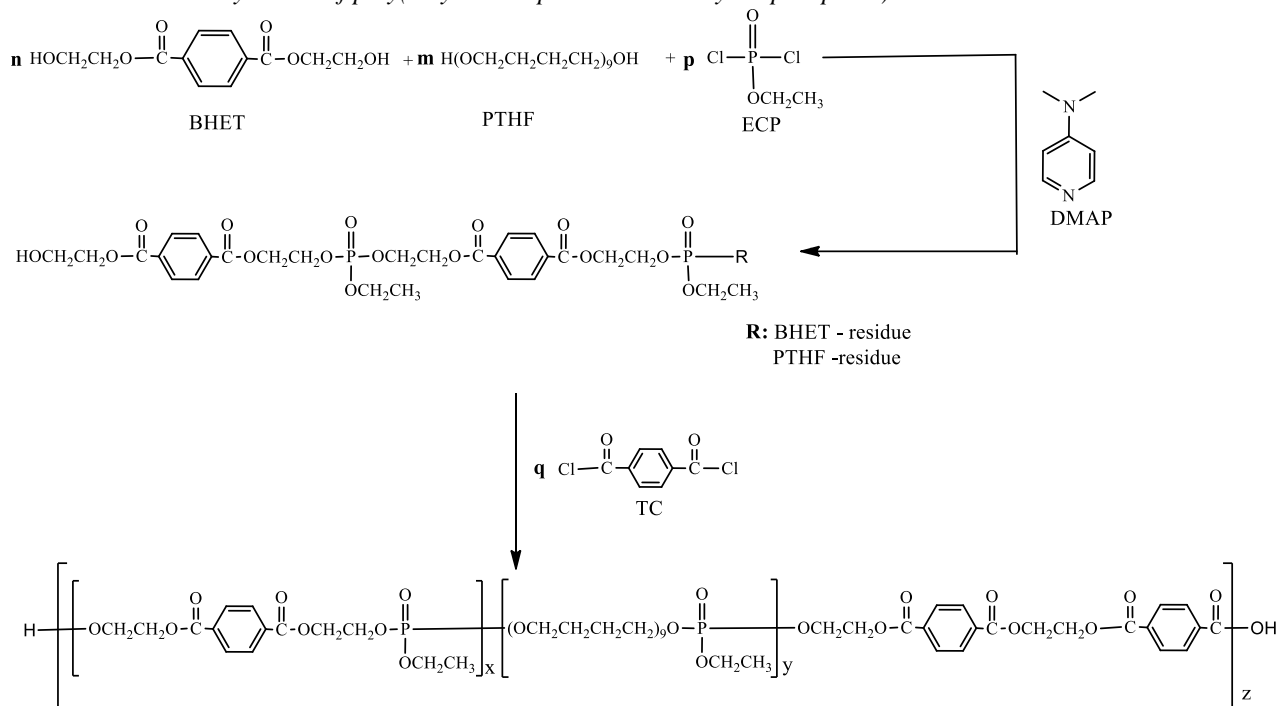


Fig. 1. Two-step synthetic scheme for the preparation of poly(alkyleneterephthalate-co-alkylenephosphate)s.

At the first step of the polycondensation process, i.e. when the reaction proceeded between ECP and the two diols and the latter being in excess, oligomeric products were obtained. The ^1H and $^{31}\text{P}\{\text{H}\}$ NMR spectra of the reaction mixture with mole ratio ECP:TC=8:2 after 9 h reaction time are presented in Fig. 2 (A and B). The spectral data were used to register the degree of ECP conversion, as well as to determine the structure and the number average molar mass of the obtained oligomers. The assignment of the signals is presented in Fig. 2. The $^{31}\text{P}\{\text{H}\}$ NMR spectrum (Fig.2B) evidences two types of P-atoms, which can be assigned to triester phosphate structures in the region from 0.16 ppm to -0.70 ppm and diester chlorophosphate at -5.06 ppm. This assumption is supported by the presence of two couples of signals for the pendant ethyl group to the P-atom in the ^1H NMR spectrum (Fig. 2A): (i) a quartet at 3.11 ppm and a triplet at 1.00 ppm for the hydrogens in the CH_2 and CH_3 groups, respectively, in the end diester phosphate and (ii) the corresponding multiplets in the region 3.79-3.58 ppm and 0.90-0.75 ppm (overlapped triplets) for the triester phosphates. The triester phosphates present 84 mol% that means, 84% of the starting ECP has undergone two substitution reactions forming two new ester bonds, while the rest 16% of the P-centers were terminal reactive moieties. The signal at 3.50 ppm is assigned to the methylene protons adjacent to the hydroxyl group in BHET unit (HOCH_2 -) and can be used for calculation of the molecular mass of the oligomers obtained at the first stage. The latter is determined taking into

consideration the sum of integral intensities of the signals for the ester methylene protons in the region from 4.30 ppm to 3.92 ppm and the integral intensity of the signal at 3.50 ppm used to calculate the integral intensities for one H-atom from the ester or the end CH_2OH groups, respectively. From their ratio it was calculated that the number average molar mass of the oligomeric species was about 900 g/mol.

In the second step the process continued with the addition of the second chloride and polycondensation of the oligomers with TC for obtaining a polymer product. Fig. 3A presents the ^1H NMR spectrum of the product PTP2/8. The signal at 8.00 ppm is due to the H-atoms of the aromatic rings while those at 3.36 ppm and 1.50 ppm are due to methylene protons in the PTHF segments. The ratio of the integral intensity assigned to one hydrogen from the aromatic structures to that from the tetramethylene oxide units is about 11 which is close to the mole ratio of (BHET+TC)/PTHF in the feeding mixture. The integral intensity of the signal at 4.60 ppm assigned to the H-atoms from the ester ethylene residues between two aromatic rings and that of the signals from 4.45 ppm to 4.00 ppm referred to the carboxy- and phosphoester methylene hydrogens were used for calculation of the content of the terephthalate and phosphate units. The calculated ratio from the spectral data is 3.9 which is consistent with the content in the starting mixture. The signal of the end CH_2OH groups appears at 3.72 ppm. It was used for the determination of the number average

V. Mitova et al.: Synthesis of poly(alkyleneterephthalate-co-alkylenephosphate)s and their blends with a linear... molar mass of PTP2/8 copolymer as in the case of the oligomeric product at the first stage. The average number of the building segments of the polymer backbone is about 17. Taking into

consideration the polymer composition its number average molar mass was calculated equal to 6 800 g/mol.

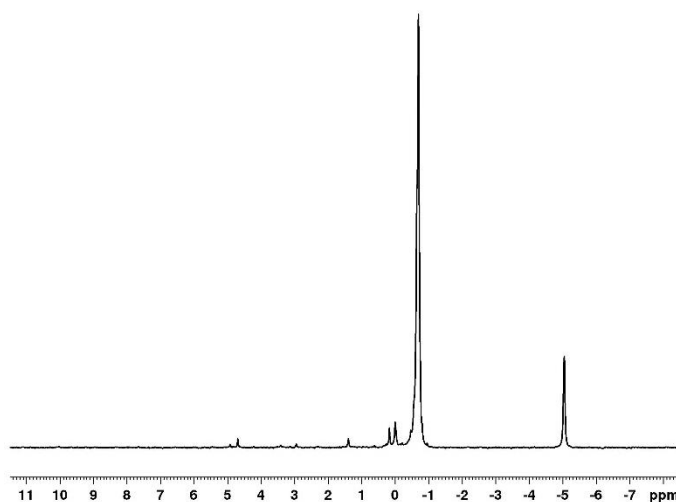
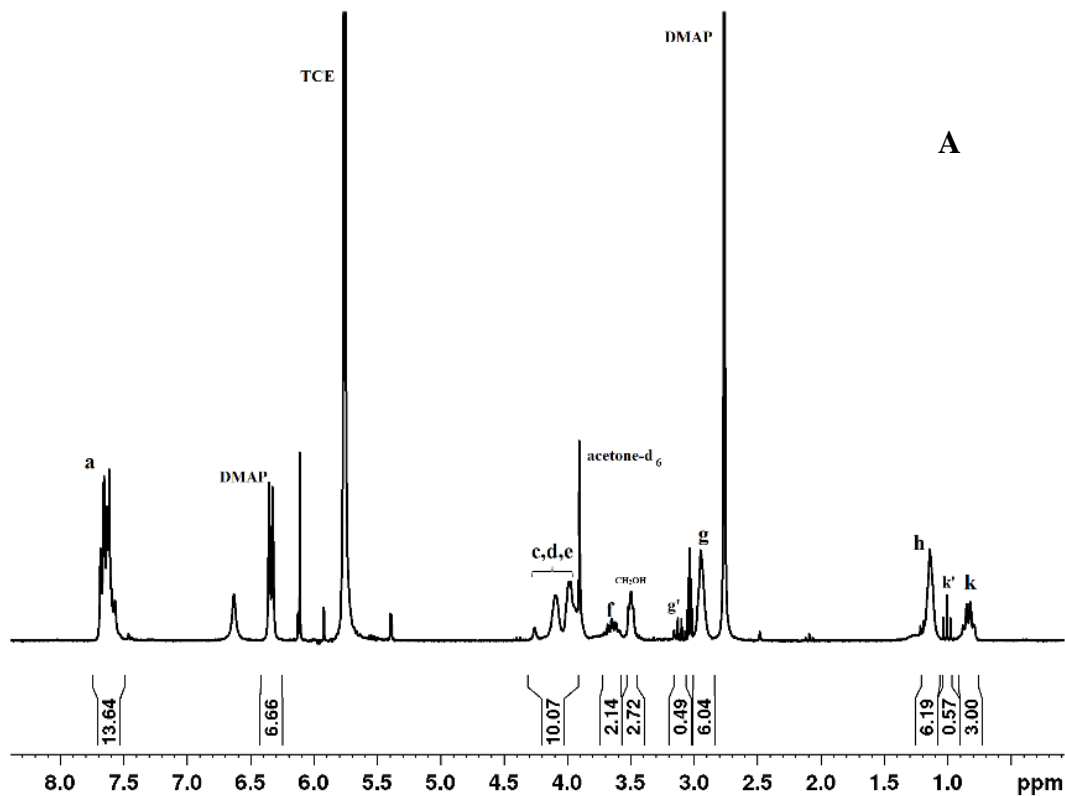
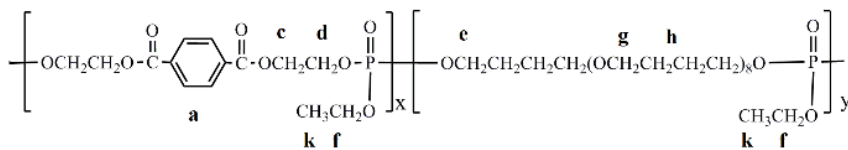


Fig. 2. ^1H (A) and $^{31}\text{P}\{\text{H}\}$ NMR (B) spectra of the reaction mixture with mole ratio ECP:TC=8:2 after 9 h reaction time

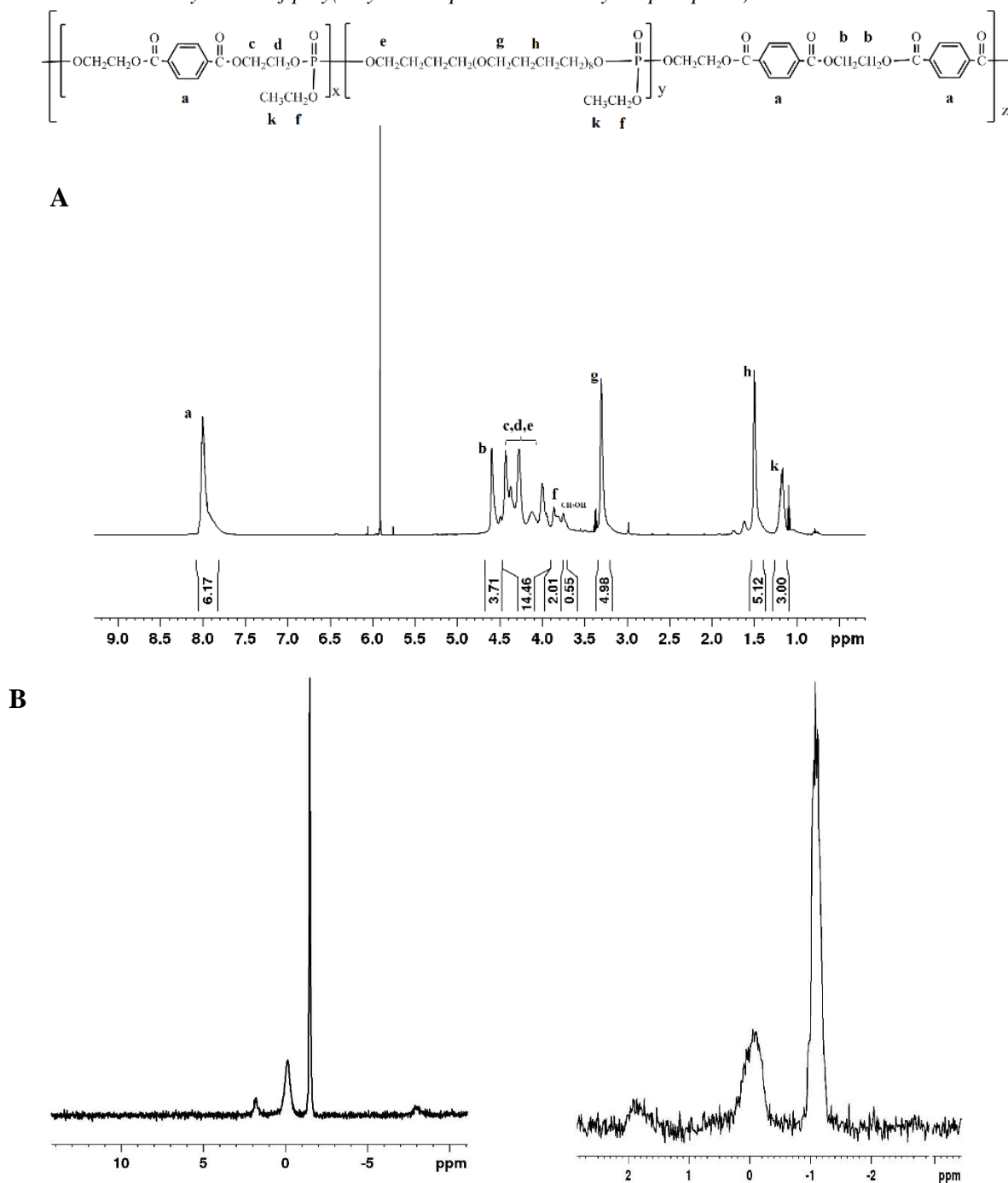


Fig. 3. ^1H (A), $^{31}\text{P}\{\text{H}\}$ (B) and $^{31}\text{P}\{\text{H}\}$ NMR (C) spectra of the copolymer PTP2/8.

The $^{31}\text{P}\{\text{H}\}$ NMR spectrum (Fig. 3B) of the copolymer PTP2/8 shows signals in the region of the triester phosphate structures which is an expected result having in mind the reaction scheme of the process. It is seen in the ^{31}P NMR spectrum that the signal at -1.48 ppm is a septet (Fig. 3C) corresponding to a P-atom coupled to three methylene groups from the triester structure.

The other two copolymers displayed signals in both the ^1H and $^{31}\text{P}\{\text{H}\}$ NMR spectra in the same

spectral regions as those for PTP2/8 discussed above. Fig. 4 presents the NMR spectra of the copolymer PTP4/6 obtained at the highest ratio of TC to ECP.

In a similar manner, the spectral data from the ^1H NMR spectrum were used for calculation of the ratios between the building structures in the copolymer backbone, as well as the number average molar mass of the product. The calculated values are listed in Table 2.

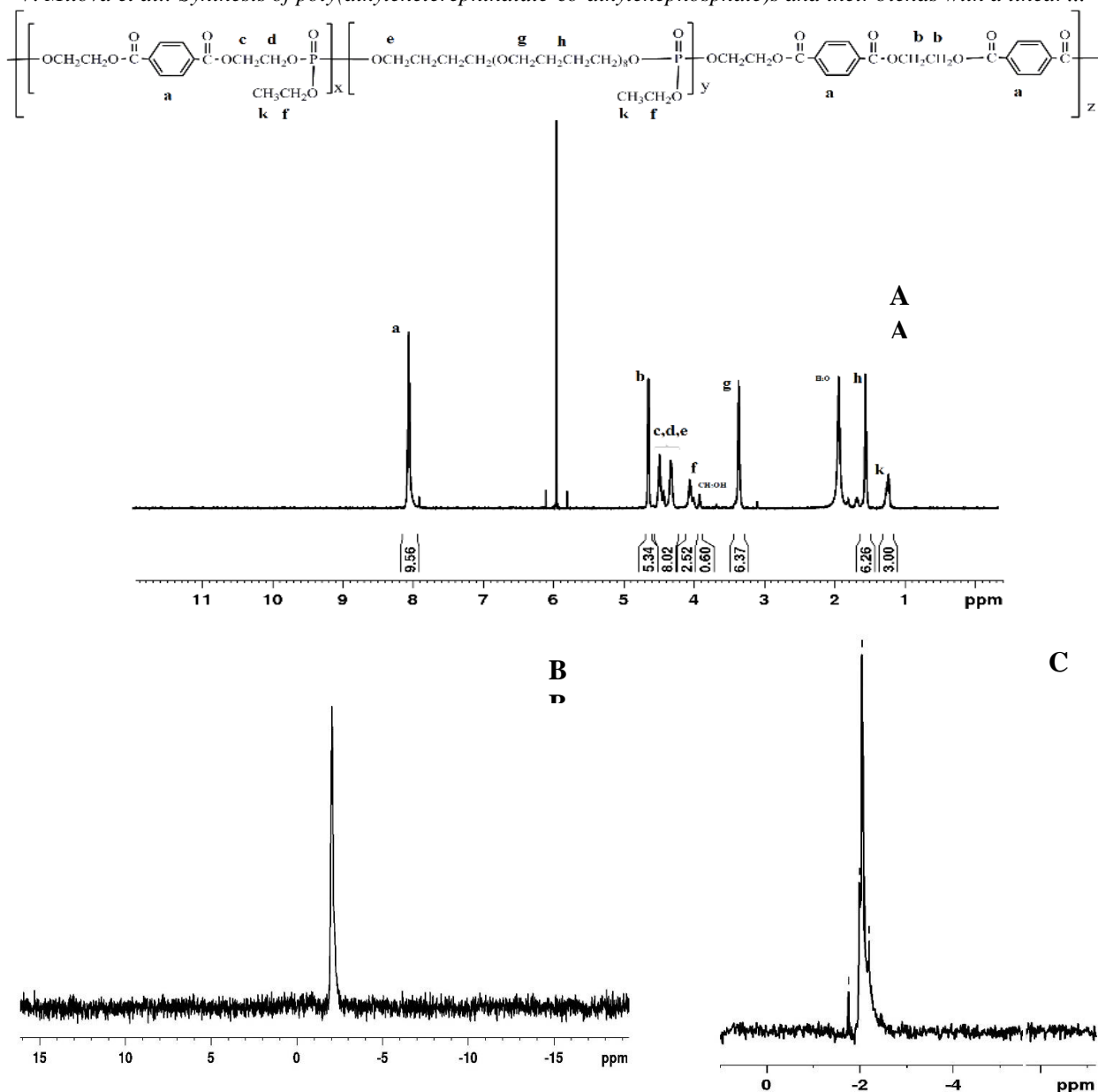


Fig. 4. ^1H (A), $^{31}\text{P}\{\text{H}\}$ (B) and ^{31}P NMR (C) spectra of the copolymer PTP4/6.

The $^{31}\text{P}\{\text{H}\}$ NMR spectrum (Fig. 4B) and the fine structure of the multiplet in the ^{31}P NMR spectrum (Fig. 4C) also evidenced the presence of the triester phosphate structures in the copolymer backbone.

Film preparation and characterization

Blending of polymers is a feasible route to impart new properties or enhance existing characteristics of the individual components of the blend. The attempts to prepare films *via* casting of PTP4/6 and PTP3/7 solutions failed while the film obtained from PTP2/8 displayed poor mechanical properties. Therefore, films were casted from the mixed solutions of PTPm/n and linear PU in

chloroform. Rectangular samples, with approximate dimensions of $17 \times 7 \times 0.26$ mm were cut off from the dried films and analyzed applying a DMA Q 800 instrument in iso-force mode. All samples were tested in a temperature sweep mode from -80 °C to 60 °C at a constant heating rate of 3 °C/min or until displacement reached 2000 μm .

During the DMA experiment, the instrument mechanically deforms the sample and the sample response to the deformation is monitored as a function of temperature. Fig. 5 presents the first derivative of the stress relaxation modulus as a function of temperature for the three blends. For comparison, the same experiment with neat PU was performed. The maximum of the curve denotes the

samples' Tg which for the neat PU is 7 °C. Blending of PU with PTP copolymers resulted into an increase in Tg but still its value was below 37 °C which means that the polymer blends retain their elastic behavior at temperatures below and close to the body temperature. The observed trend of the blends' Tg increase with the increase of the terephthalate fraction in the PTP could be assigned to the propensity of the terephthalate units to form ordered structures, as well as to the interactions between the PTP and PU macromolecules. It is known that the phosphoryl group is a strong proton acceptor and could form hydrogen bonds with the urethane segments. Similar trend was observed for

the temperature of the necking on-set (Table 3). For two of the polymer blends, PTP3/7-PU and PTP4/6-PU, the necking phenomenon started at temperatures higher than the body temperature which is an indication that they would undergo elastic deformations at 37 °C at moderate stress. For PTP2/8-PU blend, the necking started at 32 °C, i.e. the material would exhibit plastic deformation at higher temperature. This performance could be a disadvantage for applying this blend composition in a device but could be advantageous if using the same composition in a drug delivery system to control the release rate of a bioactive component.

Table 3. Experimental data from the dynamic mechanical analysis of the blends.

Sample code	Tg (°C)	Temperature of on-set of necking (°C)
PU	7	42
PTP2/8-PU	10	32
PTP3/7-PU	12	40
PTP4/6-PU	25	48

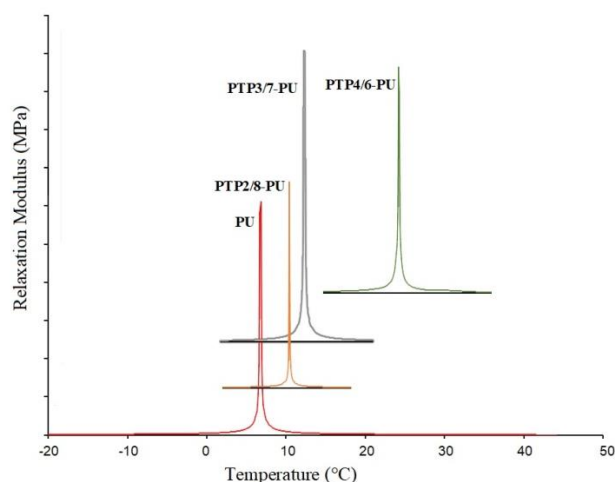


Fig. 5. Dependence of the stress relaxation modulus on temperature for the three blends and for a PU sample. Measurements were performed in iso-force mode (F= 0.5 N, heating rate of 3 °C/min).

Table 4. Data from the contact angle measurements for the PTP copolymers and PU, and their blends.

Sample code	Contact angle	Sample code	Contact angle
PU	69.4 ± 5.23	-	-
PTP4/6	52.8 ± 0.16	PTP4/6-PU	60.5±3.5
PTP3/7	34.7 ± 0.40	PTP3/7-PU	40.1 ± 4.31
PTP2/8	29.7 ± 0.24	PTP2/8-PU	31.8 ± 0.29

The relative hydrophobicity of the PTPm/n series and their blends was assessed by measuring the water-in-air contact angle. As it is seen from the determined contact angle values the hydrophilicity of the copolymers increased with the increase of the

fraction of phosphate groups in the backbone. Similar trend was found for the polilactofate copolymers with main chain composed of oligolactide segments linked with ethylphosphate moieties [11]. The obtained blends of PTPm/n-PU

V. Mitova et al.: Synthesis of poly(alkyleneterephthalate-co-alkylenephosphate)s and their blends with a linear... displayed contact angles with values between those measured for the PU and the corresponding PTP copolymer.

CONCLUSION

A series of new poly(alkyleneterephthalate-co-alkylenephosphate)s were prepared on varying the ratio of phosphate units to phthalate units from 1.5 to 4. The copolymer structure and composition were elucidated applying ^1H , $^{31}\text{P}\{\text{H}\}$ and ^{31}P NMR spectroscopy. The NMR data were used to calculate the number average molar masses of the obtained copolymers that were in the range of 4500 g/mol to 6800 g/mol. Blending with linear PU improved the film-forming properties of the copolymers. Dynamic mechanical analysis and contact angle measurements revealed that the Tg values and relative hydrophobicity of the materials depend on the content of the phosphate segments. It could be also concluded that *via* tuning the composition of the PTP/PU blends different biomedical applications of the newly developed materials could be attained.

Acknowledgement: The authors gratefully acknowledge the support by the NSF of Bulgaria (Contract No DNTC/China 01/13/2016).

REFERENCES

1. L. S. Nair, C. T. Laurencin, *Prog. Polym. Sci.*, **32**, 762 (2007).
2. K. D. Troev, *Polyphosphoesters: Chemistry and Application*, Elsevier, 2012.
3. T. Steinbach, F. R. Wurm, *Angewandte Chemie International Edition*, **54(21)**, 6098 (2015).
4. Y. Wang, H. Xia, X. Yang, J. Wang, *Journal of Polymer Science Part A: Polymer Chemistry*, **47(22)**, 6168 (2009).
5. J. Wang, S.-W. Huang, P.-C. Zhang, H.-Q. Mao, K.W. Leong, *Int. J. Pharm.*, **265**, 75 (2003).
6. S. Penczek, J. Pretula, *Macromolecules*, **26**, 2228 (1993).
7. Z. Zhao, J. Wang, H.-Q. Mao, K.W. Leong, *Adv. Drug Deliv. Rev.*, **55**, 483 (2003).
8. K. Hirota, T. Hristova, V. Mitova, T. Koda, M. Fushimi, M. Kuniya, K. Makino, H. Terada, R. Cherkezova, Shin-Ichi Yusa, N. Koseva, K. Troev, *Anticancer Research*, **36**, 1613 (2016).
9. V. Mitova, St. Slavcheva, P. Shestakova, D. Momekova, N. Stoyanov, G. Momekov, K. Troev, N. Koseva, *European Journal of Medicinal Chemistry* **72**, 127 (2014).
10. V. Mitova, T. Hristova, R. Cherkezova, N. Koseva, S.Yusa, K. Troev, *J. Appl. Polym. Sci.*, **132**, 42772 (2015).
11. M. Chaubal, B. Wang, G. Su, Z. Zhao, *Journal of Applied Polymer Science*, **90(14)**, 4021 (2003).
12. A.C.A. Wan, H.-Q. Mao, S. Wang, L.K.L.L. Ong, K. W. Leong, H. Yu, *Biomaterials*, **22**, 1147 (2001).
13. S. Wang, A.C.A. Wan, X. Xu, S. Gao, H.-Q. Mao, K. W. Leong, H. Yu. *Biomaterials*, **22**, 1157 (2001).
14. H.-J. Kim, M.-S. Kang, J. C. Knowles, M.-S. Gong, *Journal of Biomaterials Applications*, **29(3)**, 454 (2014).
15. P. Alves, P. Ferreira, H. Gil, *Biomedical Polyurethane-Based Materials*, in: *Polyurethane: Properties, Structure and Applications*, Nova Publishers, New York, 2012.
16. H.-Q. Mao, I. Shipanova-Kadiyala, Z. Zhao, W. Dang, A. Brown, K. W. Leong, *J. Biomater. Sci. Polym. Ed.*, **16(2)**, 135 (2005).

Hyperthermia in experimental models of the serotonin syndrome: influence of vigabatrin

R. P. Nikolov*, K. N. Koleva, M. H. Hristov, K. S. Yakimova

Medical University of Sofia, Faculty of Medicine, Department of Pharmacology and Toxicology, 2 Zdrave street, 1431 Sofia, Bulgaria

Received August 28, 2019, Revised January 16, 2020

Serotonin syndrome is likely to be observed as a result of an overdose of serotonergic drugs or interactions with the combined administration of two or more drugs that increase the intrasynaptic concentration of the serotonin (5-hydroxytryptamine). The aim of this study was to establish the effect of vigabatrin, a GABAergic drug, on the hyperthermic reaction in experimental serotonin syndrome in rats. We used experimental models of serotonin syndrome induced by the combined administration on male Wistar rats of: 1) the serotonin precursor 5-hydroxy-L-tryptophan (100 mg/kg b.w., *i.p.*) and the selective MAO-A inhibitor clorgyline (2 mg/kg b.w., *i.p.*); 2) the selective neuronal uptake inhibitor of serotonin fluoxetine (10 mg/kg b.w., *i.p.*) and the selective MAO-A inhibitor clorgyline (2 mg/kg b.w., *i.p.*). The experiments were conducted at ambient temperature of $22 \pm 1^\circ\text{C}$. The body temperature of the animals was measured with thermistor probes (TX-8), and monitored on multichannel recorder Iso-Thermex 16. The thermistor probes were lubricated with vaseline and inserted rectally to a depth of 6 cm. Pretreatment with vigabatrin (300 mg/kg b.w., *i.p.*) decreased significantly the hyperthermia observed in both experimental models of the serotonin syndrome in male Wistar rats. We assume that in addition to direct GABAergic mechanisms, interactions between neurotransmitters or mediator systems are involved in the response to hyperthermia in serotonin syndrome by GABAergic substances.

Keywords: serotonin syndrome; experimental models; hyperthermia; vigabatrin; rats.

INTRODUCTION

Serotonin syndrome may be observed as a result of an overdose of serotonergic drugs or due to the combined administration of two or more drugs that increase the intrasynaptic concentration of serotonin (5-hydroxytryptamine, 5-HT).

Co-administration of selective serotonin reuptake inhibitors (SSRIs) with another serotonergic drug is a more common cause of induction of severe serotonin syndrome [1]. Clinical cases of serotonin syndrome have been reported in the combination of selective serotonin reuptake inhibitors with MAO inhibitors [2-5], opioids [6-8], linezolid [9] and other drugs.

The pharmacological mechanisms that can cause serotonin syndrome are:

- increase in serotonin synthesis (e.g. 5-hydroxytryptophan);
- increase in serotonin release (e.g. amphetamines);
- inhibition of serotonin reuptake (e.g. SSRI, SNRI, TCAs);
- inhibition of serotonin metabolism (e.g. MAOIs, linezolid);
- activation of postsynaptic serotonergic receptors (e.g. buspirone, triptans).

In most common form, serotonin syndrome is characterized by a triad of symptoms – mental

status changes (confusion, agitation), neuromuscular abnormalities (clonus, tremor) and autonomic hyperactivity (tachycardia, hyperthermia) [10]. Stimulation of the 5HT_{1A} receptors triggers the development of major signs of serotonin syndrome [11]. Increased body temperature is associated with the activation of 5HT_{2A}-ergic receptors [12]. Hyperthermia is a sign of severe serotonin syndrome and is usually associated with significant mortality [13].

Medication-induced hyperthermia is resistant to the action of classical antipyretics, so their use is not recommended [14]. Administration of salicylates may even cause a worsening of the hyperthermic reaction [15].

Experimental studies demonstrated that administration of GABA or GABA-ergic drugs such as diazepam, sodium valproate, and vigabatrin caused a decrease in body temperature [16-19].

Vigabatrin (gamma-vinyl GABA; γ -vinyl-GABA) is a structural analog of gamma-aminobutyric acid. S-enantiomer is responsible for its pharmacological activity [20]. Vigabatrin enhances the central inhibitory activity of GABA *via* competitive irreversible inhibition of GABA transaminase, the mitochondrial enzyme responsible for catabolism of GABA [21,22].

* To whom all correspondence should be sent:
E-mail: rnikolov@medfac.mu-sofia.bg

Additional mechanisms involved inhibition of glial uptake of GABA [23] and stimulation of GABA release [24]. Vigabatrin is used as antiepileptic drug for treatment of infantile spasms (West syndrome) and refractory complex partial seizures [25,26].

It is essential to mention that the mortality associated with serotonin syndrome is primarily related to the presence of hyperthermia and its inadequate treatment. In this respect, the aim of this study was to investigate the effects of vigabatrin on the hyperthermic response in two different experimental models of rat serotonin syndrome.

EXPERIMENTAL

Experimental animals. The experiments were performed on male Wistar rats (weight range 200-220 g), divided into groups of 6 rats each. Rats received standard granulated rodent food (Top Mix[®], Sliven). During the studies, the animals were housed under standardized conditions: free access to water and food, room temperature 22 ± 1 °C, air humidity $55 \pm 10\%$, and light cycle 12 hours light (08:00-20:00)/12 hours dark (20:00-08:00). The experiments were carried out at the same time of the 24-hour cycle (09:00-15:00 h). The drugs were injected into the inguinal area of the experimental animals intraperitoneally with a 23 G needle.

The International Guiding Principles for Animal Research, as well as the ethical principles in the planning and conduct of experiments according to Ethics Committee for Research at the Medical University - Sofia were strictly adhered to.

Experimental substances. The substances used in the modeling of experimental serotonin syndrome were 5-hydroxy L-tryptophan (Sigma-Aldrich), fluoxetine (Sigma-Aldrich) and clorgyline (Sigma-Aldrich). Vigabatrin (Sigma-Aldrich) was studied. Vigabatrin was intraperitoneally (*i.p.*) administered in a dose of 300 mg/kg body weight before the introduction of serotonin-ergic substances. In the control groups, animals were injected *i.p.* with 0.9% solution of sodium chloride in a volume of 0.2 ml/100 g.

Animal models of serotonin syndrome. In the study we have used experimental models of serotonin syndrome induced by the combined *i.p.* administration on male Wistar rats of: 1) the serotonin precursor 5-hydroxy-L-tryptophan (100 mg/kg b.w.) and the selective MAO-A inhibitor clorgyline (2 mg/kg b.w.) [27]; 2) the selective

serotonin reuptake inhibitor fluoxetine (10 mg/kg b.w.) and the selective MAO-A inhibitor clorgyline (2 mg/kg b.w.) [28].

Body temperature monitoring. The experiments were carried out at ambient room temperature of 22 ± 1 °C. The body temperature of the animals was recorded using rectal thermistor samples (TX-8) connected to a computer-programmed multichannel device Iso-Thermex 16 (Columbus Instruments, USA). After lubrication with mineral jelly, thermistors were administered rectally at a depth of 6 cm. The body temperature of the rats was recorded before the administration of the serotonin-ergic substances, and then checked at 30-min intervals after their injection.

Data analysis and statistics. The results obtained are presented as mean \pm SEM, using One way ANOVA (InStat, USA) and graphically using Microsoft Excel software, 2003.

RESULTS AND DISCUSSION

Effects of vigabatrin on the hyperthermic reaction in a model of serotonin syndrome induced by the combined administration of 5-hydroxy-L-tryptophan and clorgyline

Vigabatrin administered *i.p.* in a dose of 300 mg/kg body weight significantly reduced the hyperthermic response, observed at 60 min, in rats with a model of serotonin syndrome induced by 5-hydroxy-L-tryptophan and clorgyline, compared to the group with a model of serotonin syndrome (5-hydroxy-L-tryptophan + clorgyline). In this model, all of the animals have died between 60 and 90 min of recordings (Fig. 1).

Effects of vigabatrin on the hyperthermic reaction in a model of serotonin syndrome induced by the combined administration of fluoxetine and clorgyline

In rats with a model of serotonin syndrome induced by fluoxetine and clorgyline, vigabatrin *i.p.* administered in a dose of 300 mg/kg b.w. caused a significant decrease in hyperthermic response between 150 and 300 min of recordings (Fig. 2).

The results of the present study indicate a decrease in the hyperthermic response observed in two different rat models of serotonin syndrome by pretreatment of vigabatrin.

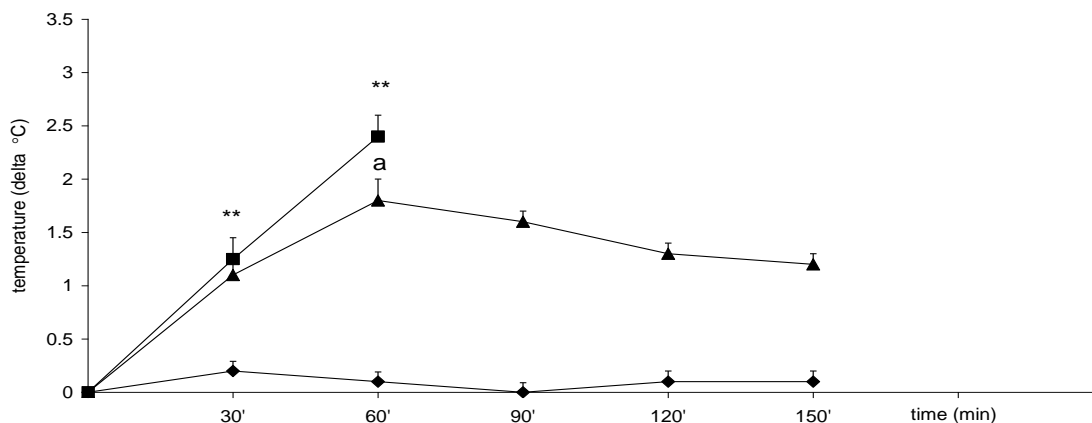


Fig. 1. Effect of vigabatrin on a serotonin syndrome model induced by 5-hydroxy L-tryptophan and clorgyline. Average change in body temperature in rats (temperature $\Delta^{\circ}\text{C}$) after *i.p.* administration of ■ 0.9 % solution of NaCl + 5- hydroxy L-tryptophan 100 mg/kg + clorgyline 2 mg/kg; *i.p.* administration of ▲ vigabatrin 300 mg/kg + 5- hydroxy L-tryptophan 100 mg/kg + clorgyline 2 mg/kg and *i.p.* administration of ◆ 0.9 % solution of NaCl. Statistical significance: compared to NaCl: ** $P < 0.01$; compared to 0.9 % solution of NaCl + 5- hydroxy L-tryptophan 100 mg/kg + clorgyline 2 mg/kg: ^a $P < 0.05$.

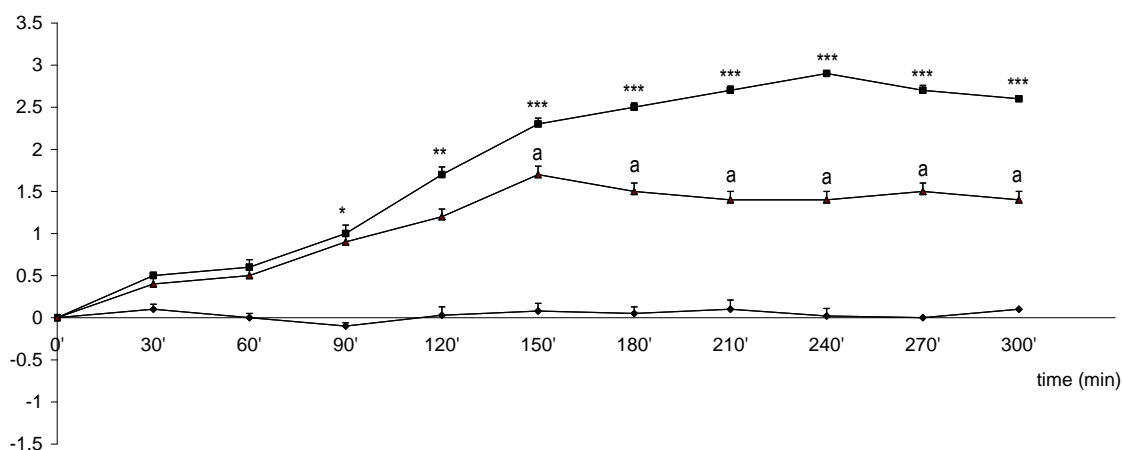


Fig. 2. Effect of vigabatrin on the hyperthermic response in a model of serotonin syndrome induced by fluoxetine and clorgyline. Average change in body temperature in rats (temperature $\Delta^{\circ}\text{C}$) after *i.p.* administration of ■ 0.9 % solution of NaCl + fluoxetine 10 mg/kg + clorgyline 2 mg/kg; *i.p.* administration of ▲ vigabatrin 300 mg/kg *i.p.* + fluoxetine 10 mg/kg *i.p.* + clorgyline 2 mg/kg *i.p.* and *i.p.* administration of ◆ 0.9 % NaCl. Statistical significance: compared to NaCl: * $P < 0.05$, ** $P < 0.01$, *** $P < 0.001$; compared to 0.9 % solution of NaCl + fluoxetine 10 mg/kg + clorgyline 2 mg/kg: ^a $P < 0.05$.

GABA is an essential central inhibitory neurotransmitter that participates in thermoregulation processes. Potentiation of GABA central inhibitory action is achieved by several different mechanisms, including allosteric modulation of GABA receptors (benzodiazepines, barbiturates, Z-drugs), direct GABA_A or GABA_B receptor agonist activity (muscimol, baclofen), increased synthesis of GABA (gabapentin, pregabalin, sodium valproate), suppression of the enzymatic degradation of GABA (vigabatrin,

sodium valproate), and inhibition of the neuronal and glial uptake of GABA (tiagabine). Central or systemic administration of diazepam, sodium valproate, and vigabatrin in rats induces dose-dependent decrease in body temperature [17-19, 29]. GABA-induced hypothermia is thought to be mediated by activation of GABA_A- and/or activation of GABA_B receptors [30,31].

We assume that in addition to direct GABA-ergic mechanisms, interactions between neurotransmitters or mediator systems are involved in influencing the hyperthermic response of

serotonin syndrome by GABA-ergic substances. Presynaptically localized GABA_B receptors influence the release of noradrenaline, dopamine and 5-hydroxytryptamine [32]. Expression of predominantly GABA_B receptors has been found in most serotonin-ergic and catecholamine-ergic neurons in brainstem nuclei which are involved in the regulation of autonomic functions [33]. The interactions between the GABA-ergic and the serotonin-ergic systems are accomplished by presynaptic heteroreceptor GABA_B-inhibition of 5-HT release or by a G-protein coupled interaction between 5-HT_{1A} and GABA_B-ergic receptors [34].

Our studies found that vigabatrin effectively attenuated the hyperthermic response in experimental serotonin syndrome in rats. The effects of the investigated GABA-mimetic drug vigabatrin on hyperthermia, associated with serotonin syndrome, support the hypothesis for the interaction between the GABA-ergic and serotonin-ergic systems in thermoregulatory processes.

Acknowledgements: This work is supported by the Bulgarian Ministry of Education and Science under National Program for Research "Young Scientists and Postdoctoral Students".

REFERENCES

1. P. K. Gillman, *Biol. Psychiatry*, **59**, 1046 (2006).
2. F. Benazzi, *Pharmacopsychiatry*, **29**, 4, 162 (1996).
3. M. A. Graber, T. B. Hoehns, P. J. Perry, *Ann. Pharmacother.*, **28**, 6, 732 (1994).
4. C. R. FitzSimmons, S.Mehta, *J. Accid. Emerg. Med.*, **16**(4), 293 (1999).
5. G. K. Isbister, P. McGettigan, A. Dawson, *J. Ann. Toxicol.*, **25**(8), 716 (2001).
6. S. Ailawadhi, K.W. Sung, L. A. Carlson, M. R. Baer, *J. Clin. Pharm. Ther.*, **32**(2), 199 (2007).
7. E. M. Altman, G. H. Manos, *Psychosomatics*, **48**, 4361 (2007).
8. M. S. Lantz, E. N. Buchalter, V. Giambanco, *Int. J. Geriatr. Psychiatry.*, **13**(5), 343 (1998).
9. D. B. Clark, M. R. Andrus, D. C. Byrd, *Pharmacother.*, **26**(2), 269 (2006).
10. H. Sternbach, *Am. J. Psychiatry.*, **148**, 705 (1991).
11. P. Birmes, D. Coppin, L. Schmitt, D. Lauque, *CMAJ*, **168**(1), 1439 (2003).
12. G. A. Gudelsky, J. I. Koenig, H. Y. Meltzer, *Neuropharmacol.*, **25**, 1307 (1986).
13. K. Nisijima, T. Yoshino, T. Ishiguro, *Psychopharmacol.*, **150**, 9 (2000).
14. S. U. Vassalo, K. A. Delaney, in: Goldfrank's Toxicologic Emergencies, L. Goldfrank, N. Flomenbaum, N. Levin (eds.), McGraw-Hill, New York, 2002.
15. E. L. Liebelt, M. K. Nichols, in: Pediatric Toxicology, T. B. Erickson, W. R. Ahrens, S. E. Aks, C. R. Baum, L. J. Ling (eds.), McGraw-Hill, New York, 2005, p. 171.
16. K. Yakimova, R. Ovcharov, *Acta Physiol. Pharmacol. Bulg.*, **15**, 50 (1989).
17. M. R. Zarrindast, M. Dibayan, *Gen. Pharmacol.*, **20**, 6, 855 (1989).
18. R. Nikolov, K. Yakimova, *J. Therm. Biol.*, **33**(8), 459 (2008).
19. R. Nikolov, K. Yakimova, *Amino Acids*, **40**, 5, 1441 (2011).
20. G. Sheean, T. Schramm, D. S. Anderson, M. J. Eadie, *Clin. Exp. Neurol.*, **29**, 107 (1992).
21. L. Gram, O. M. Larson, A. Johnsen, A. Schousboe, *Br. J. Clin. Pharmacol.*, **27**, 13 (1989).
22. R. H. Mattson, O. Petroff, D. Rothman, K. Behar, *Epilepsia*, **35**, 29 (1994).
23. J. P. Leach, G. J. Sills, A. Majid, E. Butler, A. Carswell, G. G. Thompson, M. J. Brodie, *Seizure*, **5**, 3, 229 (1996).
24. E. Ben-Menachem, in: Antiepileptic drugs, 5th edn., R. H. Levy, R. H. Mattson, B. S. Meldrum, E. Perucca (eds.), Lippincott Williams & Wilkins, Philadelphia, 2002, p. 855.
25. J. P. Mumford, D. J. Cannon, *Epilepsia*, **35**, 25 (1994).
26. J. Aicardi, J. Mumford, C. Dumas, S. Wood, *Epilepsia*, **37**, 638 (1996).
27. K. Nisijima, T. Yoshino, K.Yui, S. Katoh, *Brain Res.*, **890**, 23 (2001).
28. K. Shioga, K. Nisijima, T. Yoshino, S. Kato, *Neuropsychopharmacol. Biol. Psychiatry*, **28**, 633 (2004).
29. M. J. Swaider, J. J. Luszczki, A. Zwolan, E. Wierzchowska-Cioch, M. Wielosz, S. J. Czuczwar, *Rocz. Akad. Med. Bialymst.*, **49**, 270 (2004).
30. M. R. Zarrindast, Y. Ovessi, *Gen. Pharmacol.*, **19**, 2, 223 (1988).
31. S. M. Rawls, R. J. Tallarida, D. A. Kon, E. B. Geller, M. W. Adler, *Pharmacol. Biochem. Behav.*, **78**, 1, 83(2004).
32. W. G. Clark, J. M. Lipton, *Neurosci. Biobehav. Rev.*, **9**, 299 (1985).
33. K. J. Burman, A. O. Ige, J. H. White, F. H. Marshall, M. N. Pangalos, P. C.Emson, J. B. Minson, I. J. Llewellyn-Smith, *Brain Res.*, **970**, 35 (2003).
34. C. Mannoury la Cour, N. Hanoun, M. Melfort, R. Hen, K. P. Lesch, M. Hamon, L. Lanfumey, *J. Neurochem.*, **89**, 886 (2004).

Despite the similarities in the absorption spectra of HbO₂ and HbCO, the significant difference (> 10 times) in the quantum yields of photodissociation makes it possible to obtain selective decomposition of HbCO in the blood stream with a minimum effect on the HbO₂. The suggested method of elimination of CO from blood is based on the optical acting on HbCO in the cutaneous blood vessels through human skin. In this case we must take into account the optical properties of the human skin in order to determine the effective wavelength of the penetrating radiation. This can be achieved by calculating the action spectra of HbCO in the skin.

In our earlier work [4] we presented the calculated absorption spectra of HbCO at different depths (action spectra) and showed that their absorption spectra are transformed by the optical properties of skin into a relatively narrow spectral range.

Since the effect of laser-induced photodissociation of HbCO has been experimentally demonstrated, it is interesting to investigate the spectral dependence of the effect in the irradiation zone. There is practically no information in the literature on the connection between the quantum efficiency of the photodissociation and the wavelength of the irradiating light [5-10]. Also, most studies have been done *in vitro*, so it is reasonable to expect that the *in vivo* photolytic effect will be different from that observed in buffer solutions, considering the different biological environment and specific features of light propagation in biological tissues.

MATERIALS AND METHODS

Determination of HbCO concentration in the blood was performed by a method similar to the method of pulse oximetry which is based on the measurement of light-modulated pulse wave of blood. The values were measured using a pulse 3-wavelengths sensor operating in backscattered light, based on a standard pulse oximetry pair of V97B light emitting diodes ($\lambda = 660$ nm and 935 nm) and L-53MGC light emitting diode ($\lambda = 568$ nm) and a BPW34 silicon photodiode. Conventional pulse oximeters do not measure the presence of HbCO in arterial blood due to the close spectral characteristics of HbCO and HbO₂ during measurements [8]. Due to our original method of data processing [11] the designed 3-wavelengths measurement system provides a maximum difference in the absorption coefficients of different derivatives of hemoglobin and makes it possible to obtain a reliable measuring of the HbCO level with high accuracy (<0.2%). The system allows

continuous photoplethysmographic monitoring, recording and data storage.

The pulse oximetry sensor was placed on the first phalanx of the finger. The light was delivered to the finger from LEDs (or laser diodes) at fifteen wavelengths in the 400–940 nm spectral range. The optical power of every light source was selected to provide an approximately equal number of photons of different wavelengths incident on the irradiated skin area. The corresponding power density of irradiation taking into account the output aperture varied from 50 mW/cm² for $\lambda = 405$ nm to 125 mW/cm² for $\lambda = 940$ nm.

The measurements were taken on the fingers of 5 healthy male volunteers including non-smokers and smokers after a 12-hour nonsmoking interval in order to reduce the impact of HbCO on the accuracy of the pulse oximetry. All procedures performed in the study were in accordance with the ethical standards with informed consent obtained from each subject and approval by the institutional review board.

The irradiation beam with a diameter of 4 mm was directed at the lower front of the phalanx, at about 5 mm distance from the measuring sensor, so that direct light did not reach the surface of the photodetector. For each source in each series, 7 to 15 records were made according to the following scheme: 30 s without radiation, 30 s with radiation and 30 s without radiation. For every record the mean values and their change induced by the irradiation were calculated and then averaged over the number of records. In order to eliminate rogue results, only measurements which were within the range between $\pm 20\%$ standard deviation from the mean were included in the analysis. All results are given as mean \pm (SD). The Student's test for connected sampling was used for the statistical calculations. Statistical results with a value of $p < 0.05$ were viewed as being significant for all volunteers. The evaluation was carried out using the program "Origin 7.5".

RESULTS

Spectral Dependency

Using described above technique and method we experimentally measured the laser-induced photodissociation of HbCO in cutaneous blood vessels in the visible and near IR spectral range. We determined the parameter ΔHbCO as the difference between the initial values of HbCO before irradiation and the measurable values in the experiment. The initial values of relative HbCO concentration varied from 3.4 % up to 5.9 %.

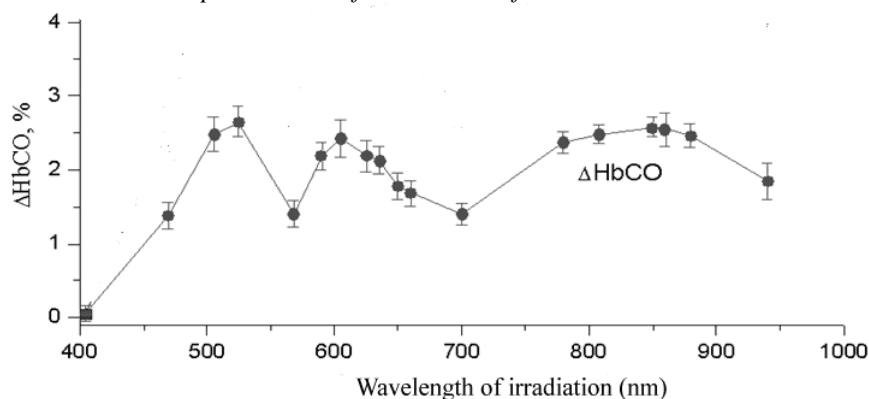


Fig. 2. Change in concentration (%) of HbCO in the arterial blood depending on the irradiation wavelength.

Using statistical analysis of measurement data obtained for all sources of radiation the parameter ΔHbCO was calculated. The results demonstrated that the rate of the HbCO in blood varies under the influence of local transcutaneous light irradiation and significantly depends on the radiation wavelength. Three absorption maxima in the spectral range near 530, 600 and 850 nm were revealed (Figure 2). The results obtained correlate well with the characteristics of light propagation in blood-filled tissues. absorption maxima in the spectral range near 530, 600 and 850 nm were revealed (Figure 2). The results obtained correlate well with the characteristics of light propagation in blood-filled tissues. Light at wavelengths below 450 nm is strongly absorbed in superficial skin layers and irradiation in this spectral range has no effect in the described experiment.

The visible light below 580 nm has a small penetration depth into the skin tissue because of its proximity to the absorption bands of some basic

skin chromophores such as hemoglobins and melanin; therefore in real tissue it can cause HbCO photodissociation only in shallow superficial skin layers. Red and especially near IR radiation penetrate much deeper into soft tissues. The experimental results obtained correlate well with the action spectra calculated in [4].

It should be noted that a 2.5% decrease in ΔHbCO occurs at the initial 5%, i.e. irradiation at spectral maxima leads to photolysis of near 50 % of HbCO molecules.

Optical Power Dependency

In this paragraph we present an *in vivo* experimental study of the efficiency of changes in HbCO molecules depending on the laser radiation power and subsequent calculation of the quantum efficiency of light interaction with HbCO in the blood at wavelengths of 525 and 605 nm, which are in the region of the maximum effect in the visible region of the spectrum.

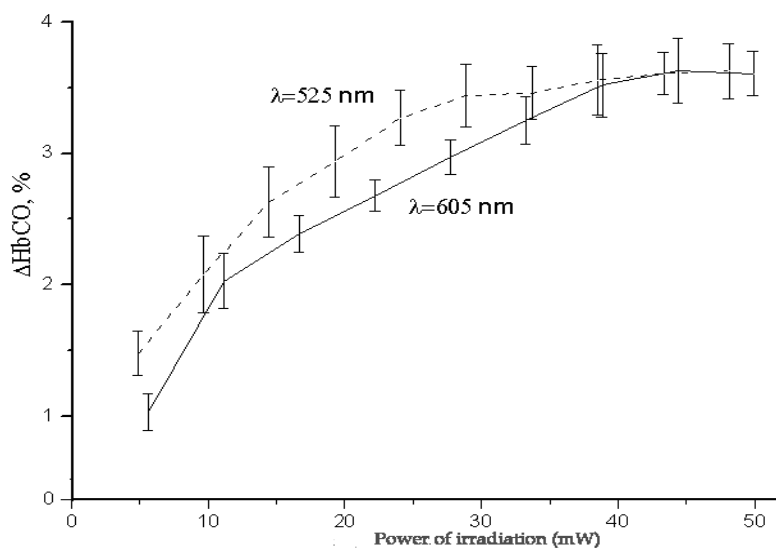


Fig. 3. Change in concentration (%) of HbCO in the arterial blood depending on the power of the irradiation

The mean values of HbCO without irradiation were 4.6 ± 0.33 SD%. Figure 3 shows the change in concentration (%) of HbCO in the arterial blood depending on the irradiation power.

As can be seen from Figure 3, the photodissociation process significantly depends on the laser radiation power and reaches saturation at the power above 50 mW (300 mW/cm^2). This means that a further increase in the number of irradiating photons does not lead to an increase in acts of dissociation of molecules in the irradiated blood. We determined the quantum efficiency of light interaction with HbCO as the ratio of relative values of ΔHbCO to the initial values of the HbCO before irradiation, so the obtained maximum values $\Delta\text{HbCO}/\text{HbCO}$ determine their quantum yields of photodissociation. We calculated a photodissociation yield of 79% for HbCO at a wavelength of 525 nm and of 76 % at a wavelength of 605 nm. The results obtained correlate well with the quantum yields of photodissociation calculated in [10].

DISCUSSION

In contrast to other studies, this study was carried out under *in vivo* conditions, so it was possible to make statements about the practicability of the effect. It should be noted that the main difference between this study and all other studies previously performed on solutions of Hb complexes is the fact that at *in vivo* condition, due to the blood flow, a constant number of photodissociation objects is provided while at *in vitro* condition the number of molecules that actually undergo photolysis, exponentially decreases.

Thus, we demonstrated that the rate of HbCO in blood varies under the influence of local transcutaneous irradiation and significantly depends on the irradiation wavelength and the irradiation power. It is evident that the observed local decrease in the initial values of HbCO during irradiation is caused by HbCO photodissociation in the blood capillary vessels.

Phototherapy of Carbon Monoxide Poisoning

The results obtained allow us to propose an approach for increasing the effectiveness of carbon monoxide decomposition. It is shown that the significant difference in the quantum yields of photodissociation of hemoglobin complexes makes possible a selective decomposition of HbCO in the blood stream with minimum effect on the HbO_2 component.

The rate of CO photodissociation from the HbCO molecule is extremely high and its quantum yield, which is almost 80%, allows us to expect

high efficiency of the proposed approach in clinical applications. Maximum photodissociation of HbCO can be reached in the lungs alveoli or in cutaneous blood vessels by irradiating at wavelengths near 530, 600 and 850 nm, which are in the region of the maximum effect in the visible and IR region of the spectrum. The spectral effectiveness of the photodissociation approximately correlates with the absorption spectrum of HbCO and the transmission spectrum of skin tissue. The required laser power and the treatment time in clinical practice should be determined according to the optical properties of the skin, the depth of penetration and the volume of blood illuminated by laser radiation.

Our approach, based on photodissociation of the blood HbCO, in combination with other existent methods (oxygen hyperventilation, hyperbaric oxygen therapy) significantly increases the efficiency of CO poisoning treatment. An important conclusion is that there is a possibility of laser-induced reduction of HbCO in the blood and thus a recovery of the oxygen-transport function of the blood. The distinctive feature of this technology is its selectivity and local action.

The results of this study cannot identify any immediate effect of the radiation on the HbCO decomposition in tissue *in vivo*. It would be reasonable if further studies on the immediate effects would take into account additional parameters, which along with the observed effects, may have a role in clinical practice.

CONCLUSION

A new approach for the treatment of CO poisoning based on the laser-induced photodissociation of HbCO in the arterial blood is proposed. The results show that there is a decrease in the concentration of HbCO in the blood under the influence of transcutaneous laser irradiation. The rates of HbCO concentration in the blood *in vivo* were experimentally measured depending on the radiation wavelength and the irradiation power. The quantum yield of photodissociation is considerably high in the spectral region of maximum effect (up to 80 %), which ensures high efficiency of photodecomposition of the HbCO in the blood. The results obtained can be used in the clinical phototherapy practice for effective treatment of CO poisoning.

Acknowledgement: *This work is partially supported by the Bulgarian Science Fund grant H29/11/2018 "Photosensitizers towards microbial resistance".*

REFERENCES

1. W. G. Zijlstra, A. Buursma, *Clinical Chemistry*, **37**(9), 1633 (1991).
2. R. Von Burg, Toxicology Update, *J. Appl. Toxicology*, **19**, 379 (1999).
3. M. Asimov, R. Asimov, A. Rubinov, A. Gisbrecht, *J. of Basic and Applied Physics*, **1**(1), 33 (2012).
4. M. Asimov, R. Asimov, A. Gisbrecht, *Proc.SPIE*, **5830**, 414 (2004).
5. W. A. Saffran, Q. Gibson, *J. Biol. Chem.*, **252**, 7955 (1977).
6. P. K. Jensen, U. Ryde, How O₂ binds to heme, *J. Biol. Chemistry*, **279**, 14561 (2004).
7. S. Franzen, L. Kiger, Heme Photolysis Occurs by *Biophysical Journal*, **80**, 2327 (2001).
8. R. O. Wright, *Ann. Emerg. Med.*, **31**, 525 (1998).
9. S. J. Barker, J. Curry, D. Redford, *Anesthesiology*, **105** (5), 892 (2006).
10. W. J. Egan, W. Brewer, *Appl. Spectroscopy*, **53**, 218 (1999).
11. S. Mamilov, S. Esman, D. Veligodski, M. Asimov, A. Gisbrecht, *J. Appl. Spectrosc.*, **81**, 432 (2014).

Mixed convection flow of a viscoelastic fluid through a vertical porous channel influenced by a moving magnetic field with Hall and ion-slip currents, rotation, heat radiation and chemical reaction

J. K. Singh^{1*}, G. S. Seth², Naveen Joshi¹ and C. T. Srinivasa¹

¹Dept. of Mathematics, V. S. K. University, Ballari-583105, INDIA

²Dept. of Applied Mathematics, IIT (ISM), Dhanbad-826004, INDIA

Received September 28, 2017; Accepted July 23, 2019

A mathematical analysis is presented for mixed convection hydromagnetic flow of an incompressible, electrically and thermally conducting and chemically reacting viscoelastic fluid through a vertical porous channel filled with porous medium. The effects of Hall and ion-slip currents, rotation, heat radiation and chemical reaction are also considered. The flow system is influenced by an applied magnetic field which is moving with same velocity as that of the moving right wall of the channel. The MHD flow in the rotating fluid system is developed due to periodic pressure gradient, movement of the right wall and buoyancy forces. The governing coupled partial differential equations solved analytically by separating the variables and the solutions for velocity, temperature and concentration are presented in closed form. In order to discuss the effects of flow governing parameters, the numerical results for velocity, fluid temperature and concentration are computed and demonstrated through graphs while the numerical results for skin friction, rate of heat and mass transfer in terms of Nusselt and Sherwood numbers are presented through tables. It is observed that moving magnetic field produces comparatively less drag force in comparison to stationary magnetic field. In case of moving magnetic field, the magnetic field raises the fluid velocity in the primary flow direction in the left half of the channel while it reduces in the right half of the channel because magnetic field is fixed relative to the moving right wall of the channel.

Keywords: Moving magnetic field, viscoelastic fluid, mixed convection, rotation, Hall and ion-slip currents.

INTRODUCTION

Investigation of combined heat and mass transfer characteristics of natural convection flows are significant due to their simultaneous occurrence in many natural systems, transport procedures and industrial applications. It is widely accepted that natural convection arises due to density variations in the field of gravity. For incompressible fluids density variation due to pressure are negligible. However, the density changes due to non-uniform heating and non-uniform species distribution cannot be neglected because they are responsible for natural convection in incompressible fluids. It is praiseworthy to note that, in a rotating fluid system natural convection can be also set up by the action of centrifugal force which is proportional to the density of the fluid. Flow and heat transfer in gas turbine is an example of such situation. Natural convection of heat and mass transfer may find some significant applications in chemical industries and in designing of control systems of heat exchangers. Many research scientists investigated heat and mass transfer natural convection flow of incompressible fluids under different considerations. Some relevant contributions on the topic are due to Angirasa *et al.* [1], Alagoa and Tay [2], Osalusi *et al.* [3], Jha and

Ajibade [4], Singh *et al.* [5], Khan *et al.* [6], Narahari and Debnath [7], Kar *et al.* [8], Barik *et al.* [9], Manglesh and Gorla [10], Chamkha and Al-Rashidi [11], Ibrahim *et al.* [12], Seth and Sarkar [13], Yabo *et al.* [14], Butt and Ali [15], Singh *et al.* [16], Iqbal *et al.* [17], Misra and Adhikary [18] and Falade *et al.* [19]. Study of transport of heat and mass through a porous medium become important because similar to magnetic force, permeability of the porous medium also produces a fluid controlling force in the flow-field. A considerable attention has been given by the researchers to the study of hydromagnetic natural convection flow of conducting fluids through porous medium in the recent years owing to its numerous applications in petrochemical industries, geothermal energy extraction, heat exchangers etc. Stimulated from the industrial applications, researchers [2, 5, 6, 8-10, 12-13, 16-19] investigated hydromagnetic natural convective flow of conducting fluids through a uniform porous medium under different situations using various computational and analytical methods. In an ionized fluid, the electrons and ions are drifting with different velocities and the diffusion velocity of electrons is much larger than that of ions (Cramer and Pai [20]). Therefore, the diffusion velocities of ions are usually neglected in Ohm's law. However, in industrial

* To whom all correspondence should be sent:

E-mail: s.jitendrak@yahoo.com

process where electromagnetic forces are large, we may not neglect the diffusion velocity of the ions. In such a case both the diffusion velocities of electrons and ions are included in Ohm's law and phenomenon of Hall and ion-slip effects comes into the picture. For such flows, the combined effects of Hall and ion-slip currents play a prominent role in the determination of flow behaviour. Combined effects of Hall and ion-slip currents on hydromagnetic flows are investigated by the researchers [21-26]. Ojjela and Kumar [27] studied the influence of Hall and ion-slip currents on unsteady MHD two-dimensional heat and mass transfer flow of a chemically reacting micropolar fluid through a porous channel. Subsequently, Hossain *et al.* [28] discussed the effects of Hall and ion-slip currents on MHD natural convection and mass transfer flow past an oscillating vertical porous plate with heat source and rotation. Moreover, Singh *et al.* [29] analysed the combined influences of Hall and ion-slip currents on heat and mass transfer natural convection flow past an oscillating vertical plate with ramped wall temperature and time dependent concentration. Combined effects of Hall and ion-slip currents on unsteady MHD natural convection flow of a rotating fluid over a vertical plate due to moving free stream is recently presented by Singh *et al.* [30]. Research studies made on non-Newtonian fluid dynamics have been drawn the attention of many researchers during last few decades due to its widespread applications in polymer sciences in manufacturing process of plastics, food processing, petrochemical engineering and biological fluids. Non-Newtonian fluids are subdivided into several categories. Viscoelastic fluids are one of the subcategories in which fluids have both the viscous and elastic attributes. Walters [31, 32] has presented a theoretical model in his classical research papers known as Walters'-B fluid model and this model opened the new scope for the engineers and scientists to study the dynamics of viscoelastic fluids. Stimulated from the widespread applications, researchers [33-41] studied the dynamics of viscoelastic fluid under different considerations. Garg *et al.* [42] analysed the heat transfer characteristic of viscoelastic MHD oscillatory natural convection flows through a vertical porous channel with Hall effects. Subsequently, Singh *et al.* [43] presented MHD oscillatory convective flow of viscoelastic fluid through a channel filled with porous medium with heat radiation and Hall current. Moreover, Ramesh and Devakar [44] discussed effects of external magnetic field and heat transfer on the peristaltic flow of Walters B fluid in a vertical channel.

Combined influences of Hall and ion-slip currents on MHD free convection boundary layer flow of non-Newtonian tangent hyperbolic fluid past a vertical surface in a porous medium with Ohmic dissipation is discussed by Gaffar *et al.* [45]. Recently, Singh *et al.* [46] considered the effects of Hall and ion-slip currents on unsteady MHD boundary layer flow of a rotating Walters-B' fluid over an infinite vertical porous plate in a uniform porous medium with fluctuating wall temperature and concentration.

In most of the research investigations, applied magnetic field is considered to be fixed relative to the fluid. However, the moving magnetic field plays a prominent role in determination of flow characteristics of the hydromagnetic flows. In this intended research study we analysed unsteady mixed convection hydromagnetic flow of a viscoelastic fluid through a vertical porous channel filled with porous medium in the presence of a moving magnetic field with Hall and ion-slip currents, rotation, heat radiation and chemical reaction. The hydromagnetic flow in the rotating fluid system is developed due to periodic pressure gradient, movement of the right wall and buoyancy forces. The governing coupled partial differential equations solved analytically by separating the variables. It is observed that suction reduces concentration in the left half of the channel while it enhances concentration in the right half of the channel because suction and injection are simultaneously taking place through left and right walls of the channel.

MATHEMATICAL MODEL OF THE PROBLEM

In the present problem we considered fully developed MHD laminar flow of an electrically and thermally conducting and chemically reacting viscoelastic fluid through a porous medium bounded by two infinite vertical porous walls ($-\infty \leq x' \leq \infty, -\infty \leq y' \leq \infty$) placed at $z = -z_0/2$ and $z = z_0/2$. The flow system is influenced by a uniform magnetic field $\vec{B} (0, 0, B_0)$ applied along a direction normal to the plane of the walls. Initially, the walls of the channel and fluid are consider being at rest and the whole flow system is rigidly rotating with a uniform angular velocity $\vec{\Omega} (0, 0, \Omega)$ about a direction normal to the plane of the walls. Since the walls of the channel are assumed to be porous, consider simultaneous suction and injection take place through the opposite walls of the channel respectively with a uniform transpiration velocity w_0 . The left wall of the channel

$z = -z_0 / 2$ is kept fixed while the right wall of the channel $z = z_0 / 2$ is moving with velocity $w_0 f'(t')$. The applied magnetic field is also considered to be moving with same velocity as that of right wall of the channel in x' -direction i.e. the magnetic field is fixed relative to the right wall of the channel. The temperature and concentration of the left wall is kept fixed while the temperature and concentration of the right wall varying periodically with the time. The MHD flow through the vertical channel is developed due to a periodic pressure gradient applied along x' -direction, oscillatory movement of the right wall of the channel and the buoyancy forces arise from temperature and concentration differences in the field of gravity. All the physical variables in this problem will be function of z' and t' because flow is fully developed and laminar. Geometry of the physical problem is presented in Fig. 1.

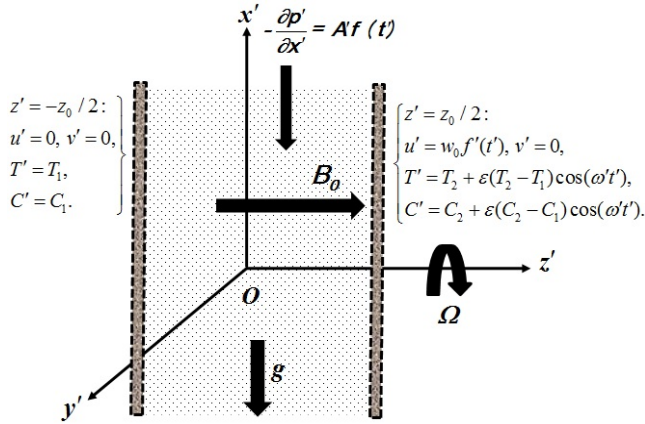


Fig. 1 Geometry of the physical problem.

Fluid is considered to be such that magnetic diffusivity of the fluid is very large, so the induced magnetic field produced by fluid motion is assumed to be negligible in comparison to applied one (Sutton and Sherman [47]). It is also assumed that there does not exist any applied and polarization voltages, so no energy is being added or extracted from the fluid by electrical means (Meyer [48]) i.e. electric field $\vec{E} = (0, 0, 0)$. In view of the above made assumptions and compatibility with the continuity equation for velocity field ($\nabla \cdot \vec{q} = 0$), solenoidal relation ($\nabla \cdot \vec{B} = 0$) and continuity equation for electric field ($\nabla \cdot \vec{J} = 0$); the fluid velocity \vec{q} , magnetic field \vec{B} and current density \vec{J} may assume as $\vec{q} = (u', v', w_0)$, $\vec{B} = (0, 0, B_0)$ and $\vec{J} = (J'_x, J'_y, 0)$ respectively.

The equations governing the motion of mixed convection flow of a viscoelastic fluid through a vertical porous channel filled with porous medium in the presence of a moving magnetic field with Hall and ion-slip currents, rotation and thermal and concentration buoyancy forces under Boussinesq approximation are described by

$$\begin{aligned} & \frac{\partial u'}{\partial t'} + w_0 \frac{\partial u'}{\partial z'} - 2\Omega v' \\ &= -\frac{1}{\rho} \frac{\partial p'}{\partial x'} + \nu \frac{\partial^2 u'}{\partial z'^2} + \frac{\beta'}{\rho} \frac{\partial^3 u'}{\partial z'^2 \partial t'} \\ & - \frac{\sigma B_0^2}{\rho(\alpha_e^2 + \beta_e^2)} [\alpha_e u' - \beta_e v' - K_1 w_0 f'(t')] \\ & - \frac{\nu u'}{k'} + g \beta_T (T' - T'_\infty) + g \beta_C (C' - C'_\infty), \end{aligned} \quad (1)$$

$$\begin{aligned} & \frac{\partial v'}{\partial t'} + w_0 \frac{\partial v'}{\partial z'} + 2\Omega u' = \nu \frac{\partial^2 v'}{\partial z'^2} + \frac{\beta'}{\rho} \frac{\partial^3 v'}{\partial z'^2 \partial t'} \\ & - \frac{\sigma B_0^2}{\rho(\alpha_e^2 + \beta_e^2)} [\beta_e u' - \alpha_e v'] - \frac{\nu v'}{k'}, \end{aligned} \quad (2)$$

$$0 = -\frac{1}{\rho} \frac{\partial p'}{\partial z'}, \quad (3)$$

where $\alpha_e = 1 + \beta_e \beta_i$ and

$$K_1 = \begin{cases} 1 & \text{when } B_0 \text{ is moving and} \\ & \text{fixed relative to the moving} \\ & \text{porous wall,} \\ 0 & \text{when } B_0 \text{ is stationary} \\ & \text{and fixed relative to the fluid.} \end{cases}$$

Equation (3) shows the constancy of pressure in a direction normal to the plane of the channel walls. The pressure gradient term $-(1/\rho)(\partial p'/\partial y')$ is not present in equation (2) because there is a net cross flow in y' -direction.

The fluid considered being optically thin with a relatively low density, then the energy equation with heat radiation is

$$\frac{\partial T'}{\partial t'} + w_0 \frac{\partial T'}{\partial z'} = \frac{k}{\rho C_p} \frac{\partial^2 T'}{\partial z'^2} - \frac{4\alpha^2 (T' - T_1)}{\rho C_p}. \quad (4)$$

The concentration equation with first order chemical reaction is given by

$$\frac{\partial C'}{\partial t'} + w_0 \frac{\partial C'}{\partial z'} = D \frac{\partial^2 C'}{\partial z'^2} - K'(C' - C_1). \quad (5)$$

The conditions to be satisfied at the boundary walls of the channel are

$$\left. \begin{aligned} & \text{At } z' = \frac{z_0}{2} : \left\{ \begin{aligned} & u' = w_0 f'(t'), v' = 0, \\ & T' = T_2 + \varepsilon(T_2 - T_1) \cos(\omega t'), \\ & C' = C_2 + \varepsilon(C_2 - C_1) \cos(\omega t'). \end{aligned} \right\} \quad (6) \\ & \text{At } z' = -\frac{z_0}{2} : \left\{ \begin{aligned} & u' = v' = 0, T' = T_1, C' = C_1. \end{aligned} \right\} \end{aligned}$$

To non-dimensionalize the equations governing the fluid motion i.e. equations (1)-(5) and boundary conditions (6), we define the following non-dimensional quantities:

$$\left. \begin{aligned} & z = z' / z_0, x = x' / z_0, u = u' / U_0, \\ & v = v' / U_0, t = t' w_0 / z_0, \omega = \omega' z_0 / w_0, \\ & f = f' / w_0, T = (T' - T_1) / (T_2 - T_1), \\ & C = (C' - C_1) / (C_2 - C_1). \end{aligned} \right\} \quad (7)$$

Using the non-dimensional quantities defined in equation (7), to the equations (1) and (2) and then combining both, we get the following non-dimensional equation

$$\begin{aligned} S \left(\frac{\partial q}{\partial t} + \frac{\partial q}{\partial z} + \frac{\partial p}{\partial x} \right) &= \frac{\partial^2 q}{\partial z^2} + \beta \frac{\partial^3 q}{\partial z^2 \partial t} \\ -X_3 q + G_T T + G_C C - K_1^* f(t), \end{aligned} \quad (8)$$

where

$$\left. \begin{aligned} & q = u + iv, S = z_0 w_0 / \nu, K^2 = \Omega z_0^2 / \nu, \\ & M^2 = \sigma B_0^2 z_0^2 / \rho \nu, k_1 = k' / z_0^2, \\ & \beta = \beta' w_0 / z_0 \nu, G_T = g \beta_T z_0^2 (T_2 - T_1) / \nu w_0, \\ & G_C = g \beta_C z_0^2 (C_2 - C_1) / \nu w_0. \end{aligned} \right\}$$

The energy equation (4) and concentration equation (5) in non-dimensional form become

$$S \Pr \left(\frac{\partial T}{\partial t} + \frac{\partial T}{\partial z} \right) = \frac{\partial^2 T}{\partial z^2} - N^2 T, \quad (9)$$

$$SSc \left(\frac{\partial C}{\partial t} + \frac{\partial C}{\partial z} \right) = \frac{\partial^2 C}{\partial z^2} - K_2 C, \quad (10)$$

where $\Pr = \nu \rho C_p / k, N^2 = Q_0 z_0^2 / k, Sc = \nu / D, K_2 = K' z_0^2 / D.$

The conditions at the boundary walls of the channel in non-dimensional form become

$$\left. \begin{aligned} & \text{At } z = 1/2 : q = T = C = f(t) = 1 + \varepsilon \cos(\omega t), \\ & \text{At } z = -1/2 : q = T = C = 0. \end{aligned} \right\} \quad (11)$$

The coupled partial differential equations (8)-(10) together with the boundary conditions (11) describe the mathematical model of the present physical problem which is required to be solved.

SOLUTION OF THE PROBLEM

Since the MHD flow through the vertical channel is developed due to a periodic pressure gradient applied along x' -direction, oscillatory movement of the right wall of the channel and the buoyancy forces arise from temperature and concentration differences. Thus, the temperature, concentration, fluid velocity and pressure gradient along x' -direction are assumed as

$$T(z, t) = T_0(z) + \frac{\varepsilon}{2} (T_1(z) e^{i\omega t} + T_2(z) e^{-i\omega t}), \quad (12)$$

$$C(z, t) = C_0(z) + \frac{\varepsilon}{2} (C_1(z) e^{i\omega t} + C_2(z) e^{-i\omega t}), \quad (13)$$

$$q(z, t) = q_0(z) + \frac{\varepsilon}{2} (q_1(z) e^{i\omega t} + q_2(z) e^{-i\omega t}), \quad (14)$$

$$-\frac{\partial p}{\partial x} = A \left(1 + \frac{\varepsilon}{2} (e^{i\omega t} + e^{-i\omega t}) \right). \quad (15)$$

Using equations (12)-(15) to the PDE's system given by equations (8)-(10), these reduces to the following system of ODE's

$$T_0'' - S \Pr T_0' - N^2 T_0 = 0, \quad (16)$$

$$C_0'' - SSc C_0' - K_2 C_0 = 0, \quad (17)$$

$$q_0'' - S q_0' - X_3 q_0 = -K_1^* - G_T T_0 - G_C C_0, \quad (18)$$

$$T_1'' - S \Pr T_1' - (N^2 + i\omega S \Pr) T_1 = 0, \quad (19)$$

$$C_1'' - SSc C_1' - (K_2 + i\omega SSc) C_1 = 0, \quad (20)$$

$$\begin{aligned} & (1 + i\omega\beta) q_1'' - S q_1' - (X_3 + i\omega S) q_1 \\ & = -K_1^* - G_T T_1 - G_C C_1, \end{aligned} \quad (21)$$

$$T_2'' - S \Pr T_2' - (N^2 - i\omega S \Pr) T_2 = 0, \quad (22)$$

$$C_2'' - SSc C_2' - (K_2 - i\omega SSc) C_2 = 0, \quad (23)$$

$$\begin{aligned} & (1 - i\omega\beta) q_2'' - S q_2' - (X_3 - i\omega S) q_2 \\ & = -K_1^* - G_T T_2 - G_C C_2. \end{aligned} \quad (24)$$

The conditions at the boundary walls of the channel after use of equations (12) to (14) yield

$$\left. \begin{aligned} & \text{At } z = 1/2 : T_0 = T_1 = T_2 = 1, \\ & C_0 = C_1 = C_2 = 1, q_0 = q_1 = q_2 = 1. \\ & \text{At } z = -1/2 : T_0 = T_1 = T_2 = 0, \\ & C_0 = C_1 = C_2 = 0, q_0 = q_1 = q_2 = 0. \end{aligned} \right\} \quad (25)$$

Solving equations (16)-(24) subject to the boundary conditions (25), the solution for temperature, concentration and fluid velocity are given by

$$T_i = \frac{e^{r_i z - \frac{s_i}{2}} - e^{s_i z - \frac{r_i}{2}}}{2 \sinh\left(\frac{r_i - s_i}{2}\right)}, \quad i = 0, 1, 2, \quad (26)$$

$$C_i = \frac{e^{\frac{u_i z - v_i}{2}} - e^{\frac{v_i z - u_i}{2}}}{2 \sinh\left(\frac{u_i - v_i}{2}\right)}, \quad i = 0, 1, 2, \quad (27)$$

$$q_i = \frac{e^{\frac{s_i z - y_i}{2}} - e^{\frac{y_i z - s_i}{2}}}{2 \sinh((x_i - y_i)/2)} + \frac{K_1^{**}}{X_3} \left[1 + \frac{e^{s_i z} \sinh(y_i/2) - e^{y_i z} \sinh(x_i/2)}{2 \sinh((x_i - y_i)/2)} \right] + \frac{G_T}{2 \sinh((r_i - s_i)/2) \sinh((x_i - y_i)/2)} \times \left[\begin{aligned} & E_r e^{\frac{s_i}{2}} \left\{ e^{s_i z} \sinh\left(\frac{r_i - y_i}{2}\right) - e^{y_i z} \sinh\left(\frac{r_i - x_i}{2}\right) \right\} \\ & - e^{r_i z} \sinh\left(\frac{x_i - y_i}{2}\right) \left\{ -E_{s_i} e^{\frac{r_i}{2}} \left\{ e^{s_i z} \sinh\left(\frac{s_i - y_i}{2}\right) \right. \right. \right. \\ & \left. \left. \left. - e^{y_i z} \sinh\left(\frac{s_i - x_i}{2}\right) - e^{s_i z} \sinh\left(\frac{x_i - y_i}{2}\right) \right\} \right\} \right] + \frac{G_C}{2 \sinh((u_i - v_i)/2) \sinh((x_i - y_i)/2)} \times \left[\begin{aligned} & E_{u_i} e^{\frac{v_i}{2}} \left\{ e^{u_i z} \sinh\left(\frac{u_i - y_i}{2}\right) - e^{v_i z} \sinh\left(\frac{u_i - x_i}{2}\right) \right\} \\ & - e^{u_i z} \sinh\left(\frac{x_i - y_i}{2}\right) \left\{ -E_{v_i} e^{\frac{u_i}{2}} \left\{ e^{v_i z} \sinh\left(\frac{v_i - y_i}{2}\right) \right. \right. \right. \\ & \left. \left. \left. - e^{v_i z} \sinh\left(\frac{v_i - x_i}{2}\right) - e^{v_i z} \sinh\left(\frac{x_i - y_i}{2}\right) \right\} \right\} \right] \end{aligned} \right] \quad (28)$$

where $i = 0, 1, 2$.

Substituting the expressions for T_i , C_i and q_i , $i = 0, 1, 2$ from equations (26), (27) and (28) to the equations (12), (13) and (14) respectively, the solutions for temperature, concentration and fluid velocity are, respectively, obtained.

Skin friction at the left and right walls of the channel in the primary and secondary flow directions can be obtained by using equations (28) in the following expressions

$$\left. \begin{aligned} \tau_L &= \tau_{xL} + i\tau_{yL} \\ &= \left[\frac{\partial q_0}{\partial z} + \frac{\varepsilon}{2} \left(\frac{\partial q_1}{\partial z} e^{i\omega t} + \frac{\partial q_2}{\partial z} e^{-i\omega t} \right) \right]_{z=-1/2}, \\ \tau_R &= \tau_{xR} + i\tau_{yR} \\ &= \left[\frac{\partial q_0}{\partial z} + \frac{\varepsilon}{2} \left(\frac{\partial q_1}{\partial z} e^{i\omega t} + \frac{\partial q_2}{\partial z} e^{-i\omega t} \right) \right]_{z=1/2} \end{aligned} \right\} \quad (29)$$

The rate of heat transfer at the left and right walls of the channel in terms of Nusselt number are presented in the following form

$$\left. \begin{aligned} Nu_L &= Nu_{L0} + \frac{\varepsilon}{2} (Nu_{L1} e^{i\omega t} + Nu_{L2} e^{-i\omega t}), \\ Nu_R &= Nu_{R0} + \frac{\varepsilon}{2} (Nu_{R1} e^{i\omega t} + Nu_{R2} e^{-i\omega t}), \end{aligned} \right\} \quad (30)$$

where

$$\left. \begin{aligned} Nu_{Li} &= \frac{(r_i - s_i) e^{-(r_i + s_i)/2}}{2 \sinh((r_i - s_i)/2)}, \quad i = 0, 1, 2, \\ Nu_{Ri} &= \frac{r_i e^{(r_i - s_i)/2} - s_i e^{-(r_i - s_i)/2}}{2 \sinh((r_i - s_i)/2)}, \quad i = 0, 1, 2. \end{aligned} \right\} \quad (31)$$

The rate of mass transfer at the left and right walls of the channel in terms of Sherwood number are presented in the following form

$$\left. \begin{aligned} Sh_L &= Sh_{L0} + \frac{\varepsilon}{2} (Sh_{L1} e^{i\omega t} + Sh_{L2} e^{-i\omega t}), \\ Sh_R &= Sh_{R0} + \frac{\varepsilon}{2} (Sh_{R1} e^{i\omega t} + Sh_{R2} e^{-i\omega t}), \end{aligned} \right\} \quad (32)$$

where

$$\left. \begin{aligned} Sh_{Li} &= \frac{(u_i - v_i) e^{-(u_i + v_i)/2}}{2 \sinh((u_i - v_i)/2)}, \quad i = 0, 1, 2, \\ Sh_{Ri} &= \frac{u_i e^{(u_i - v_i)/2} - v_i e^{-(u_i - v_i)/2}}{2 \sinh((u_i - v_i)/2)}, \quad i = 0, 1, 2. \end{aligned} \right\} \quad (33)$$

NUMERICAL RESULTS AND DISCUSSION

The analytical solutions for fluid velocity, temperature, species concentration, skin friction, Nusselt number and Sherwood number have been derived in the previous section in terms of various flow governing parameters. The influences of these flow governing parameters on fluid velocity, temperature, species concentration, skin friction, heat and mass transfer at the walls of the channel are computed numerically and presented in graphical and tabular forms by taking $A = 1$, $G_T = 4$, $G_C = 5$, $Pr = 0.71$, $N = 2$, $Sc = 0.22$, $K_2 = 0.2$ and $\omega t = \pi/2$. The velocity profiles are displayed in figures 2-9 and it can be easily observed from figures 2-9 that moving magnetic field ($K_1 = 1$) produces comparatively less drag force in comparison to stationary magnetic field ($K_1 = 0$). Figures 10-11 and 12-13 depict the temperature and concentration profiles respectively.

Figures 2 and 3, respectively, demonstrate the variations in the velocity profiles for various values of Hall current parameter β_e and ion-slip current parameter β_i . It is observed that both the Hall and ion-slip currents raise the fluid velocity in the primary flow direction when magnetic field is fixed relative to the fluid (magnetic field is stationary) i.e. when $K_1 = 0$ while this effect of Hall and ion-slip currents is reversed when magnetic field is fixed relative to the moving wall of the channel (magnetic field is moving) i.e. when $K_1 = 1$. In

both the cases when $K_1 = 1$ and $K_1 = 0$, Hall current accelerates the fluid flow in the secondary flow direction while ion-slip current decelerates it in the secondary flow direction. Our result upholds the well known result that Hall current develops the secondary motion in the flow-field. Influence of rotation parameter K^2 on the velocity profiles are depicted in figures 4. In both the cases when $K_1 = 1$ and $K_1 = 0$, rotation (Coriolis force) has tendency to reduce the fluid flow in the primary flow direction while this tendency of rotation is reversed on the fluid flow in the secondary flow direction. It is well accepted that rotation induces secondary motion in the flow-field, our result also agrees with it. Velocity profiles for distinct values of magnetic parameter M^2 are displayed in figures 5. It is noticed that magnetic field suppress the fluid velocity in both the primary and secondary flow directions when $K_1 = 0$, which is due to the fact that magnetic field produces a drag force in the flow-field whose nature is to resist the fluid motion. But when $K_1 = 1$, the magnetic field enhances the fluid velocity in the primary flow direction in the left half of the channel and the fluid velocity in the secondary flow direction throughout the channel while this effect of magnetic field on the fluid velocity in the primary flow direction in the right half of the channel is upturned because magnetic field is fixed relative to the moving right wall of the channel. Deviations in the velocity profiles due to variations in permeability of the porous medium k_1 are presented in figures 6. Figures 6 illustrate that velocity profiles in both the primary and secondary flow directions rise on raising the permeability of the porous medium which implies that the Darcian drag force tends to decelerate the fluid velocity in both the primary and secondary flow directions. Figures 7 demonstrate the effects of the porosity of the walls i.e. suction/injection S on the fluid velocity. When $K_1 = 0$, suction tends to increase the fluid velocity in the primary flow direction and secondary flow direction in the right half of the channel while this trend of velocity in the secondary flow direction is upturned in the left half of the channel. When $K_1 = 1$, suction tends to decrease the fluid velocity in the secondary flow direction and primary flow direction in the left half of the channel while this trend of velocity in the primary flow direction is upturned in the right half of the channel. This may be due to the fact that suction is taking place through the left wall of the channel while the injection is taking place through

the right wall of the channel. Influences of oscillations ω on the velocity are shown in the figures 8. When $K_1 = 0$, rise in frequency of oscillations gives rise in fluid velocity in both the primary and secondary flow directions. When $K_1 = 1$, increase in frequency of oscillations gives rise in fluid velocity in the primary flow direction and secondary flow direction in the right half of the channel while this effect is reversed on the fluid flow in the secondary flow direction in left half of the channel. Figures 9 exhibit the variations in the velocity profiles due to change in viscoelastic nature of the fluid i.e. β . It can be seen from figures 9 that, when $K_1 = 0$, the fluid velocity in the primary flow direction falls whereas the fluid velocity in the secondary flow direction rise on raising the viscoelastic parameter. On raising the viscoelastic parameter fluid velocity is rising in both the primary and secondary flow directions when $K_1 = 1$. Figures 10 and 12 depict the influence of suction on fluid temperature and concentration respectively. Suction has tendency to reduce fluid temperature. Suction reduces concentration in the left half of the channel while it enhances concentration in the right half of the channel because suction and injection are simultaneously occurring through left and right walls of the channel. Figures 11 and 13 demonstrate that oscillations tend to rise the fluid temperature and concentration.

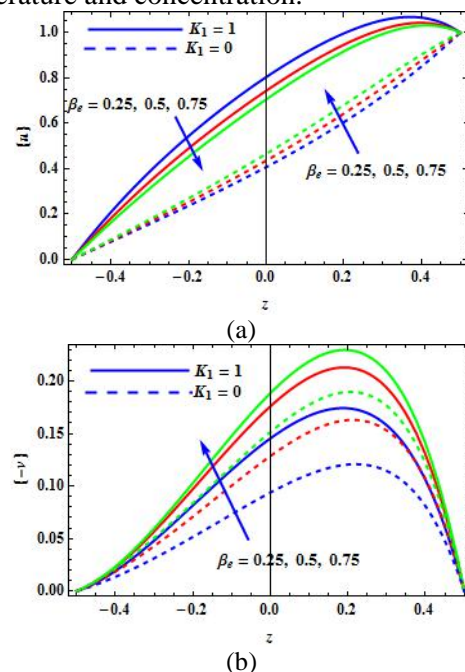
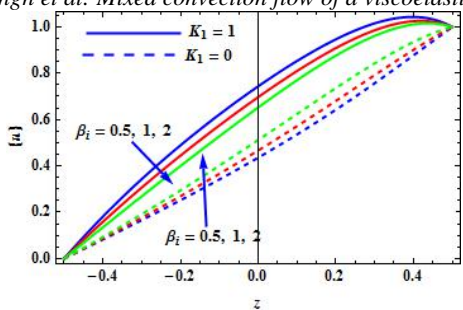
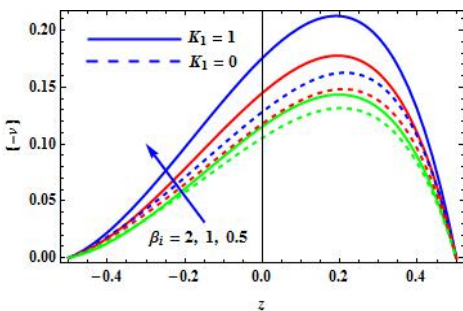


Fig. 2 Velocity profiles in the (a) primary and (b) secondary flow directions when $\beta_i = 0.5$, $K^2 = 1$, $M^2 = 9$, $k_1 = 0.3$, $S = 2$, $\omega = 3$ and $\beta = 0.25$.

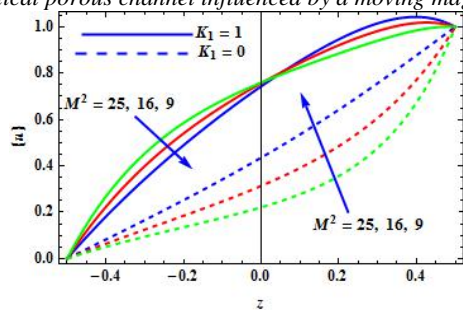


(a)

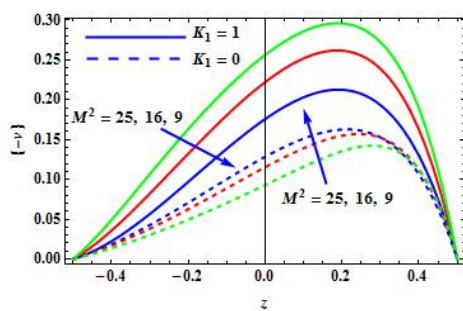


(b)

Fig. 3 Velocity profiles in the (a) primary and (b) secondary flow directions when $\beta_e = 0.5$, $K^2 = 1$, $M^2 = 9$, $k_1 = 0.3$, $S = 2$, $\omega = 3$ and $\beta = 0.25$.

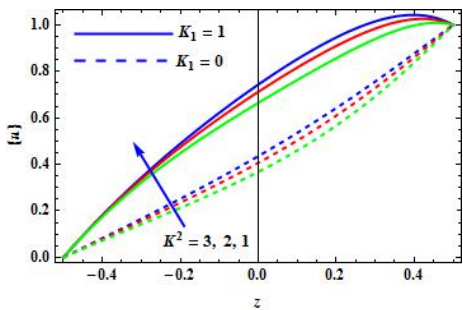


(a)

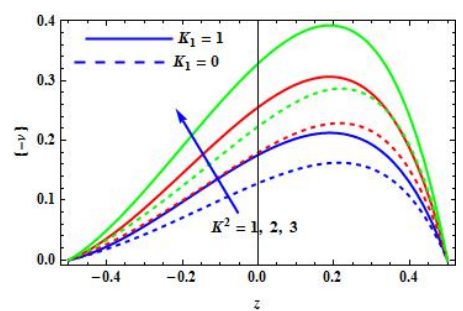


(b)

Fig. 5 Velocity profiles in the (a) primary and (b) secondary flow directions when $\beta_e = 0.5$, $\beta_i = 0.5$, $K^2 = 1$, $k_1 = 0.3$, $S = 2$, $\omega = 3$ and $\beta = 0.25$.

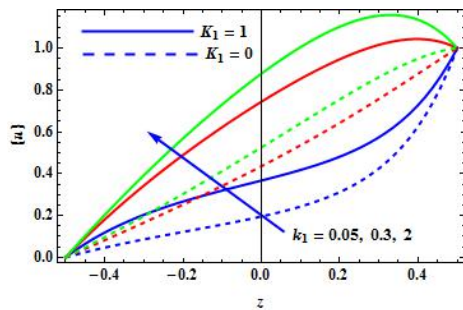


(a)

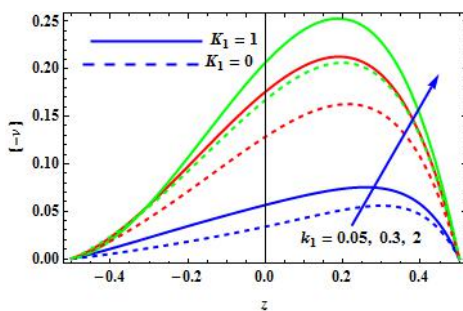


(b)

Fig. 4 Velocity profiles in the (a) primary and (b) secondary flow directions when $\beta_e = 0.5$, $\beta_i = 0.5$, $M^2 = 9$, $k_1 = 0.3$, $S = 2$, $\omega = 3$ and $\beta = 0.25$.

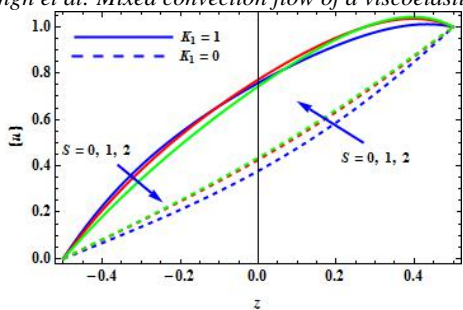


(a)

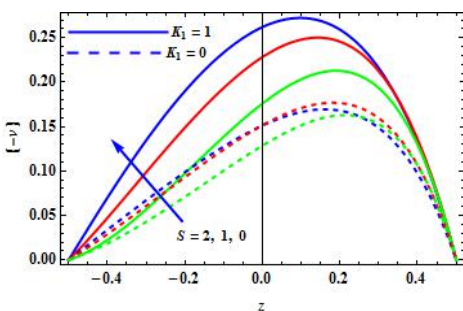


(b)

Fig. 6 Velocity profiles in the (a) primary and (b) secondary flow directions when $\beta_e = 0.5$, $\beta_i = 0.5$, $K^2 = 1$, $M^2 = 9$, $S = 2$, $\omega = 3$ and $\beta = 0.25$.

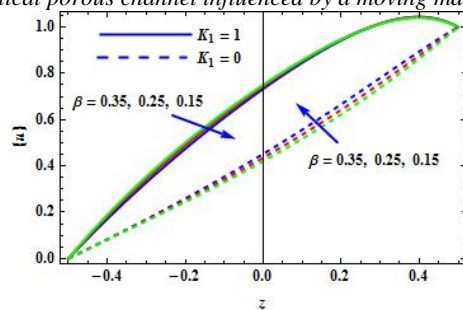


(a)

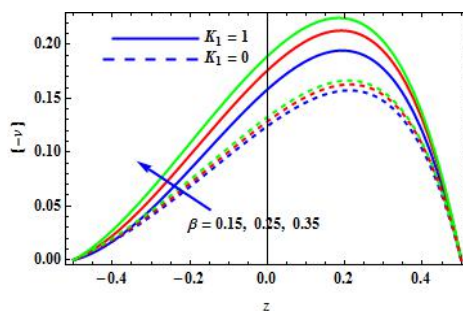


(b)

Fig. 7 Velocity profiles in the (a) primary and (b) secondary flow directions when $\beta_e = 0.5$, $\beta_i = 0.5$, $K^2 = 1$, $M^2 = 9$, $k_1 = 0.3$, $\omega = 3$ and $\beta = 0.25$.

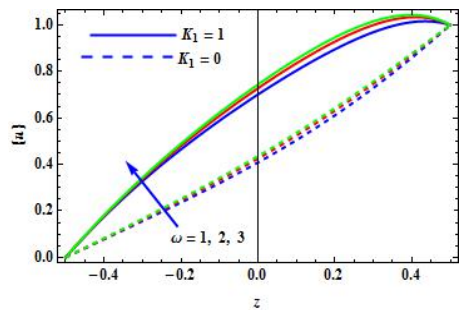


(a)

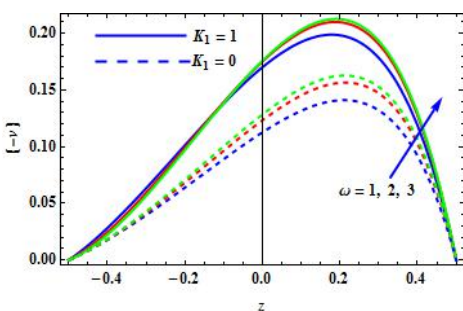


(b)

Fig. 9 Velocity profiles in the (a) primary and (b) secondary flow directions when $\beta_e = 0.5$, $\beta_i = 0.5$, $K^2 = 1$, $M^2 = 9$, $k_1 = 0.3$, $S = 2$ and $\omega = 3$.



(a)



(b)

Fig. 8 Velocity profiles in the (a) primary and (b) secondary flow directions when $\beta_e = 0.5$, $\beta_i = 0.5$, $K^2 = 1$, $M^2 = 9$, $k_1 = 0.3$, $S = 2$ and $\beta = 0.25$.

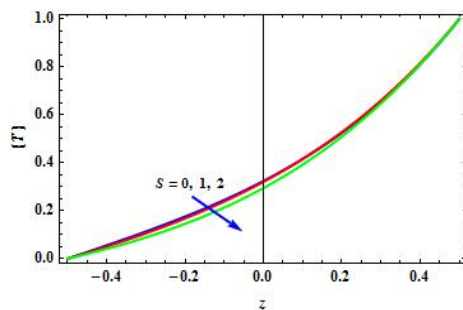


Fig. 10 Temperature profiles when $\omega = 3$.

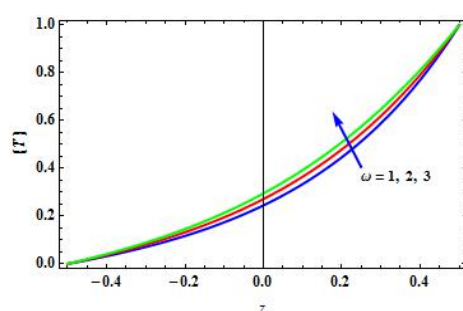


Fig. 11 Temperature profiles when $S = 2$.

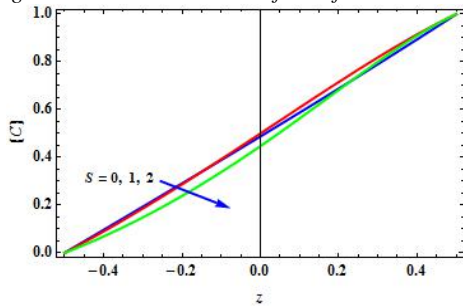


Fig. 12 Concentration profiles when $\omega = 3$.

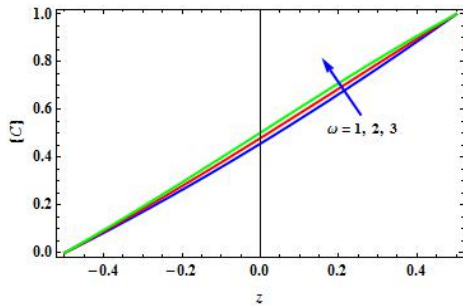


Fig. 13 Concentration profiles when $S = 2$.

Table 1 depicts the influences of flow governing parameters on the skin friction at the moving right wall of the channel in case of both the moving and stationary magnetic field. In case of both the

moving and stationary magnetic field, skin friction at the moving wall in the primary flow direction fall down on raising Hall and ion-slip currents while the skin friction at the moving wall in the secondary flow direction raise on rising Hall current, rotation, strength of applied magnetic field, permeability of the porous medium, suction and frequency of oscillations. Ion-slip current has tendency to reduce skin friction at the moving wall in the secondary flow direction. When magnetic field is moving, skin friction at the moving wall in the primary flow direction is reduced by magnetic field and viscoelastic property of the fluid while it is enhanced by suction and frequency of oscillations. When magnetic field is stationary, skin friction at the moving wall in the primary flow direction is raised by rotation, magnetic field and viscoelastic property of the fluid while it is reduced by permeability of the porous medium, suction and frequency of oscillations. Table 2 demonstrates the influences of flow governing parameters on heat and mass transfer at both the walls of the channel. Suction tends to decrease both the heat and mass transfer at the left wall and mass transfer at the right wall of the channel. Oscillations raise both the heat and mass transfer at the left wall while it reduces these at the right wall of the channel.

Table 1 Skin friction at the moving right wall of the channel.

β_e	β_i	K^2	M^2	k_1	S	ω	β	$K_1 = 1$		$K_1 = 0$	
								$-\tau_{xR}$	τ_{yR}	τ_{xR}	τ_{yR}
0.5	0.5	1	9	0.3	2	3	0.25	0.9293	1.7302	1.2124	1.4781
0.25	0.5	1	9	0.3	2	3	0.25	1.2022	1.4109	1.6016	1.1385
0.75	0.5	1	9	0.3	2	3	0.25	0.7939	1.8636	0.8507	1.6641
0.5	1	1	9	0.3	2	3	0.25	0.6951	1.4592	0.8958	1.3118
0.5	2	1	9	0.3	2	3	0.25	0.5277	1.1833	0.4365	1.1251
0.5	0.5	2	9	0.3	2	3	0.25	0.7261	2.4984	1.4001	2.1039
0.5	0.5	3	9	0.3	2	3	0.25	0.4304	3.2281	1.6489	2.6869
0.5	0.5	1	16	0.3	2	3	0.25	0.5632	2.2158	2.7083	1.6595
0.5	0.5	1	25	0.3	2	3	0.25	0.1130	2.6637	4.1999	1.8005
0.5	0.5	1	9	0.05	2	3	0.25	-3.629	0.9086	5.0610	0.7859
0.5	0.5	1	9	2	2	3	0.25	2.1401	1.9506	0.2239	1.7246
0.5	0.5	1	9	0.3	1	3	0.25	0.7556	1.7313	1.2761	1.4282
0.5	0.5	1	9	0.3	0	3	0.25	0.3752	1.6410	1.5523	1.2701
0.5	0.5	1	9	0.3	2	2	0.25	0.8140	1.7024	1.2788	1.4312
0.5	0.5	1	9	0.3	2	1	0.25	0.5241	1.5749	1.4369	1.2782
0.5	0.5	1	9	0.3	2	3	0.35	0.8706	1.7912	1.3868	1.4920
0.5	0.5	1	9	0.3	2	3	0.15	0.9537	1.5787	0.9644	1.4144

Table 2 Heat and mass transfers at the channel walls.

S	ω	Nu_L	Nu_R	Sh_L	Sh_R
2	3	0.3801	2.0217	0.9602	0.8190
1	3	0.4851	1.9957	0.9849	0.9094
0	3	0.5514	2.0746	0.9934	1.0133
2	2	0.3434	2.3001	0.9051	0.9608
2	1	0.3003	2.5931	0.8483	1.1045

CONCLUSIONS

A mathematical analysis has been presented for mixed convection MHD flow of a rotating viscoelastic fluid through a vertical porous channel filled with porous medium in the presence of a moving magnetic field. The influences of some significant flow governing parameters on these flow variables have been thoroughly discussed in the previous section. Some significant observations are précised below:

- Hall and ion-slip currents raise the fluid velocity in the primary flow direction when magnetic field is stationary. This effect is upturned when magnetic field is moving.
- In case of moving magnetic field, the magnetic field raises the fluid velocity in the primary flow direction in the left half of the channel while this effect is upturned in the right half of the channel because magnetic field is fixed relative to the moving right wall of the channel. Suction shows reverse behaviour as that of magnetic field on the fluid velocity in the primary flow direction.
- Suction reduces concentration in the left half of the channel while it enhances concentration in the right half of the channel because suction and injection are simultaneously taking place through left and right walls of the channel.
- When magnetic field is stationary, magnetic field has tendency to enhance skin friction at the moving wall in the primary flow direction. This tendency is upturned when magnetic field is moving because magnetic field is fixed relative to the moving wall.

NOMENCLATURE

B_0	applied magnetic field (T)
C	non-dimensional species concentration
C'	species concentration (mol / m^3)
C_1	concentration at left wall (mol / m^3)
C_2	a constant concentration (mol / m^3)
C_p	specific heat at constant pressure ($J / kg.K$)
D	chemical molecular diffusivity (m^2 / s)
K	rotation parameter
g	acceleration due to gravity (m / s^2)
G_c	solulal Grashof number
G_T	thermal Grashof number
k	thermal conductivity of the fluid ($W / m.K$)
k'	permeability (m^2)
k_1	permeability parameter
K'	chemical reaction constant
K_2	chemical reaction parameter
M	magnetic parameter

N	heat radiation parameter
Pr	Prandtl number
τ_L	non-dimensional skin friction at the left wall
τ_R	non-dimensional skin friction at the right wall
S	suction/injection parameter
Sc	Schmidt number
t	non-dimensional time
t'	time (s)
T	non-dimensional fluid temperature
T'	fluid temperature (K)
T_1	Temperature at left wall (K)
T_2	a constant temperature (K)
u	non-dimensional velocity in x' -direction
v	non-dimensional velocity in y' -direction
x	non-dimensional coordinate along the channel wall
z	non-dimensional coordinate normal to channel wall

Greek symbols

α	mean radiation absorption coefficient
β	viscoelastic parameter
β_c	volumetric coefficient of concentration expansion
β_e	Hall current parameter
β_i	ion-slip current parameter
β_T	volumetric coefficient of thermal expansion (K^{-1})
ν	kinematic viscosity (m^2 / s)
ρ	fluid density (kg / m^3)
σ	electrical conductivity (S / m)
ω	frequency parameter

APPENDIX

$$X_1 = (1/k_1) + (M^2 \alpha_e / (\alpha_e^2 + \beta_e^2)),$$

$$X_2 = (2K^2) + (M^2 \beta_e / (\alpha_e^2 + \beta_e^2)),$$

$$X_3 = X_1 + iX_2, \quad K_1^* = K_1 M^2 / (\alpha_e^2 + \beta_e^2),$$

$$r_0 = (S Pr + \sqrt{(S Pr)^2 + 4N^2}) / 2,$$

$$r_{1,2} = (S Pr + \sqrt{(S Pr)^2 + 4(N^2 \pm i\omega S Pr)}) / 2,$$

$$s_0 = (S Pr - \sqrt{(S Pr)^2 + 4N^2}) / 2,$$

$$s_{1,2} = (S Pr - \sqrt{(S Pr)^2 + 4(N^2 \pm i\omega S Pr)}) / 2,$$

$$u_0 = (SSc + \sqrt{(SSc)^2 + 4K_2}) / 2,$$

$$u_{1,2} = (SSc + \sqrt{(SSc)^2 + 4(K_2 \pm i\omega SSc)}) / 2,$$

$$v_0 = (SSc - \sqrt{(SSc)^2 + 4K_2}) / 2,$$

$$v_{1,2} = (SSc - \sqrt{(SSc)^2 + 4(K_2 \pm i\omega SSc)}) / 2,$$

$$E_{r_0} = 1 / (r_0^2 - Sr_0 - X_3), \quad K_1^{**} = K_1^* + SA,$$

$$E_{r_{1,2}} = 1 / ((1 \pm i\omega\beta)r_{1,2}^2 - Sr_{1,2} - (X_3 \pm i\omega S)),$$

$$E_{s_0} = 1 / (s_0^2 - Ss_0 - X_3),$$

$$E_{s_{1,2}} = 1 / ((1 \pm i\omega\beta)s_{1,2}^2 - Ss_{1,2} - (X_3 \pm i\omega S)),$$

$$E_{u_0} = 1 / (u_0^2 - Su_0 - X_3),$$

$$E_{u_{1,2}} = 1 / ((1 \pm i\omega\beta)u_{1,2}^2 - Su_{1,2} - (X_3 \pm i\omega S)),$$

$$E_{v_0} = 1 / (v_0^2 - Sv_0 - X_3),$$

$$E_{v_{1,2}} = 1 / ((1 \pm i\omega\beta)v_{1,2}^2 - Sv_{1,2} - (X_3 \pm i\omega S)).$$

REFERENCES

1. D. Angirasa, G.P. Peterson, I. Pop, *Numerical Heat Transfer, Part A: Applications: An International Journal of Computation and Methodology*, **31**, 255 (1997).
2. K. D. Alagoa, G. Tay, *Astr. Phys. Space Sci.*, **260**, 455 (1999).
3. E. Osalusi, J. Side, R. Harris, *Int. Comm. Heat Mass Transfer*, **35**, 908 (2008).
4. B K. Jha, A. O. Ajibade, *Proc. IMechE: Part E: J. Process Mechanical Engineering*, **224**, 91 (2010).
5. K. D. Singh K. Chand, S. Sharma, *Int. J. Math. Sci. Engg. Appls. (IJMSEA)*, **6**, 317 (2012).
6. I. Khan, K. Fakhra, S. Shafie, *J. Phys. Soc. Japan*, **80**, 104401 (2011).
7. M. Narahari, L. Debnath, *ZAMM*, **93**, 38 (2013).
8. M. Kar, G. C. Dash, S. N. Sahoo and P. K. Rath, a porous medium with heat source and *J. Eng. Thermophysics*, **22**, 203 (2013).
9. R. N. Barik G. C. Dash, M. Kar, *J. Fluids*, **2013** (2013), 297493.
10. A. Manglesh, M.G. Gorla, *Indian J. Pure Appl. Math.*, **44**, 743 (2013).
11. A. J. Chamkha, S. S. Al-Rashidi, *Heat Transfer Research*, **44**, 215 (2013).
12. S. Md. Ibrahim K. Gangadhar, N.B. Reddy, *J. Appl. Fluid Mech.*, **8**, 529 (2015).
13. G. S. Seth, S. Sarkar, *Bulg. Chem. Comm.*, **47** 66 (2015).
14. I. B. Yabo, B. K. Jha, J-E. Lin, *Appl. Mathematics*, **7**, 2354 (2016).
15. A. S. Butt, A. Ali, *J. Appl. Mech. Tech. Phys.*, **57**, 27 (2016).
16. J. K. Singh, N. Joshi, S. G. Begum, C. T. Srinivasa, *Frontiers in Heat and Mass Transfer*, **7**, 24 (2016).
17. Md. F. Iqbal and S. Ahmad, K. Ali and Md. Ashraf, *J. Porous Media*, **19**, 821 (2016).
18. J. C. Misra and S. D. Adhikary, *Alexandria Engineering Journal*, **55**, 287 (2016).
19. J. A. Falade, J.C. Ukaegbu, A.C. Egere, S. O. Adesanya, MHD oscillatory flow through a porous channel saturated with porous medium, *Alexandria Engineering Journal*, **56**, 147 (2017).
20. K.R. Cramer, S.I. Pai, *Magneto-fluid-dynamics for Engineers and Applied Physicists*, McGraw-Hill, New York (1973).
21. V. Javeri, *Heat Mass Transfer*, **8**, 193 (1975).
22. V. M. Soundalgekar, N. V. Vighnesam and H. S. Takhar, Hall and ion-slip effects in the MHD Couette flow with heat transfer, *IEEE Trans. Plasma Sci.*, **7**, 178 (1979).
23. P.C. Ram, H.S. Takhar, *Fluid Dyn. Res.*, **11**, 99 (1993).
24. H.S. Takhar, B.K. Jha, *J. MHD Plasma Res.*, **8**, 61 (1998).
25. E.M. Abo-Eldahab, M.A.E. Aziz, *Physica Scripta*, **61**, 344 (2000).
26. E.F. Elshehawey, N.T. Eldabe, E.M. Elbarbary, N.S. Elgazery, *Canad. J. Phys.*, **82**, 701 (2004).
27. O. Ojjela, N. N. Kumar, *International Scholarly Research Notices*, **2014** 646957 (2014).
28. M.D. Hossain, M.A. Samad, M.M. Alam, *Procedia Eng.*, **105**, 56 (2015).
29. J. K. Singh, P. Rohidas, N. Joshi, S. Ghousia Begum, *Int. J. Heat Technol.*, **35**, 37 (2017).
30. J. K. Singh, G. S. Seth, S. Ghousia Begum, *Diffusion Foundations*, **11**, 146 (2017).
31. K. Walters, The motion of a elastico-viscous liquid contained between coaxial cylinders, *Quarterly J. Mech. Appl. Math.*, **13**, 444 (1960).
32. K. Walters, *Quarterly J. Mech. Appl. Math*, **15**, 63 (1962).
33. G. Chakraborty, P. R. Sengupta, *Proc. Nat. Acad. Sci.*, **65**, 75 (1994).
34. V. Sharma, G.C. Rana, *Int. J. Appl. Mech. Eng.*, **6**, 843 (2001).
35. R.C. Sharma, P. Kumar, S. Sharma, *Int. J. Appl. Mech. Eng.*, **7**, 433 (2002).
36. M.M. Nandeppanavar, M.S. Abel, J. Tawade, *Commun. Nonlinear Sci. Numer. Simul.*, **15**, 1791 (2010).
37. T.B. Chang, A. Mehmood, O.A. Beg, M. Narahari, M.N. Islam, F. Ameen, *Commun. Nonlinear Sci. Numer. Simul.*, **16**, 216 (2011).
38. P. G. Siddheshwar, U. S. Mahabaleshwar, *Int. J. Nonlinear Mech.*, **40**, 807 (2005).

- J. K. Singh et al: Mixed convection flow of a viscoelastic fluid through a vertical porous channel influenced by a moving magnetic...*
39. I.J. Uwanta, B.Y. Isah, M.O. Ibrahim, *Int. J. Comput. Appl.*, **36**, 17 (2011).
 40. O. Prakash, D. Kumar, Y.K. Dwivedi, *J. Phys.*, **79**, 1457 (2012).
 41. T. Hayat, S. Asad, M. Mustafa, H.H. Alsulami, *Chinese Physics B*, **23**, 084701 (2014).
 42. B. Garg, K.D. Singh, A. Bansal, *Kragujevac J. Sci.*, **36**, 19 (2014).
 43. K.D. Singh, B. Garg, A. Bansal *Proc. Indian Nat. Sci. Acad.*, **80**, 333 (2014).
 44. K. Ramesh, M. Devakar, *J. Aerosp. Eng.*, **29** 04015050 (2016).
 45. S.A. Gaffar, V.R. Prasad, E.K. Reddy, *Int. J. Appl. Comput. Math.*, **3**, 859 (2017).
 46. J. K. Singh, N. Joshi, P. Rohidas, *J. Mechanics* (2017).
DOI: [10.1017/jmech.2017.25](https://doi.org/10.1017/jmech.2017.25)
 47. G. Sutton, A. Sherman, Engineering Magnetohydrodynamics, *McGraw-Hill*, New York, 1965.
 48. R.C. Meyer, *J. Aerosp. Sci.*, **25**, 564 (1958).

A chemometric method for contamination sources identification along the Oum Er Rbia river (Morocco)

A. Benamar¹, F. Z. Mahjoubi^{1,2*}, Gomaa A. M. Ali^{3,4}, F. Kzaiber², A. Oussama¹

¹ *Université Sultan Moulay Slimane, Laboratoire de Spectro-chimie Appliquée et Environnement, Faculté des Sciences et Techniques de Beni Mellal, Morocco*

² *Université Sultan Moulay Slimane, Ecole Supérieure de Technologie de Beni Mellal, Laboratoire d'Ingénierie et Technologies Appliquées (LITA), Morocco*

³ *Chemistry Department, Faculty of Science, Al-Azhar University, 71524, Assiut, Egypt*

⁴ *Center of Nanoscience and Applications (ACNA), Al-Azhar University, 71524, Assiut, Egypt*

Received October 1, 2019; Revised October 6, 2019

In the present work, a chemometric tool, namely, principal component analysis was used to understand the behavior of sampling stations, relationship between measured variables and to classify sampling locations into groups of similar water quality characteristics. The samples (24) were collected in the 8 sampling stations located along the Oum Er Rbia river, in three different campaigns from 2016 to 2017. The study area includes several sensible sampling points such as sources (S1), upstream and downstream of Khenifra (S2), Zawiat Cheikh (S3, S4), Kasbat Tadla (S5, S6) and Dar Oulad Zidouh (S7, S8) cities. Several physicochemical variables were measured such as temperature (of water and air), pH, electrical conductivity, total hardness, dissolved oxygen, complete alkalimetric title, oxidizability, turbidity, chlorides, sulfates, nitrates, nitrites, ammonium, Fe, Zn, Pb, Cu, Cd, Cr and Ni. Results revealed that principal component analysis applied to the data analysis as chemometric approach reduced the number of variables in the first two PCs that captured 65 and 19% of the variance for PC1 and PC2, respectively, with a total variance of 84%. The principal component analysis showed the similarity between the sampling locations according to their water characteristics, the possible correlations between the variables studied and finally classified the sampling points to three groups (GR1, GR2 and GR3), according to the water quality characteristics of each site. The result demonstrated that chemometric method used in this work is effective and often useful for analysis, interpretation and classification of this river water based on the physicochemical loading of each sampling point.

Keywords: Oum Er Rbia river, Chemometric, Principal component analysis, Scores plot, Loadings plot, Bi-plot.

INTRODUCTION

Water is an important and precious natural resource for different uses (domestic, industrial and agricultural). It is an element basis for a healthy life and is directly attached to human survival. So, the consciousness of the limited amount of unpolluted water available to mankind is on the rise [1-6]. Water pollution, defined as physical, chemical, or biological degradations caused by human activity, disrupts living conditions and aquatic balances thereby compromising their multiple uses [7-11]. However, the quality of surface water is influenced by natural processes (soil erosion, precipitation, evaporation) as well as by human activity (agriculture, urban and industrial wastewater) [12, 13].

Rivers are considered as the net receivers of the different anthropogenic pollutants [14]. Rivers are systems that carry a significant load of dissolved and particulate matter from natural and anthropogenic origin in one direction [15]. Environmental control campaigns for rivers water, produce large amounts of analytical data that are

not always easy to interpret [16, 17]. In this context, chemometric techniques are important numerical methods and more appropriate tools that allow significant data reduction and interpretation, to extract useful information [18]. The use of different multivariate statistical techniques (principal component analysis (PCA)) for the interpretation of the analytical results seems an interesting solution for a better understanding of the water quality distribution and the ecological states of the investigated environments [19]. PCA is a mathematical procedure used widely in chemometric data analysis, representing a multivariate technique [20, 21]. Chemometric tools are usually chosen to uncover information hidden in the complex data sets [22]. PCA was realized by eigenvalue decomposition of the correlation matrix of the obtained data sets [23, 24]. It was applied to visualize the similarities between the samples analyzed, and also the trace element content [25-27]. The principal idea for utilizing this chemometric tool (PCA) was the reduction of the number of variables studied, called principal components (PCs).

* To whom all correspondence should be sent:
E-mail: mahjoubi.fatimazahra@gmail.com

PCs explain the global variations within the data to let the components more interpretable [28]. It is a statistical tool that projects data from a large dimensional space over a two-dimensional space, covered by some uncorrelated factors. For the studied dataset, it allows revealing the relationship between the water samples collected over the investigated period and the parameters measured for the consecutive filtering units, and also it can elucidate the relationships among these parameters. In recent years, the PCA approach has gained a lot of attention in chemometrics, due to its computational efficiency [29]. PCA is primarily used to determine general relationships between data. It is a very widely applied method for the interpretation of analytical data, especially on water quality. Several investigations carried out on the application of chemometric tools for water data analysis were reported in the literature by many researchers [17, 30-35].

The objectives of the present work are to obtain more detailed information about the global changes of the monitored physicochemical parameters along the river in three sampling expeditions (2016 to 2017), to explain the variation, similarities between sampling locations, correlations between variables studied and finally to classify sampling locations according to their water quality characteristics and to apply chemometric tools such as PCA.

MATERIAL AND METHODS

Area description

The system under study (Oum Er Rbia river) is located in the Oum Er Rbia basin. It is one of the most populated basins in Morocco, it is located in the center-west of Morocco (Fig. 1), at 31°19.33'-33° 22.21"N lat. and 5°8.55'-8° 22.53 W long and

covering an area of about 48,070 km² which represents nearly 7% of the country's surface area [36]. It is rich in renewable resources with more than 3,130 Mm³, a quarter of the resources of Morocco. The studied river is approximately 550 km long with a mean flow of 117 m³/s from the Middle Atlas to 1800 m, 40 km from the Khénifra city, and crosses the Tadla plain, the coastal plateau, and discharges in the Atlantic Ocean at Azemmour city. Serou, Derna, and El Abid (Fig. 1) rivers are its main tributaries. At the river level, several dams and reservoirs have been built whose objective is the supply of water for domestic, industrial and irrigation uses as well as the production of hydroelectrical energy. In addition, untreated municipal sewage ends up in the Oum Er Rbia river and its tributaries from neighboring cities.

Analytical procedures

The temperature measurements were carried out using a mercury thermometer, the pH was measured using a pH meter INOLAB pH7110, the electrical conductivity (EC) was measured by a conductimeter INOLAB cond720 and the turbidity was determined by a turbidimeter HACH 2100N.

Ammonium, nitrite and nitrate ions were determined by the indophenol blue, sulfanilamide and sulfanilamide methods, respectively, after reduction in a column of cadmium. The oxidizability was measured by hot oxidation in an acid medium by potassium permanganate. The total hardness (TH) was determined by complex titration with EDTA with indicator Eriochrome Black T; chlorides were determined by volumetric determination with mercuric nitrate. The measurement of dissolved oxygen (DO) content was done by the iodometric method. Sulfates were measured using the nephelometric method with barium sulfate, and the complete alkalimetric title (CAT) was determined by titrimetry.

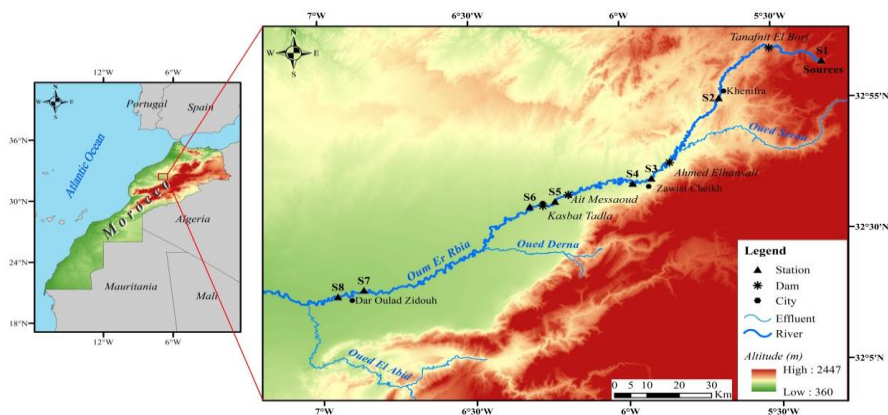


Fig. 1. Map of the study area and sampling stations along the Oum Er Rbia river.

A. Benamar et al: A chemometric method for contamination sources identification along the Oum Er Rbia river...

All analyses were carried out according to the Moroccan standard NM 03.7.001(N.M 03.7.001).

The metals concentrations (Pb, Cu, Ni, Cr, Fe, Cd, and Zn) were measured by inductively coupled plasma optical emission spectrometry (ICP-OES) using a Perkin Elmer Optima 8000 apparatus.

Sampling stations

Because of the various activities identified in the study area (liquid discharges from neighboring cities and agricultural activities in the Oum Er Rbia watershed), eight sampling stations (S1 to S8) distributed along the Oum Er Rbia river were used to represent the overall states of the stream according to the activities in its vicinity and to cover all possible pollution sources of the river. The exact sampling stations were: sources (S1), upstream and downstream of Khenifra (S2), Zawiya Cheikh (S3, S4), Kasbat Tadla (S5, S6) and Dar Oulad Zidouh (S7, S8) cities. A total of 24 water samples were collected along the river, all sites were sampled during three sampling expeditions, in April 2016, August 2016, and February 2017.

Sampling procedures

The river water samples were collected from the selected eight monitoring stations (S1-S8). The sampling was done at the sampling site approximately 30 cm below the water surface using a polyethylene bottle with a 1.5 L capacity previously rinsed 3 times with the water from the station. The collected samples were refrigerated (± 4 °C) in isothermal boxes, and transported to the laboratory quickly after sampling for testing.

Data analysis

Data statistical treatments were performed using the IBM SPSS Statistics 25 software packages. Chemometric treatments were performed using the Unscrambler X software version 10.2 from CAMO (Computer-Aided Modeling, Trondheim, Norway).

RESULTS AND DISCUSSION

Physicochemical parameters studied

The obtained analytical results for each physicochemical parameter during the three sampling periods along Oum Er Rbia River are represented in box-whiskers plots as follows in Fig. 2.

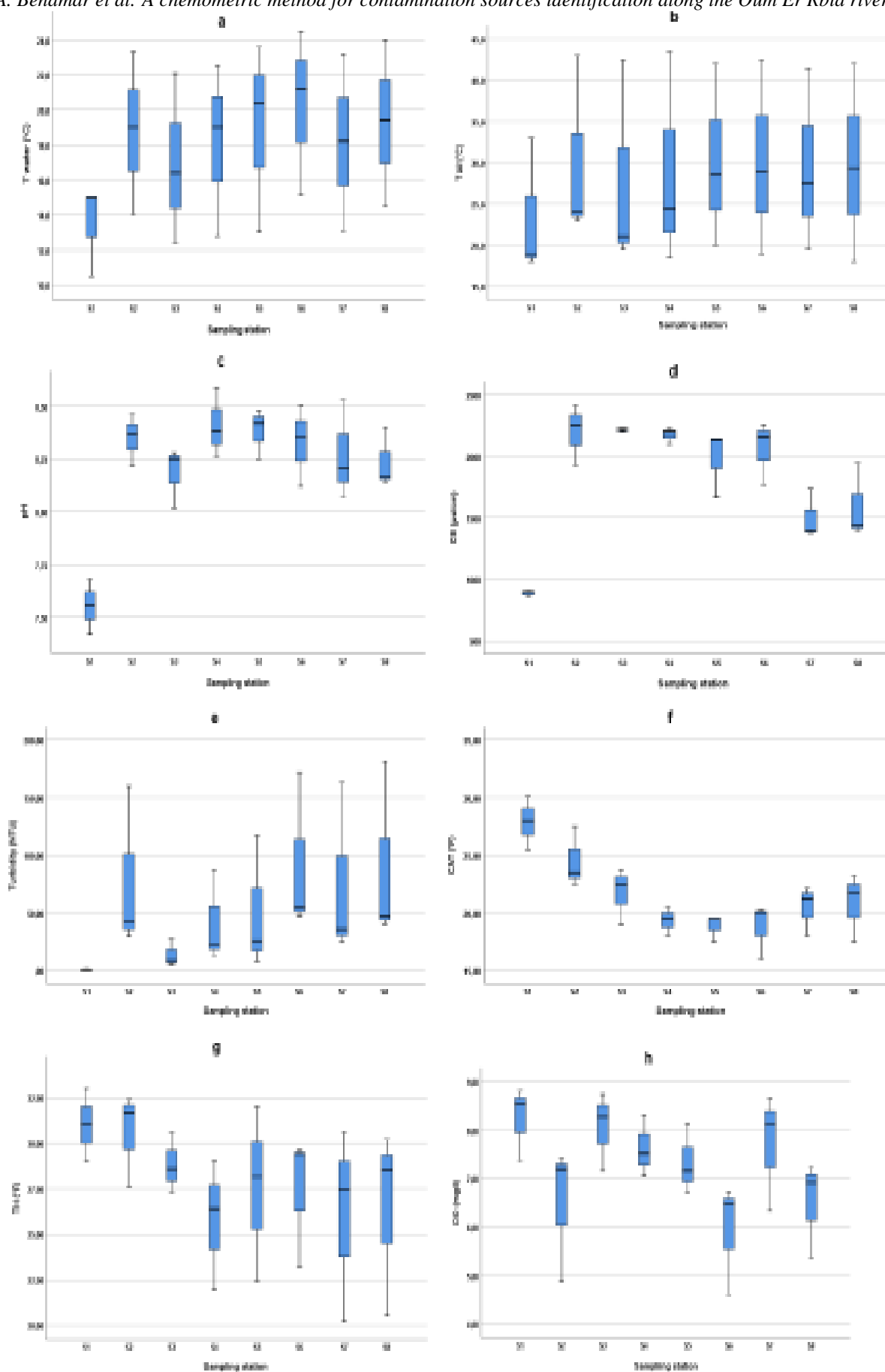
The variables are the temperature of the water, the temperature of the air, pH, EC, TH, DO, CAT, oxidizability, turbidity, chlorides (Cl^-), sulfates (SO_4^{2-}), nitrates (NO_3^-), nitrites (NO_2^-), ammonium (NH_4^+), Fe, Zn, Pb, Cu, Cd, Cr and Ni. The spatiotemporal variation of the 21 variables studied

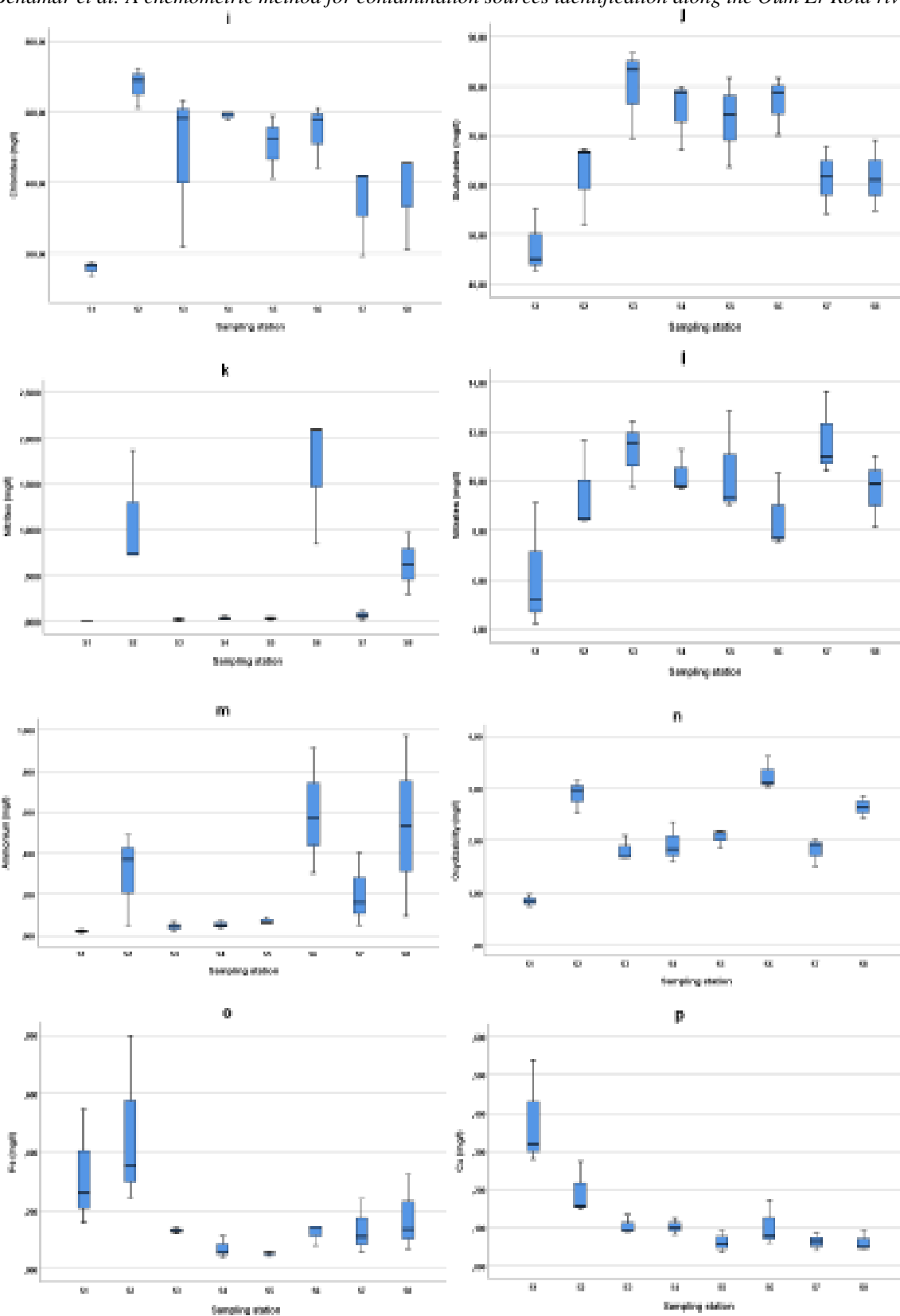
in three sampling expeditions at all locations (S1-S8) is shown in Fig. 2.

The water temperature of the different stations studied varies between 14 and 25 °C. The main reason for this difference in temperature values between all sites may be due to the large difference in altitude along the Oum Er Rbia river, the geographical characteristics of each station and the period of sampling. Nitrates present minimum values at S2, S6, and S8 stations, which can be related to the agricultural activity and excessive use of fertilizers. The maximum value of DO is observed at location S1 (sources) in all sampling periods and low values are observed at S2, S6, and S8 stations because of the discharging of wastewater from neighboring cities at S2, S6 and S8 stations. There are several variables (turbidity, oxidizability, ammonium and nitrites) at the S2, S6 and S8 locations that show maximum values mainly caused by the influence of the wastewater input in the river from Khenifra (S2), Kasbat Tadla (S6) and Dar Oulad Zidouh (S8) cities without treatment. The highest concentrations of total hardness, alkalinity, and heavy metals are recorded at the location S1, which is a result of the water's own characteristics. The lowest values of pH, chlorides, sulfates and EC are observed at station S1. The interpretation of the obtained results from the box-whiskers plots diagrams and the analysis of the correlations between the variables from one sampling site to another requires time, important verification and comparison between all the physicochemical parameters at the level of each diagram from one period to another and between all sampling locations. To distinguish and understand the relationship and variation between all physicochemical parameters investigated and the sampling locations along the Oum Er Rbia river, the application of chemometric methods is necessary.

Descriptive statistics

Preliminary exploratory data analysis was performed using univariate descriptive statistics. The descriptive statistics (minimum, maximum with mean and standard deviations) were computed for each physicochemical parameter during three sampling expeditions of the 21 water quality variables at the eight stations on the river, and are summarized in Table 1.





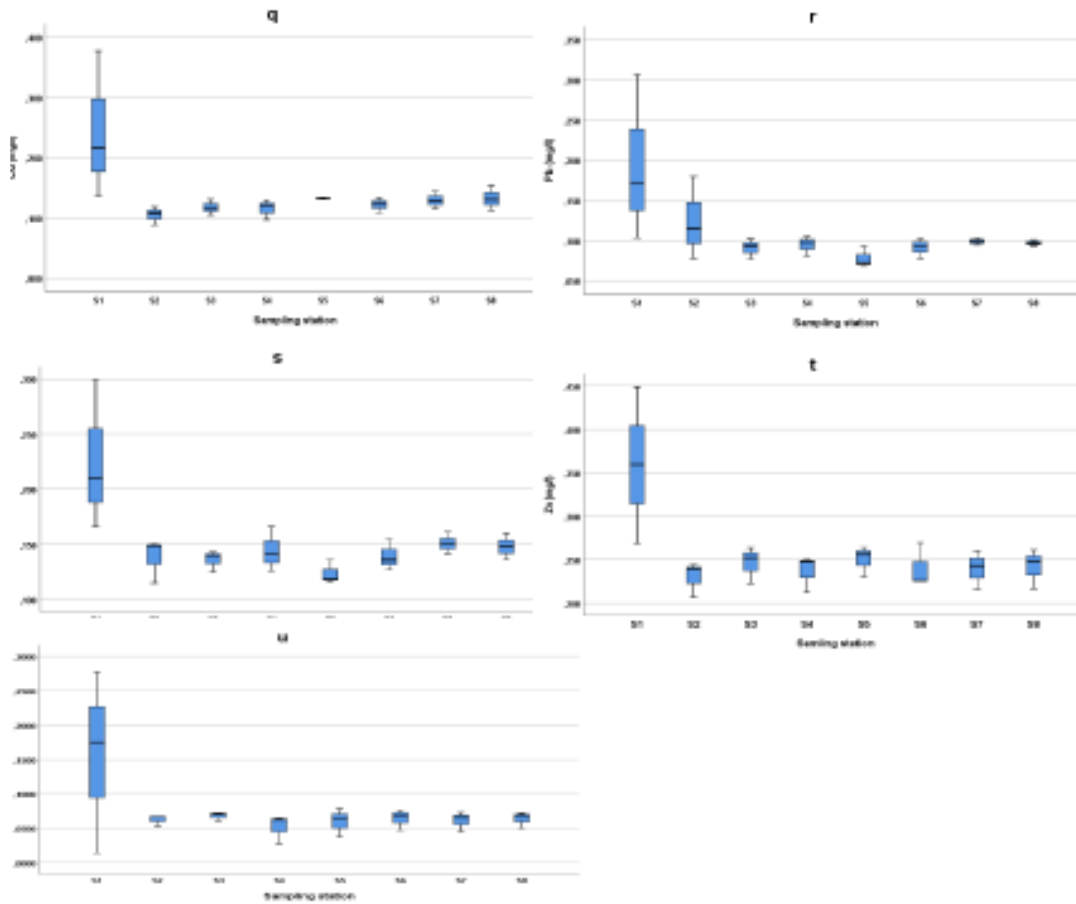


Fig. 2. Spatial and temporal distribution of (a) water temperature, (b) air temperature, (c) pH, (d) electrical conductivity, (e) turbidity, (f) complete alkalimetric title, (g) total hardness, (h) dissolved oxygen, (i) chlorides, (j) sulfates, (k) nitrites, (l) nitrates, (m) ammonium, (n) oxydizability, (o) iron, (p) copper, (q) cadmium, (r) lead, (s) nickel, (t) zinc and (u) chromium in the sampling stations along Oum Er Rbia river.

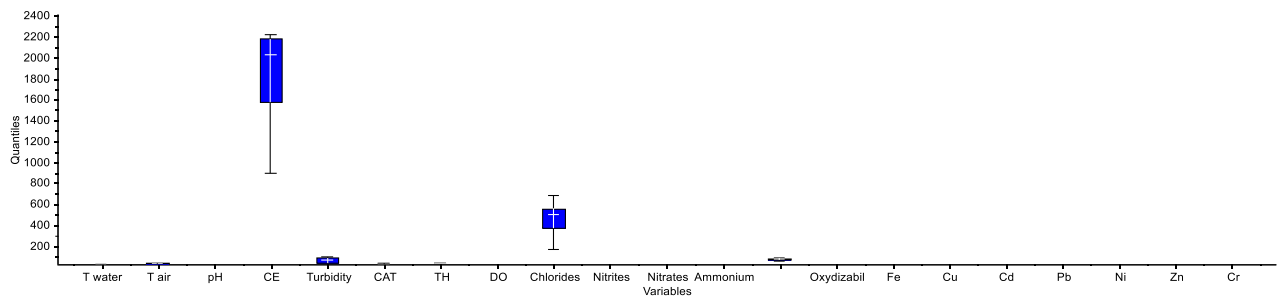


Fig. 3. Average and standard deviation graph of the different variables.

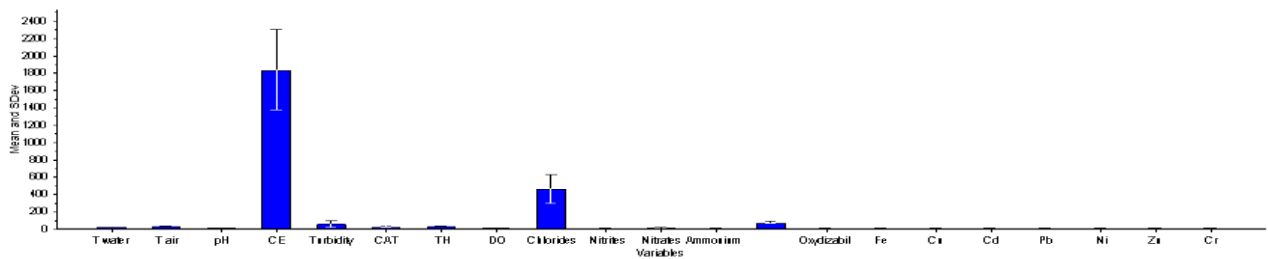


Fig. 4. Box-whiskers plot of the different variables.

Table 1. Global statistics of physicochemical parameters at the river level.

Parameter	Minimum	Maximum	Mean	Std. Deviation
Temperature of water (°C)	10	24.5	18.0083333	2.0622649
Temperature of air (°C)	18.0	43.5	28.6875000	2.3193800
pH	7.42	8.59	8.21416667	0.2775800
CE (µS/cm)	856	2420	1827.58333	468.50100
Turbidity (NTU)	0.43	182.00	54.8383333	34.405800
CAT (°F)	16.00	30.05	21.5395833	3.1679800
TH (°F)	20.18	33.00	27.9408333	2.0047000
DO (mg/L)	4.62	8.80	7.23708333	0.8296400
Chlorides (mg/L)	134.9	724.9	458.184167	162.67510
Nitrites (mg/L)	0.003	2.090	0.44646250	0.6375330
Nitrates (mg/L)	4.22	13.64	9.67541667	1.7311900
Ammonium (mg/L)	0.011	0.973	0.22737500	0.2291872
Sulfates (mg/L)	42.66	86.70	67.1666667	10.881905
Oxidizability (mg/L)	0.75	3.61	2.15708333	0.7510911
Fe (mg/L)	0.042	0.799	0.18525000	0.1395100
Cu (mg/L)	0.036	0.539	0.13458333	0.107850
Cd (mg/L)	0.088	0.378	0.13733333	0.044290
Pb (mg/L)	0.069	0.307	0.10875000	0.036820
Ni (mg/L)	0.115	0.300	0.15070833	0.031290
Zn (mg/L)	0.207	0.449	0.25562500	0.042340
Cr (mg/L)	0.0143	0.2780	0.07322083	0.033690

Table 2. Sampling stations projection in the space formed by PC1 and PC2.

Scores	PC1	PC2	Scores	PC1	PC2
S1	8.9227	0.5402	S5	-1.6504	-1.5890
S2	-0.9534	2.7306	S6	-2.8586	2.4601
S3	-0.1489	-2.2069	S7	-0.5592	-1.2333
S4	-1.4422	-1.9354	S8	-1.3101	1.2336

Table 3. Variables projection in PC1 and PC2 space.

X Loading	PC1	PC2	X Loading	PC1	PC2
Temperature of water	-0.2578	0.1236	Ammonium	-0.1288	0.3741
Temperature of air	-0.2602	0.0654	Sulfates	-0.2016	-0.1771
pH	-0.2626	-0.0425	Oxydizability	-0.2145	0.2996
CE	-0.2180	-0.0435	Fe	0.1168	0.3291
Turbidity	-0.1921	0.2757	Cu	0.2438	0.1526
CAT	0.2332	0.1488	Cd	0.2558	0.0229
TH	0.1729	0.1936	Pb	0.2526	0.1554
DO	0.1660	-0.3825	Ni	0.2575	0.0704
Chlorides	-0.2079	0.0660	Zn	0.2612	0.0150
Nitrites	-0.1114	0.4306	Cr	0.2632	0.0755
Nitrates	-0.1886	-0.2773			

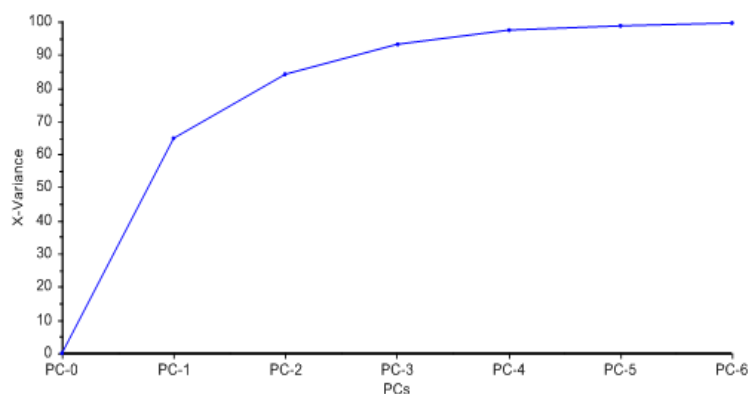


Fig. 5. Explained variance of each PC.

Mean and standard deviations were used for PCA pre-treatment. Prior to applying the principal components analysis to the data matrix, data sets were examined to visualize the weight and influence of each measured variable on the chemometric model by applying the descriptive statistics (mean, standard deviation, median, quintiles) as shown in Figs. 3 and 4.

From the original data of the raw results obtained, variation between all physicochemical parameters was observed. The descriptive statistics show a large difference in the statistical data of all variables studied in the 8 sampling stations along the river. In a first step, we compared the different variances of the 21 variables with each other. It is evident from this dataset that the variables differ considerably and show non-homogeneous dispersions. The unit of measurement and/or the measuring range changes according to the nature of the parameter.

Figs. 3 and 4 show that some variables (physicochemical parameters) like electrical conductivity, turbidity, chlorides and sulfates, are important values, therefore they will have a major influence on the chemometric model compared to other parameters. Consequently, pretreatment is necessary, which is performed by subtracting the corresponding column mean from each data element and dividing it by the corresponding column standard deviation. As a result, the variables have the unitary variances (scale) and consequently, they will have the same importance in the application and construction of the principal components analysis model.

Chemometric analysis

Like all chemometric tools, PCA treats all types of datasets, that is, tables containing many individuals and few variables (or *vice versa*), or many individuals and many variables. Chemometric data analysis methods such as PCA

provide powerful tools for the analysis and interpretation of large multivariate data of physicochemical analysis parameters. This approach can represent the total variability of the original data in a minimum number of principal components. Principal components analysis is a multivariate analysis method that is being increasingly utilized to visualize data because a large amount of information can be compared fluently in simple graphical form, which is very difficult to do using number tables or univariate statistics [37]. PCA is an exploratory data analysis that is primarily utilized to establish global relationships between data. Occasionally, more complex questions need to be answered. The objective of PCA is to determine underlying information from multivariate raw data.

The average values of each parameter at each station were grouped in a mathematical data matrix composed of 21×8 elements. A total of 8 rows represent water samples formed by 21 variables. PCA was applied using The Unscrambler software. The principal components were obtained by the linear combination of the initial variables which are more or less correlated to them. These components, therefore, define a space of reduced dimension in which are projected the initial variables accounting for the maximum information.

According to Fig. 5, the PCA model obtained from the pretreated dataset is defined by 4 PCs with a total variance of 96% but the results can be interpreted by the first two PCs with a variance of 84%. The first two PCs were extracted and utilized in two-dimensional bivariate plots. The first principal component covers as much of the maximum variation in the dataset as possible. The second principal component is orthogonal to the first and usually covers remaining variation as possible but less than the first component, and so on [38]. Because the first and second principal components generally cover a big part of the total

variance, a regrouping of samples, according to the effect of all variables within the two-dimensional plane, is possible by plotting against each of the first two column vectors (the first two principal components: PC1 and PC2) of data matrix [39].

The loadings of variables, scores of sampling stations and bi-plot of the sampling stations and variables have been plotted. The analysis of the sampling locations distribution in the plan formed by the principal components PC1 and PC2 allows highlighting the similarities and dissimilarities existing between the sites according to their physicochemical composition. To investigate the eight sampling points along the Oum Er Rbia river, the scores for sampling sites computed and represented in the graph shown in Fig.6 indicate and identify the links between all studied sampling stations. The scores plot represents the dispersion of the different samples in the space formed by the first two principal components PC1 and PC2 to better understanding the distribution of locations and relationships between sampling stations. The distance between the samples indicates their similarity or dissimilarity. The first principal component represented 65% of information

whereas the second explained only 19% with a total variance of 84% in the dataset. From the scores plot (Fig. 6) and Table 2, it was observed that the samples S1, S5, S6 and S8 are well expressed by the first principal component, while the samples S2, S3, S4 and S7 are well represented by the second principal component in the PCA model obtained from the data matrix. According to the scores plot, we observed that the samples S2, S6 and S8 are close to each other which means that the three sampling stations have similar characteristics. The same explanation was applied for the group formed by the following samples, S3, S4, S5, and S7. The scores plot is used to show the relation between sampling locations based on their nearness or similarity. Sampling site S1 has different properties compared to the other sites (far from other samples in the scores plot diagram). This technique showed easily the sampling sites that have the same physicochemical characteristics and the same degree of pollution along the river. Several researchers have used the scores plot of principal components to elucidate the pattern of the distribution of sampling sites [40-42].

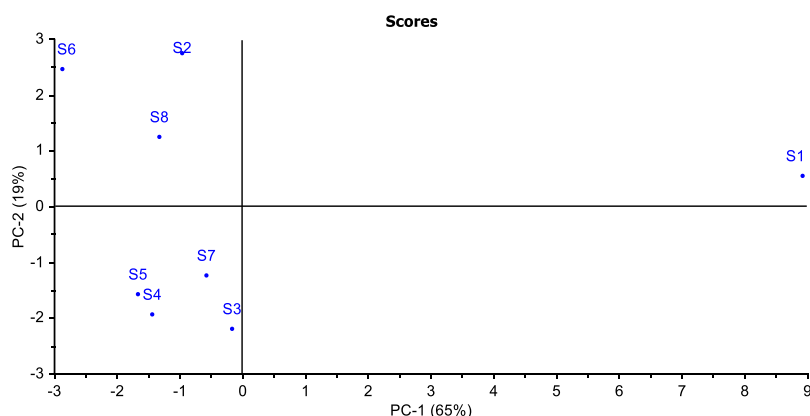


Fig. 6. Scores plot of the river water samples in each sampling station.

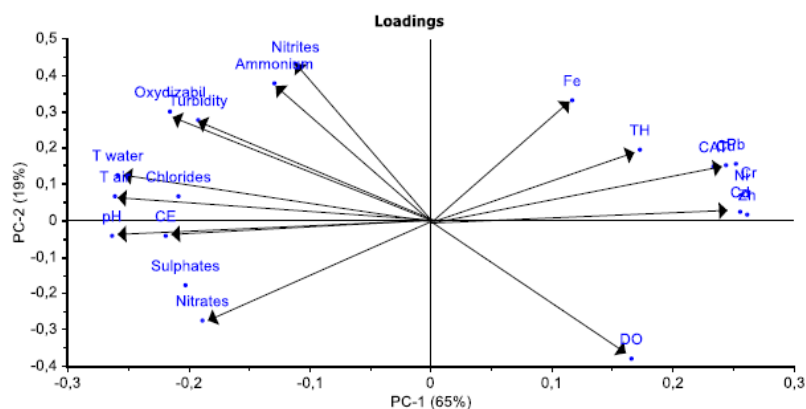


Fig. 7. Variables PCA loadings plot.

In this work, a bivariate correlation that is a statistical tool was used to understand the relationship between all physicochemical parameters investigated.

Fig. 7 shows PCA loadings plot which describes the distribution of the variables in the space formed by the first two principal components explaining 84% of the variance in the original experimental data. From the loadings plot (Fig. 7) and Table 3, all variables possessed higher loading and are well distributed on PC1–PC2 subspace, with no one being predominant, they are all very important and explain a lot of weight that helps to describe the dataset variation at the PCA model developed. PC1 (65% of the total variance) is mainly contributed and characterized by loadings of the variables: temperature of air, temperature of water, CE, Ni, Zn Pb, Cd, Cr, Cu, sulfates, CAT, chlorides and pH, whereas the variables: DO, TH, oxidizability, Fe, nitrites, nitrates, turbidity and ammonium are more important in the second principal component PC2 (19% of the variance). The study of the bivariate linear correlation between the investigated physical and chemical parameters gives information on the associations and relations between them. The correlation was calculated after mean centering and standardization of the raw data from the obtained results. The overall correlation between the

different physicochemical parameters is shown in Table 4 and the loadings plot (Fig. 7).

The analysis of the variables showed both positive and negative correlations between the different parameters studied. The positive correlation between the air temperature and the water temperature and the positive correlation between pH and temperature indicates that in most natural waters, pH is usually between 6 and 8.5, whereas in warm water it is between 5 and 9.

A positive correlation was observed between the EC and the chlorides which is due to the mineral character that could be related to the substrate. In addition, a high conductivity translates either abnormal pH, most often high salinity, which was observed along the river. Another positive correlation was observed between oxidizability and turbidity, because of the presence of various organic particles, clay of colloids, plankton, etc. Turbidity can be favored by rainfall. Positive correlations in river water samples of the study area are clearly present between HT and CAT; ammoniacal nitrogen and nitrites; between all heavy metals, etc. The significant positive correlation found between all heavy metals studied suggests that these elements are derived from a common source, mainly from parent rock and carbonate minerals [43].

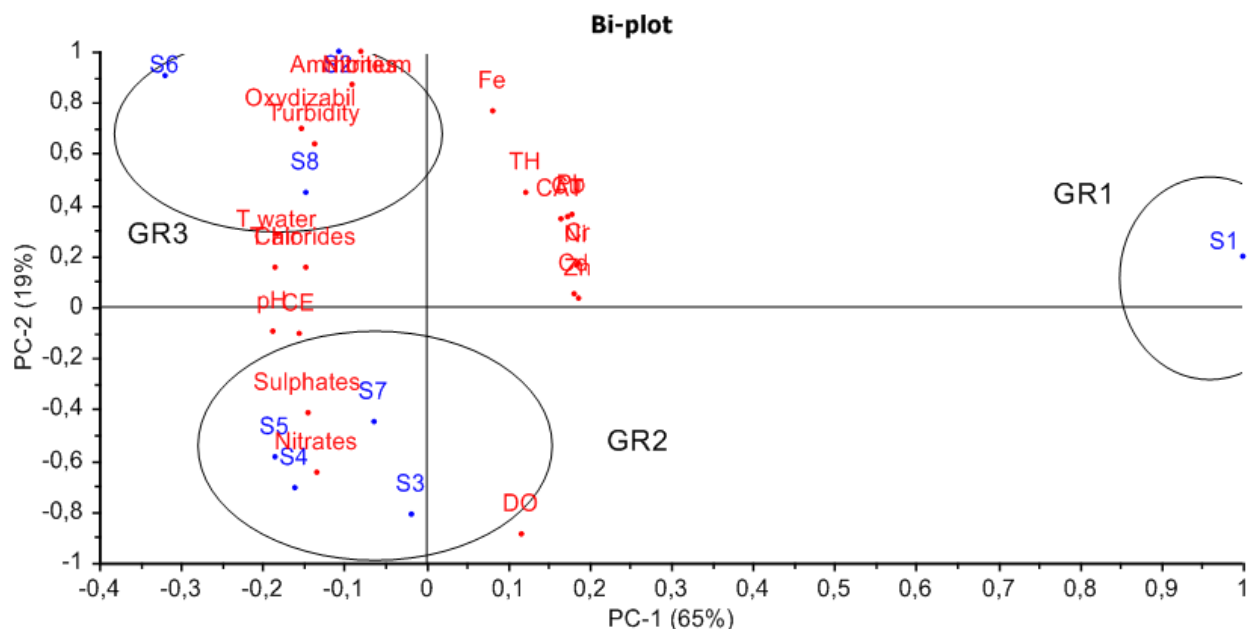


Fig. 8. Bi-plot of scores and loadings on the plane defined by the first two principal components (PC1-PC2). There was a strong positive correlation between the following pairs of physicochemical parameters: temperature of air/temperature of water (0.972), oxidizability/turbidity (0.854), ammonium/nitrites (0.855), chlorides/CE (0.941), TH/CAT (0.851), temperature of water/pH (0.896) and between all heavy metals (0.256 to 0.989). Negative correlations were observed for the following pairs of parameters: DO/temperature of water (-0.800), oxidizability/DO (-0.950), ammonium/DO (-0.909), nitrates/DO (-0.916), temperature of water/heavy metals (-0.321 to 0.874).

A. Benamar et al: A chemometric method for contamination sources identification along the Oum Er Rbia river...

Table 4. Matrix of correlation between the variables on all stations studied.

	T water	T air	pH	CE	Turbidity	CAT	TH	DO	Chlorides	Nitrites	Nitrates	Ammonium	Sulfates	Oxidizability	Fe	Cu	Cd	Pb	Ni	Zn	Cr
T water	1	0.972**	0.896**	0.664	0.863**	-0.802*	-0.582	-0.800*	0.692	0.592	0.502	0.675	0.581	0.897**	-0.321	-0.817*	-0.837**	-0.828*	-0.857**	-0.880**	-0.874**
T air	0.972**	1	0.946**	0.691	0.823*	-0.782*	-0.577	-0.688	0.721*	0.454	0.643	0.537	0.558	0.819*	-0.293	-0.854**	-0.891**	-0.855**	-0.910**	-0.932**	-0.929**
pH	0.896**	0.946**	1	.833*	0.637	-0.821*	-0.614	-0.513	0.832*	0.296	0.732*	0.312	0.710*	0.703	-0.388	-0.859**	-0.952**	-0.899**	-0.949**	-0.963**	-0.983**
CE	0.664	0.691	0.833*	1	0.282	-0.586	-0.234	-0.380	0.941**	0.318	0.567	0.120	0.856**	0.621	-0.223	-0.591	-0.887**	-0.741*	-0.870**	-0.816*	-0.812*
Turbidity	0.863**	0.823*	0.637	0.282	1	-0.510	-0.461	-0.871**	0.412	0.701	0.258	0.857**	0.122	0.854**	-0.009	-0.574	-0.587	-0.495	-0.531	-0.672	-0.619
CAT	-0.802*	-0.782*	-0.821*	-0.586	-0.510	1	0.851**	0.369	-0.479	-0.145	-0.640	-0.302	-0.775*	-0.508	0.813*	0.914**	0.703	0.931**	0.794*	0.747*	0.827*
TH	-0.582	-0.577	-0.614	-0.234	-0.461	0.851**	1	0.161	-0.148	0.095	-0.602	-0.242	-0.446	-0.244	0.791*	0.818*	0.490	0.724*	0.494	0.580	0.665
DO	-0.800*	-0.688	-0.513	-0.380	-0.871**	0.369	0.161	1	-0.519	-0.916**	0.065	-0.909**	-0.200	0.950**	-0.135	0.342	0.487	0.357	0.459	0.523	0.456
Chlorides	0.692	0.721*	0.832*	0.941**	0.412	-0.479	-0.148	-0.519	1	0.451	0.419	0.199	0.669	0.700	-0.012	-0.465	-0.847**	-0.605	-0.798*	-0.787*	-0.767*
Nitrites	0.592	0.454	0.296	0.318	0.701	-0.145	0.095	-0.916**	0.451	1	-0.253	0.855**	0.145	0.863**	0.306	-0.075	-0.336	-0.126	-0.258	-0.337	-0.235
Nitrates	0.502	0.643	0.732*	0.567	0.258	-0.640	-0.602	0.065	0.419	-0.253	1	-0.094	0.570	0.196	-0.477	-0.837**	-0.772*	-0.806*	-0.769*	-0.785*	-0.813*
Ammonium	0.675	0.537	0.312	0.120	0.857**	-0.302	-0.242	-0.909**	0.199	0.855**	-0.094	1	0.056	0.831*	0.084	-0.319	-0.327	-0.262	-0.266	-0.395	-0.314
Sulfates	0.581	0.558	0.710*	0.856**	0.122	-0.775*	-0.446	-0.200	0.669	0.145	0.570	0.056	1	0.436	-0.639	-0.684	-0.725*	-0.828*	-0.792*	-0.672	-0.720*
Oxidizability	0.897**	0.819*	0.703	0.621	0.854**	-0.508	-0.244	-0.950**	0.700	0.863**	0.196	0.831*	0.436	1	0.033	-0.523	-0.720*	-0.564	-0.679	-0.735*	-0.668
Fe	-0.321	-0.293	-0.388	-0.223	-0.009	0.813*	0.791*	-0.135	-0.012	0.306	-0.477	0.084	-0.639	0.033	1	0.670	0.256	0.674	0.407	0.295	0.427
Cu	-0.817*	-0.854**	-0.859**	-0.591	-0.574	0.914**	0.818*	0.342	-0.465	-0.075	-0.837**	-0.319	-0.684	-0.523	0.670	1	0.814*	0.969**	0.871**	0.865**	0.911**
Cd	-0.837**	-0.891**	-0.952**	-0.887**	-0.587	0.703	0.490	0.487	-0.847**	-0.336	-0.772*	-0.327	-0.725*	-0.720*	0.256	0.814*	1	0.860**	0.942**	0.989**	0.969**
Pb	-0.828*	-0.855**	-0.899**	-0.741*	-0.495	0.931**	0.724*	0.357	-0.605	-0.126	-0.806*	-0.262	-0.828*	-0.564	0.674	0.969**	0.860**	1	0.939**	0.880**	0.930**
Ni	-0.857**	-0.910**	-0.949**	-0.870**	-0.531	0.794*	0.494	0.459	-0.798*	-0.258	-0.769*	-0.266	-0.792*	-0.679	0.407	0.871**	0.942**	0.939**	1	0.934**	0.950**
Zn	-0.880**	-0.932**	-0.963**	-0.816*	-0.672	0.747*	0.580	0.523	-0.787*	-0.337	-0.785*	-0.395	-0.672	-0.735*	0.295	0.865**	0.989**	0.880**	0.934**	1	0.985**
Cr	-0.874**	-0.929**	-0.983**	-0.812*	-0.619	0.827*	0.665	0.456	-0.767*	-0.235	-0.813*	-0.314	-0.720*	-0.668	0.427	0.911**	0.969**	0.930**	0.950**	0.985**	1

**Correlation is significant at the 0.01 level (2-tailed)

*Correlation is significant at the 0.05 level (2-tailed)

A high negative correlation is observed between water temperature and DO. DO concentrations have an inverse relationship with stream temperatures so that as temperatures increase, less DO is contained in the water [44, 45]. The concentration of DO in water is generally related to the effects of several factors such as temperature, salinity and eutrophication. Another negative correlation is marked between oxidizability and DO, it is due to the consumption of dissolved oxygen by microorganisms in order to degrade the organic matter (high oxidizability). Nitrite is also negatively correlated to DO. The loadings plot as a step in this chemometric analysis is an efficient method that fluently shows the relationship between all physicochemical parameters studied.

The distribution of samples on the bi-plot graph shows that it is possible to isolate different groups of samples more easily. The loadings of variables and scores of sampling stations were plotted and the obtained results are presented in Fig. 8. The bi-plot graph shows the interpretation of the relation between the samples and the behavior of the variables in the PCs space formed by the first two principal components. It was employed in this study to obtain groups of sampling stations based on the similarity of the water physicochemical composition and the water quality characteristics. The Oum Er Rbia water river reveals the presence of three groups (GR1, GR2 and GR3) of water. The first group (GR1) included the station S1, situated in the upstream of the river (the sources). It is characterized by water with low temperature; the pollutant parameters are low compared to the other groups, highly loaded in some parameters such as total hardness, CAT and heavy metals; this site is characterized by good quality water compared to the other stations. The second group of river water (GR2) essentially includes the stations S3, S4, S5 and S7, expressed by the two PCs and situated on the upstream and downstream (S3, S4) of Zawiat Cheikh, and upstream of Kasbat Tadla and Dar Oulad Zidouh cities, respectively. This group is characterized by the abundance of DO, nitrates, and sulfates, with significant chlorides and EC values comparable to those of the first group. The stations constituting the second group are affected by agricultural activities practiced in the study area and have moderate pollution. The third group (GR3) is constituted by the stations (S2, S6 and S8) located on the downstream of Khenifra, Kasbat Tadla and Dar Oulad Zidouh cities. This group indicated the presence of pollution indices which are: oxidizability, turbidity, nitrites, ammonium, and chlorides because of the discharging of wastewater from neighboring cities directly into the

river without any prior treatment. This group is characterized by higher values of temperature and lower water quality than the other two groups; the group includes stations having the highest pollution sources. This group corresponds to the zones with a higher urban influence.

CONCLUSIONS

In this work, the surface water samples collected at different locations along the Oum Er Rbia river were analyzed for various physical and chemical parameters in three sampling times from 2016 to 2017. The application of a chemometric tool such as principal component analysis based on the analysis of data obtained offered the possibility to simplify the aquatic environment results analysis and interpretation. The principal component analysis model reduced the number of variables in the first two PCs with a total variance of 84% and showed the similarity between the sampling locations according to their water characteristics, the possible correlations between the variables studied. The chemometric technique applied to data analysis showed and successfully suggested the existence of three clearly separated groups of water: GR1 (S1), GR2 (S3, S4, S5 and S7) and GR3 (S2, S6 and S8). The anthropogenic activities mainly affecting the water quality along the river are urban, in particular at locations S2, S6 and S8, and agricultural activities, especially in all other zones except S1. This study demonstrated that the integration of chemometric approach can be used as a suitable and effective tool, while saving time, simplifying the study, to reduce the cost of monitoring river water and classify the locations according to the pollution state of each sampling station.

REFERENCES

1. M. Azizian, F. Boano, P.L.M. Cook, R.L. Detwiler, M.A. Rippy, S.B. Grant, *Water Resour. Res.*, **53**(5), 3941 (2017).
2. A.Ž. Kostić, N.Đ. Pantelić, L.M. Kaluđerović, J.P. Jonaš, B.P. Dojčinović, J.B. Popović-Djordjević, *Exposure and Health*, **8**(2), 227 (2016).
3. H. Sadegh, G.A.M. Ali, Potential Applications of Nanomaterials in Wastewater Treatment: Nano-adsorbents Performance, in: H. Athar, A. Sirajuddin (Eds.) *Advanced Treatment Techniques for Industrial Wastewater*, IGI Global, Hershey, PA, USA, 2019, p. 51.
4. H. Sadegh, G.A.M. Ali, H.J. Nia, Z. Mahmoodi, Nanomaterial Surface Modifications for Enhancement of the Pollutant Adsorption From Wastewater, *Nanotechnology Applications in Environmental Engineering* 2019, p. 143.
5. H. Sadegh, G.A.M. Ali, S. Agarwal, V.K. Gupta, *Int. J. Environ. Res.*, **13**(3), 523 (2019).

6. F.Z. Mahjoubi, A. Khalidi, M. Abdennouri, N. Barka, *Desalin. Water Treat.*, **57**(45), 21564 (2016).
7. H.H. Abdel Ghafar, G.A.M. Ali, O.A. Fouad, S.A. Makhlof, *Desalin. Water Treat.*, **53**(11), 2980 (2015).
8. S.P. Lee, G.A.M. Ali, H. Algarni, K.F. Chong, *J. Mol. Liq.*, **277**, 175 (2018).
9. S. Agarwal, H. Sadegh, Monajjemi Majid, A.S.H. Makhlof, G.A.M. Ali, A.O.H. Memar, R. Shahryari-ghoshekandi, I. Tyagi, V.K. Gupta, *J. Mol. Liq.*, **218**, 191 (2016).
10. H. Sadegh, G.A.M. Ali, A.S.H. Makhlof, K.F. Chong, N.S. Alharbi, S. Agarwal, V.K. Gupta, *J. Mol. Liq.*, **258**, 345 (2018).
11. M. Farnane, A. Elhalil, A. Machrouhi, F. Mahjoubi, M. Sadiq, M. Abdennouri, S. Qourzal, H. Tounsadi, N. Barka, *Desal. Wat. Treat*, **100**, 204 (2017).
12. R.O. Strobl, P.D. Robillard, *J. Environ. Manage.*, **87**(4), 639 (2008).
13. A. Elhalil, S. Qourzal, F.Z. Mahjoubi, R. Elmoubarki, M. Farnane, H. Tounsadi, M. Sadiq, M. Abdennouri, N. Barka, *Emerging Contam.*, **2**(1), 42 (2016).
14. S. Sabater, D. Barceló, N. De Castro-Català, A. Ginebreda, M. Kuzmanovic, M. Petrovic, Y. Picó, L. Ponsatí, E. Tornés, I. Muñoz, *Environ. Pollut.*, **210**, 303 (2016).
15. Z. Zhang, F. Tao, J. Du, P. Shi, D. Yu, Y. Meng, Y. Sun, *J. Environ. Manage.*, **91**(12), 2483 (2010).
16. M. Felipe-Sotelo, J. Andrade, A. Carlosena, R. Tauler, *Anal. Chim. Acta*, **583**, 128 (2007).
17. T. Kowalkowski, R. Zbytniewski, J. Szejna, B. Buszewski, *Water Res.*, **40**(4), 744 (2006).
18. P. Satheeshkumar, A.B. Khan, *Environ. Monit. Assess.*, **184**(6), 3761 (2012).
19. V. Simeonov, J. Stratis, C. Samara, G. Zachariadis, D. Voutsas, A. Anthemidis, M. Sofoniou, T. Kouimtzis, *Water Res.*, **37**(17), 4119 (2003).
20. M. Mezzelani, S. Gorbi, D. Fattorini, G. d'Errico, M. Benedetti, M. Milan, L. Bargelloni, F. Regoli, *Aquat. Toxicol.*, **180**, 306 (2016).
21. F. Tan, Z. Lu, *Ecol. Indic.*, **48**, 31 (2015).
22. B. Vandeginste, D. Massart, S. De Jong, D. Massart, L. Buydens, Handbook of chemometrics and qualimetrics: Part B, 1998.
23. M. Olenycz, A. Sokołowski, A. Niewińska, M. Wołowicz, J. Namieśnik, H. Hummel, J. Jansen, *Oceanologia*, **57**(2), 196 (2015).
24. H.G. Touahri, Z. Boutiba, W. Benguedda, S. Shaposhnikov, *Mar. Pollut. Bull.*, **110**(1), 52 (2016).
25. I.N. Bolotov, O.S. Pokrovsky, Y. Auda, J.V. Bespalaya, I.V. Vikhrev, M.Y. Gofarov, A.A. Lyubas, J. Viers, C. Zouiten, *Chem. Geol.*, **402**, 125 (2015).
26. S. Pain-Devin, C. Cossu-Leguille, A. Geffard, L. Giambérini, T. Jouenne, L. Minguez, B. Naudin, M. Parant, F. Rodius, P. Rousselle, *Aquat. Toxicol.*, **155**, 52 (2014).
27. C.D. Robinson, L. Webster, C. Martínez-Gómez, T. Burgeot, M.J. Gubbins, J.E. Thain, A.D. Vethaak, A.D. McIntosh, K. Hylland, *Mar. Environ. Res.*, **124**, 21 (2017).
28. K.K. Lehtonen, R. Turja, H. Budzinski, M.-H. Devier, *Mar. Environ. Res.*, **119**, 207 (2016).
29. W. Wu, D. Massart, S. De Jong, *Chemom. Intell. Lab. Syst.*, **37**(2), 271 (1997).
30. A. Ismail, M.E. Toriman, H. Juahir, S.M. Zain, N.L.A. Habir, A. Retnam, M.K.A. Kamaruddin, R. Umar, A. Azid, *Mar. Pollut. Bull.*, **106**(1), 292 (2016).
31. S.C. Azhar, A.Z. Aris, M.K. Yusoff, M.F. Ramli, H. Juahir, *Procedia Environ. Sci.*, **30**, 79 (2015).
32. D. Brodnjak-Vončina, D. Dobčnik, M. Novič, J. Zupan, *Anal. Chim. Acta*, **462**(1), 87 (2002).
33. C. Mendiguchía, C. Moreno, M.D. Galindo-Riaño, M. García-Vargas, *Anal. Chim. Acta*, **515**(1), 143 (2004).
34. S. Platikanov, D. Baquero, S. González, J. Martín-Alonso, M. Paraira, J.L. Cortina, R. Tauler, *Sci. Total Environ.*, **667**, 552 (2019).
35. D. Tripathi, D. Singh, S. Tripathi, *Int. J. Chem., Mater. Environ. Res.*, **3**(3), 42 (2016).
36. A. Barakat, M. El Baghdadi, J. Rais, B. Aghezzaf, M. Slassi, *Int. Soil Water Conserv. Res.*, **4**(4), 284 (2016).
37. D. Bingol, Ü. Ay, S. Bozbas, N. Uzgören, *Mar. Pollut. Bull.*, **68**, (2013).
38. D. Kara, *Food Chem.*, **114**(1), 347 (2009).
39. H. Diraman, H. Dibeklioglu, *J. Am. Oil Chem. Soc.*, **86**(7), 663 (2009).
40. F.D. Cid, R.I. Antón, R. Pardo, M. Vega, E. Caviedes-Vidal, *Anal. Chim. Acta*, **705**(1-2), 243 (2011).
41. N. Ruggieri, M. Castellano, M. Capello, S. Maggi, P. Povero, *Mar. Pollut. Bull.*, **62**(2), 340 (2011).
42. C. Vialle, C. Sablayrolles, M. Lovera, S. Jacob, M.-C. Huau, M. Montréjaud-Vignoles, *Water Res.*, **45**(12), 3765 (2011).
43. A. Chandrasekaran, R. Ravisankar, N. Harikrishnan, K. Satapathy, M. Prasad, K. Kanagasabapathy, *Spectrochim. Acta, Part A*, **137**, 589 (2015).
44. S.C. Chapra, Surface water-quality modeling, Waveland press, 2008.
45. M. Jalali, Z. Kolahchi, *Soil Sediment Contam.*, **18**(5), 576 (2009).

Instructions about Preparation of Manuscripts

General remarks: Manuscripts are submitted in English by e-mail. The text must be prepared in A4 format sheets using Times New Roman font size 11, normal character spacing. The manuscript should not exceed 15 pages (about 3500 words), including photographs, tables, drawings, formulae, etc. Authors are requested to use margins of 2 cm on all sides.

Manuscripts should be subdivided into labelled sections, e.g. INTRODUCTION, EXPERIMENTAL, RESULTS AND DISCUSSION, etc. **The title page** comprises headline, author(s)' names and affiliations, abstract and key words. Attention is drawn to the following:

a) **The title** of the manuscript should reflect concisely the purpose and findings of the work. Abbreviations, symbols, chemical formulae, references and footnotes should be avoided. If indispensable, abbreviations and formulae should be given in parentheses immediately after the respective full form.

b) **The author(s)**' first and middle name initials and family name in full should be given, followed by the address (or addresses) of the contributing laboratory (laboratories). **The affiliation** of the author(s) should be listed in detail (no abbreviations!). The author to whom correspondence and/or inquiries should be sent should be indicated by an asterisk (*) with e-mail address.

The abstract should be self-explanatory and intelligible without any references to the text and containing up to 250 words. It should be followed by keywords (up to six).

References should be numbered sequentially in the order, in which they are cited in the text. The numbers in the text should be enclosed in brackets [2], [5, 6], [9–12], etc., set on the text line. References are to be listed in numerical order on a separate sheet. All references are to be given in Latin letters. The names of the authors are given without inversion. Titles of journals must be abbreviated according to Chemical Abstracts and given in italics, the volume is typed in bold, the initial page is given and the year in parentheses. Attention is drawn to the following conventions: a) The names of all authors of a certain publications should be given. The use of “*et al.*” in the list of references is not acceptable; b) Only the initials of the first and middle names should be given. In the manuscripts, the reference to author(s) of cited works should be made without giving initials, e.g. “Bush and Smith [7] pioneered...”. If the reference carries the names of three or more authors it should be quoted as “Bush *et al.* [7]”, if Bush is the first author, or as “Bush and co-workers [7]”, if Bush is the senior author.

Footnotes should be reduced to a minimum. Each footnote should be typed double-spaced at the bottom of the page, on which its subject is first mentioned. **Tables** are numbered with Arabic numerals on the left-hand top. Each table should be referred to in the text. Column headings should be as short as possible but they must define units unambiguously. The units are to be separated from the preceding symbols by a comma or brackets. Note: The following format should be used when figures, equations, etc. are referred to the text (followed by the respective numbers): Fig., Eqns., Table, Scheme.

Schemes and figures. Each manuscript should contain or be accompanied by the respective illustrative material, as well as by the respective figure captions in a separate file. As far as presentation of units is concerned, SI units are to be used. However, some non-SI units are also acceptable, such as °C, ml, l, etc. Avoid using more than 6 (12 for review articles) figures in the manuscript. Since most of the illustrative materials are to be presented as 8-cm wide pictures, attention should be paid that all axis titles, numerals, legend(s) and texts are legible.

The authors are required to submit the text with a list of three individuals and their e-mail addresses that can be considered by the Editors as potential reviewers. Please note that the reviewers should be outside the authors' own institution or organization. The Editorial Board of the journal is not obliged to accept these proposals.

The authors are asked to submit **the final text** (after the manuscript has been accepted for publication) in electronic form by e-mail. The main text, list of references, tables and figure captions should be saved in separate files (as *.rtf or *.doc) with clearly identifiable file names. It is essential that the name and version of the word-processing program and the format of the text files is clearly indicated. It is recommended that the pictures are presented in *.tif, *.jpg, *.cdr or *.bmp format.

The equations are written using “Equation Editor” and chemical reaction schemes are written using ISIS Draw or ChemDraw programme.

EXAMPLES FOR PRESENTATION OF REFERENCES

REFERENCES

1. D. S. Newsome, *Catal. Rev.–Sci. Eng.*, **21**, 275 (1980).
2. C.-H. Lin, C.-Y. Hsu, *J. Chem. Soc. Chem. Commun.*, 1479 (1992).
3. R. G. Parr, W. Yang, *Density Functional Theory of Atoms and Molecules*, Oxford Univ. Press, New York, 1989.
4. V. Ponec, G. C. Bond, *Catalysis by Metals and Alloys (Stud. Surf. Sci. Catal., vol. 95)*, Elsevier, Amsterdam, 1995.
5. G. Kadinov, S. Todorova, A. Palazov, in: *New Frontiers in Catalysis (Proc. 10th Int. Congr. Catal., Budapest (1992), L. Guczi, F. Solymosi, P. Tetenyi (eds.), Akademiai Kiado, Budapest, 1993, Part C, p. 2817.*
6. G. L. C. Maire, F. Garin, in: *Catalysis. Science and Technology*, J. R. Anderson, M. Boudart (eds.), vol. 6, Springer Verlag, Berlin, 1984, p. 161.
7. D. Pocknell, *GB Patent 2 207 355* (1949).
8. G. Angelov, PhD Thesis, UCTM, Sofia, 2001, pp. 121-126.
9. JCPDS International Center for Diffraction Data, *Power Diffraction File*, Swarthmore, PA, 1991.
10. *CA* **127**, 184 762q (1998).
11. P. Hou, H. Wise, *J. Catal.*, in press.
12. M. Sinev, private communication.
13. <http://www.chemweb.com/alchem/articles/1051611477211.html>.

Texts with references which do not match these requirements will not be considered for publication!!!

CONTENTS

<i>R.A. Muminov, S.A. Radzhapov, A.K. Saymbetov, R.K. Manatbayev, Yo.K. Toshmurodov, N.M. Japashov, N.B. Kuttybay, A.G. Georgiev</i> , Optimization technology of large-size Si(Li) p-i-n structures for X-ray detectors.....	5
<i>Y.S. Demircioğlu, H.C. Sakarya, Y. Süzen</i> , Synthesis, X-ray crystal structure and spectroscopic studies of benzothiazole Schiff base.....	9
<i>S. Ceker, O. Capik, M. Sengül, R. Jaberi, G. Agar</i> , The antioxidant and antimutagenic properties of different extracts of <i>Crataegus monogyna subsp. monogyna</i> collected from the Eastern Anatolia region of Turkey.....	14
<i>N.N. Gohil, D.I. Brahmabhatt</i> , Synthesis, characterization and biological evaluation of some new pyrazolyl bipyridyl substituted dicoumarins.....	18
<i>A. Mushtaq, A. Israr, M. Fahad, J. Ahmed</i> , Mechanical analysis of additively manufactured polylactic acid in fused deposition modelling.....	29
<i>K. Sivakumar, V. Chandrasekaran</i> , Synthesis, characterization, deoxyribonucleic acid interaction and antimicrobial studies of Schiff base binuclear transition metal complexes	47
<i>R. Song, Y. Wang, J.J. Liu</i> , Manufacturing of artificial core based on transparent soil technology: A preliminary experimental study on various grains and pore fluids,.....	56
<i>N. Botoucharov, M. Stefanova, St. Marinov</i> , Geochemical appraisal of Stefanets Member (Etropole Formation) from the eastern part of the West Forebalkan, Bulgaria.....	62
<i>S.H. Abbas, H.H. Abbas, H.K. Musa</i> , Synthesis, characterization, kinetic and thermodynamic evaluation from TG-DTA analysis of new nickel(II) mixed ligands complexes of a bidentate salicylaldehyde Schiff bases and 1,10-phenanthroline.....	68
<i>R. Tomova, S. Asenova, B. Atanasova, K. Tzoneva, M. Slavova</i> , Flame atomic absorption determination of serum copper and zinc in disordered bone metabolism.....	76
<i>M. Tajbakhsh, M. Fakhimi Abarghouei, H. Alinezhad, Kh. Niknam</i> , CO ₂ capture on diethanolamine-grafted NaY zeolite	81
<i>G. Borisov, T. Dimitrov, D. Paskalev, E. Slavcheva</i> , Low-cost AEM water electrolysis with flat stainless steel electrodes.....	86
<i>R.M. Khan, A. Mushtaq, Z.U. Ali, S. Abbasi, R.N. Lodhi, S.M. ul Haq, S.A. Shakeel</i> , Development and characterization of walnut shell and date seeds powder in low-density polyethylene.....	90
<i>M.A.P. Rocha, N.P. Merlo, M.R. Franco Júnior, N.R.A.F. Rocha, W.A. Pereira</i> , Removal of caprylic acid impregnated on resins using organic solvents and water.....	98
<i>S. R. Hassan, I. Dahlan</i> , Investigation and optimization of a novel MAHB reactor for COD and lignin removal and methane production using response surface methodology (RSM) and artificial neural network (ANN).....	102
<i>E. Valipour</i> , Determination of an effective immunogenic peptide against <i>Acinetobacter baumannii</i>	114
<i>I. E. Ismailov, I. K. Ivanov, V. Ch. Christov</i> , Trifunctionalized allenes. Part V. Competitive electrophilic cyclization and cycloisomerization of 4-phosphorylated 5-hydroxy-5-methylhexa-2,3-dienoates.....	121
<i>V. Mitova, N. Koseva, Z. Todorova, P. Tuleshkov, K. Troev</i> , Synthesis of poly-(alkyleneterephthalate-co-alkylenephosphate)s and their blends with a linear polyurethane	129
<i>R.P. Nikolov, K.N. Koleva, M.H. Hristov, K.S. Yakimova</i> , Hyperthermia in experimental models of the serotonin syndrome: influence of vigabatrin.....	138
<i>S. Mamilov, S. Yesman, V. Mantareva, E. Borisova, A. Gisbrecht</i> , Optical method for reduction of carbon monoxide intoxication.....	142
<i>J. K. Singh, G.S. Seth, Naveen Joshi, C.T. Srinivasa</i> , Mixed convection flow of a viscoelastic fluid through a vertical porous channel influenced by a moving magnetic field with Hall and ion-slip currents, rotation, heat radiation and chemical reaction.....	147
<i>A. Benamar, F.Z. Mahjoubi, Goma A.M. Ali, F. Kzaiber, A. Oussama</i> , A chemometric method for contamination sources identification along the Oum Er Rbia river (Morocco)..	159
<i>Instruction to authors</i>	172